UNIVERSITY OF CALIFORNIA

SANTA CRUZ

CLOUDS AND HAZES IN EXOPLANETS AND BROWN DWARFS

A dissertation submitted in partial satisfaction of the
requirements for the degree of

Doctor of Philosophy

in

ASTRONOMY & ASTROPHYSICS

by

Caroline Victoria Morley

June 2016

The Dissertation of Caroline Victoria Morley
is approved:

_____

Professor Jonathan Fortney, Chair

_____

Dr. Mark Marley

_____

Professor Andy Skemer

_____

Dean Tyrus Miller
Vice Provost and Dean of Graduate Studies

Table of Contents

List of Figures

xxi

List of Tables

Abstract

Clouds and Hazes in Exoplanets and Brown Dwarfs

by

Caroline Victoria Morley

The formation of clouds significantly alters the spectra of cool substellar atmospheres from terrestrial planets to brown dwarfs. In cool planets like Earth and Jupiter, volatile species like water and ammonia condense to form ice clouds. In hot planets and brown dwarfs, iron and silicates instead condense, forming dusty clouds. Irradiated methane-rich planets may have substantial hydrocarbon hazes. During my dissertation, I have studied the impact of clouds and hazes in a variety of substellar objects. First, I present results for cool brown dwarfs including clouds previously neglected in model atmospheres. Model spectra that include sulfide and salt clouds can match the spectra of T dwarf atmospheres; water ice clouds will alter the spectra of the newest and coldest brown dwarfs, the Y dwarfs. These sulfide/salt and ice clouds potentially drive spectroscopic variability in these cool objects, and this variability should be distinguishable from variability caused by hot spots.

Next, I present results for small, cool exoplanets between the size of Earth and Neptune. They likely have sulfide and salt clouds and also have photochemical hazes caused by stellar irradiation. Vast resources have been dedicated to characterizing the handful of super Earths and Neptunes accessible to current telescopes, yet of the planets smaller than Neptune studied to date, all have radii in the near-infrared consistent with being constant in wavelength, likely showing that these small planets are consistently enshrouded in thick hazes and clouds.

For the super Earth GJ 1214b, very thick, lofted clouds of salts or sulfides in high metallicity (1000× solar) atmospheres create featureless transmission spectra in the near-infrared. Photochemical hazes also create featureless transmission spectra at lower metallicities. For the Neptune-sized GJ 436b, its thermal emission and transmission spectra combine indicate a high metallicity atmosphere, potentially heated by tides and affected by disequilibrium chemistry. I show that despite the challenges, there are promising avenues for understanding small planets: by observing thermal emission and reflected light, we can break the degeneracies and constrain the atmospheric compositions. These future observations will provide rich diagnostics of molecules and clouds in small planets.

Acknowledgments

This dissertation would not have been possible without the people surrounding and supporting me. First and foremost, I would like to thank Professor Jonathan Fortney for being an incredible thesis advisor for the past six years. From the time I began working with him, his support has been invaluable. He instilled not just scientific expertise but also the confidence I needed to be successful. His patience and thoughtful advice have shaped me into the scientist and person I am today. He also fostered a collaborative and dynamic research group, and I would like to thank the current and former Fortney research group members over the years, including Eric Lopez, Michael Line, Tyler Robinson, Daniel Thorngren, Kat Feng, Neil Miller, Chris Mankovich, Vivien Parmentier, Eliza Kempton, and Katie Morzinski.

I would like to thank my mentor and member of my thesis committee, Dr. Mark Marley. His unparalleled intuition for planetary atmospheres has been immensely valuable throughout my years working with him. I would also like to thank the other member of my thesis committee, Professor Andy Skemer, for guidance during my last year of my PhD and for showing me that the riskiest projects are the most fun. I would also like to thank Adam Burgasser for serving on my Qualifying Committee and writing postdoc application letters, Francis Nimmo for serving on my Qualifying Committee, and Heather Knutson for writing postdoc application letters.

I would like to thank the community in the Astronomy department at UC Santa Cruz for creating an intellectually vibrant place to do science. In particular, I thank the community of graduate students who have shaped this department into such a welcoming, supportive

environment.

I thank Scott Morrison for being my rock throughout these years. He has been the calm to balance the storm and without him I would not have made it this far. Thank you for listening to every practice talk, reading every paper, and removing every one of my over-exuberant commas.

I would like to thank my parents for their support, not just during my PhD but during all of the 22 years I have been in school. They have been there for me through the high points and the low, celebrating achievements and being voices of reason during the challenges. I also thank my sister Julia, for her support and, at low points, for reminding me that at least I didn't go to medical school.

I would like to thank my officemates through the years of my PhD, including Jennifer Burt, Claire Dorman, Angie Wolfgang, Justin Brown, Emily Cunningham, Eric Lopez, and Elizabeth Lovegrove. I am grateful for the conversations both serious and not, for always being there to read important emails before I send them, and for making these six years pretty fantastic.

The text of this dissertation includes reprints, included with permission of the listed co-authors, of the following previously published material:

- Morley, C. V., Fortney, J. J., Marley, M. S., Visscher, C., Saumon, D., & Leggett, S. K. 2012, ApJ, 756, 172

- Morley, C. V., Fortney, J. J., Kempton, E. M.-R., Marley, M. S., Visscher, C., & Zahnle, K. 2013, ApJ, 775, 33

- Morley, C. V., Marley, M. S., Fortney, J. J., Lupu, R., Saumon, D., Greene, T., & Lodders, K. 2014, ApJ, 787, 78

- Morley, C. V., Marley, M. S., Fortney, J. J., & Lupu, R. 2014, ApJ, 789, L14

- Morley, C. V., Fortney, J. J., Marley, M. S., Zahnle, K., Line, M., Kempton, E., Lewis, N., & Cahoy, K. 2015, ApJ, 815, 110

Chapter 1

Introduction

Over the first twenty years, the study of exoplanets has grown from a rush of initial discovery to a more expansive era of in-depth characterization. The number of known planets has quintupled during the last six years, now numbering over 1600 confirmed planets and nearly four thousand additional *Kepler* planet candidates. Current ground- and space-based instrumentation has proven capable of detecting the atmospheres of many of those planets, and those observations have provided at least as many questions as answers about these planets, which are strikingly more diverse that the planets studied for decades in our own solar system.

We are moving toward an understanding of exoplanet compositions, initially detecting molecules and now analyzing metal enhancements and elemental compositions like carbon-to-oxygen ratios, which provide insights into the formation mechanisms of planets. We are also studying the dynamics of atmospheres, including their heating and circulation. This characterization begins with low-hanging fruit like hot Jupiters and then progresses toward smaller planets on the way to studying habitability in temperate rocky planets. It has become increas-

ingly clear in the last decade that clouds and hazes both create barriers to and provide keys for

understanding atmospheric compositions, chemistry, and physics.

Brown dwarfs are key set of laboratories for developing our understanding of sub-

stellar atmospheres, as they have the temperatures of exoplanets but are observationally more

accessible. Brown dwarfs are the massive cousins to exoplanets, born as the low-mass tail of

star formation in molecular clouds. They never reach the core temperatures needed to fuse hy-

drogen into helium as stars, but they share the effective temperatures of young and middle-aged

exoplanets, cooling like a planet as they age. Brown dwarfs have now been discovered span-

ning temperatures from thousands of Kelvin to just $\sim$250 K, and we can easily obtain spectra

since most brown dwarfs lack a nearby host star. These favorable observations compared to

those obtainable for exoplanets mean that we can study the physics and chemistry of substellar

atmospheres in brown dwarfs in exquisite detail, likely a decade before we can obtain similar

results for exoplanets with the same temperatures.

In this PhD thesis, I will discuss the development of models to characterize substellar

atmospheres including the effect of clouds and hazes, which play an important role in shaping

their spectra. I will apply these simulations in six chapters, each chapter consisting of a paper

published in or submitted to the Astrophysical Journal or the Astrophysical Journal Letters, and

discussing objects spanning from brown dwarfs to super Earths in mass.

1.1 Observations of Transiting Exoplanet Atmospheres

There are four observational techniques currently used to probe transiting exoplanet atmospheres:

1. Transmission spectroscopy, in which a planet's apparent radius as a function of wavelength is measured during transit.

2. Thermal emission spectroscopy, in which a planet's flux is inferred by measuring the change in total light during the planet's occultation.

3. Phase curve photometry and spectroscopy, in which the planet's brightness is measured over a full or partial orbit.

4. High spectral resolution spectroscopy, in which the planet's spectral lines are measured at high spectral resolution to detect molecules and measure the planet's motion.

Here, I will focus on the first two techniques, transmission spectroscopy and thermal emission spectroscopy. These are the most common techniques used to study transiting planets and the techniques used in this work.

1.1.1 Transmission Spectroscopy

During a transit, light from a host star passes through the atmosphere of the transiting planet. Because the opacity of the atmosphere varies with wavelength, the radius of the planet will appear to vary with wavelength. The depth of features in the transmission spectrum scales as $N_H \times 2HR_p/R_*$, where N_H (the number of scale heights probed) is set by the opacities in-

volved ($\sim$1–10), H is the atmospheric scale height, R_p is the planetary radius, and R_* is the stellar radius (Seager and Sasselov, 2000; Hubbard *et al.*, 2001). The scale height is defined as

$$H = \frac{kT}{Mg},\tag{1.1}$$

where k is Boltzmann's constant, T is the atmospheric temperature, M is the mean mass of a molecule, and g is the acceleration due to gravity on the planetary surface. The size of features is thus expected to be inversely proportional to the mean molecular weight μ of the atmosphere. By measuring the depth of transit features, we probe the mean molecular weight of the atmosphere and can thus probe whether the atmosphere is H/He-rich ($\mu \sim 2.3$) or a higher mean molecular weight H_2O ($\mu \sim 18$) atmosphere (Miller-Ricci *et al.*, 2009).

This technique was first demonstrated successfully in Charbonneau *et al.* (2002), in which the 589.3 nm sodium doublet was detected in the atmosphere of HD 209458b using the STIS instrument on *HST*. Since that pioneering work, we have measured transmission spectra of dozens more hot Jupiters in both optical and near-infrared wavelengths. There have been challenges as the field has blossomed; some early detections of molecules (e.g., Swain *et al.*, 2008) have not stood the test of time, as measurements using instruments like NICMOS on *HST* have been plagued by systematic effects that overwhelm the tiny signatures from the atmospheres themselves (Gibson *et al.*, 2011).

The installation of Wide-Field Camera 3 (WFC3) on *HST* during the last servicing mission in 2009 has increased our sensitivity to measure transmission spectra of exoplanets (Berta *et al.*, 2012; Gibson *et al.*, 2012; Ranjan *et al.*, 2014). A specialized mode of observing

for transiting planets called 'spatial scan mode,' where the star is allowed to drift over the frame through the observation, has further improved precision, and these observations are now much less plagued with systematic effects that overwhelm the atmospheric signal (Deming *et al.*, 2013; Wakeford *et al.*, 2013; Kreidberg *et al.*, 2014a). Now armed with the technical capability of detecting molecular features in transmission spectra, groups set out to observe the spectra of planets spanning a range of sizes and temperatures.

1.1.1.1   Clouds and/or Hazes in Hot Jupiters

A variety of hot Jupiters have now been observed in transmission, and they appear to have diverse characteristics (Pont *et al.*, 2012; Gibson *et al.*, 2012; Wakeford *et al.*, 2013; Ranjan *et al.*, 2014; Sing *et al.*, 2016). The sample of 10 targets presented recently in Sing *et al.* (2016) has a range of planetary temperature, surface gravity, mass and radii, and the data have relatively uniform wavelength coverage from 0.3 to 5 μm from *HST* and Warm *Spitzer*. Their spectra are remarkably heterogenous, showing different slopes, different strengths of alkali features in the optical, and different strengths of water vapor absorption in the near-infrared. This variety is interpreted to show a continuum from clear to cloudy or hazy (Sing *et al.*, 2016). Clouds and hazes obscure features in the optical and near-infrared and can cause slopes towards blue wavelengths in the optical due to the higher efficiency of scattering by small particles at shorter wavelengths.

It has not yet been determined *why* hot Jupiters show this variety in their appearances, or what drives the physical differences between these objects. Yet, if their effect is not included in models used to interpret transmission spectrum data, clouds and hazes can change our in-

terpretation of the compositions of planets. For example, while Madhusudhan *et al.* (2014) interpreted muted water vapor features as being due to a sub-solar water abundance, Benneke (2015) show that it is more likely that these planets have standard compositions but are affected by clouds or hazes. This cautionary tale demonstrates that clouds and hazes, while informative and interesting themselves, must be accounted for to properly constrain the gas composition of an atmosphere from its transmission spectrum.

1.1.1.2 The Vexing Case of GJ 1214b

Pushing this transmission technique to characterize super Earths and Neptunes is a major goal, both using current instrumentation and future telescopes like the James Webb Space Telescope (*JWST*). Smaller planets are more of a challenge to study because of their small transit depths. However, small planets around small stars have a larger transit depth, allowing us to use this technique more easily. It is for these reasons that one of the first major campaigns with WFC3 was to measure the transmission spectrum of the super Earth GJ 1214b. GJ 1214b is the first planet discovered by the MEarth survey, a ground-based transit survey designed to find planets around M dwarfs (Charbonneau *et al.*, 2009). It orbits a small star (spectral type M4.5), which has a radius of just 0.216 R_{Sun}. This means that even though the planet is only 2.7 R_{Earth}, the transit depth is over 1%. Since the system is only 14.6 parsec away, the *H* band apparent magnitude is ∼9. The deep transit depth and relative brightness of the star make GJ 1214b the most favorable small planet for atmospheric characterization, and as such it was targeted extensively.

Predictions based on atmospheric models suggested that cloud-free H/He atmospheres

would have detectable transmission spectrum signatures (Miller-Ricci and Fortney, 2010), while high mean molecular weight atmospheres would appear to be featureless. GJ 1214b has a mass and radius that could be consistent with either a rocky core with a low mean molecular weight H/He atmosphere, or with a volatile rich water ice composition (Nettelmann *et al.*, 2011; Rogers and Seager, 2010), so the first observations were designed to break this composition degeneracy and determine the bulk composition of the planet. When the first observations showed a featureless spectrum (Bean *et al.*, 2010; Désert *et al.*, 2011; Crossfield *et al.*, 2011; Croll *et al.*, 2011; Berta *et al.*, 2012; de Mooij *et al.*, 2012; Murgas *et al.*, 2012; Teske *et al.*, 2013; Fraine *et al.*, 2013), this was largely interpreted as a potentially very high mean molecular weight atmosphere.

However, these featureless spectra could also be interpreted as a H/He-rich atmosphere with clouds or hazes obscuring the predicted features. Howe and Burrows (2012) showed that by placing haze layers composed of polyacetylene, tholin, or sulfuric acid with different ad hoc number densities, particle sizes, and pressure levels for each material, a hydrogen-rich atmosphere with a haze layer is generally consistent with the observations.

Chapter 3 of this work, published first in 2013 (Morley *et al.*, 2013), delves more deeply into this problem. We include clouds and hazes that are expected to form in cool atmospheres, including sulfide and salt clouds and photochemical carbon-based hazes. The clouds are modeled within a modified version of the Ackerman and Marley (2001) cloud model, described in more detail in Section 1.3.3. The photochemical hazes are calculated using the results of photochemistry models (Miller-Ricci Kempton *et al.*, 2012; Zahnle *et al.*, 2009a). Our results showed that a variety of physically plausible clouds and hazes could cause the observed

featureless transmission spectrum of GJ 1214b. Disentangling high mean molecular weight atmospheres from cloudy H/He-rich atmospheres would take higher S/N observations.

An intensive campaign was launched, using 60 orbits of *HST* time to measure 15 additional transits of GJ 1214b with *HST*/WFC3, covering the water absorption feature between 1.1 and 1.7 μm. These additional observations combined are at high enough precision that a high mean molecular weight atmosphere composed of water, methane, or carbon dioxide could have been detected. Instead, the observations revealed a featureless spectrum to high precision, indicating that GJ 1214b requires opacity from clouds or hazes to obscure its transmission spectrum, regardless of the overall composition of its atmosphere (Kreidberg *et al.*, 2014a).

1.1.1.3 Clouds and Hazes in Other Small Planets

Around the same time as GJ 1214b's featureless spectrum was measured, results for two other small planets using the same instrument also showed evidence for muted transmission spectra. Observations of the super Earth HD 97658b, and the Neptune-sized GJ 436b and GJ 3470b have featureless spectra measured with WFC3 within their measurement uncertainties (Knutson *et al.*, 2014a,b; Ehrenreich *et al.*, 2014). In fact, the only planet in the super-Earth to Neptune mass range for which a statistically significant feature has been measured is HAT-P-11b. Water vapor absorption was detected using WFC3 with an amplitude of 250 parts per million (Fraine *et al.*, 2014). The size of this feature is consistent with a H/He-rich atmosphere with a somewhat more metal-enhanced atmosphere than Neptune's (several hundred times solar metallicity composition) or a less enriched atmosphere with features muted by clouds or hazes.

Chapter 6 of this work considers how best to move forward to characterize these

small planets, which all appear to be metal-enhanced and/or cloudy/hazy, limiting our ability to measure features in transmission to learn about their atmospheres. We determine which planetary properties can lead to the very flat transmission spectra observed for GJ 1214b itself, and additionally determine what properties would be predicted for somewhat cooler (450 K) and hotter (>1000 K) planets. We predict the transmission spectra at longer wavelengths (accessible to *JWST)*, as well as the thermal emission and reflected light from both cloudy and hazy small planets. We find that there are promising avenues moving forward to distinguish between cloudy and hazy planets, measure molecular features, and characterize these enigmatic planets.

1.1.2 Thermal Emission Spectroscopy

The second technique that has been used to study transiting planets is thermal emission spectroscopy, where instead of probing transmission of starlight through the limb of the planet's atmosphere, we measure the thermal flux emerging from the planet itself. Dozens of planets have also been observed in thermal emission with secondary eclipse spectroscopy or spectrophotometry. With this technique, a star is observed as a planet is occulted by the star in its orbit. Just before the occultation, the planet is full-phase from Earth and we observe the light from both the star and the planet. During the occultation, we observe the flux from the star alone. By differencing the observations inside and outside of the time of occultation, we can determine the flux of the planet itself.

The powerhouse for this technique has been the *Spitzer* Space Telescope, both during its cryogenic operation and after its cryogenic mission operating as Warm *Spitzer*. In part because *Spitzer* was never designed for the high precision photometry on bright stars necessary

9

for observing transiting planets, much like the early transmission spectra observations, the early years of secondary eclipse observations were plagued with systematic effects that took special observing and data analysis techniques to overcome. Techniques such as pixel-mapping have reduced systematic effects from effects like intrapixel sensitivity.

Emission photometry from *Spitzer* has been used to infer planet characteristics such as temperature inversions (e.g., Knutson *et al.*, 2008), disequilibrium chemistry (Stevenson *et al.*, 2010), and non-solar C/O ratio (Madhusudhan *et al.*, 2011b). However, many of these initial results have not stood the test of time. Repeating observations and reanalyzing older observations has changed interpretations. For example, Diamond-Lowe *et al.* (2014) reanalyzed the full set of publicly available data for HD 209458b, and find that there is no longer evidence for a thermal inversion.

It has therefore become clear to the community that repeating observations to understand systematic errors is critical. In fact, Hansen *et al.* (2014) found that the majority of the 44 planets with published eclipse measurements have underestimated errors, and their measured photometry does not contain sufficient information to distinguish them from blackbodies.

1.1.2.1   Case Study: GJ 436b

One of the planets for which *Spitzer* observations have been repeated multiple times is GJ 436b. To date a total of 18 secondary eclipses and 8 transits have been observed with *Spitzer*, along with 7 transits with *HST* (Deming *et al.*, 2007; Demory *et al.*, 2007; Gillon *et al.*, 2007a; Stevenson *et al.*, 2010; Beaulieu *et al.*, 2011; Knutson *et al.*, 2011, 2014a). GJ 436b is a Neptune-sized planet discovered using the radial velocity method by Butler *et al.* (2004).

Though the discovery paper had a non-detection of the transit, it was discovered to transit by Gillon *et al.* (2007b) and at the time was the smallest transiting planet. Its high planet-to-star radius ratio made it a favorable target for observations; in fact it was the smallest planet found while *Spitzer* was operating cryogenically, and thus the smallest object for which we have observations from 3.6 to 24 μm.

The first secondary eclipse measurements of GJ 436b were taken at 8 μm (Deming *et al.*, 2007; Demory *et al.*, 2007). The eclipses timing revealed that GJ 436b has a high eccentricity, $\sim$0.15, which remains a surprising result since tidal circularization timescales should be fast for a planet in a short orbit like GJ 436b, and no companion to pump the eccentricity has been found to date.

Stevenson *et al.* (2010) published the first multi-wavelength thermal emission spectrum of GJ 436b, measuring photometric points at 3.6, 4.5, 5.8, 8.0, 16, and 24 μm. From these observations, Stevenson *et al.* (2010) concluded that its atmosphere may be in chemical disequilibrium, surprisingly rich in CO and CO_2 compared to the CH_4-rich composition that would be expected in equilibrium. Additional studies have reanalyzed these observations and observed additional secondary eclipses (Knutson *et al.*, 2011; Lanotte *et al.*, 2014); this reanalysis reveals a somewhat shallower 3.6 μm eclipse, but interpretations still favor high CO and CO_2 and low CH_4 abundances.

It has been a challenge to find self-consistent models that adequately explain GJ 436b's thermal emission. Line *et al.* (2011) used disequilibrium chemistry simulations to model the effect of photochemistry, but they were not able to reproduce the low observed methane abundance. Moses *et al.* (2013) found that high metallicities (230–1000$\times$ solar favor the high

CO and CO_2 abundances inferred from the observations. Agúndez *et al.* (2014), noting the high eccentricity of GJ 436b, study the effect of tidal heating deep in the atmosphere on the chemistry and find that efficient tidal heating and high metallicities fit the observed photometry best.

We build on these previous studies in Chapter 7 of this work, fitting the full set of observed *Spitzer* data as well as the transmission spectrum measured with *HST*/WFC3 with both self-consistent models and retrieval models. We find using this powerful set of modeling tools there is evidence for both very high ($\sim 1000\times$ solar) metallicity and tidal heating in its atmosphere. Observations of its thermal spectrum with *JWST* will provide crucial tests of these results, building on this rich and puzzling set of broadband *Spitzer* photometry.

1.2   Observations of Brown Dwarf Atmospheres

Transiting planet science has exploded during the last ten years, but our understanding of their atmospheres has built on a decades-long campaign to understand the atmospheres of brown dwarfs. The first confirmed brown dwarf was announced in tandem with the discovery of 51 Peg b, the first exoplanet around a main sequence star, at Cool Stars 9 in 1995. Since then the fields of exoplanet and brown dwarf characterization have emerged in parallel. Unlike for exoplanets, where spectra are low resolution and often low S/N, brown dwarfs are comparatively easy to observe with standard spectrographs on 4 to 8 meter class telescopes. Hundreds of brown dwarfs now have measured spectra in the optical and near-infrared.

While exoplanets are just gaining enough high fidelity observations to start classify-

ing planets into groups based on observations of their atmospheres, brown dwarf research has always been centered on classifying and comparing objects using their spectra. While in early brown dwarf research, theory led observations, predicting their existence and their spectra, in a modern era, brown dwarf science is observation-driven with theorists working to explain the plethora of observations. Brown dwarf science revolves around spectral typing of objects by comparing their spectra to standard templates for each spectral type. Deviations from those standards indicate different properties in those atmospheres, such as low gravity or unusual dustiness.

Our current understanding of brown dwarf evolution is the following. Brown dwarfs are born in molecular clouds like stars, and at their time of formation have high effective temperatures; all brown dwarfs initially have high enough effective temperatures to be classified as M dwarfs. They cool over time and as they cool, they move through the spectral sequence (Burrows *et al.*, 1997). More massive brown dwarfs will initially have higher temperatures and cool more slowly than less massive brown dwarfs, such that by 10 Gyr an object at the high end of the brown dwarf mass range (75 M_J or equivalently 0.07 M_{Sun}) will have a temperature of $\sim$ 1300 K, whereas a low-mass brown dwarf (13 M_J would have a temperature cooler than 300 K (Burrows *et al.*, 1997). Some examples of M, L, and T dwarf spectra as well as Jupiter's spectrum are shown in Figure 1.1.

M dwarfs have spectral features from metal hydrides and oxides such as FeH, CrH, and TiO. These bands wane in importance as the brown dwarf cools and becomes an L dwarf, due to the condensation of these materials into cloud particles in the atmosphere, while molecular bands from gases like H_2O and CO increasingly carve the emergent spectra. As the refractory

13
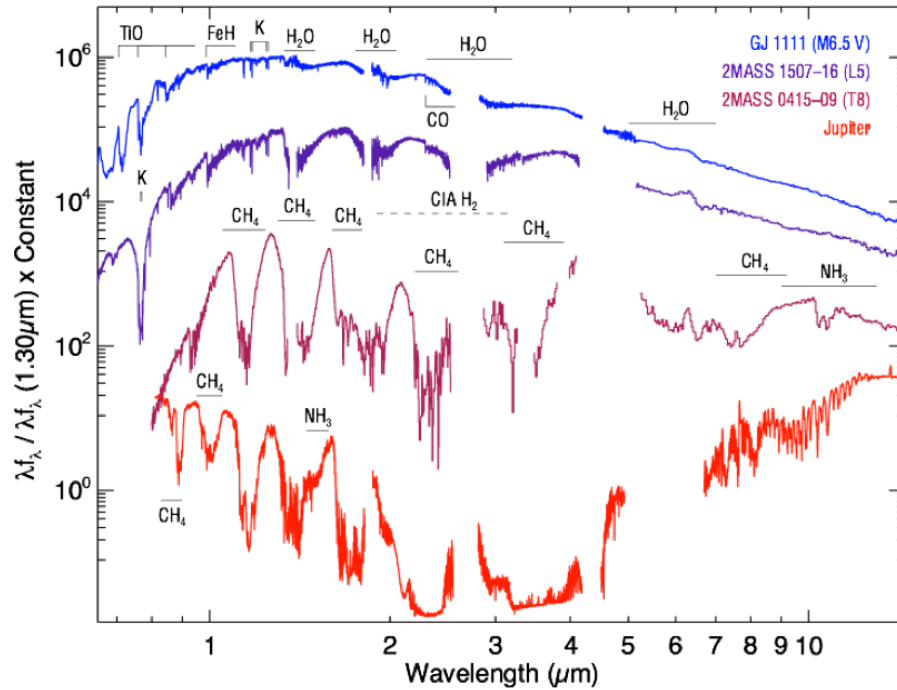
Figure 1.1: The evolution of spectra from late M dwarfs to cold planets. Late M dwarfs are similar to blackbodies with features from metal hydrides and oxides, alkalis, and molecules like water. L dwarfs have more pronounced features, including strong pressure-broadened alkali lines. T dwarfs see the emergence of methane bands throughout the spectrum and have deeply carved, non-blackbody-like spectra, looking most similar to Jupiter, which has similar features but is only ∼130 K. Figure courtesy M. Cushing.

clouds of materials like Al_2O_3, Fe, and Mg_2SiO_4 form, they redden the near-infrared spectra as shown in Figure 1.2, suppressing flux within windows between molecular bands where, in the absence of clouds, we would see deep hot layers. These means that from the first discovery and characterization of L dwarfs, clouds were a critical component of spectral models. Many cloud modeling approaches emerged to deal with cloud condensation; these approaches can vary in both the big picture and the details (see Section 1.3).

As a brown dwarf cools further, the chemistry and cloud properties change. At effec-

tive temperatures around 1300 K, the dominant C-bearing gas in chemical equilibrium in the photosphere changes from CO in hotter objects to CH_4 in colder objects. Objects begin to be classified as T dwarfs when methane absorption bands appear in the near-infrared. At the same effective temperature, clouds dramatically decrease in optical depth. These changes in chemistry and cloud properties cause a brown dwarf to brighten at wavelengths in the near-infrared such as *Y* and *J* band, becoming bluer in the near-infrared.

Early T dwarfs appear to be almost completely cloud-free, with little evidence for cloud opacity. The reason for this dramatic change from very cloudy to completely clear over a small ($\sim$100 K) temperature range is not well understood. The mechanism seems to involve the breakup of clouds (rather than a more gradual dispersal or sinking), causing some brown dwarfs in the L/T transition to be rather dramatically variable at the wavelengths where clouds affect the flux the most (e.g. *J* band) (Radigan *et al.*, 2012, 2014).

The story gets less well understood as objects cool further to late T dwarfs and Y dwarfs. Some objects at these temperatures appear to show the redder near-infrared colors typical of cloudier objects. This emergence of redder objects coincides with the condensation temperatures of the next major species to condense in substellar atmospheres: the alkali metals, which condense into alkali sulfides and salts (e.g. Na_2S, KCl) (Visscher *et al.*, 2006). In Chapter 2, first published in Morley *et al.* (2012), we include for the first time the formation of these sulfide and salt clouds in cool substellar atmospheres. We find that with thin (f_{sed}=4–5) salt and sulfide clouds we are able to reproduce the near-infrared spectra of these red cool objects. These results mean that even for T dwarfs, thought to be cloud-free, we may still have to include opacity of thin clouds in their atmospheres.
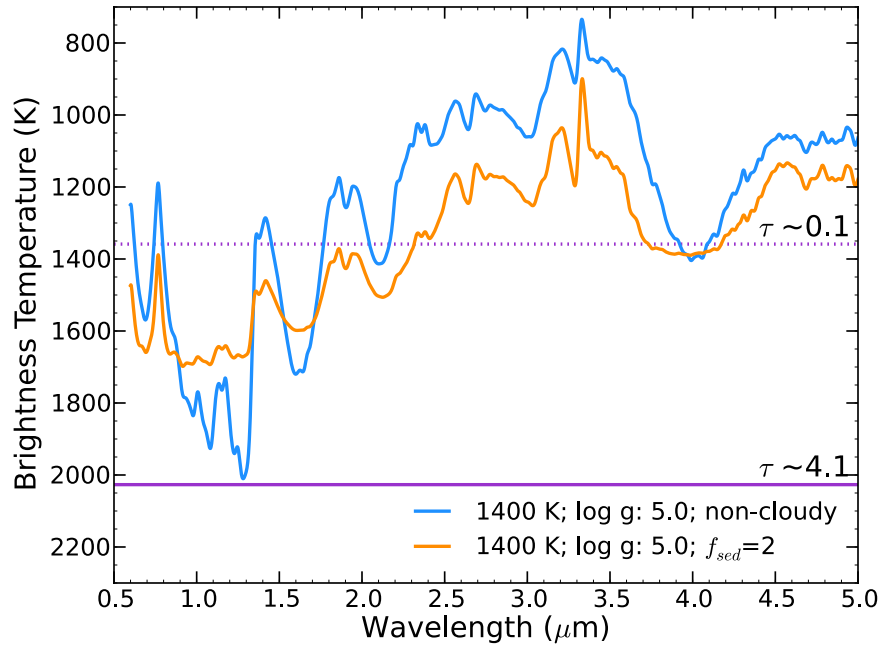
Figure 1.2: Effect of clouds on brown dwarf spectra. Brightness temperatures of two models with effective temperatures of ∼1400 K are shown. The cloud-free model is shown in blue; in the cloud-free model, deep, hot layers (1800–2000 K) are probed in the near-infrared (1–1.5 μm). The location of the forsterite cloud is indicated by purple lines, showing the top (defined as $\tau_{\text{cloud}} = 0.1$ and bottom of the cloud layer. The cloudy model is shown in orange; the cloud opacity limits the depth probed in the near infrared and warms the atmosphere, causing higher brightness temperatures at longer wavelengths.

Indeed, since the publication of Morley et al. (2012), there have been other indications that sulfide and salt clouds may be forming in cool T dwarfs. Mid-late T dwarfs have now been observed to show spectral variability (e.g., Buenzli et al., 2012), which may be another indication that they have thin clouds. In addition, retrieval models have shown a systematic depletion of sodium and potassium abundance as objects cool through the T dwarf sequence, providing additional evidence that the alkalis are condensing and being removed from the gas phase (Line et al., 2015).

In 2011, the first brown dwarfs cooler than effective temperatures of ∼500 K were discovered using the *Wide-Field Infrared Survey Explorer* (*WISE*) (Cushing *et al.*, 2011). These objects, dubbed Y dwarfs, begin to show evidence of ammonia absorption bands in the near-infrared. Most of the objects in this spectral class are ∼350–450 K. However in 2014, Luhman (2014) discovered an object in the *WISE* dataset that appears to be colder than the Earth, around ∼250 K. These cold objects, with temperatures approaching those of the planets in our own solar system (e.g. Jupiter has an effective temperature of ∼130 K), are cold enough that volatiles like water ice will begin to condense in their atmospheres. Chapter 4 presents models of these Y dwarfs, from 200 to 450 K, including the effect of water ice condensation. We find that water clouds become optically thick in objects below ∼350–375 K. These coldest objects indeed must have planet-like masses (under 13 M_J) to have cooled to their observed temperatures within the age of the universe, so these present us with proxies for the types of distant planets that will be characterized with future reflected-light space-based coronagraphs like the Wide-Field Infrared Survey Telescope (*WFIRST*).

1.2.1 The Connection Between Brown Dwarfs and Giant Planets

Brown dwarfs have strong similarities to giant exoplanets, and as young brown dwarfs and directly-imaged planets have been discovered, the gap between brown dwarfs and planets has narrowed. Figure 1.3 shows a color-magnitude diagram containing both brown dwarfs and directly-imaged planets. The planets have many similarities to the brown dwarf population. There are also important differences; for a given spectral type, the near-infrared colors of planets are systematically redder than brown dwarfs of a corresponding spectral type. This has been

used as evidence of differences in cloud properties between old field brown dwarfs and planets.

As young brown dwarfs with the masses of planets have been discovered, it has become clear that isolated young brown dwarfs look very similar to their planetary counterparts (Liu *et al.*, 2013); there exists a population of free-floating objects with the red colors of these planetary companions. These similarities indicate that gravity likely has a strong role in cloud properties. The physical reasons for this effect needs to be better understood as more of these objects, both companions and free-floating objects, are found. As described in Section 8.3, this will be a major area for applications of cloud models in the future, and critical for understanding planets over their lifetimes.

1.3   Modeling Clouds and Hazes In Brown Dwarfs and Exoplanets

It is clear from observations of both exoplanets and brown dwarfs that clouds play a major role in substellar atmospheres. Many of the current open questions concerning observations of both types of objects lie in our more complete understanding of clouds and hazes. A number of techniques have been developed to model these clouds and in turn fit spectra of their thermal emission, transmission spectra, and reflected light spectra.

Condensation of various species into clouds has been predicted to play an important role in brown dwarf atmospheres since before the first brown dwarfs were even discovered (Lunine *et al.*, 1986). As an atmosphere cools, different materials are expected to transition from gas-phase to solid- or liquid-phase, just as water vapor in cooling air on Earth condenses to form water ice or liquid. In brown dwarfs and planets, the materials condensing range from

refractory materials like corundum (Al_2O_3), silicates (Mg_2SiO_3, Mg_2SiO_4), and Fe, to alkali salts and sulfides (MnS, Na_2S, KCl, ZnS), to volatiles (H_2O, NH_3).

1.3.1 Physics and Chemistry of Cloud Formation

Cloud formation is complex. It involves hydrodynamics, radiation, and convection, as well as particle nucleation and growth, sedimentation, and sticking properties. Many of these aspects are not well understood. In fact, even in Earth climate models, clouds remain one of the biggest sources of uncertainty; for example, clouds can either heat or cool the atmosphere depending on the details of their properties. In exoplanets and brown dwarfs, the clouds are made, for the most part, of exotic materials that are even less well-studied in the conditions in which they are forming clouds.

Cloud formation is generally believed to start with seed particles in the atmosphere; this is because to truly homogeneously nucleate from the gas phase into liquid or solid phase, highly supersaturated conditions must exist. Heterogeneous nucleation onto small aerosols requires very low super saturation, and in practice is the primary nucleation process in solar system planets (Rossow, 1978). This process will occur for a given species at temperatures and pressures where it is cold enough that the vapor pressure of the gas exceeds the saturation vapor pressure. The details of this process, including the speed at which this condensation occurs and the rate at which particles grow, are treated somewhat differently by different modeling approaches.

Once a cloud particle has formed, it will settle gravitationally in the atmosphere, to the planet's surface if a surface exists or to a hotter layer of the atmosphere where it evaporates

again (the latter is the only case we consider for the brown dwarfs and super Earths we model in this work). Convection and mixing in the atmosphere loft the gas back up to cooler layers again, where it will condense once more.

1.3.2 Approaches to Modeling Clouds in Substellar Atmospheres

There are several main approaches to modeling clouds. These treat the microphysics of cloud formation in a variety of levels of detail, from kinetics models that trace each step of cloud nucleation, growth, and settling to parameterized models that reduce the number of free parameters in the model and required computational times.

The first approach, led by Helling & Woitke for brown dwarfs, treats the microphysics in a detailed way, attempting to determine the formation rates of cloud particles, their locations in the atmosphere, and the heterogeneous compositions of cloud particles as different materials condense onto them (Helling and Woitke, 2006; Helling *et al.*, 2008a; Witte *et al.*, 2009, 2011; de Kok *et al.*, 2011). They model the detailed physics of grain growth/evaporation, sedimentation in phase non-equilibrium, element deletion, and their interactions. In practice, they insert seed particles at the tops of planetary atmospheres and trace their compositions, sizes, etc. as they sink through the atmosphere, condensing other materials onto them to form 'dirty grains.'

The other branch of cloud modeling imagines an atmosphere in which gas is mixed from the deep atmosphere up to the temperature at which is begins to condense: the cloud base. Early cloud models treated two limiting cases of cloud formation. For example in the 'dusty' and 'cond' prescriptions, clouds were treated as if they were in chemical equilibrium with the gas phase, but their opacity was only included in the 'dusty' models (Allard *et al.*, 2001).

The modern picture also includes settling of particles. Cloud particles and vapor are mixed upwards by turbulent mixing in the atmosphere, while grains settle downwards as they form, with larger grains settling at higher speeds. In essence this approach is finding an equilibrium where the mixing rates upwards are equal to the falling rates downwards, modeling the 3D atmosphere in a parameterized 1D sense. This is computationally efficient and allows cloud models to be calculated in tandem with a radiative-convective equilibrium model to calculate pressure-temperature profiles. As such, this approach has been the favored approach by most groups to model large grids of spectra used to compare with observed brown dwarfs (Allard *et al.*, 2003, 2007; Ackerman and Marley, 2001; Marley *et al.*, 2002; Cooper *et al.*, 2003).

1.3.3 The Ackerman and Marley (2001) Cloud Model

The Ackerman and Marley (2001) model is the approach that is employed in the cloud modeling in this thesis, and so I will describe it in more detail here.

There are two versions of the Ackerman and Marley (2001) model that are used throughout our work. One version is coupled to the radiative transfer calculations, so a converged model will have a temperature structure that is self-consistent with the clouds. The other version is a stand-alone cloud model, which calculates the cloud distribution for a given pressure-temperature profile, without recalculating the profile in radiative-convective equilibrium.

The Ackerman and Marley (2001) approach avoids treating the microphysical processes forming clouds in brown dwarf and planetary atmospheres. Instead, it calculates a mass balance: both gas and condensate are mixed upwards by turbulent mixing in each layer of the

atmosphere, while condensates are transported downward by sedimentation. This balance is achieved using the equation

$$-K_{zz}\frac{\partial q_t}{\partial z} - f_{\text{sed}}w_*q_c = 0, \tag{1.2}$$

where K_{zz} is the vertical eddy diffusion coefficient, q_t is the mixing ratio of condensate and vapor, q_c is the mixing ratio of condensate, w_* is the convective velocity scale, and f_{sed} is a parameter that describes the efficiency of sedimentation in the atmosphere.

Solving this equation allows us to calculate the total amount of condensate in each layer of the atmosphere. We calculate the modal particle size using the sedimentation flux and by prescribing a lognormal size distribution of particles, given by

$$\frac{dn}{dr} = \frac{N}{r\sqrt{2\pi}\ln\sigma}\exp\left[\frac{\ln^2(r/r_g)}{2\ln^2\sigma}\right] \tag{1.3}$$

where N is the total number concentration of particles, r_g is the geometric mean radius, and σ is the geometric standard deviation. We fix σ at 2.0 and calculate the falling speeds of particles within this distribution assuming viscous flow around spheres (and using the Cunningham slip factor to account for gas kinetic effects). We calculate the other parameters in equation 6.1 (K_{zz} and w_*) using mixing length theory and by prescribing a lower bound for K_{zz} of 10^5 cm^2/s, which represents the residual turbulence due to processes such as breaking gravity waves in the radiative regions of the atmosphere.

This process allows us to calculate the mode particle size in each layer of the atmosphere using calculated or physically motivated values for all parameters except for the free

22

parameter f_{sed}. In general, we find larger particles (which have higher terminal velocities) in the bottom layers of a cloud and smaller particles (which have lower terminal velocities) in the upper layers. A high sedimentation efficiency parameter f_{sed} results in vertically thinner clouds with larger particle sizes, whereas a lower f_{sed} results in more vertically extended clouds with smaller particles sizes. As a result, a higher f_{sed} corresponds to optically thinner clouds and a lower f_{sed} corresponds to optically thicker clouds.

The Ackerman and Marley (2001) cloud model code computes the available quantity of condensible gas above the cloud base by comparing the local gas abundance (accounting for upwards transport by mixing via K_{zz}) to the local condensate vapor pressure p_{vap}. In cases where the formation of condensates does not proceed by homogeneous condensation we nevertheless compute an equivalent vapor pressure curve.

1.3.4   Effect of Clouds on Substellar Atmospheres

When clouds form in substellar atmospheres, they affect the atmosphere in a number of different ways. First, they increase the overall opacity of the atmosphere; this means that for a self-luminous object with a given effective temperature, the pressure-temperature profile of the atmosphere is hotter. This has a number of effects on an object's spectrum. At wavelengths where there is little gas opacity, in a cloud-free object flux will emerge from deep, hot layers of the atmosphere. Clouds increase the opacity at these wavelengths, which means that a cloudy object will be fainter than a cloud-free object. In contrast, at wavelengths where there is more significant gas opacity, it is the gas, not the clouds that limit how deeply we can see. Since the pressure-temperature profile is warmed by the cloud, the cloudy object will be brighter than

a cloud-free object. These factors mean that in general, cloud-free objects will have stronger absorption features in their thermal emission spectra, whereas cloudy objects will have smaller features and become more like a blackbody with the effective temperature of the cloud-top.

At the same time, clouds are often efficient scatterers and typically increase the overall albedo of a planet. For exoplanets that are heated from the top by light from their host stars, clouds can actually cool the planet's pressure-temperature profile rather than warming it, because light is reflected from the cloud tops before it is absorbed by gases in the atmosphere to heat the atmosphere. The balance of these effects is important for understanding the energy budget of planetary atmospheres. The albedo spectrum contains information about the cloud composition (which changes its scattering properties), the cloud top height, and the abundances of gaseous absorbers in the atmosphere.

Lastly, for transmission spectra, planets with clouds at high altitudes always have smaller features than cloud-free planets. Clouds can have a stronger effect on transmission spectra than on thermal emission spectra because of the longer slant path length through the planet's terminator (Fortney, 2005). Since transmission spectra probe lower pressures in the atmosphere, the altitude of the cloud is the most important factor in determining the effect of clouds on spectra.

1.3.5 Modeling Photochemical Hazes in Substellar Atmospheres

Photochemical hazes form in the atmospheres of all of the solar system's giant planets (e.g. Gautier and Owen, 1989) and therefore it is likely that they form in some subset of exoplanets as well. However, the atmospheres of many of the planets found to date are very

different environments from solar system planets, so the role of photochemistry in these planets remains very much an open question.

Solar system giant planet atmospheres are cool and methane-dominated. Due to its large UV photodissociation cross section, methane breaks apart in the upper atmosphere of irradiated planets and produces rich carbon chemistry in the atmosphere. Models that include UV dissociation of methane find that molecules such as C_2H_2, C_2H_4, C_2H_6, CH_3, HCN, and C_6H_6 exist in far greater abundance than would be expected from chemical equilibrium calculations (Yung *et al.*, 1984; Zahnle *et al.*, 2009a; Moses *et al.*, 2011; Miller-Ricci Kempton *et al.*, 2012). In very cold planets like Uranus and Neptune, molecules like C_2H_2 condense directly into solid particles, creating an acetylene haze in the atmosphere (Marley and McKay, 1999a). In warmer exoplanets such as GJ 1214b, simple molecules like C_2H_2 are too volatile to condense; however, it is possible that these volatile molecules continue to interact chemically and form larger hydrocarbons which would condense in a warmer atmosphere. The pathways for this putative haze formation require both theoretical and laboratory work to better understand.

Our approach to understand the possible effect of hazes in planets like GJ 1214b was first presented in Morley *et al.* (2013). In this approach, we introduce a parameter f_{haze}, which is defined as the mass fraction of 'soot precursors' (C_2H_2, C_2H_4, C_2H_6, C_4H_2, and HCN) that become solid haze particles in the atmosphere. We calculate the abundance of soot precursors using disequilibrium chemistry codes including the effect of photochemistry (Zahnle *et al.*, 2009a; Miller-Ricci Kempton *et al.*, 2012; Line *et al.*, 2011) and place the resulting mass into particles, varying the mode particle size. The hazes are placed in the layers where the soot precursors form, effectively assuming low sedimentation rates in the atmosphere.

1.4 Structure of this Work

This introduction has demonstrated the importance of studying clouds and hazes in brown dwarf and exoplanet atmospheres and explained how those clouds and hazes are typically modeled. The following chapters consider clouds and hazes in greater detail. The chapters are presented in chronological order as they were written and published. Chapters 2, 4, and 5 consider clouds in brown dwarfs. Chapter 2 includes sulfide and salt clouds in T dwarf atmospheres for the first time and shows how including these clouds may improve fits between models and observed spectra. Chapter 4 includes water ice clouds in a grid of brown dwarf models for the newly discovered Y dwarfs, from 200–450 K. Chapter 5 discusses variability in T and Y dwarf atmospheres, determining that clouds and pressure-temperature profile perturbations can be distinguished by observing spectral variability. The remaining three chapters (3, 6, and 7) in the body of this thesis present results for super Earth and Neptune-sized transiting planets. Chapter 3 and 6 both focus on the prototypical super Earth GJ 1214b, which has been observed to have a featureless transmission spectrum. Chapter 7 considers both the transmission and thermal emission spectra of GJ 436b to determine the properties of this Neptune-sized planet. In Chapter 8, I discuss future steps and projects that will further our understanding of clouds in substellar atmospheres, to the eventual goal of characterizing the properties of a suite of exoplanets from Jupiter to Earth mass in detail.
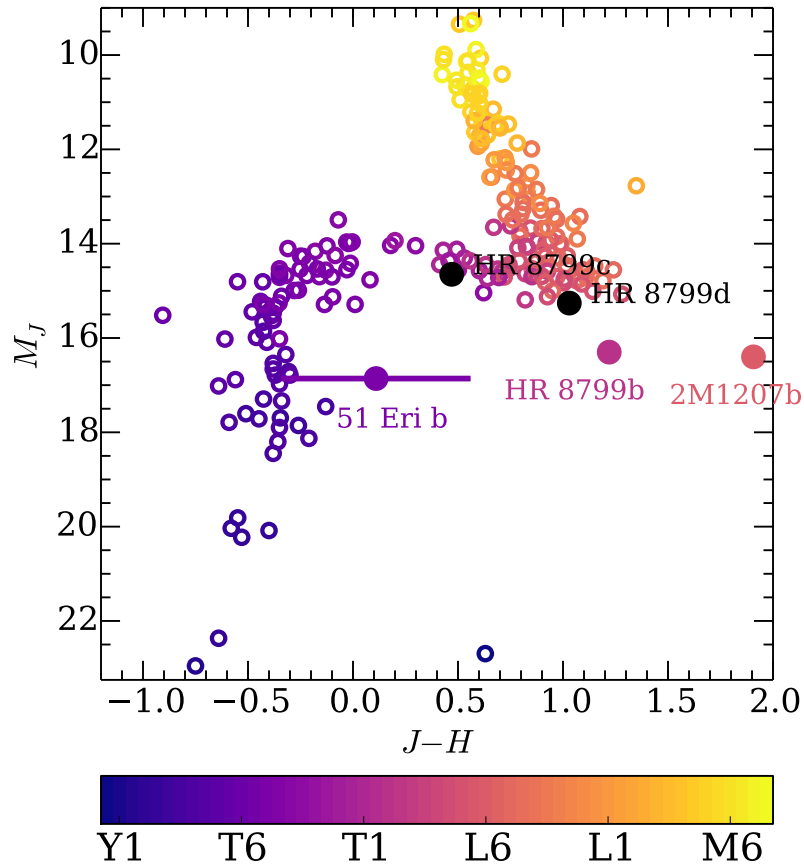
Figure 1.3: Color-Magnitude Diagram of Brown Dwarfs and Directly-Imaged Planets. Brown dwarfs are shown as open circles and directly-imaged planets are shown as filled circles with error bars. The color of the point indicates the spectral type of the object. Directly-imaged planets look similar but not identical to their brown dwarf brethren. In particular, for the few directly-imaged planets that have been spectral typed, their near-infrared colors appear to be redder than brown dwarfs of corresponding spectral types.
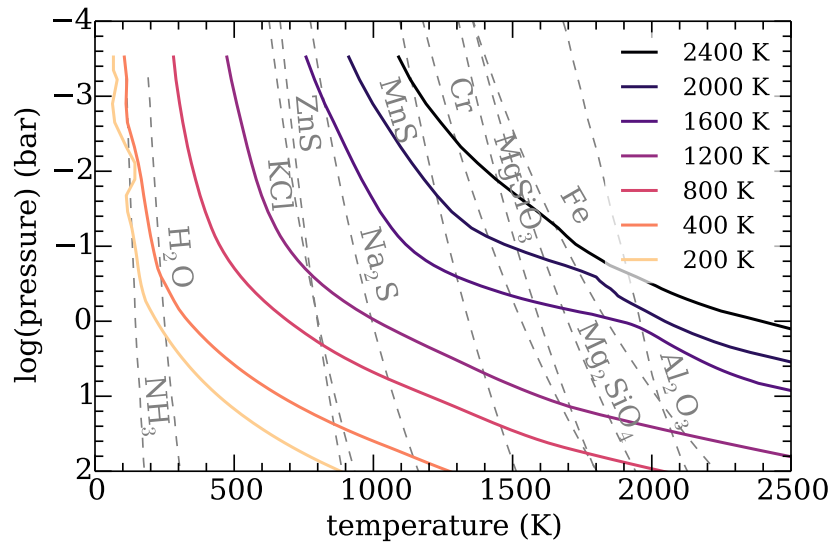
Figure 1.4: Pressure-temperature profiles and condensation curves from T_{eff}=2400 to 200 K.

28

Chapter 2

Neglected Clouds in T and Y Dwarf Atmospheres

2.1 Introduction

Since the first brown dwarfs were discovered two decades ago (Becklin and Zuckerman, 1988; Nakajima *et al.*, 1995), hundreds more brown dwarfs have been discovered using wide field infrared surveys. These substellar objects, too low in mass to fuse hydrogen in their cores, range in mass from ~ 13 to 75 M_{J} and are classified by their spectra into L, T, and most recently Y dwarfs (Kirkpatrick, 2005; Cushing *et al.*, 2011). Without hydrogen fusion as an internal energy source, brown dwarfs never reach a main-sequence state of constant luminosity; instead, they cool over time and will transition through the brown dwarf spectral sequence as different molecules and condensates form in their atmospheres. To model their atmospheres accurately requires an understanding of both the chemistry and physics of the materials that will

condense into clouds.

2.1.1 Modeling L and T Dwarfs

2.1.1.1 L dwarfs

Grain or condensate formation has been predicted to play an important role in L dwarf atmospheres since before the first brown dwarfs were discovered (Lunine *et al.*, 1986, 1989). Modern equilibrium thermochemical models predict that a variety of different condensates will form in L dwarf atmospheres (Fegley and Lodders, 1994; Lodders, 1999); by comparing models to observations, it is now well-established that a variety of refractory materials condense in L dwarfs (see, e.g. Tsuji *et al.*, 1996; Allard *et al.*, 2001; Marley *et al.*, 2002; Burrows *et al.*, 2006; Cushing *et al.*, 2008). The condensates that appear to dominate, based on the abundances of elements available to condense, are corundum (Al_2O_3), iron (Fe), enstatite ($MgSiO_3$), and forsterite (Mg_2SiO_4), and these species form cloud layers, removing atoms found within the clouds from the lower pressure atmosphere above (Fegley and Lodders, 1996; Lodders and Fegley, 2002; Lodders, 2003; Lodders and Fegley, 2006; Visscher *et al.*, 2010). Within windows between major molecular absorption bands, there is little gas opacity so, in models without clouds, the emergent flux comes from hotter layers deep within the atmosphere. Cloud opacity tends to suppress the flux in the near-infrared within these windows; a thick cloud layer limits the depth from which the planet can radiate, removing some of the flux at these wavelengths, and forcing it to other wavelengths (Ackerman and Marley, 2001).

When the opacity of these clouds is included in radiative-convective equilibrium models of brown dwarf atmospheres, the resulting model spectra match those of observed L dwarfs

(Cushing *et al.*, 2006, 2008; Saumon and Marley, 2008; Stephens *et al.*, 2009). Observations show that there is a range of colors for a given spectral type, which are believed to be associated with cloud variations or metallicity, but the details of this are not fully understood. Regardless, observed colors and spectra of L dwarfs cannot be well-matched without a significant cloud layer (Burrows *et al.*, 2006).

2.1.1.2 T Dwarfs

As a brown dwarf continues to cool, it undergoes a significant transformation in its observed spectrum when it reaches an effective temperature of approximately 1400 K. Objects cooler than this transitional effective temperature begin to show methane absorption features in their near-infrared spectra and, when these features appear, are classified as T dwarfs (Burgasser *et al.*, 2002; Kirkpatrick, 2005). Within a small range of effective temperature, the iron and silicate clouds become dramatically less important. Marley *et al.* (2010) show that this transition could potentially be explained by the breaking up of these cloud layers into patchy clouds, but the details of the transition are still very much unknown. However, the recent discovery of highly photometrically variable early T dwarfs suggests that cloud patchiness may indeed play a role (Radigan *et al.*, 2012; Artigau *et al.*, 2009). Regardless, as the clouds dissipate, the atmospheric windows in the near-infrared clear. Flux emerges from deeper, hotter atmospheric layers, and the brown dwarf becomes much bluer in $J - K$ color (see Figure 2.1).

2.1.1.3 History of Modeling T Dwarfs

The first T dwarf discovered, Gl229B (Nakajima *et al.*, 1995; Oppenheimer *et al.*, 1995), was modeled by Marley *et al.* (1996), Allard *et al.* (1996), Fegley and Lodders (1996), and Tsuji *et al.* (1996) using cloud-free models. These models assume that the condensate-forming materials have been removed from the gas phase, but do not contribute to the cloud opacity. Early T dwarfs are generally quite well-modeled using cloudless atmospheric models. However, recent observations of cooler T dwarfs suggest that T dwarfs of type T8 or later ($T_{\text{eff}} \lesssim$ 800 K) appear to be systematically redder in $J-K$ and $J-H$ colors than the cloudless models predict (see Figure 2.1).

One of the challenges of modeling brown dwarf spectra is the uncertainties in the absorption bands of major gas species such as methane and ammonia, as well as absorption due to collisional processes. Recent work by Saumon *et al.* (2012) has modeled a range of brown dwarfs using improved line lists for ammonia from Yurchenko *et al.* (2011) and an improved treatment of the pressure-induced opacity of H_2 collisions from Richard *et al.* (2012). This work improves the accuracy of model near-infrared spectra and reddens the $J-K$ colors of the model spectra with effective temperatures between 500 and 1500 K. The color shift is due to decreased opacity in K band from collision-induced absorption and, for $T_{\text{eff}} \lesssim$ 500 K model only, increased ammonia opacity in J band. However, these improvements do not change the colors enough to match the colors of the coolest T dwarfs.

Clouds are a natural way to redden near-infrared spectra. Cloud opacity limits the emergent flux most prominently in J band, so it reddens the $J-K$ and $J-H$ colors of the
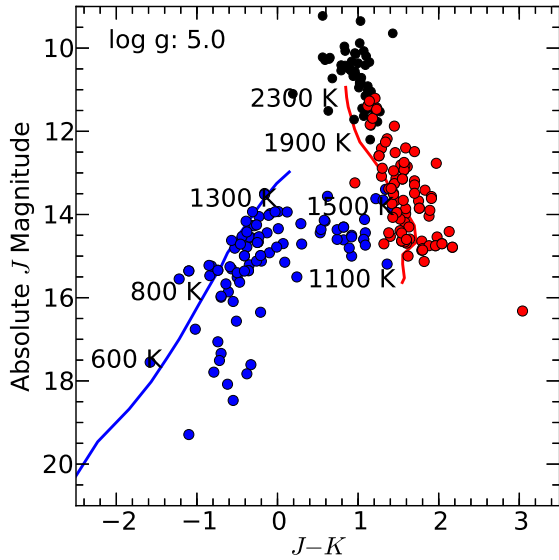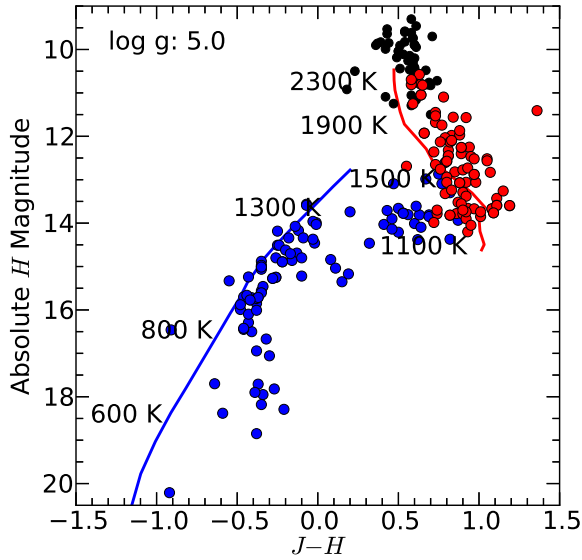
Figure 2.1: Color-magnitude diagrams of L and T dwarfs. *Top:* Observed brown dwarf $J-H$ color is plotted against the absolute H magnitude for all known brown dwarfs with measured parallax. M dwarfs are plotted as black circles, L dwarfs as red circles, and T dwarfs as blue circles. Observational data are from Dupuy and Liu (2012). Models are plotted as solid lines. Blue lines are cloudless models and red lines are cloudy (f_{sed}=2) models that include iron, silicate, and corundum clouds. Each labeled temperature marks the approximate location of the model with that effective temperature. The surface gravity of all models is log g =5.0 (1000m/s^2). *Bottom:* Same as above, but $J-K$ color is plotted against the absolute K magnitude.

33

models. Burgasser *et al.* (2010) suggest that the remnants of the iron and silicate clouds could redden these cool T dwarfs, but here we suggest instead that the formation of other condensates, which naturally arise from equilibrium chemistry calculations, may play an important role.

2.1.1.4   Y Dwarfs

The proposed spectral class Y encompasses brown dwarfs that have cooled below $T_{\text{eff}}\sim500$ K; a handful of these cool objects have recently been discovered (Cushing *et al.*, 2011; Kirkpatrick *et al.*, 2012). At these temperatures, NH_3 begins to play a more significant role in shaping the near-infrared spectra, and sodium and potassium wane in importance in the optical because they condense into clouds. Appreciable amounts of H_2O and NH_3 will condense into clouds at $T_{\text{eff}}\sim350$ K and ~200 K, respectively, and will further alter Y dwarf spectra. As we discover and characterize more of these cold objects, the study of clouds will be crucial to understand their spectral characteristics.

2.1.2   Secondary Cloud Layers

Silicate, iron, and corundum, which are the condensates that dominate the cloud opacity in our L dwarf models, are not the only condensates that thermochemical models predict will form in substellar atmospheres as they cool. Other condensates will form at lower temperatures and add to the cloud opacity via the same physical processes that formed the iron and silicate cloud layers. In cool substellar atmospheres, Na_2S (sodium sulfide) has been predicted to play a potentially significant role (Lodders, 1999; Lodders and Fegley, 2006; Visscher *et al.*, 2006). Other species expected to condense at these lower temperatures (roughly 600 to 1400 K) include

Cr, MnS, ZnS, and KCl.

To our knowledge, none of these five condensates have been included in a brown dwarf atmosphere model before now. Marley (2000) estimated column optical depths for several of these species and recognized that Na_2S could be important at low T_{eff} but did not include this species in subsequent modeling because of lack of adequate optical constant data. Burrows *et al.* (2001, 2002) noted that Na_2S and KCl will condense in cool T dwarfs, but also noted that the indices of refraction are difficult to find. Helling and collaborators (Helling and Woitke, 2006) also recognized that some of these species will form condensates in some cases but also did not compute model atmospheres that included this opacity source. Fortney (2005) noted that some of these species might be detectable in extrasolar planet transit spectra which probe a longer path length through the atmosphere.

2.2 Methods

2.2.1 Cloud Model

To model cloudy T dwarf atmospheres, we modify the Ackerman and Marley (2001) cloud model. This model has successfully been used to model the effects of the iron, silicate, and corundum clouds on the spectra of L dwarfs (Saumon and Marley, 2008; Stephens *et al.*, 2009). Here, we do not include the opacity of iron, silicate, and corundum clouds; based on observed trends, we assume that the opacity of these clouds becomes negligible for the early T dwarfs. We instead include Cr, MnS, Na_2S, ZnS, and KCl.

The Ackerman and Marley (2001) approach avoids treating the highly uncertain mi-

crophysical processes that create clouds in brown dwarf and planetary atmospheres. Instead, it aims to balance the advection and diffusion of each species' vapor and condensate at each layer of the atmosphere. It balances the upward transport of vapor and condensate by turbulent mixing in the atmosphere with the downward transport of condensate by sedimentation. This balance is achieved using the equation

$$-K_{zz}\frac{\partial q_t}{\partial z} - f_{\text{sed}}w_*q_c = 0, \tag{2.1}$$

where K_{zz} is the vertical eddy diffusion coefficient, q_t is the mixing ratio of condensate and vapor, q_c is the mixing ratio of condensate, w_* is the convective velocity scale, and f_{sed} is a parameter that describes the efficiency of sedimentation in the atmosphere.

This calculation provides the total amount of condensate at each layer of the atmosphere. The distribution of particle sizes at each level of the atmosphere is represented by a log-normal distribution in which the modal particle size is calculated using the sedimentation flux. A high sedimentation efficiency parameter f_{sed} results in vertically thinner clouds with larger particle sizes, whereas a lower f_{sed} results in more vertically extended clouds with smaller particles sizes. As a result, a higher f_{sed} corresponds to optically thinner clouds and a lower f_{sed} corresponds to optically thicker clouds.

The Ackerman and Marley (2001) cloud model code computes the available quantity of condensible gas above the cloud base by comparing the local gas abundance (accounting for upwards transport by mixing via K_{zz}) to the local condensate vapor pressure p_{vap}. In cases where the formation of condensates does not proceed by homogeneous condensation we nevertheless

compute an equivalent vapor pressure curve as described in Section 2.2.4.2.

2.2.2 Atmosphere Model

The cloud code is coupled to a 1D atmosphere model that calculates the pressure-temperature profile of an atmosphere in radiative-convective equilibrium. The atmosphere models are described in McKay *et al.* (1989); Marley *et al.* (1996); Burrows *et al.* (1997); Marley and McKay (1999b); Marley *et al.* (2002); Saumon and Marley (2008); Fortney *et al.* (2008b). This methodology has been successfully applied to modeling brown dwarfs with both cloudy and clear atmospheres (Marley *et al.*, 1996, 2002; Burrows *et al.*, 1997; Saumon *et al.*, 2006, 2007; Leggett *et al.*, 2007a,b; Mainzer *et al.*, 2007; Blake *et al.*, 2007; Cushing *et al.*, 2008; Geballe *et al.*, 2009; Stephens *et al.*, 2009).

In the atmosphere model, the thermal radiative transfer is determined using the "source function technique" presented in Toon *et al.* (1989). Within this method, it is possible to include Mie scattering of particles as an opacity source in each layer. Our opacity database for gases, described extensively in Freedman *et al.* (2008), includes all the important absorbers in the atmosphere. This opacity database includes two significant updates since Freedman *et al.* (2008), which are described in Saumon *et al.* (2012): a new molecular line list for ammonia (Yurchenko *et al.*, 2011) and an improved treatment of the pressure-induced opacity of H_2 collisions (Richard *et al.*, 2012).

Both the cloud model and the chemical equilibrium calculations (see Section 2.2.4) are coupled with the radiative transfer calculations and the pressure-temperature profile of the atmosphere; this means that a converged model will have a temperature structure that is self-

37

consistent with the clouds and chemistry.

2.2.3 Mie Scattering by Cloud Particles

We calculate the effect of the model cloud distribution on the flux using Mie scattering theory to describe the cloud opacity. Assuming that particles are spherical and homogeneous, we calculate the scattering and absorption coefficients of each species for each of the particle sizes within the model. In order to make these scattering calculations, we need to understand the optical properties (the real and imaginary parts of the index of refraction) of each material.

The optical properties were found from a variety of diverse sources, summarized in Table 2.1. To calculate Mie scattering within the model atmosphere, we use a grid of optical properties at wavelengths from 0.268 to 227 μm. Where data were not available, we extrapolated the available data, following trends for similar known molecules.

The molecules with the most complete published optical properties are ZnS and KCl, both of which are obtained from Querry (1987), who tabulates the optical constants for 24 different minerals.

Optical properties for Cr are published in Stashchuk *et al.* (1984) from 0.26 to 15 μm. The optical properties from 15 μm to 227 μm were linearly extrapolated from these experimental data following the trend of the optical properties of Fe. Various extrapolations were tested; the choice of optical properties beyond 15 μm does not change the results of the calculations in any meaningful way.

Optical properties for MnS are published in Huffman and Wild (1967), from 0.09 to 13 μm. Optical properties from 15 μm to 227 μm are extrapolated, following the trends of the
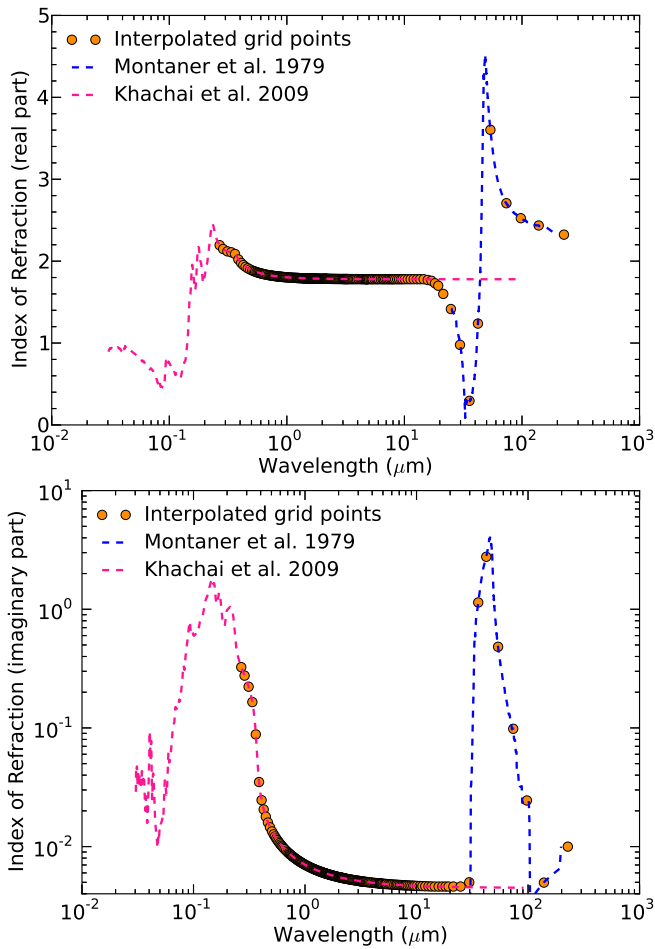
Figure 2.2: Na$_2$S index of refraction. The real and imaginary parts of the sodium sulfide index of refraction from the two sources used are plotted as a function of wavelength. Montaner *et al.* (1979) observational data are shown as a blue dashed line. Khachai *et al.* (2009) calculations are shown as a pink dashed line. The interpolated values used for the Mie scattering calculation are shown as pink circles.

Table 2.1: Sources of Optical Properties

Species	Source	Wavelength Range
KCl	Querry (1987)	0.22-167 μm
ZnS	Querry (1987)	0.22-167 μm
MnS	Huffman and Wild (1967)	0.09-13 μm
Cr	Stashchuk *et al.* (1984)	0.26-15 μm
Na$_2$S	Montaner *et al.* (1979)	25-198 μm
	Khachai *et al.* (2009)	0.03-91 μm

other two studied sulfide condensates ZnS and Na$_2$S.

The optical properties for Na$_2$S, the clouds with the largest optical depth, are combined from two different sources. Montaner *et al.* (1979) provides experimental data in the infrared, from 25 to 198 μm. Khachai *et al.* (2009) provides first principles calculations of the optical properties from 0.03 to 91 μm. In the region of overlap, the Montaner *et al.* (1979) laboratory values are used. The real and imaginary parts of the index of refraction are plotted in Figure 2.2.

2.2.4 Chemistry Models

2.2.4.1 Gas Phase Chemistry

The abundances of molecular, atomic, and ionic species are calculated using thermochemical equilibrium following the models of Fegley and Lodders (1994, 1996); Lodders (1999); Lodders and Fegley (2002); Lodders (2002, 2003); Lodders and Fegley (2006); Lodders (2009). We adopt solar-composition elemental abundances from Lodders (2003). The differences between Lodders (2003) and newer abundance measurements (e.g. Asplund *et al.*,

2009) are not large enough to significantly alter the condensation temperatures considered in the paper. Lodders (2003) abundances were therefore selected for consistency with previous modeling efforts by our groups. The abundances of condensate-forming elements are listed in Table 2. We assume uniform heavy element abundance ratios over a range of metallicities from [Fe/H] = -0.5 to [Fe/H] = +0.5 in order to explore the metallicity dependence of the condensation temperature expressions.

2.2.4.2   Cloud Condensation Chemistry

A simplified equilibrium condensation approach is used to calculate saturation vapor pressures and condensation curves (see Figure 3) for Cr, MnS, Na_2S, ZnS, and KCl as a function of pressure, temperature, and metallicity, based upon the more comprehensive thermochemical models of Lodders & Fegley (see 2.2.4.1) and Visscher *et al.* (2006, 2010). In each case, we consider condensation from the most abundant Cr-, Mn-, Na-, Zn-, and K-bearing gas phases at the cloud base as predicted by the chemical models. The relative mass of each cloud (relative to Na_2S) is listed in Table 3, assuming complete removal of available condensate material from the gas phase.

Chromium metal is the most refractory of the clouds considered here and condenses from monatomic Cr gas via the reaction

$$Cr = Cr(s). \tag{2.2}$$

Table 2.2: Abundances of condensate-forming elements

Element	$A(El)^a$	Major condensate
Fe	7.54 ± 0.03	Fe
Si	7.61 ± 0.02	Mg_2SiO_4, $MgSiO_3$
Mg	7.62 ± 0.02	Mg_2SiO_4, $MgSiO_3$
O	8.76 ± 0.05	Mg_2SiO_4, $MgSiO_3$, Al_2O_3, H_2O
Al	6.54 ± 0.02	Al_2O_3, $CaAl_{12}O_{19}$, $CaAl_2O_4$, $Ca_2Al_2SiO_7$
Na	6.37 ± 0.03	Na_2S
Zn	4.70 ± 0.04	ZnS
Mn	5.58 ± 0.03	MnS
S	7.26 ± 0.03	Na_2S, ZnS, MnS
Cr	5.72 ± 0.05	Cr
K	5.18 ± 0.05	KCl
Cl	5.33 ± 0.06	KCl

Note. — ^{a} Where $A(El) = \log[n(El)/n(H)] + 12$

where '(s)' indicates a solid phase. The condensation condition for Cr-metal is defined by

$$p_{Cr}^* \geq p_{Cr}', \qquad (2.3)$$

where p_{Cr}' is the saturation vapor pressure of Cr gas in equilibrium with Cr-metal and p_{Cr}^* is the partial pressure of Cr below the cloud for a solar-composition gas ($p_{Cr}^* = q_{Cr}^* p_t$, where q_{Cr}^* is the mole fraction abundance of Cr and p_t is the total atmospheric pressure). Upon condensation, the thermodynamic activity of Cr-metal is unity and the equilibrium constant (K_p) expression for reaction (2.3) can be written as

$$p_{Cr}' = K_p^{-1}. \qquad (2.4)$$

Substituting for the temperature-dependent value of K_p, the saturation vapor pressure of Cr

above the cloud base can be estimated using the expression

$$\log p'_{\text{Cr}} \approx 7.490 - 20592/T, \tag{2.5}$$

for T in Kelvin and p in bars. Below the cloud, we assume that Cr gas is approximately representative of the elemental Cr abundance in solar composition gas (see Table 2.3):

$$\log p^*_{\text{Cr}} \approx -6.052 + \log p_t + [\text{Fe/H}]. \tag{2.6}$$

The condensation temperature as a function of the total atmospheric pressure (p_t) and metallicity can therefore be approximated by setting $p^*_{\text{Cr}} = p'_{\text{Cr}}$ and rearranging to give

$$10^4/T_{\text{cond}}(\text{Cr}) \approx 6.576 - 0.486 \log p_t - 0.486[\text{Fe/H}]. \tag{2.7}$$

This expression yields a condensation temperature near ~ 1520 K at 1 bar and solar metallicity (cf. Lodders and Fegley, 2006), and shows that greater total pressures and/or metallicities will lead to higher condensation temperatures. Condensation of Cr-metal effectively removes gas-phase chromium from the atmosphere, and the abundances of Cr-bearing gases rapidly decrease with altitude above the cloud.

Our modeling of sulfide condensation chemistry follows that of Visscher *et al.* (2006), and the condensation reactions and temperature-dependent expressions presented here are taken from that study. The deepest sulfide cloud expected in brown dwarf atmospheres is MnS, which

forms via the reaction

$$H_2S + Mn = MnS(s) + H_2, \tag{2.8}$$

The formation of the MnS cloud is limited by the total manganese abundance, which is 2% of the sulfur abundance in a solar-composition gas. The condensation curve for MnS is thus derived by exploring the chemistry of monatomic Mn, which is the dominant Mn-bearing gas near the cloud base. Using results from Visscher *et al.* (2006), the saturation vapor pressure of Mn above the cloud is given by

$$\log p'_{Mn} \approx 11.532 - 23810/T - [Fe/H], \tag{2.9}$$

where the metallicity dependence comes from H_2S (the dominant S-bearing gas) remaining in the gas phase above the MnS cloud base. By setting $p^*_{Mn} = p'_{Mn}$, the MnS condensation curve is approximated by Visscher *et al.* (2006):

$$10^4/T_{cond}(MnS) \approx 7.447 - 0.42 \log p_t - 0.84[Fe/H], \tag{2.10}$$

giving a condensation temperature near ~ 1340 K at 1 bar in a solar-metallicity gas.

The Na_2S cloud is the most massive of the metal sulfide clouds expected to form in brown dwarf atmospheres because Na is more abundant than either Mn or Zn in a solar-composition gas (see Table 2.3). Sodium sulfide condenses via the net thermochemical reaction

$$H_2S + 2Na = Na_2S(s) + H_2. \tag{2.11}$$

44

The mass of the Na$_2$S cloud is limited by the elemental abundance of sodium, which is 13% of the abundance of sulfur in a solar composition gas. Using results from Visscher *et al.* (2006), the saturation vapor pressure of Na above the cloud base is given by

$$\log p'_{\text{Na}} \approx 8.550 - 13889/T - 0.50[\text{Fe/H}], \tag{2.12}$$

where the metallicity dependence results from H$_2$S remaining in the gas phase above the Na$_2$S cloud and from the stoichiometry of Na and H$_2$S in the condensation reaction. The condensation temperature (where $p^*_{\text{Na}} = p'_{\text{Na}}$) is given by Visscher *et al.* (2006):

$$10^4/T_{\text{cond}}(\text{Na}_2\text{S}) \approx 10.045 - 0.72 \log p_t - 1.08[\text{Fe/H}], \tag{2.13}$$

indicating condensation near $\sim$ 1000 K at 1 bar in a solar-metallicity gas.

The ZnS cloud layer forms via the reaction

$$\text{H}_2\text{S} + \text{Zn} = \text{ZnS}(\text{s}) + \text{H}_2, \tag{2.14}$$

The formation of the ZnS cloud is limited by the total Zn abundance, which is 0.3% of the S abundance in a solar-composition gas. Using results from Visscher *et al.* (2006), the saturation vapor pressure of Zn over condensed ZnS is given by

$$\log p'_{\text{Zn}} \approx 12.812 - 15873/T - [\text{Fe/H}] \tag{2.15}$$

The condensation curve (where $p_{Zn}^* = p_{Zn}'$) is approximated by Visscher *et al.* (2006):

$$10^4/T_{cond}(ZnS) \approx 12.527 - 0.63 \log p_t - 1.26[Fe/H], \qquad (2.16)$$

giving a condensation temperature of ~ 800 K at 1 bar in a solar-metallicity gas.

Our treatment of KCl condensation chemistry is similar to that for Cr-metal and the metal sulfides. With decreasing temperatures, KCl replaces neutral K as the dominant K-bearing gas in brown dwarf atmospheres (Lodders, 1999; Lodders and Fegley, 2006). The KCl cloud layer is thus expected to form via the net thermochemical reaction

$$KCl = KCl(s), \qquad (2.17)$$

and condenses as a solid over the range of conditions considered here. The vapor pressure of KCl above condensed KCl(s) is given by

$$\log p_{KCl}' \approx 7.611 - 11382/T, \qquad (2.18)$$

derived from the equilibrium constant expression for the condensation reaction. The mass of the KCl cloud is limited by the total potassium abundance, which is 70% of the chlorine abundance in a solar-composition gas (Lodders, 2003). Note that other K-bearing species may remain relatively abundant near cloud condensation temperatures, particularly at higher pressures (e.g., see Fegley and Lodders 1994 and Lodders 1999 for a more detailed discussion of chemical speciation). However, KCl is the dominant K-bearing gas near the cloud base for the relevant

$P - T$ conditions expected in cool brown dwarf atmospheres (see Figure 3) over the range of metallicities (-0.5 to +0.5 dex) considered here. For simplicity we therefore assume that KCl is approximately representative of the elemental K abundance below the cloud, given by

$$\log p^*_{\text{KCl}} \approx -6.593 + \log p_t + [\text{Fe/H}].$$ (2.19)

The condensation temperature as a function of pressure and metallicity is estimated by setting $p^*_{\text{KCl}} = p'_{\text{KCl}}$ and rearranging to give

$$10^4/T_{\text{cond}}(\text{KCl}) \approx 12.479 - 0.879 \log p_t - 0.879[\text{Fe/H}],$$ (2.20)

yielding a condensation temperature near ~ 800 K at 1 bar in a solar-metallicity gas (cf. Lodders, 1999; Lodders and Fegley, 2006). In general, the condensation curve expressions demonstrate that condensation temperatures increase with total pressure, as illustrated in Figure 4. Furthermore, higher metallicities are expected to result in higher condensation temperatures and more massive cloud layers in brown dwarf atmospheres. In each case, the saturation vapor pressures of cloud-forming species rapidly decrease with altitude above the cloud layers.

2.2.5 Comparison to Other Cloud Models

The Ackerman and Marley (2001) model is one method of several that have been applied to cloudy brown dwarf atmospheres. Helling *et al.* (2008a) review various cloud modeling techniques and compare model predictions for various cases. The most important conceptual differences between these approaches lies in the assumptions of how condensed phases interact

47

Table 2.3: Abundances of Condensate-Forming Species

condensate	p_x^* below cloud base[a]	cloud mass[b]
Cr	$p_{Cr}^* \approx 8.87 \times 10^{-7} p_t m$	0.30
MnS	$p_{Mn}^* \approx 6.32 \times 10^{-7} p_t m$	0.36
Na$_2$S	$p_{Na}^* \approx 3.97 \times 10^{-6} p_t m$	1.00
ZnS	$p_{Zn}^* \approx 8.45 \times 10^{-8} p_t m$	0.05
KCl	$p_{KCl}^* \approx 2.55 \times 10^{-7} p_t m$	0.12
Fe	$p_{Fe}^* \approx 5.78 \times 10^{-5} p_t m$	20.85

Note. — [a]Where p_x^* is the partial pressure (in bars) of each gas phase species x below the predicted cloud base using solar-composition abundances from Lodders (2003), p_t is the total atmospheric pressure, and the metallicity factor m is defined by $\log m = $ [Fe/H]. [b]Total condensate mass relative to the Na$_2$S cloud. Values for Fe shown for comparison.

with the gas.

In the chemical equilibrium approach (e.g. Allard *et al.*, 2001), condensed phases remain in contact with the gas phase and can continue to react with the gas even at temperatures well below the condensation temperature. As an example, when following this approach, Fe grains which first condense at temperatures of over 2000 K react with atmospheric H$_2$S to form FeS below 1000 K. In the condensation chemistry approach we employ here, the condensed phases are assumed to sediment out of the atmosphere and are not available to interact with gas phases at temperatures below the condensation temperature. Thus Fe grains form a discrete cloud layer and do not react to form FeS. H$_2$S consequently remains in the gas phase and reacts to form condensates as outlined in Section 2.4.2. Jupiter is an excellent example of the applicability of this framework, as the presence of H$_2$S in the observable atmosphere is only

possible because Fe is sequestered in a deep cloud layer, which prevents the formation of FeS which otherwise deplete other gas phase S species (Fegley and Lodders, 1994). The presence of alkali absorption in T dwarfs likewise demonstrates the applicability of condensation chemistry (Marley *et al.*, 2002). A detailed comparison of true equilibrium condensation and cloud condensate removal from equilibrium can be found in Fegley and Lodders (1994); Lodders and Fegley (2006) and references therein.

A different approach is taken by Helling & Woitke (Helling and Woitke, 2006) who follow the trajectory of tiny seed particles of TiO_2 that are assumed to be emplaced high in the atmosphere and sink downwards. As the seeds fall through the atmosphere they collect condensate material. In Helling and Woitke (2006) and numerous follow on papers (Helling *et al.*, 2008a; Witte *et al.*, 2009, 2011; de Kok *et al.*, 2011) this group models the microphysics of grain growth given these conditions. Because the background atmosphere is not depleted of gaseous species until the grains fall through the atmosphere, a compositionally very different set of grains are formed. In particular they predict 'dirty' grains composed of layers of varying condensates.

A direct comparison between the predictions of the various cloud modeling schools is often difficult because of differing assumptions of elemental abundances and the background thermal profile. Modeling tests in which predictions of the various groups are compared to data would be illuminating, but this is far beyond the scope of the work reported here.

2.2.6 Evolution Model

In order to calculate absolute magnitudes of the modeled brown dwarfs, we use the results of evolution models which determine the radius of a brown dwarf as it cools and contracts over its lifetime. We use the evolution models of Saumon and Marley (2008) with the surface boundary condition from cloudless atmospheres. Using a cloudless boundary condition instead of one consistent with these clouds changes the calculated magnitudes of the models very slightly, but does not change the overall trends or results.

2.2.7 Model Grid

To analyze the effect of these clouds, we generate a grid of 182 model atmospheres at effective temperatures and surface gravities spanning the full range of T dwarfs. We calculate pressure-temperature profiles and synthetic spectra for atmospheres from 400 to 1300 K (50 to 100 K increments), with $\log(g)$ (cgs) of 4.0, 4.5, 5.0, and 5.5 and cloud sedimentation efficiency parameter f_{sed}=2, 3, 4, and 5. For this study, we use only solar metallicity composition. We then compare these, both photometrically and spectroscopically, to observed T dwarfs.

2.3 Results

2.3.1 Model Pressure-Temperature Profiles

In Figure 2.3, we show the pressure-temperature profiles of models with effective temperatures of 400 K, 600 K, 900 K, and 1300 K. The surface gravity of the 400 K models is $\log g$=4.5; for the hotter models, $\log g$=5.0. We plot models with two different cloud sedimen-
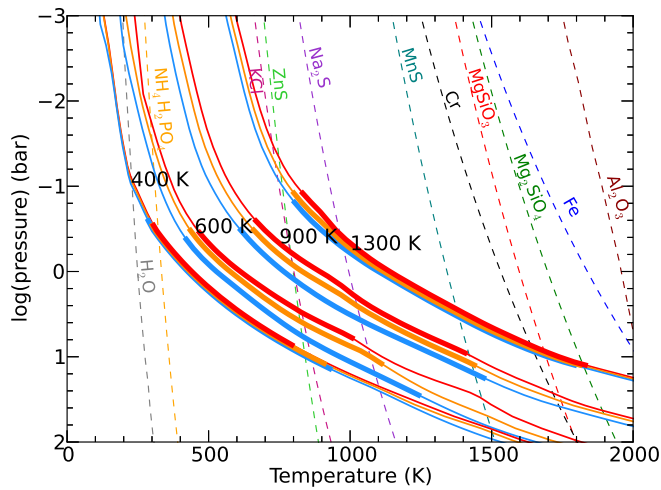
Figure 2.3: The pressure-temperature profiles of model atmospheres are plotted. Models at 400, 600, 900, and 1300 K are shown, and the effective temperature of the model is labeled on the plot. The surface gravity of the 400 K model is log g=4.5; for the hotter models, log g=5.0. We show cloudless models in blue, and cloudy models with f_{sed}=2 (red) and 4 (orange). Condensation curves for each condensate species are plotted. The cloudy models include the condensates Cr, MnS, Na$_2$S, ZnS, and KCl. Note that for each case, increasing the cloud thickness increases the temperature at a given atmospheric pressure. The 1-6 μm photosphere of each model is shown as a thicker line.

tation efficiencies which include only the Na_2S, MnS, ZnS, Cr, and KCl clouds. Because Na_2S and MnS are by far the most dominant cloud species (see Section 2.3.3), as a shorthand we refer to this collection of clouds as 'sulfide clouds.'

The condensation curves of major and minor species predicted to form by equilibrium chemistry are also plotted. The location of a given cloud base is expected to be where the pressure-temperature profile of the model atmosphere crosses the condensation curve. Each model crosses the condensation curve of each species at very different pressures and, to a lesser extent, temperatures, so we expect that the significance of the clouds will be strongly controlled by the effective temperature of the model.

The cloudy 400 K and 600 K models have two convection zones. All 900 and 1300 K models have a single deep convection zone.

For all models, it is clear that, as in previous cloudy models of L dwarfs, adding cloud opacity has a "blanketing" effect on the model, increasing the temperature of the atmosphere for a given atmospheric pressure. As the cloud becomes optically thicker, the entire pressure-temperature profile becomes hotter; thus, on a plot of pressure-temperature profiles such as Figure 2.3, increasing the cloud opacity moves the whole profile to the right.

2.3.2   Model Spectra

In Figures 2.4 and 2.5, we show the spectra of the same example models at 1300, 900, 600, and 400 K: Figure 2.4 shows the wavelength-dependent brightness temperatures from these models, while 2.5 shows the model fluxes computed from the top of the atmosphere. The brightness temperature gives some insight into the depth into the atmosphere probed at each
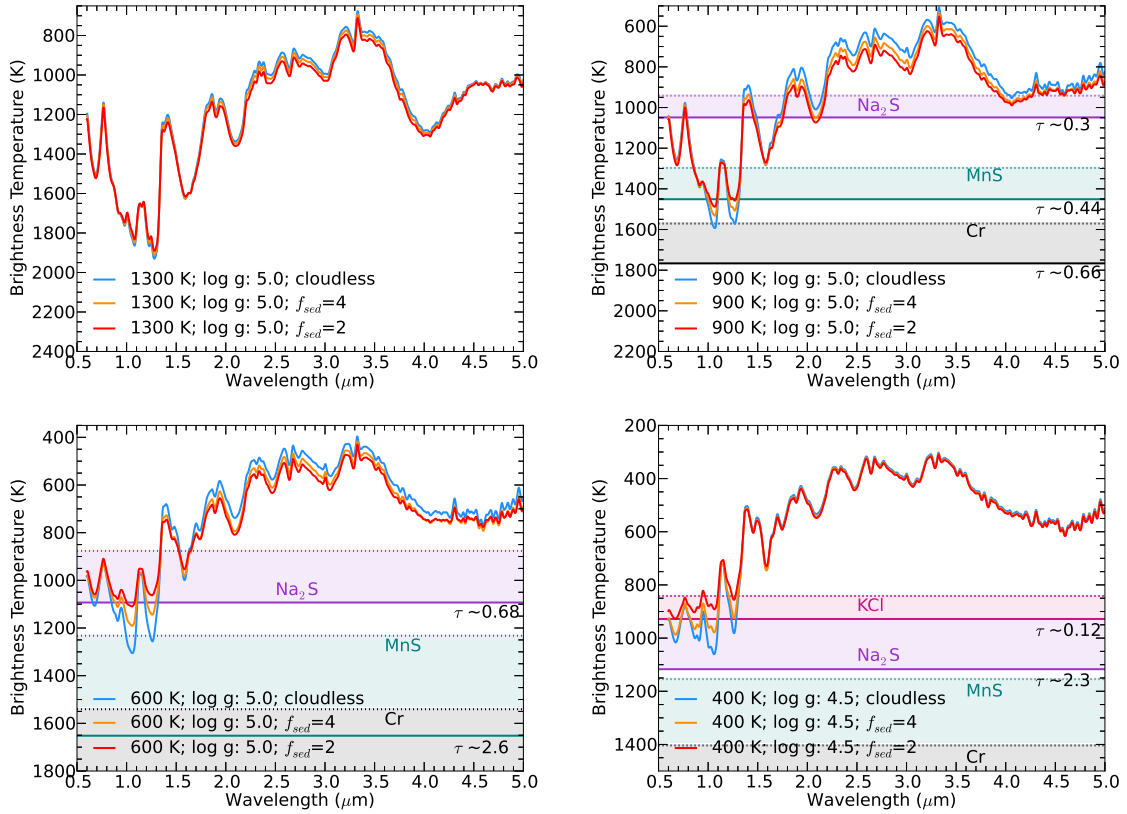
Figure 2.4: The model spectra are plotted as brightness temperature vs. wavelength. cloudless, f_{sed}=2, and f_{sed}=4 models are shown. The solid horizontal line indicates the temperature at the base of the each cloud, and the dashed horizontal line denotes the temperature of the layer in which column extinction optical depth of the cloud reaches 0.1. Note that for all clouds in the T_{eff} 1300 K model, the column optical depth model never exceeds 0.1. The maximum column optical depth of the Na2S clouds (τ at the cloud base) is calculated using the f_{sed}=4 models and labeled on each plot.
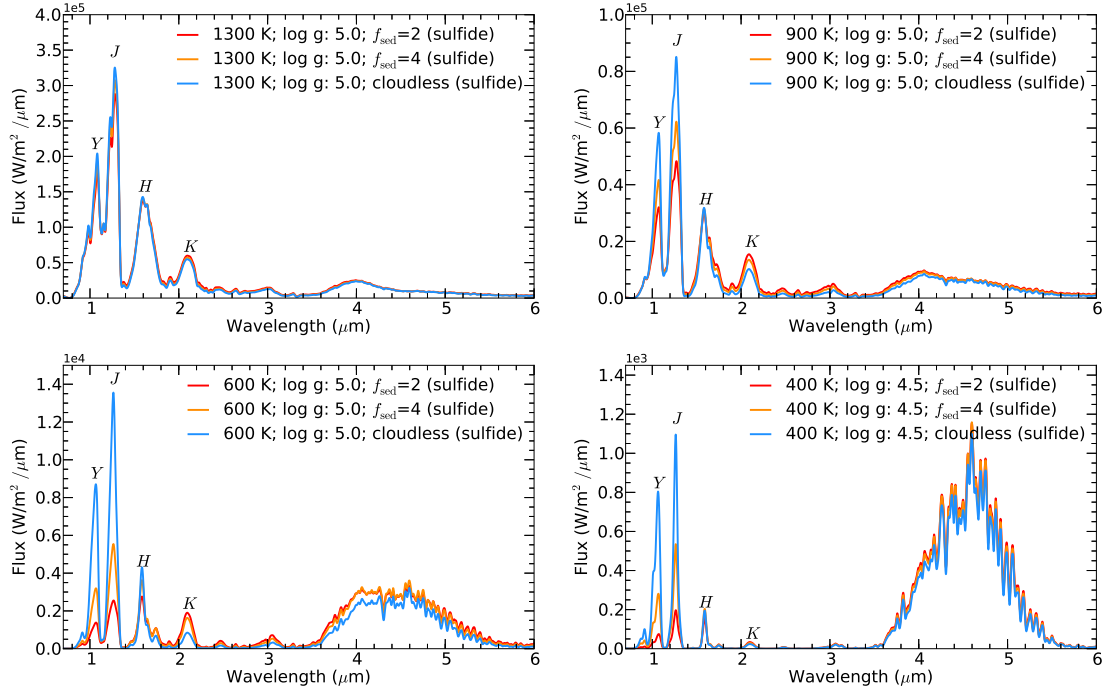
Figure 2.5: Model spectra. From top to bottom, T_{eff}=1300 K, log g=5.0; T_{eff}=900 K, log g=5.0; T_{eff}=600 K, log g=5.0; T_{eff}=400 K, log g=4.5. We show cloudy models with f_{sed}=2 and 4 which include the condensates Cr, MnS, Na$_2$S, ZnS, and KCl and cloudless models for comparison. Note that for the T_{eff}=400 K, T_{eff}=600 K and T_{eff}=900 K models, the cloudy models are progressively fainter in Y and J bands and brighter in K band as the sedimentation efficiency decreases. In contrast, for the T_{eff}=1300 K case, the clouds do not significantly change the spectrum.
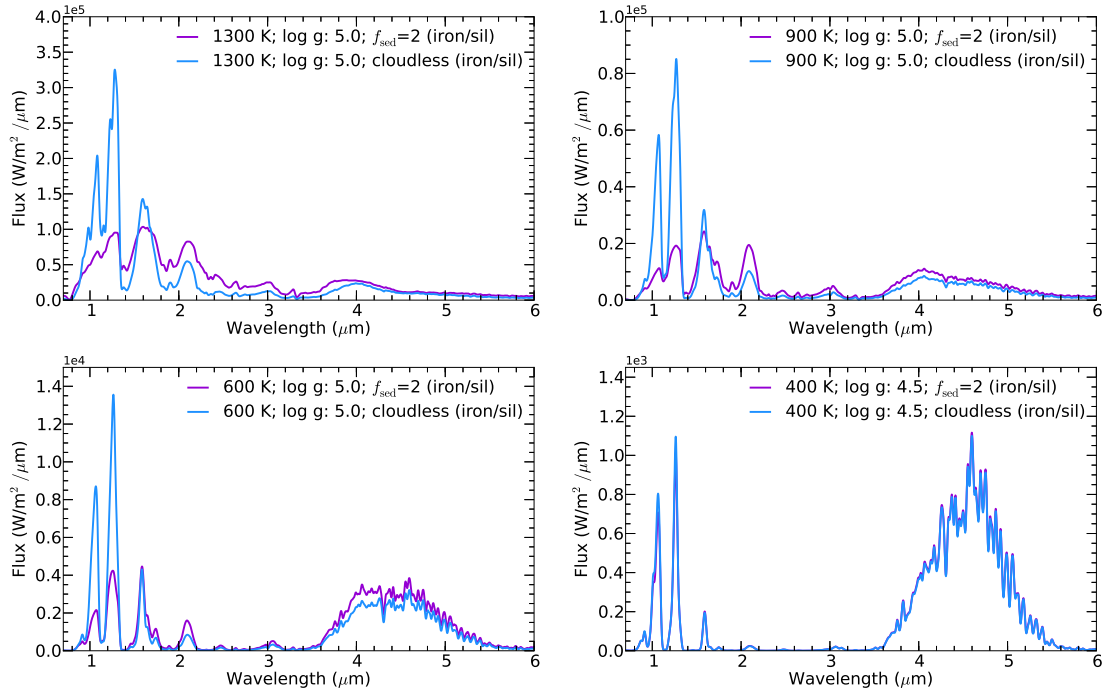
Figure 2.6: Model spectra with iron/silicate clouds. As in Figure 2.5, from top to bottom, T_{eff}=1300 K, log g=5.0; T_{eff}=900 K, log g=5.0; T_{eff}=600 K, log g=5.0; T_{eff}=400 K, log g=4.5. We show cloudy models with iron/silicate/corundum clouds (no sulfide clouds) with f_{sed}=2 and cloudless models for comparison. Note that these clouds, unlike the sulfide clouds in Figure 2.5, significantly change the shape of the 1300 K model.

wavelength. Flux from 0.8 to 1.3 μm comes from the deepest, hottest layers of the atmosphere. Clouds change the flux in this wavelength range by limiting the depth from which flux emerges; conversely, the clouds do not change the depth probed between ~2 and 5 μm because the clouds form below the layers from which most of the flux is emerging. However, the hotter atmospheric temperatures at a given pressure (see Figure 3) lead to slightly higher fluxes at these wavelengths. Though not plotted here, flux in the mid-infrared also comes from above the cloud layer and is slightly higher because the entire pressure-temperature profile is hotter.

For the hottest of these models (T_{eff}=1300 K), the cloudy spectra look almost identical to the cloudless spectrum. This model is too hot to have much mass of these condensed species form in the photosphere. For a cooler model (T_{eff}=900 K), the cloudy spectra look different from the cloudless spectrum. As we decrease the sedimentation efficiency f_{sed} in the model, the flux in Y and J bands decreases and the flux in K band increases.

For the coldest two models shown (T_{eff}=400, 600 K), the cloudy spectra look dramatically different from the cloudless spectrum in the near-infrared; even the thinnest cloud considered here (f_{sed}=5) causes the flux in Y and J to decrease by 50% and the flux in K to correspondingly increase. Decreasing the sedimentation efficiency enhances this effect.

Figure 2.6 shows the effect of the iron and silicate clouds on the spectra of models with the same effective temperatures (1300 K, 900 K, 600, and 400 K) and surface gravity. Note that unlike the sulfide clouds, these iron and silicate clouds substantially change the shape of the 1300 K and 900 K models by suppressing the flux in Y, J, and H and increasing the flux in K band and the mid-infrared. This strong effect at higher temperatures is due to the large amount of iron and silicate condensed in the visible atmosphere at those temperatures.

2.3.3 Cloud Structure in Model Atmospheres

Figure 3.4 shows the distribution of clouds in the model atmospheres for the three example cases. The locations of iron, silicate, and corundum clouds, using models that only include those clouds—the standard Saumon and Marley (2008) cloud configuration—are plotted for reference. The column optical depth is given by Equation 16 in Ackerman and Marley (2001), which calculates the cumulative geometric scattering optical depth by cloud particles through the atmosphere.

For the 1300 K model, all of the sulfide clouds have tiny optical depths in the photosphere and do not affect the emergent spectra. The silicate and iron clouds would have significant optical depth (τ=2-3) and would substantially change the emergent spectra.

For the 900 K model, all of the sulfide clouds have a column optical depth smaller than 1 in the photosphere. KCl and ZnS have tiny optical depth ($\tau < 2 \times 10^{-2}$) and will not create an observable change in the spectrum. Na_2S and MnS have optical depth between 0.1 and 1 and will change the model spectra slightly.

For the 600 K model, Na_2S is the most important condensate opacity source. KCl has a small optical depth and ZnS has a negligible optical depth. This result is expected, based on the abundances of each species (see Table 2.3). The other two clouds, MnS and Cr, are below the near-infrared photosphere, so also do not change the spectrum. The silicate and iron clouds would also be below the photosphere.

Using our full grid of models, we can examine the importance of the Na_2S cloud as a function of T_{eff} and surface gravity. Figure 2.8 shows how the column optical depth of this

57
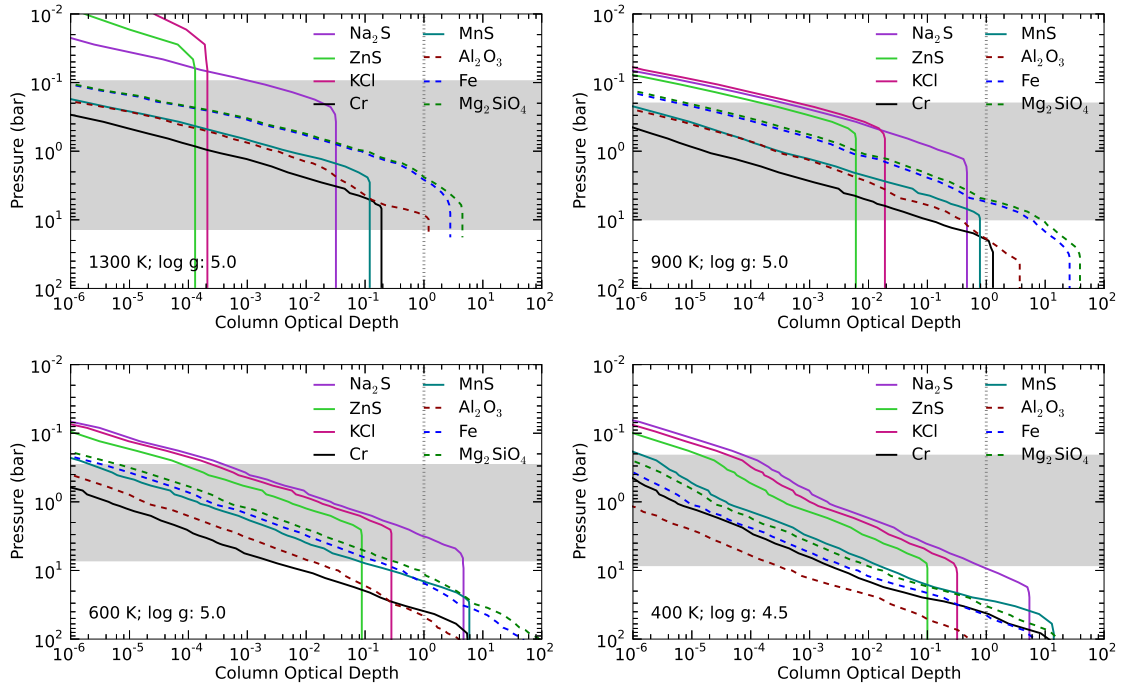
Figure 2.7: Pressure vs. column optical depth. The column optical depth of each cloud species is plotted. The solid lines denote the clouds examined in this study: Na_2S, ZnS, KCl, Cr, and MnS. The dashed lines show the column optical depths of models that include only the more refractory clouds corundum (Al_2O_3) iron (Fe), and forsterite (Mg_2SiO_4) to show where those clouds would form in comparison to the sulfide clouds. All models use f_{sed}=2. The shaded grey area shows the region of the atmosphere which lies within the λ = 1 to 6 μm photosphere. Note that the Na_2S cloud is by far the most important of the added clouds for the 600 K model in the near-infrared. Also note that if the Al_2O_3, Fe, and Mg_2SiO_4 persisted to effective temperatures of 900-1300 K, they would be quite visible, which would not match observations.

58
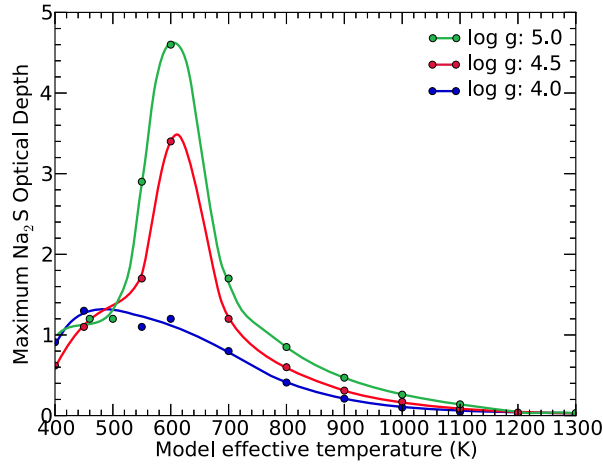
Figure 2.8: The column optical depth of the Na$_2$S cloud above the bottom of the 1-6 μm photosphere in each model is plotted as a function of model effective temperature. The curves connecting the points are there to guide the eye. Three different surface gravities are shown and all models use f_{sed}=2. The column optical depth peaks at temperatures of about 600 K, and models with higher surface gravity have a greater Na$_2$S column optical depth.

cloud varies from 400-1300 K and log g from 4.0-5.0 for a constant value of the parameter f_{sed}. Moving to T_{eff} values below 1300 K, the Na$_2$S cloud grows in importance as it forms progressively deeper in the atmosphere, so that there is larger mass of condensate in the cloud. The maximum optical depth of the Na$_2$S cloud at pressure levels above the bottom of the 1-6 μm photosphere is largest for models with T_{eff} of 600 K. At lower T_{eff}, much of the cloud opacity is below the visible atmosphere. The optical depth within the photosphere is significant ($\tau \gtrsim 1$) for models between 400 and 700 K.

Figure 2.8 indicates that the cloud optical depth within the photosphere is largest for higher surface gravity atmospheres for a constant value of f_{sed}. However, this does not necessarily predict that higher gravity brown dwarfs will have thicker clouds than lower gravity brown dwarfs because the parameter f_{sed} is not necessarily independent of gravity.

2.4 Comparison with Observations

2.4.1 Color-Magnitude Diagrams

In Figure 2.9, we plot the photometric colors in the near-infrared of all brown dwarfs with measured parallaxes and apparent J and K magnitude errors smaller than 0.2 magnitudes (Dupuy and Liu, 2012; Faherty *et al.*, 2012). We also plot the calculated photometric colors of our suite of cloudless and cloudy models from 400-1300 K with several representative surface gravities. In Section 2.4.1 we discuss the general trends of the photometric colors of models at various effective temperatures and cloud sedimentation efficiencies. In Section 2.4.2 we compare our model results to the photometric observations.

As discussed in Sections 2.3.2 and 2.3.3, clouds in T dwarf atmospheres tend to suppress the flux in Y and J bands and increase the flux in K band. The flux shift from J to K gives cloudy models larger (redder) $J-K$ and $J-H$ colors than cloudless models.

In Figure 2.9, the hottest cloudy models have nearly the same near-infrared colors as cloudless models. As we decrease the effective temperature of a cloudy model, more cloud material condenses; the model has a redder photometric color than a cloudless model with the same T_{eff}. If we reduce the sedimentation efficiency (f_{sed}) of the cloud, the cloud becomes optically thicker, and the model has a redder photometric color.

The upper panels, which show $J-K$ photometric colors, show that our sulfide cloud models can easily reach the colors of red T dwarfs, with f_{sed} values of 4-5. The bulk of the T dwarf population is bluer than the f_{sed}=5 model. However, the cooler T dwarfs are generally well-matched by the models. In $J-H$, the color directly affected by cloud opacity limiting the

depth to which one sees, the model colors are an excellent match to the data. The cloudy models are a much better match than the corresponding cloud-free models.

2.4.2 Comparison to Observed T Dwarfs

2.4.2.1 Expected Surface Gravity of T dwarfs

Based on Saumon and Marley (2008) evolution models and assuming that observed brown dwarfs will have ages less than 10 Gyr, we expect that the coldest objects modeled, between 400-600 K, will have surface gravities less than log g=5.2. Hotter objects, between 1000 and 1300 K, will have surface gravities less than log g=5.5.

2.4.2.2 Cloud Sedimentation Efficiency

For the L dwarfs, we are generally able to match photometric colors by including silicate, iron, and corundum clouds with a sedimentation efficiency parameter of f_{sed}=2±1 (Stephens *et al.*, 2009; Saumon and Marley, 2008). However, for these cooler T dwarfs, models with these sulfide clouds with f_{sed}=2 are redder than observed brown dwarfs. If we assume f_{sed} is larger—around 4 or 5—we are able to match observed colors. The cloud model does not explicitly suggest any physical mechanism for why f_{sed} would be different. However, since these objects are about 1000 K cooler than L dwarfs, it would not be surprising if these objects populate a different physical regime, and would have substantially different rates of atmospheric mixing and cloud condensation. Indeed, a large increase in f_{sed} with lower T_{eff} values is one way to quickly clear away the silicate and iron clouds (Knapp *et al.*, 2004)
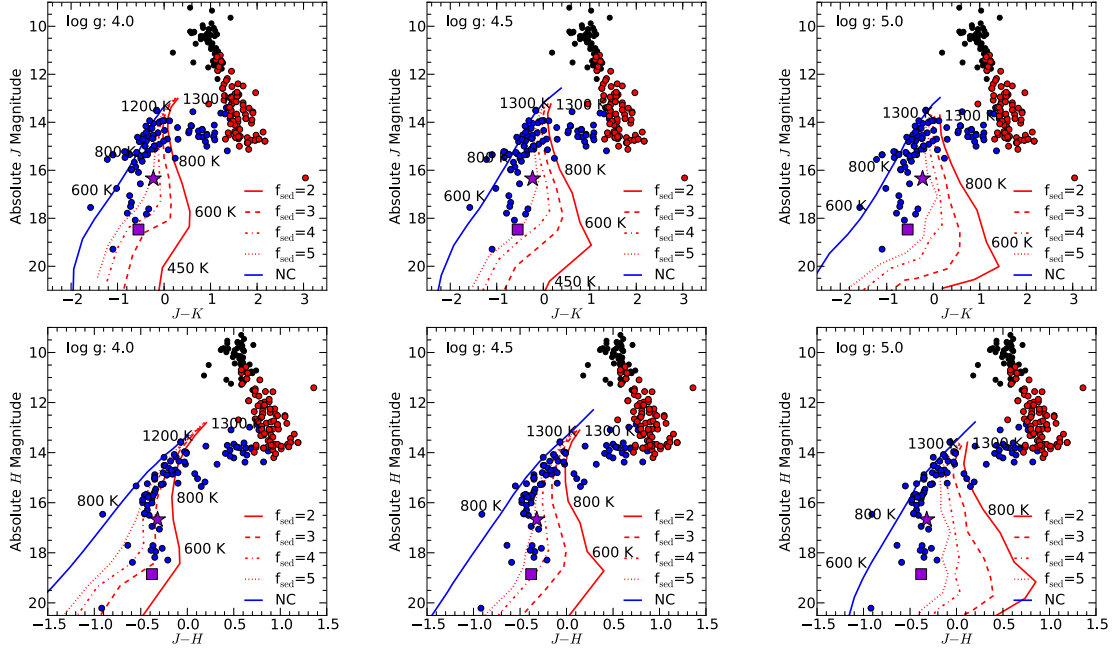
Figure 2.9: Color-magnitude diagrams for M, L, and T dwarfs. As in Figure 2.1, observed ultracool dwarf color is plotted against the absolute magnitude for all known brown dwarfs with measured parallax. In the top 3 plots, $J-K$ color is plotted against absolute J magnitude; in the bottom 3 plots, $J-H$ color is plotted against absolute H magnitude. All photometry is in the MKO system. M dwarfs are plotted as black circles, L dwarfs as red circles, and T dwarfs as blue circles. Observational data are from Dupuy and Liu (2012); Faherty *et al.* (2012). The locations of the brown dwarfs Ross 458C and UGPS 0722-05, the objects to which we compare model spectra to observations in Figures 11 and 12, are shown with a purple star and square symbol, respectively. *Models.* Models are plotted as lines. Each labeled temperature marks the approximate locations of the model with that effective temperature. Three representative gravities are plotted: from left plot to right plot, log g=4.0, 4.5, and 5.0. Blue lines are cloudless models and red lines are cloudy models (f_{sed}=5, 4, 3, and 2 from left line to right line in each plot) that include the opacity of only the newly added clouds—Na$_2$S, Cr, MnS, ZnS, and KCl.

2.4.2.3 WISE Color-Color Diagrams

Cushing *et al.* (2011) announced the discovery of six proposed Y dwarfs found by the WISE mission. Objects around the T-to-Y transition are cold enough to have NH_3 absorption features in the near infrared.

We have obtained near-infrared photometry for two proposed Y0 dwarfs discovered using the Wide-field Infrared Survey Explorer (WISE) by Cushing et al. (2011). *YJH* was obtained for WISEP J140518.40+553421.5 and *YJ* for J154151.65−225025.2, using the near-infrared imager NIRI (Hodapp *et al.*, 2003) on the Gemini-North telescope on Mauna Kea, Hawaii. The photometry is on the Mauna Kea Observatories system (Tokunaga and Vacca, 2005).The data were obtained via the Gemini queue program GN-2012A-Q-106 on 2012 February 10; the program aims to supplement and improve on the photometry presented in the discovery paper. Individual exposure times of 60 s were used at *Y* and *J*, and 30 s at *H*; a 9-position dither pattern with 10" offsets was repeated as necessary for sufficient signal to noise. The total exposure time for WISEP J140518.40+553421.5 was 9 minutes at *Y* and *J* and 58.5 minutes at *H*; for WISEP J154151.65-225025.2 the total exposure time was 18 minutes at each of *Y* and *J*. Data were reduced in a standard fashion and flatfielded with calibration lamps on the telescope. The UKIRT faint standards FS 133 and 136 were used for photometric calibration; *J* and *H* were taken from Leggett *et al.* (2006), and *Y* from the UKIRT online catalog (http://www.jach.hawaii.edu/UKIRT/astronomy/calib/phot cal/fs ZY MKO wfcam.dat).

The final reduced magnitudes are: $Y = 21.41 \pm 0.10$, $J = 21.06 \pm 0.06$ and $H = 21.41 \pm 0.08$ for WISEP J140518.40+553421.5; $Y = 21.63 \pm 0.13$ and $J = 21.12 \pm 0.06$ for WISEP
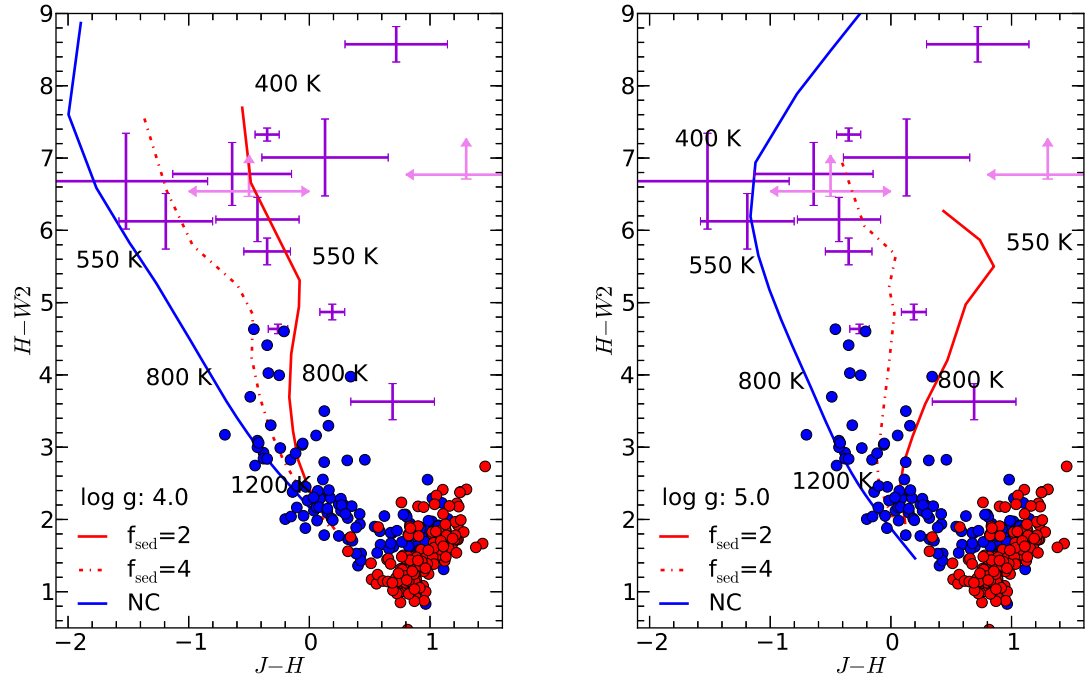
Figure 2.10: Color-color diagrams using WISE and near infrared data. Observed $J-H$ versus $H-W2$ colors of L and T dwarfs (Kirkpatrick *et al.*, 2011) and proposed WISE Y dwarfs (Cushing *et al.*, 2011; Kirkpatrick *et al.*, 2012) are plotted. For J and H bands we use MKO photometry. L and T dwarfs are plotted as red and blue dots, respectively. WISE Y dwarfs are plotted as purple error bars; Y dwarfs with magnitude upper limits are shown in pink. Model photometric colors are shown as solid and dashed lines; the blue line shows a cloudless model and the red lines show two cloudy models (from left to right, f_{sed}=4 and f_{sed}=2). Each labeled temperature marks the approximate location of the models with that effective temperature. Many of these cold brown dwarfs have photometric colors closer to the cloudy models than the cloud-free model. The left plot shows log g=4.0 and the right plot shows log g=5.0.

J154151.65-225025.2.

Figure 2.10 shows how clouds will effect these cold objects. $H - W2$ is a useful temperature indicator for these objects, while $J - H$ is sensitive to both the cloud structure and gravity. As the T_{eff} of the non cloudy models decreases from 800 to 500 K, the models become progressively bluer in $J - H$ color. However, most of the proposed WISE Y dwarfs are redder than the cloudless model. The models that include the sulfide clouds match their colors better. This result tentatively suggests that for objects colder than T dwarfs, the sulfide clouds remain important. Of course, for objects with effective temperatures of $\sim$350 K, water will condense; at that point, H_2O clouds should contribute to the spectra (e.g. Burrows *et al.*, 2003a).

2.4.3 Comparison to Observed T Dwarf Spectra

We now compare model spectra to two relatively cold, red T dwarfs, Ross 458C and UGPS 0722–05. The near-infrared spectra of these two objects are not well-matched by cloudless T dwarf spectra; by including our neglected clouds, which for these cool objects are dominated by the Na_2S cloud, we match their spectra more accurately.

We compare models to both near-infrared spectra and near- and mid-infrared photometry. As in previous studies of brown dwarfs (Cushing *et al.*, 2008; Stephens *et al.*, 2009), we find that in different bands, the observations are best fit by models of different parameters. In this study, we focus on finding models that fit the shape of the spectra in the near-infrared where clouds play a significant role.

2.4.3.1 Ross 458C

Ross 458C is a late-type T dwarf (T7–9) which is separated by over 1100 AU from a pair of M star primaries. It has anomalously red near-infrared colors ($J-K=-0.21\pm0.06$). Burgasser *et al.* (2010) obtained spectroscopic observations with the FIRE spectrograph (Simcoe *et al.*, 2008, 2010) on the Magellan Baade 6.5 meter telescope at Las Campanas Observatory. They fit the spectrum using cloudless and cloudy models (which include only the opacity of the iron, silicate, and corundum clouds) and find that cloudy models fit significantly better than cloudless models. Burgasser *et al.* (2010) conclude that cloud opacity is necessary to reproduce the spectral data and invoke a reemergence of the iron and silicate clouds. We instead assume that the iron and silicate clouds are depleted, as we observe generally in other T dwarfs, and investigate the effect of the sulfide clouds.

In Figure 2.11 we show the FIRE spectrum and the best fitting cloudy and cloudless models. We also show photometry in *J*, *H*, and *K* (Dupuy and Liu, 2012), WISE photometry (Kirkpatrick *et al.*, 2012), and Spitzer photometry (Burningham *et al.*, 2011). The spectra used to generate these results differ somewhat from those in Burgasser *et al.* (2010) because we use models that include recent improvements to the opacity database (Saumon *et al.*, 2012) for both ammonia and the pressure-induced opacity of H_2 collisions. All models are fit by eye to the observations.

Like Burgasser *et al.* (2010), we find that clouds are essential to match the spectrum of Ross 458C. Figure 2.11 shows the best fitting cloudless model and the two best fitting cloudy models (one including the iron and silicate clouds and the other including the sulfide clouds).

The cloudless model is a poor representation of the spectral data; the flux in *Y* and *J* is too high and the flux in *H* and *K* is too low. The cloudy models are better representations of the relative flux in each band.

Burgasser *et al.* (2010) found that the surface gravity of Ross 458C must be low (log *g*=4.0) for models to match the observed spectrum. Likewise, we find that our best-fitting models have surface gravities of 4.0 (cloudless), 3.7 (silicate clouds), and 4.0 (sulfide clouds).

We conclude that we do not need to invoke a reemergence of iron and silicate clouds into the photosphere of Ross 458C to reproduce the observed spectrum. Instead, we are able to reproduce the spectrum using the sulfide clouds which are naturally expected to form in the photospheres of cool T dwarfs. Section 2.5.2 contains additional discussion on which cloud species we expect to be important.

The very red slope to the L band spectrum of Ross 458C—much redder than all the models—is reminiscent of the behavior of some cloudy L dwarfs, including 2MASS2224 and DE 0255 (L3.5 and L9 respectively) and may be a signature of very small dust grains (Stephens *et al.*, 2009).

The discrepancies at 4.5 μm are likely to be a result of non-equilibrium chemistry, which is not included in these models. This effect is discussed in more detail in Section 2.4.4.

2.4.3.2   UGPS J072227.51-054031.2

UGPS J072227.51-054031.2 (hereafter UGPS 0722–05) is a T9 or T10 dwarf with an effective temperature of approximately 500 K, discovered by Lucas *et al.* (2010). Previous spectral analysis with cloudless models has been unsuccessful at modeling the flux in the near-

infrared in Y and J bands (Leggett *et al.*, 2012).

In Figure 2.12 we plot the near-infrared spectra published in Lucas *et al.* (2010) and Leggett *et al.* (2012) with the cloudy and cloudless models that are fit by eye to be the closest representations of the data. We also show J, H, K and Spitzer photometry (Lucas *et al.*, 2010) and WISE photometry (Kirkpatrick *et al.*, 2012). These models have similar temperatures and gravities to previous studies; Leggett *et al.* (2012) presented fits with T_{eff} between 492 and 550 K and log g=3.52 to 5.0, whereas our fits have T_{eff} of 600 K (cloudless) and 500 K (with sulfide clouds) and both have log g=4.5.

Note that the flux in Y and J in cloudless models is systematically too high. The opacity of the sulfide clouds provides a natural mechanism to decrease the flux in Y and J and increase the flux in H and K bands. The match to the models is still not perfect. This may be due in part to incomplete line lists for methane; these cold objects have a significant amount of CH_4 in the atmosphere, which absorbs strongly in the near infrared. The discrepancy at 4.5 μm is most likely due to absorption of CO as a result of non-equilibrium chemistry (see Section 2.4.4). Outstanding issues in T dwarf modeling are discussed in Section 2.5.3.

2.4.4 Non-Equilibrium Chemistry

We note that both of our preferred sulfide cloud models predict brighter M band (4.5 μm) photometry than is observed. This is likely a consequence of our neglect of non-equilibrium mixing of CO in this study. As first predicted by Fegley and Lodders (1996), such mixing is an important process in the atmospheres of brown dwarfs (Noll *et al.*, 1997; Marley *et al.*, 2002; Saumon *et al.*, 2006; Stephens *et al.*, 2009) as it is in solar system giants (Bar-

shay and Lewis, 1978) and the relative impact of the mixing increases with decreasing gravity (Hubeny and Burrows, 2007; Barman *et al.*, 2011a). Absorption by excess atmospheric CO decreases the thermal emission in M band and is likely responsible for the mismatches seen in Figures 2.11 and 2.12, particularly for the lower gravity Ross 458C.

The formation of the clouds considered in this study does not involve the species most affected by non-equilibrium chemistry such as CO and CH_4. The cloud models will therefore be only minimally affected by the changes in the pressure-temperature profile of the atmosphere due to the changes in gas opacity. However, the overall spectra of models will look quite different in regions where CO absorbs strongly, such as the 4.5 μm feature, so future, more comprehensive fits of sulphide cloud models to observations will have to include non-equilibrium models.

2.5 Discussion

2.5.1 Formation of Clouds

Clouds must form in brown dwarf atmospheres as they cool; there is no way to avoid the condensation of different species as the atmosphere reaches lower effective temperatures. In these models, we parameterize the opacity of clouds by creating a distribution of cloud material in the atmosphere which has a distribution of cloud particle sizes. Within the models, we can change those distributions. A cloud that sediments into a small number of large particles will settle into a thin layer and will not significantly change the emergent spectrum; the same cloud material organized into an extended cloud with small particle sizes will have a dramatic effect

on the model spectrum.

For these reasons, we require a model of cloud particle sizes and distribution as well as the underlying chemistry. When we consider models that include new or different clouds, we do not change any of the underlying chemistry of condensation; we change the opacity of the condensate particles and in doing so modify the effect that the cloud formation has on emergent flux.

2.5.2 Sulfide or Silicate Clouds?

Burgasser *et al.* (2010) invoked the reemergence of silicate clouds to explain the spectrum of Ross 458C. We suggest instead that the initial emergence of sulfide clouds would have a similar effect on the spectrum and provide a more natural explanation for the results.

From observations, it is clear that the range in T dwarf colors just following the L/T transition is small; spectra of T dwarfs show no evidence that clouds still affect the emergent flux for objects slightly cooler than this transition. This observation suggests that the iron and silicate clouds have dissipated between 1400 and 1200 K (for typical field dwarfs) and are no longer important in T dwarf atmospheres. If iron and silicate clouds were sometimes important in T dwarf atmospheres, we would expect to see a population of relatively quite red objects at effective temperatures between that of Ross 458C and the L dwarfs; no brown dwarf with these properties has been observed.

As T dwarfs cool, the range in observed infrared colors increases; a population of red T dwarfs develops, which are redder in the near-infrared than cloudless models predict. Based on these observations, we favor a mechanism that cannot strongly alter T_{eff}~900-1200 K T

dwarf atmospheres, but naturally reddens $T_{\text{eff}} \lesssim 800$ K T dwarfs.

The emergence of sulfide clouds provides that natural explanation for this range in T dwarf colors at low effective temperatures. Just as the iron and silicate clouds condense in the photospheres of L dwarfs and change their observed spectra, the sulfide clouds begin to condense in the photospheres of T dwarfs with temperatures cooler than 900 K, changing their observed spectra.

We have not yet investigated whether the sulfide clouds will have identifiable spectral features that would confirm their presence in T dwarf atmospheres, but given the features in the sulfide indices of refraction (see Figure 2.2) these features would likely be in the mid-infrared.

2.5.3 Outstanding Issues In T Dwarf Models

There are several challenges in modeling T dwarfs that have not yet been addressed in these calculations. Because of the high densities in brown dwarf atmospheres, sodium and potassium bands at optical wavelengths are extremely pressure-broadened in T dwarf spectra (Tsuji *et al.*, 1999; Burrows *et al.*, 2000; Allard *et al.*, 2005, 2007). The wings of these broadened bands extend into the near-infrared in *Y* and *J* bands, creating additional opacity at those wavelengths. For these calculations, we use the line broadening treatment outlined in Burrows *et al.* (2000), which is somewhat *ad hoc* and potentially creates some inaccuracies in the model flux in *Y* and *J* bands. A calculation of the molecular potentials for potassium and sodium in these high pressure environments, as is carried out in Allard *et al.* (2005, 2007), would improve the accuracy of these models.

Another challenge in modeling T dwarf spectra is the inadequacies of methane opacity

calculations; methane is the only important gas-phase absorber with inadequate opacity measurements or calculations. Uncertainties in methane absorption bands create inaccuracies in T dwarf models, especially in H band where it is a very strong absorber (Saumon *et al.*, 2012).

2.5.4 Breakup of Na$_2$S Cloud

Sulfide clouds could form partial cloud layers with patchy clouds. One way to infer patchy cloud cover is to observe variability in photometric colors; variability can indicate high-contrast cloud features rotating in and out of view. Radigan *et al.* (2012) studied objects at the L/T transition and inferred that the iron and silicate clouds could be in the process of breaking up and forming patchy clouds in those atmospheres. A similar study of the variability of cool T dwarfs could reveal a similar physical process in sulfide clouds.

2.5.5 Constraining Cloud Models with More Data

A larger number of high fidelity spectra of the coldest T dwarfs would help to constrain these cloudy models. Currently there are a few objects with effective temperatures cooler than 700 K with moderate resolution spectra. A larger sample of objects would give us better statistics on the overall population of T dwarfs, with different surface gravities, metallicities, and cloud structures.

2.5.6 Water Clouds

At cooler effective temperatures, water clouds will condense in brown dwarf atmospheres (Burrows *et al.*, 2003a). Oxygen is 300 times more abundant than sodium in a solar-

composition gas and the silicate clouds only use 20% of the total oxygen in the atmosphere, so water clouds will be much more massive and important in shaping the emergent flux. As missions like WISE find colder objects (Kirkpatrick *et al.*, 2011; Cushing *et al.*, 2011) and these objects are observed spectroscopically, future models of brown dwarfs will need to include the condensation of these more volatile clouds.

Before the water clouds condense, Lodders (1999); Lodders and Fegley (2006) predict that RbCl and CsCl will condense; however, the abundances of Cs and Rb are very low (Lodders, 2003) so these clouds will be optically thin. If equilibrium conditions prevail, $NH_4H_2PO_4$ would also condense (Fegley and Lodders, 1994; Visscher *et al.*, 2006) with a mass similar to that of the Na_2S cloud. Whether $NH_4H_2PO_4$ condenses or P remains in the gas phase as PH_3 (as on Jupiter and Saturn) deserves further study to examine potential effects on the spectra of the coolest brown dwarfs.

2.5.7 Application to Exoplanet Atmospheres

Observations and models of T dwarfs provide a testbed to study planetary atmospheres. While brown dwarfs are more massive than planets, the atmospheres of T dwarfs have similar effective temperatures to those of young giant planets (Burrows *et al.*, 1997; Fortney *et al.*, 2008b). The study of T dwarfs provides crucial tests of cloudy atmosphere models that will be applicable to directly-imaged exoplanet atmospheres.

Cloud models designed originally for brown dwarfs are already being applied to exoplanets. Cloud models with iron and silicate clouds were originally developed to model L dwarf atmospheres; these models have been successfully applied to observations of the only directly

imaged multiple planet system, HR 8799. Several studies of the HR 8799 planets have shown that the iron and silicate clouds play a significant role in their atmospheres (Marois *et al.*, 2008; Barman *et al.*, 2011a; Galicher *et al.*, 2011; Bowler *et al.*, 2010; Currie *et al.*, 2011; Madhusudhan *et al.*, 2011a; Marley *et al.*, 2012).

As instruments like the Gemini Planet Imager and SPHERE begin to discover new planets in the next few years, we will be able to apply brown dwarf models to colder planetary atmospheres in which clouds will likely play a key role in shaping their spectra.

2.6 Summary

Cloud formation is a natural and unavoidable phenomenon in cool substellar atmospheres. At temperatures cooler than those of L dwarfs, chemistry dictates that additional condensates, beyond the silicates and iron, must form. We have examined the effect of including the most abundant of these lower-temperature condensates, Cr, MnS, Na_2S, ZnS, and KCl, in brown dwarf model atmospheres. Within the framework of the Ackerman and Marley (2001) cloud model, we have investigated the opacity of these clouds over a wide range of parameter space, across the relevant range of T dwarfs, to the warmest Y dwarfs. From our suite of models from 400 to 1300 K, log g=4.0 to 5.5, f_{sed}=2 to 5, we have shown the likely role that these low-T_{eff} clouds, dominated by sulfides, play in these cool atmospheres.

Model spectra were compared to two T dwarfs, Ross 458C and UGPS 0722–05. These two objects have red near-infrared colors and are not well-matched by cloudless models. Model spectra that include the sulfide clouds match the observed spectra of both objects

more accurately than cloudless models.

The photometric colors of the cloudy models were calculated and compared to the full population of brown dwarfs with parallax measurements. This analysis shows that the sulfide clouds provide a mechanism to match the near-infrared colors of observed brown dwarfs. The agreement is particularly good in $J-H$, while in $J-K$ the models are somewhat too red. WISE observations of the coolest T dwarfs and warmest Y dwarfs indicate the these new models fit observations better than cloud-free models.

Our results indicate that understanding the opacity of condensates in brown dwarf atmospheres of all T_{eff} is necessary to accurately determine the physical characteristics of the observed objects.
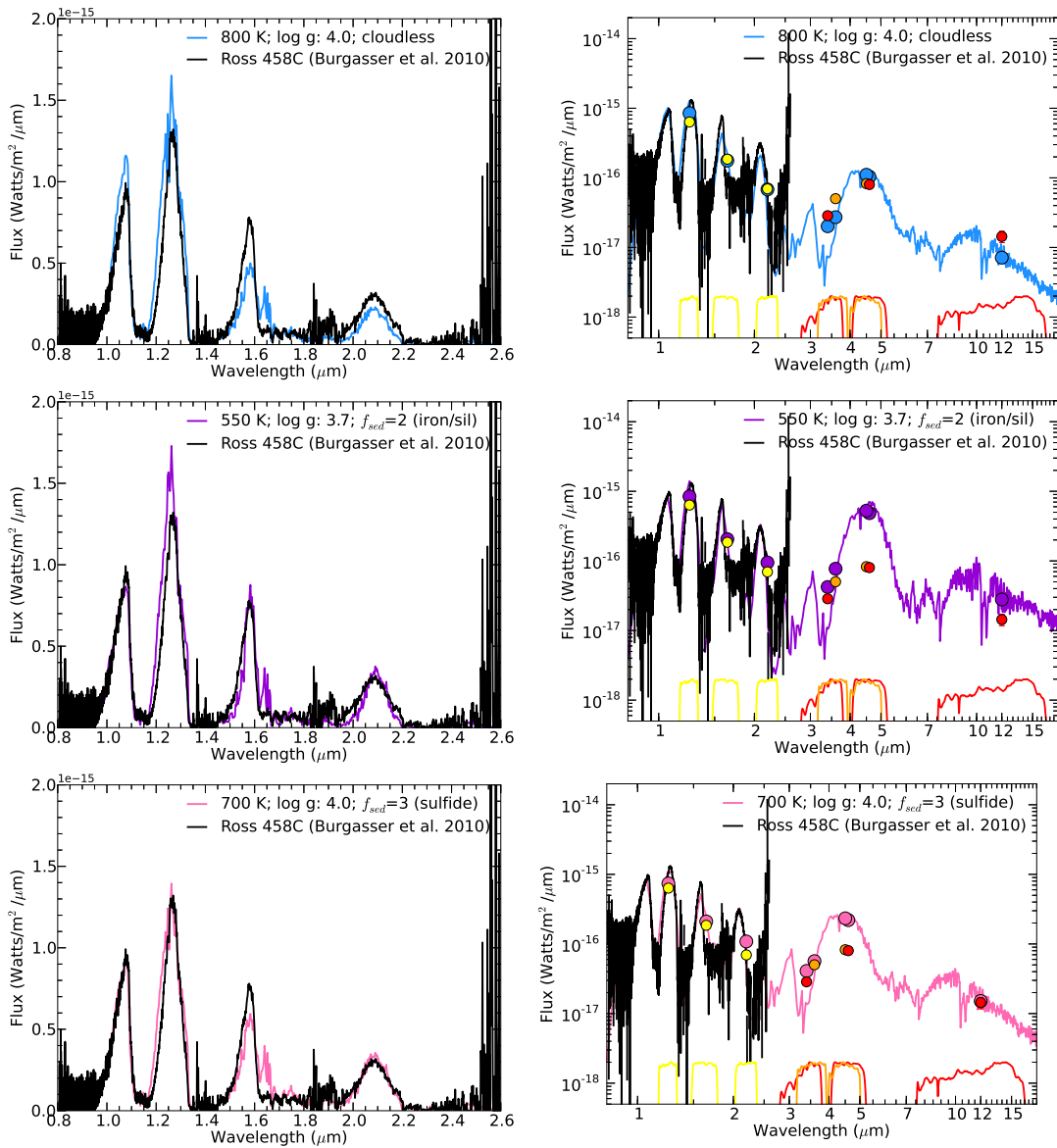
Figure 2.11: Ross 458C near-infrared spectrum comparison between data and models. Three different models are compared to the observed spectrum and photometry of Ross 458C from Burgasser *et al.* (2010). The left panels show the near-infrared spectra; the right panels show the same spectra and models with near- and mid-infrared photometry. Yellow points show J, H, and K photometry; orange show Spitzer [3.6] and [4.5] photometry; red show WISE $W1$, $W2$, and $W3$ photometry. The filters for the photometric bandpasses are shown with corresponding colors along the bottom. The top row shows a cloudless model spectrum that best matches the data, which has an effective temperature of 800 K and surface gravity log g=4.0. The middle row shows the best matching cloudy spectrum using iron and silicate clouds. The bottom row shows the best matching cloudy spectrum using sulfide clouds. Both cloudy models have significantly lower effective temperature (100-250 K cooler) than the cloudless best-matching model.
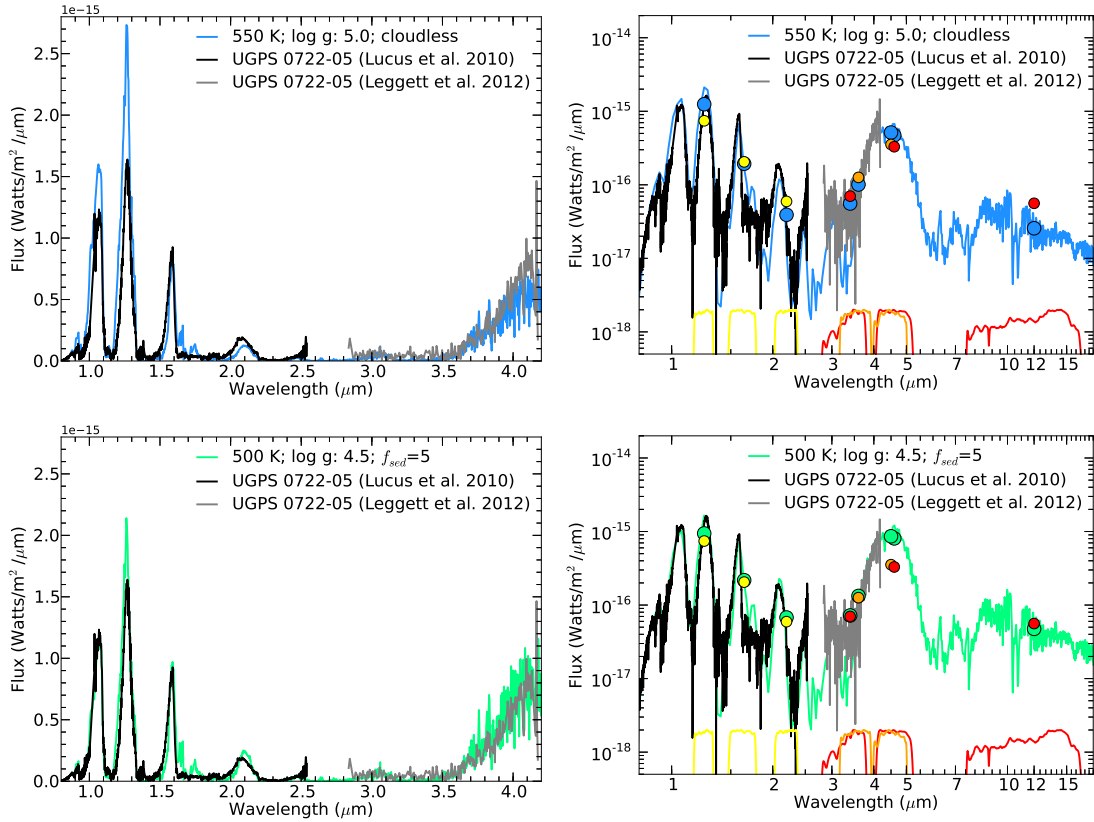
Figure 2.12: UGPS 0722–05 near-infrared spectrum comparison. Two different models are compared to the observed spectrum of UGPS 0722–05 from Lucas *et al.* (2010). As in Figure 2.11, the left panels show the near-infrared spectra; the right panels show the same spectra and models with near- and mid-infrared photometry. Yellow points show J, H, and K photometry; orange show Spitzer [3.6] and [4.5] photometry; red show WISE $W1$, $W2$, and $W3$ photometry. The filters for the photometric bandpasses are shown with corresponding colors along the bottom. The top plot shows a cloudless model spectrum that best matches the data, which has an effective temperature of 550 K and surface gravity log g=5.0. The bottom plot shows the best matching cloudy spectrum using sulfide clouds; it has an effective temperature of 500 K, log g=4.5, and f_{sed}=5.

Chapter 3

Quantitatively Assessing the Role of Clouds in the Transmission Spectrum of GJ 1214b

3.1   Introduction

The transiting super-Earth GJ 1214b is the first planet discovered by the MEarth survey (Charbonneau *et al.*, 2009) and is currently the only super-Earth that has been observed using transmission spectroscopy. The planet's mass and radius are $6.16\pm0.91M_{\oplus}$ and $2.71\pm0.24R_{\oplus}$ respectively (Anglada-Escudé *et al.*, 2013), giving it a low bulk density of 1.68 g cm^{-3}. This density is consistent with either a water-rich planet or planet with a dense iron/rock core and hydrogen/helium envelope (Nettelmann *et al.*, 2011; Seager *et al.*, 2007; Rogers and Seager, 2010). Rogers and Seager (2010) proposed three general mechanisms by which GJ 1214b may have accumulated its atmosphere. The planet may have accreted a hydrogen/helium envelope from the stellar nebula, outgassed a hydrogen envelope from a rocky planet, or contain

a high water content in the interior with a hydrogen-depleted, water-rich envelope. Nettelmann *et al.* (2011) argue that the water-rich hypothesis would require unreasonably large bulk water-to-rock ratios, suggesting that the atmosphere must be at least partially composed of hydrogen and helium. By measuring the composition of GJ 1214b's atmosphere using transmission spectroscopy, we can potentially distinguish between these hypotheses.

3.1.1   Transmission spectroscopy

During a transit, the light from the host star passes through the atmosphere of the transiting planet. Because the opacity of the atmosphere varies with wavelength, the radius of the planet will appear to vary with wavelength. The depth of features in the transmission spectrum scales as $N_H \times 2HR_p/R_*$, where N_H (the number of scale heights probed) is set by the opacities involved ($\sim 1-10$), H is the atmospheric scale height, R_p is the planetary radius, and R_* is the stellar radius (Seager and Sasselov, 2000; Hubbard *et al.*, 2001). The scale height H is inversely proportional to the mean molecular weight μ of the atmosphere. By measuring the depth of transit features, we probe the mean molecular weight of the atmosphere and can thus probe whether the atmosphere is H/He-rich ($\mu \sim 2.3$) or a higher mean molecular weight H_2O ($\mu \sim 18$) atmosphere (Miller-Ricci *et al.*, 2009).

Cloud opacity, due to equilibrium and non-equilibrium processes, can be readily seen in the atmosphere of every planet and moon with an atmosphere in our solar system. These include sulfuric acid clouds on Venus (Prinn, 1973), water and carbon dioxide clouds on Mars (Montmessin *et al.*, 2006; Whiteway *et al.*, 2009), ammonia clouds on Jupiter (Baines *et al.*, 2002), ammonia and water clouds on Saturn (Sromovsky *et al.*, 1983; Baines *et al.*, 2009;

Sánchez-Lavega *et al.*, 2011), methane clouds and tholin haze on Titan (Brown *et al.*, 2010; de Kok *et al.*, 2007), and methane-derived clouds and hazes on Uranus (Pollack *et al.*, 1987; Irwin *et al.*, 2007; Karkoschka and Tomasko, 2009) and Neptune (Hammel *et al.*, 1989; Max *et al.*, 2003; Gibbard *et al.*, 2003). It has long been recognized that clouds could impact the transmission spectrum of transiting exoplanets as well (Seager and Sasselov, 2000; Brown, 2001; Hubbard *et al.*, 2001). Furthermore, at the slant viewing geometry relevant for transmission spectroscopy, it has been suggested that long light path lengths through the atmosphere could lead even minor condensates to become optically thick, thereby obscuring gaseous absorption features (Fortney, 2005).

Transmission spectroscopy has been successfully used to probe the atmospheres of hot Jupiters, enabling the detection of atoms, molecules, and even clouds (e.g. Charbonneau *et al.*, 2002; Pont *et al.*, 2008; Sing *et al.*, 2008). For GJ 1214b, if the atmosphere is H/He-rich the features are predicted to change the planet's radius by $\sim$0.1% which would be detectable with current instruments (Miller-Ricci and Fortney, 2010). If the atmosphere is instead water-rich with $\mu \sim 18$, the features will be a factor of ~ 10 smaller and the spectrum could appear featureless at the observational precision of current instrumentation.

3.1.2 Observations of GJ 1214b's atmosphere

Numerous observations of the transmission spectrum of GJ 1214b have been made from optical through near-infrared wavelengths from both ground and space. Bean *et al.* (2010), using the Very Large Telescope, found that the transmission spectrum is featureless between 0.78 and 1.0 μm. Désert *et al.* (2011)'s broad-band photometric observations using the *Spitzer*

Space Telescope at 3.6 and 4.5 μm showed a flat spectrum. The high resolution NIRSPEC spectrum from Crossfield *et al.* (2011) also showed a featureless spectrum. Croll *et al.* (2011), contradicting the other measurements, found a deeper *K*-band (2.2 μm) transit using the Canada France Hawaii Telescope, consistent with the larger features of an H_2-rich atmosphere. Berta *et al.* (2012) obtained a near-IR spectrum using Wide Field Camera 3 on the *Hubble Space Telescope* and found a transmission spectrum consistent with a featureless specturm. de Mooij *et al.* (2012) observed the transit of GJ 1214b in the optical bands *g*, *r*, *i*, *I* and *z* and near-infrared bands K_s and K_c and found all but the *g*-band observation to be consistent with a featureless spectrum. The *g*-band point has a slightly higher radius, possibly indicative of scattering. Murgas *et al.* (2012) observed GJ 1214b using the Gran Telescopio Canarias with a narrow-band tunable filter at three bands: one centered on the line core of Hα and two in the continuum, centered on either side. Their data are consistent with previous observations, but show a high intrinsic scatter. Fraine *et al.* (2013) re-observed the transit of GJ 1214b with *Spitzer* and in *I*+*z* bands from the ground; their results are also consistent with a featureless spectrum or a water-vapor atmosphere, and find that their best-fitting model has a transit radius that increases into the optical, indicative of a scattering constituent in the upper atmosphere. Recently Teske *et al.* (2013) obtained optical spectra in *R*, *V*, and *g'* bands consistent with a flat spectrum.

We note that some of the observations disagree with each other to high significance, especially in the near-infrared *K*-band. Impartially, we adopt the errors published in the literature and accept that no model will agree with all points.

3.1.3 Previous cloud and haze models of GJ 1214b

Fortney (2005) suggested that in the slant viewing geometry of transmission spectroscopy, minor condensates could have appreciable optical depth. These minor condensates and hazes would lead to weaker than expected or undetected gaseous absorption features.

Several previous studies have included some of the effects of clouds in GJ 1214b's atmosphere. One method of including cloud opacity is to include an ad hoc opaque level at the pressure level in the atmosphere required to reproduce the observations, which represents an optically thick (at all wavelengths) cloud deck (e.g. Berta *et al.*, 2012). Benneke and Seager (2012) developed a Bayesian retrieval method for super-Earths which can incorporate this type of opaque level to represent a cloud. In a more sophisticated cloud treatment, Howe and Burrows (2012) incorporate a range of haze layers into GJ 1214b atmospheres. In each of their models, they include a haze composed of polyacetylene, tholin, or sulfuric acid. They test a range of different ad hoc number densities, particle sizes, and pressure levels for each cloud material. They find that a hydrogen-rich atmosphere with a haze layer is generally consistent with the observations, but cannot rule out a water-rich atmosphere. Their result serves as a useful parameter study, demonstrating that clouds within a hydrogen-rich atmosphere can match the observations.

3.1.4 Clouds from equilibrium and disequilibrium processes

Previous cloud studies of GJ 1214b have invoked clouds as a way of matching the transmission spectrum observations, but these studies all lack a physical basis for choosing the cloud-forming material, the amount of cloud material, and the distribution of the cloud in the

atmosphere; that is, a cloud layer could match observations, but no chemistry models were used to determine where clouds form and from what materials. While these studies do find that clouds can reproduce the observations, a remaining essential question is how plausible these clouds are given the conditions in the planet's atmosphere. In this study, we include two sets of physically-motivated clouds—based on two types of chemistry models—that are expected to form in the planet's atmosphere (Miller-Ricci Kempton *et al.*, 2012), and explore their effects in detail.

The first set of clouds are those that form as a result of equilibrium chemistry. Equilibrium clouds have been extensively studied in brown dwarfs; silicate and iron clouds condense in L dwarfs (e.g. Tsuji *et al.*, 1996; Allard *et al.*, 2001; Marley *et al.*, 2002; Burrows *et al.*, 2006; Cushing *et al.*, 2008; Visscher *et al.*, 2010) and sulfide and chloride clouds condense in T dwarfs (Lodders and Fegley, 2006; Visscher *et al.*, 2006; Morley *et al.*, 2012).

The other set of clouds we include form as a result of disequilibrium chemistry; we include a photochemically-produced haze layer. We follow the photochemical destruction of CH_4 and the corresponding creation of higher order hydrocarbons, with a photochemical model. Although we do not follow the photochemical pathways completely to haze formation, the model is used to determine the abundance and vertical distribution of haze precursors.

Photochemical hazes form in the atmospheres of all of the solar system's giant planets (e.g. Gautier and Owen, 1989). While GJ 1214b is significantly warmer than any of these planets, it is cool enough that methane is still the most abundant carbon-bearing species (Miller-Ricci Kempton *et al.*, 2012). Due to its large UV photodissociation cross section, methane breaks apart in the upper atmosphere of irradiated planets and produces rich carbon chemistry

in the atmosphere. Models that include UV dissociation of methane find that molecules such as C_2H_2, C_2H_4, C_2H_6, CH_3, HCN, and C_6H_6 exist in far greater abundance than would be expected from chemical equilibrium calculations (Yung *et al.*, 1984; Zahnle *et al.*, 2009a; Moses *et al.*, 2011; Miller-Ricci Kempton *et al.*, 2012).

3.1.5 Other approaches to cloud formation in brown dwarfs

There are of course many ways to model clouds in planetary atmospheres (Marley *et al.*, 2013), and because we approach the problem by extending the models which have been used mainly for brown dwarf science, we will briefly describe the differences between the approaches here. For a much more extensive comparison, Helling *et al.* (2008a) review various cloud modeling techniques and compare model predictions for various cases.

Many modeling groups apply the general assumptions of equilibrium chemistry that we apply here (e.g. Tsuji *et al.*, 1996; Allard *et al.*, 2001; Marley *et al.*, 2002; Burrows *et al.*, 2006; Cushing *et al.*, 2008; Visscher *et al.*, 2010), though these models differ in the details of their approaches. A detailed comparison of true equilibrium condensation and cloud condensate removal from equilibrium can be found in Fegley and Lodders (1994); Lodders and Fegley (2006) and references therein.

Instead of assuming equilibrium chemistry to calculate cloud properties, Helling & Woitke (Helling and Woitke, 2006) follow tiny seed particles of TiO_2 in the upper atmospheres of brown dwarfs, which they assume to be advected from deeper layers, and follow the particles they as sink downwards. As these seed particles fall through the atmosphere, they collect condensate material. In Helling and Woitke (2006) and numerous follow on papers (Helling *et al.*,

2008a; Witte *et al.*, 2009, 2011; de Kok *et al.*, 2011) this group models the microphysics of grain growth given these conditions. They predict 'dirty' grains composed of layers of varying condensates. This model has been applied to self-luminous giant planets and brown dwarfs but has not yet been applied to transiting super-Earths like GJ 1214b.

3.2 Methods

3.2.1 Atmospheric composition

The only planets in a similar mass range to GJ 1214b with well-characterized atmospheric compositions are Uranus and Neptune. Both planet's atmospheres are $\sim 50\times$ solar abundance in carbon, mostly in the form of methane (Fletcher *et al.*, 2010). Other elements cannot easily be studied in those atmospheres because the planets are cold and most species are condensed into clouds below the visible atmosphere.

Although it is well-established that planetary atmospheres in our own system have enhanced metallicities, the composition of exoplanet atmospheres is not yet well understood. In this analysis, we include solar composition models and $50\times$ solar metallicity ([M/H]=1.7) models. The enhanced metallicity models are enhanced uniformly in all heavy elements.

3.2.2 Equilibrium cloud models

In GJ 1214b's atmosphere, assuming thermochemical equilibrium, a variety of substances are condensed in the upper atmosphere. Figure 5.3 shows pressure–temperature (*P–T*) profiles of model atmospheres with hydrogen/helium rich compositions. The top panel shows

solar composition models and condensation curves; the bottom panel shows $50\times$ solar metallicity composition models. Cloud-free models are shown as solid lines and cloudy models are shown as dashed lines. The models used to calculate these profiles are discussed in Section 3.2.5. The condensation curves, shown as colored dashed lines, show where each element or molecule exists in the solid or liquid phase assuming chemical equilibrium; the condensation curve represents the pressures and temperatures where the vapor pressure of a gas is equal to its saturation vapor pressure. To the left of the curve, we assume that vapor in excess of the saturation vapor pressure is condensed and has settled toward the cloud base. In this approach, the cloud base is located where the P–T profile meets the condensation curve, with some vertical extent above that point. The iron and silicate clouds exist extremely deep in the atmosphere, as they do on Jupiter. Na_2S, ZnS, MnS, Cr, and KCl form higher in the atmosphere.

The opacity of Na_2S, ZnS, MnS, Cr, and KCl clouds have recently been included in T dwarf atmospheres by Morley *et al.* (2012), using the equilibrium condensation approach of Visscher *et al.* (2006) within the framework of the well-established Ackerman and Marley (2001) treatment for cloud formation and settling in brown dwarf and giant planet atmospheres. Model atmospheres using this cloud treatment generally match the spectra of cloudy L dwarfs over a wide parameter range Cushing *et al.* (2008); Stephens *et al.* (2009). We use the methods developed and described in Morley *et al.* (2012) to include the same clouds in a super-Earth atmosphere.

The major differences between the Morley *et al.* (2012) models for brown dwarf atmospheres and the models here are the irradiation of the planet by the host star and the enhanced metallicity of the atmosphere for some models. Morley *et al.* (2012) published saturation vapor

pressure and condensation curves for [M/H]= −0.5 and +0.5. For this study, a higher metallicity, [M/H]= 1.7, was necessary. We calculated the condensation temperature for KCl and ZnS based on a model GJ 1214b *P–T* profile. We found that, for this particular model atmosphere, the saturation vapor pressure and condensation curves were very close to the values we would have found by extrapolating the Morley *et al.* (2012) vapor pressure and condensation curves. Since the differences due to the extrapolation are small for the gases in question, we adopted the same curves in this study.

To flatten transmission spectrum features in the near-IR, the clouds must be present and optically thick at *slant* viewing geometry above $\sim 10^{-3}$ bar. Only KCl and ZnS form that high in the atmosphere for this planet (see Figure 5.3), so for the models here, we include only the KCl and ZnS clouds. Na_2S will also form, but generally too deep to become optically thick at the low pressure levels probed in transmission spectra. We assume that the KCl and ZnS form into homogeneous, spherical particles, unlike the heterogeneous compositions that have been favored by Helling *et al.* (2008b).

The particle sizes and vertical thickness of the cloud are calculated using the parametrized value f_{sed} in the Ackerman and Marley (2001) framework. This value is equal to the ratio of the sedimentation velocity to the updraft velocity. A high sedimentation efficiency f_{sed} forms a cloud with large particles that settles into a thin layer; a low f_{sed} forms a more extended cloud with smaller particles.

3.2.3 Photochemistry models

The photochemistry model used to generate the properties of the hydrocarbon haze layer is described in detail in Miller-Ricci Kempton *et al.* (2012). The lower boundary conditions of the models assume chemical equilibrium at depths of 1000 bar. This is generally a good assumption because the reactions proceed very quickly at the higher pressures and temperatures encountered deep in the atmosphere. The upper boundary condition assumes a zero flux lid, meaning that no mass is being lost from the upper atmosphere, at 1 μbar.

There are 500+ reactions in the photochemical model, many of which are anchored by laboratory experiments, including nearly all of the experiments involving abundant and stable molecules (Zahnle *et al.*, 2009a; Miller-Ricci Kempton *et al.*, 2012; Moses *et al.*, 2011; Baulch *et al.*, 1992). Very well studied reaction rates, for example those encountered during combustion, are accurate to within 10 percent. Very poorly studied reactions between more minor atmospheric species may be inaccurate to a factor of several. The details of the uncertainties of individual reaction rates are somewhat beyond the scope of this work.

At the time of publication of Miller-Ricci Kempton *et al.* (2012), the UV spectrum of GJ 1214 had not been observed; instead, the study focused on two end-cases: a quiet M dwarf and an active M dwarf (AD Leo). Recently, France *et al.* (2013) published a UV spectrum of the GJ 1214 host star. For the host star in the photochemistry model, we use this observed UV spectrum from 1150 to 3100 Å and a PHOENIX model atmosphere spectrum with a stellar effective temperature of 3026 K and a stellar radius of 0.211 $R_\odot$ from 3100 to 10000 Å (Hauschildt *et al.*, 1999). We have calculated new solar metallicity and 50$\times$ solar metallicity models with the new

spectrum. Figure 3.2 shows the results of the photochemistry calculations for the two values of the eddy diffusion coefficient used in this study: $K_{zz}= 10^7$ and 10^9 cm^2 s^{-1}.

3.2.4 Hydrocarbon haze

As described above, for the equilibrium clouds, our model parametrizes the cloud properties with a single value, f_{sed}; this model inherently assumes that the condensation of particles can be described by an equation for saturation vapor pressure which is an analytic function of atmospheric temperature and pressure. The formation of a hydrocarbon haze layer by polymerization is more complex and cannot be described simply and analytically in the same way as a function of temperature and pressure. The more complicated situation means that we cannot use the single parameter f_{sed}, but instead must calculate based on the photochemistry the amount of haze in each layer, and explore how changing parameters like particle size affects the transmission spectrum.

3.2.4.1 Forming soots from second-order hydrocarbons

The highest order hydrocarbons produced by the Miller-Ricci Kempton *et al.* (2012) and Zahnle *et al.* (2009a) models are the second-order hydrocarbons acetylene (C$_2$H$_2$), ethylene (C$_2$H$_4$), and ethane (C$_2$H$_6$). Higher-order hydrocarbon chemistry (e.g., >C$_3$H$_x$) in reducing, high-temperature, low-pressure planetary environments like GJ 1214b remains incompletely understood, and current photochemical and kinetics models (which generally derive reaction rates from combustion studies under much more oxidizing conditions) do not capture all possible chemical pathways for producing higher-order hydrocarbons that form soots in exoplanet

89

atmospheres (e.g., see Moses *et al.* (2011) discussion on C_3–C_6 chemistry).

Because the hydrocarbon chemistry is truncated at C_2H_x, polymerization beyond C_2H_x is not included. When conditions favor polymerization carbon will instead pool in C_2H_x species, because longer carbon chains are not allowed. We can estimate how favorable conditions are for polymerization by comparing the quantities of reducing and oxidizing species in the atmosphere. If there are more oxidizing species (OH), oxidation by OH will inhibit hydrocarbon polymerization. If there are instead more reactive reducing species (including C_2H, C_2H_3, CH, CH_2, CH_3, CN), then hydrocarbon polymerization is not inhibited and is expected to continue at some rate (to date not well constrained by either experiments or kinetic theory). We calculate the amount of oxidizing and reducing material in each model atmosphere and determine that the amount of reducing material is larger—often many orders of magnitude larger—than the amount of oxidizing material at the pressure levels where soots are expected to form. Each soot precursor will therefore react many times with these reducing radicals before interacting with an OH molecule, growing progressively larger until it become involatile enough to condense to form a solid soot-like haze particle. Figure 3.3 shows an example of this comparison for a photochemistry model with 50× solar composition and K_{zz}=10^9 cm^2 s^{-1}. This is not unexpected in a cool atmosphere like GJ 1214b's (T$_{\text{eff}}$ ∼550 K) with a relatively inactive host star (see Zahnle *et al.* (2009a) for more details).

For the hydrogen-dominated atmospheres of the solar system, Jupiter's atmosphere receives the largest incident flux and has a haze that is the most optically thick. As reviewed in West *et al.* (2004) there have been some progress in modeling the vertical distribution and particle sizes of this Jovian haze. A central problem, and the one we encounter here, is the lack of

understanding of the processes that allow for the progression from from complex hydrocarbons (originally derived from methane destruction) to $\sim$0.01 μm particles. Friedson *et al.* (2002) and Wong *et al.* (2003) have made the most progress on this front, suggesting first the homogeneous nucleation of the PAH pyrene at high altitudes, followed by heterogeneous nucleation of other molecules upon these seed particles, followed by coagulation and further heterogeneous nucleation during particle sedimentation.

In these Jovian haze models (West *et al.*, 2004, see), tiny particles are assumed to homogeneously nucleate, and then the processes of coagulation, sedimentation, and eddy diffusion lead to particle growth and movement within the atmosphere. By following these processes the particle sizes and number densities as a function of atmospheric pressure can be calculated and compared to observations (Rages *et al.*, 1999, e.g.). Given the exploratory nature of our work, we further simplify this kind of calculation by assuming that the second-order hydrocarbons C_2H_2, C_2H_4, and C_2H_6 and HCN in GJ 1214b's atmosphere continuously polymerize to form complex hydrocarbons like soot. We further assume that this process happens with the same constant efficiency in each layer of the atmosphere. We treat this efficiency as a free parameter. Hazes are thus most likely to form at altitudes where these soot precursors (C_2H_2, HCN) are produced in abundance via photochemical and thermochemical processes. The soot precursors are most favored when CH_4 is abundant, as is the case for GJ 1214b, and will be enhanced further for high C/O ratios (Moses *et al.*, 2013).

3.2.4.2 Calculating the hydrocarbon haze properties

To determine the amount of material available to form hydrocarbon haze, we use the results from photochemistry models. These results give us the mixing ratio of each species at each pressure level in the atmosphere (see Figure 3.2). We calculate the number density of each species at each height in our model and multiply by the mean molecular weight of each species to calculate the mass density of C_2H_2, C_2H_4, C_2H_6, and HCN in each model layer. We sum the densities of these four species to find the total mass in soot precursors. A fraction of the total mass of soot precursors goes into forming the haze we model here: we multiply the total mass by our parametrized "efficiency"—that is, the fraction of haze precursors that actually form haze particles—to find the mass of the haze particles in a given layer. For each layer,

$$M_{\text{haze}} = f_{\text{haze}} \times (M_{C_2H_2} + M_{C_2H_4} + M_{C_2H_6} + M_{\text{HCN}}) \tag{3.1}$$

where f_{haze} is the prescribed efficiency, M_x is the mass of material in each species within each model layer from the photochemical model, and M_{haze} is the calculated mass of haze particles in that layer.

From the total mass of haze particles in each layer, we calculate how many particles form. We choose a mode particle size and establish a log-normal particle distribution; we calculate the number of particles by summing over the distribution for each of our chosen particle sizes.

We base our particle size distribution and physical properties on those found in experiments of soots on Earth. For example, Kim *et al.* (1999) finds that diesel soot particles can have

mode particle sizes between 0.05 and 0.5 μm with a relatively log-normal distribution around the mode. We use an average material density from Slowik *et al.* (2004) of 2.0 g cm^{-3}; note that while soots often form as low-density fluffy aggregates on Earth, we use the density only to calculate the number of particles formed, so the density of the solid soot material must be used. We use soot optical properties (the real and imaginary parts of the refractive index) tabulated in the software package OPAC (Optical Properties of Aerosols and Clouds) (Hess *et al.*, 1998), which we linearly extrapolate for wavelengths longer than 40 μm. The extrapolation affects the spectrum negligibly between 40 and 230 μm.

When calculating the transmission spectrum, equilibrium chemistry abundances are used. Miller-Ricci Kempton *et al.* (2012) showed that the disequilibrium abundances of carbon and nitrogen species will change the calculated spectrum very slightly, but will not change the overall shape of the spectrum.

3.2.5 Atmosphere model

The equilibrium cloud code is coupled to a 1D atmosphere model that calculates the pressure–temperature profile of an atmosphere in radiative–convective equilibrium. This methodology has been successfully applied to modeling solar system planets and moons, brown dwarfs, and exoplanets, with both cloudy and clear atmospheres; the models are described in McKay *et al.* (1989); Marley *et al.* (1996); Burrows *et al.* (1997); Marley and McKay (1999b); Marley *et al.* (2002); Fortney *et al.* (2005); Saumon and Marley (2008); Fortney *et al.* (2008b).

The atmosphere model utilizes the radiative transfer techniques described in Toon *et al.* (1989). Within this method, it is possible to include Mie scattering of particles as an

opacity source in each layer. Our opacity database for gases, described extensively in Freedman *et al.* (2008), includes all the important absorbers in the atmosphere. This opacity database includes two significant updates since Freedman *et al.* (2008), which are described in Saumon *et al.* (2012): a new molecular line list for ammonia (Yurchenko *et al.*, 2011) and an improved treatment of collision induced H_2 absorption (Richard *et al.*, 2012).

The equilibrium cloud model is coupled with the radiative transfer calculations and the pressure-temperature profile of the atmosphere; this means that a converged model will have a temperature structure that is self-consistent with the clouds. Figure 5.3 shows an example of how clouds change the *P–T* structure of an irradiated planet; the deep atmosphere of a cloudy model (dashed line) is cooler than the corresponding cloud-free model (solid line) at a given pressure in the atmosphere. This cooling is due to the opacity of the cloud, which prevents the stellar flux from warming those deep layers of the atmosphere, the so-called anti-greenhouse effect.

The photochemical output is calculated based on a converged cloud-free model, and so does not have this same self-consistency. The opacity of the cloud is included during the *P–T* structure calculation, ensuring that the atmosphere is in radiative–convective equilibrium, but a shift in the *P–T* profile does not change the location of the haze layer.

We calculate the effect of the model cloud distribution on the flux using Mie theory to describe the cloud opacity. Assuming that particles are spherical and homogeneous, we calculate the scattering and absorption coefficients of each species for each of the particle sizes within the model.

3.2.6 Transmission spectrum

The transmission spectrum model calculates the optical depths for light along the tangent path through the planet's atmosphere. The model is extensively described in Fortney *et al.* (2003) and Shabram *et al.* (2011). Cloud layer cross-sections generated from the model atmosphere are treated as pure absorption, and are added to the wavelength-dependent cross-sections of the gas.

3.2.7 Model grid

We run models with solar composition and $50\times$ solar composition, with two different heat redistribution parameters from fully redistributed (planet-wide average) to a dayside-average. We include equilibrium clouds at a variety of different values of sedimentation efficiency f_{sed}: 0.1, 0.25, 0.5, and 1.0. We include a hydrocarbon haze with mode particle sizes of 0.01, 0.05, 0.1, 0.2, 0.5, 0.75, and 1.0μm and soot-producing efficiencies (f_{haze}) from 0.1 to 5% ($50\times$ solar) and 5-25% (solar).

3.3 Results

We find a variety of cloudy models that are consistent with the majority of data for GJ 1214b. In general, optically thicker clouds are favored by high metallicity, efficient hydrocarbon polymerization (high f_{haze}), rapid vertical mixing, and more vertically extended (low f_{sed}) clouds with smaller particle sizes.

3.3.1 Optical depths of clouds

In order to match the observations of GJ 1214b's transmission spectrum, the cloud must be optically thick relatively high in the atmosphere (roughly 10^{-3} bar), masking the strong absorption features in the infrared that would otherwise be present. Figure 3.4 shows the slant optical depth at 1 μm of four representative models. The slant optical depth along the terminator is a factor of $\sim$20 larger than the vertical optical depth for GJ 1214b (see Fortney, 2005). The three enhanced-metallicity models shown become optically thick at mbar pressures; the solar composition model becomes optically thick too deep in the atmosphere to obscure the transmission spectrum.

3.3.2 Equilibrium clouds

Figures 3.5 and 3.6 show cloud-free and cloudy model spectra that include KCl and ZnS clouds. Figure 3.5 shows solar composition models and Figure 3.6 shows enhanced-metallicity $50\times$ solar composition models.

Examining the solar composition model spectra (Figure 3.5) and data by eye, the features in the infrared are larger in the models than in the data, even for f_{sed}= 0.1 clouds. This suggests that if GJ 1214b does have a solar-metallicity atmosphere, these clouds alone are not likely to be fully obscuring the near-infrared spectrum.

However, in the enhanced-metallicity models (Figure 3.6), the f_{sed}= 0.1 models become optically thick high enough in the atmosphere to match the observations. Models with higher values of f_{sed} (i.e. thinner clouds) have features in the optical and infrared larger than the data show. Hotter models (with inefficient heat redistribution) match better than models with

efficient planet-wide redistribution because the P–T profile crosses the condensation curve at a higher altitude, forming the cloud higher in the atmosphere. For the cloudy models shown in Figure 3.6, the mode particle sizes calculated by the cloud model range between 0.02 μm at low pressures (10^{-6} to 10^{-5} bar) to $\sim$10 μm near the cloud base.

3.3.2.1 Chi-squared analysis

In addition to fitting by-eye, we perform a simple chi-squared analysis to understand the validity of our fits. We tested an algorithm similar to that used in Cushing *et al.* (2008) in which we weight by the width of the band fitted, to avoid treating spectroscopy much more heavily than photometry. We get qualitatively identical results for the best-fitting models with and without this weighting parameter, so for simplicity we present the unweighted results here.

At solar metallicity, for cloud-free models, the reduced chi-squared (χ^2_{red}) is 37.9 and 26.2 respectively for the dayside and planet-wide models. For the cloudy f_{sed}= 0.1 models, χ^2_{red} is 8.2 (dayside) and 5.8 (planet-wide). In comparison, for a 100% water atmosphere (spectrum shown in Figure 3.12), χ^2_{red} is 1.4. In agreement with the by-eye fit, all solar composition models fit more poorly than a steam atmosphere.

At 50$\times$ solar metallicity, χ^2_{red} for the cloud-free models is 17.7 (planet-wide) and 31.5 (dayside). For the cloudy f_{sed}= 0.1 models, χ^2_{red} is 4.4 (planet-wide) and 1.9 (dayside). For all $f_{sed}$$\geq$0.2, $\chi^2_{red}$$>$ 5. f_{sed}= 0.1 models with partially inefficient redistribution are the only models the match the data as well as a water atmosphere. In section 3.4.1 we discuss how this sedimentation efficiency compares to brown dwarfs and whether it appears to be physically reasonable.

3.3.3 Hydrocarbon haze

Figures 3.7, 3.8, 3.9, and 3.10 show examples of the extensive grid of models that include a hydrocarbon haze layer. In these four figures, the effects of the four parameters we vary are shown.

Figure 3.7 illustrates the effect of changing the mean particle size on the transmission spectrum. Each of the models shown has the same f_{haze} value (3%) and uses the same photochemistry (50× solar, $K_{zz}=10^9$ cm^2 s^{-1}), so the mass of haze particles in each model is identical, isolating the effect of particle size. Small particles are generally more optically thick because, given the same total haze mass, smaller particles have a higher number density. For the smallest particle sizes (0.01 μm), scattering by haze particles causes the transmission spectrum to rise into the optical. For larger particles, they scatter less efficiently at optical wavelengths. For particle sizes above ∼0.25 μm, the opacity of the haze particles is relatively gray for optical through near-infrared wavelength and the resulting spectrum is more flat.

Figure 3.8 illustrates the effect of changing the fraction of haze precursors that actually form into haze particles (defined here as f_{haze}, see equation 3.1). The models shown each have the same photochemistry (50× solar, $K_{zz}=10^9$ cm^2 s^{-1}) and particle sizes (0.05 μm) to isolate the effect of changing the fraction of soot precursors that become haze particles. As expected, increasing f_{haze} increases the optical depth of the haze, obscuring the molecular features in the spectrum.

Figure 3.9 shows how vertical mixing, parametrized as K_{zz} in the photochemistry models, affects the transmission spectra. The same metallicity (50× solar), particle size (0.1

μm) and f_{haze} (3%) are used, and K_{zz} is varied from 10^7–10^9 cm^2 s^{-1}. Generally, we find that the eddy diffusion coefficient K_{zz} affects the haze-forming efficiency needed to reproduce the observations. The stronger the vertical mixing, the larger the quantity of soot precursors (see also Figure 3.2). This means that models with K_{zz}=10^9 cm^2 s^{-1} have more optically thick haze than K_{zz}=10^7 cm^2 s^{-1}; if vertical mixing is more efficient, a lower fraction of soot precursors need to form into haze material to match the observations.

Figure 3.10 shows the effect of metallicity on the model transmission spectra. Unsurprisingly, we find that the 50$\times$ solar metallicity models have significantly more soot precursors (see Figure 3.2), as there are a factor of 50 more heavy elements in the atmosphere. This means that if the same fraction of soot precursors become haze particles, the high metallicity model will have more mass in haze and therefore a more optically thick atmosphere. Indeed, we find that very few of the models at solar metallicity have an optically thick haze layer.

3.3.3.1 Best-fitting hydrocarbon haze models

In general, we find a range of models with a hydrocarbon haze layer that can match most of the observations. The best-fitting models all have 50$\times$ solar metallicity. For the less vigorous mixing (K_{zz}=10^7 cm^2 s^{-1}), models with small particle sizes (0.01 to 0.1 μm) and f_{haze} of 3-5% match the data; for more vigorous mixing (K_{zz}=10^9 cm^2 s^{-1}), models with small particles (0.01 to 0.1 μm) and f_{haze} of 1-5% match the data, as do medium-sized particles (0.25 μm) with f_{haze} from 3-5%. This parameter space of models is summarized in Figure 3.11, which shows the well-fitting parameter space as light shaded regions and the poor-fitting parameter space as darker shaded regions.

At solar metallicity, a very small subset of the parameter space resulted moderately well-fitting models. No models with solar metallicity and $K_{zz}=10^7$ cm^2 s^{-1} had a χ^2_{red} less than 4. For the more vigorous $K_{zz}=10^9$ cm^2 s^{-1}, only a single model had a reasonably good fit ($\chi^2_{red}=3$), which had particle sizes of 0.25 μm and $f_{haze}=25\%$. This f_{haze} value represents a quarter of soot precursors forming into condensed haze solids, which seems quite high.

These results generally suggest that if GJ 1214b has an enhanced metallicity atmosphere like Neptune, there is a large range of particle size distributions and photochemical efficiencies that can result in an obscuring haze in the atmosphere.

3.3.4 Combinations of cloud layers

In a planetary atmosphere, a number of different cloud and haze layers can form. For example, in Titan's atmosphere, there is both a high photochemical hydrocarbon haze and a deeper methane cloud. To examine this for GJ 1214b, we include both the equilibrium KCl and ZnS clouds and the hydrocarbon soot layer in a set of solar composition models, to see if by including both clouds we could match the spectrum without enhancing the metallicity of the atmosphere.

We ran a small set of models with favorable equilibrium cloud parameters (no heat redistribution to the night side, $f_{sed}=0.1$) and hydrocarbon haze parameters ($f_{haze}=5$-10%, $K_{zz}=10^9$ cm^2 s^{-1}). However, none of these models fit the data as well as the enhanced-metallicity equilibrium cloud models, enhanced-metallicity hydrocarbon haze models, or a high mean molecular weight water-rich model.

3.4 Discussion

3.4.1 Physical nature of low f_{sed} values

As discussed in Section 3.2.2, the particle sizes and vertical thickness of the equilibrium KCl and ZnS clouds are calculated using the parametrized value f_{sed}, which is equal to the ratio of the sedimentation velocity to the updraft velocity. A high sedimentation efficiency f_{sed} forms a cloud with large particles that settles into a thin layer; a low f_{sed} forms a more extended cloud with small particles.

This model has been used most frequently for studies of brown dwarfs. Studies of L dwarfs find that $f_{sed} \sim 1$–3 for the majority of field L dwarfs (Stephens *et al.*, 2009; Saumon and Marley, 2008). Similarly, Morley *et al.* (2012) found that for sulfide clouds in T dwarfs, $f_{sed} \sim 4$–5.

In this study, we find that the value needed to fit the observations is $f_{sed} = 0.1$, a sedimentation efficiency more than ten times lower than those of brown dwarfs. However, this low value may not be unreasonable for an irradiated planetary atmosphere. In Ackerman and Marley (2001), values of f_{sed} for Earth clouds are calculated. They find that for clouds that form high in Earth's atmosphere—stratocumulus clouds—f_{sed} is less than 1, with values for specific case studies ranging from 0.2 (North Sea) to 0.3–0.5 (California). The clouds we model in GJ 1214b form within a nearly-isothermal radiative region of the atmosphere, so we expect them to behave more like Earth stratocumulus clouds than the deeper tropospheric cumulus clouds, which have high f_{sed} (2–6), more similar to brown dwarfs.

f_{sed} is the ratio of the sedimentation velocity to the updraft velocity which is equal

to K_{zz}/L, where L is the mixing length. A low f_{sed} could be caused by many different things. (1) If the cloud particles are fluffy aggregates, they would have a slow sedimentation velocity. (2) If K_{zz} is large, like those of hot Jupiters (Showman *et al.* (2009) finds that hot Jupiters have $K_{zz} \sim 10^{11}$cm^2 s^{-1}), then the updraft velocity will be large. (3) If the mixing length L is small (due to a mean molecular weight gradient or wave breaking effects), then the atmosphere will be stably stratified, and f_{sed} will be small.

There is already clear observational evidence of a cloud layer very high in the atmosphere of hot Jupiter HD 189733 (Pont *et al.*, 2008; Sing *et al.*, 2011; Pont *et al.*, 2012). The spectral slope of the observations suggests opacity due to Rayleigh scattering, which would be due to quite small (sub-micron) sized particles. The cloud layer obscures gaseous absorption features from the blue to the near infrared. Based on its optical properties, the obscuring cloud layer has been suggested to be composed on small enstatite particles (Lecavelier Des Etangs *et al.*, 2008), which would have to be kept aloft high in the planet's atmosphere due to inefficient sedimentation.

3.4.2 Distinguishing between a steam and cloudy atmosphere

GJ 1214b's transmission spectrum is often described as 'flat' or 'featureless,' but in reality, its features are just too small to detect with current signal-to-noise observations. While we find that with current data, a hydrogen-helium rich model with clouds can fit just as well as a 100% water model, if we can improve the precision in the near-infrared, there are features that allow us to distinguish between these possibilities (see also Benneke and Seager, 2012).

Figure 3.12 shows how two sample cloudy models compare to a 100% water model.

The hydrocarbon haze model is deliberately chosen to show the large extent to which the haze layer can obscure the near-infrared features and flatten the spectrum. One feature of cloudy spectra, absent in the 100% water spectrum, is that there are flat regions between features, especially at 0.9, 1.1, and 1.3 μm. This is the pressure level where the clouds become optically thick; above this level, one can see gas opacity features, but all features below are obscured. A higher signal-to-noise spectrum in the near-infrared from 1 to 1.8 μm should be able to distinguish between these possibilities.

The spectra also look different in regions where additional species absorb more strongly than water vapor. For example, between 2.2 and 2.4 μm there is a strong methane band. (Note that this part of the spectrum has particularly conflicting results to date). Similarly, the feature at 1.7 μm is due to methane and the feature at 2.0 μm is due to CO_2. These bands would be completely lacking in a pure water atmosphere. By resolving regions of the spectrum where additional absorbers, if they exist, dominate, we could differentiate between a pure water atmosphere and a hydrogen/helium-rich atmosphere with many absorbers including clouds.

Figure 3.13 shows the same models as Figure 3.12, but for longer wavelengths (1–20μm). For both cloudy models shown, because the cloud particles are relatively small they do not absorb as efficiently in the mid-infrared as they do in the near-infrared. The cloud opacity decreases significantly, and even in models with a thick obscuring haze layer in the near-infrared, the atmosphere becomes clear of haze at mid-infrared wavelengths. Gaseous water and methane features dominate the transmission spectrum beyond 3–4 μm. Promisingly, this suggests that even if many exoplanet atmospheres' features are obscured in the wavelengths accessible from the ground or from *HST*, the wavelengths probed by the *James Webb Space*

Telescope will be less sensitive to haze obscuration.

However, atmospheres with mixed H_2O/H_2-rich compositions can also fit the data; Berta *et al.* (2012) finds that any atmosphere with a mass fraction of water higher than 70% can fit the observations. Distinguishing a mixed atmosphere from a cloudy H_2-rich atmosphere would be more challenging as features such as methane may also appear. The chemistry of such extremely high metallicity atmospheres is not currently well-understood and is a subject of ongoing study (Moses *et al.*, 2012).

3.4.3 Photochemical processes

This work, and that of Zahnle *et al.* (2009a) and Miller-Ricci Kempton *et al.* (2012), suggests that photochemistry could be extremely important for interpreting the spectra of cool exoplanets. We find that there is a large range of parameter space for a photochemical haze that can obscure the transmission spectrum of a hydrogen and helium dominated atmosphere. In this work, we parametrized the chemical processes expected to polymerize 2nd-order hydrocarbons. As part of our ongoing and future work we seek to identify and characterize the key chemical pathways expected to produce higher-order hydrocarbons in the upper atmospheres of irradiated exoplanets.

The spectral signatures of photochemically-produced gases were not included in these spectra, but it has been suggested that these would have relatively small signatures (Miller-Ricci Kempton *et al.*, 2012). Detecting additional soot precursors like benzene rings, polycyclic aromatic hydrocarbons, or other polymers with high-resolution spectroscopy would further constrain photochemical haze creation.

3.4.4 C/O ratio

Recent work has shown that planets may have some range in carbon and oxygen abundances (Madhusudhan *et al.*, 2011c,b; Madhusudhan, 2012; Moses *et al.*, 2013). In particular, Moses *et al.* (2013) studied the effect of C/O ratio on disequilibrium processes such as photochemistry and vertical mixing. They find that in atmospheres with a high C/O ratio, the abundances of soot precursors such as HCN and C_2H_2 are significantly enhanced. If GJ 1214b did have a high C/O ratio, it may be even easier to form a layer of optically thick soot.

3.5 Conclusions

Previous work by Howe and Burrows (2012) has shown that by adding an ad-hoc haze layer, the observations of GJ 1214b can be reproduced. Here, we showed that two types of clouds that may naturally emerge from equilibrium or non-equilibrium chemistry considerations, in an enhanced-metallicity atmosphere, can reproduce the observations of GJ 1214b. We presented results that show that clouds that form as a result of equilibrium chemistry, as they perhaps do on brown dwarfs, can reproduce the observations of GJ 1214b if they are lofted high in the atmosphere and the sedimentation efficiency parameter f_{sed} is low (0.1). This value is significantly different than the values of $f_{sed} \sim 1$–3 for L dwarfs or ~ 4–5 for T dwarfs, but is potentially quite reasonable for high altitude clouds in an irradiated planet.

We showed that models including hydrocarbon haze that forms as a result of photochemistry can also flatten GJ 1214b's spectrum. We used a 1D photochemical kinetics model to calculate the vertical distribution and available mass of molecules that are produced on the path-

way to haze formation. With haze-forming efficiencies between 1% and 5%, we found equally well-fitting models with modal particle sizes from 0.01 to 0.25μm. We conclude that, while more work on understanding the chemical processes of forming hydrocarbons is necessary, it is very plausible that GJ 1214b's spectrum is obscured by a layer of soot.

Although there are of course uncertainties in the detailed implementation of the cloud models, we stress that both kinds of clouds emerge naturally from either equilibrium chemistry or photochemical arguments. In particular, haze formation has the possibility to lead to the obscuration of gaseous absorption features over a wide range of planetary parameter space, from super-Earths to giant planets, over a wide range in planetary temperature.
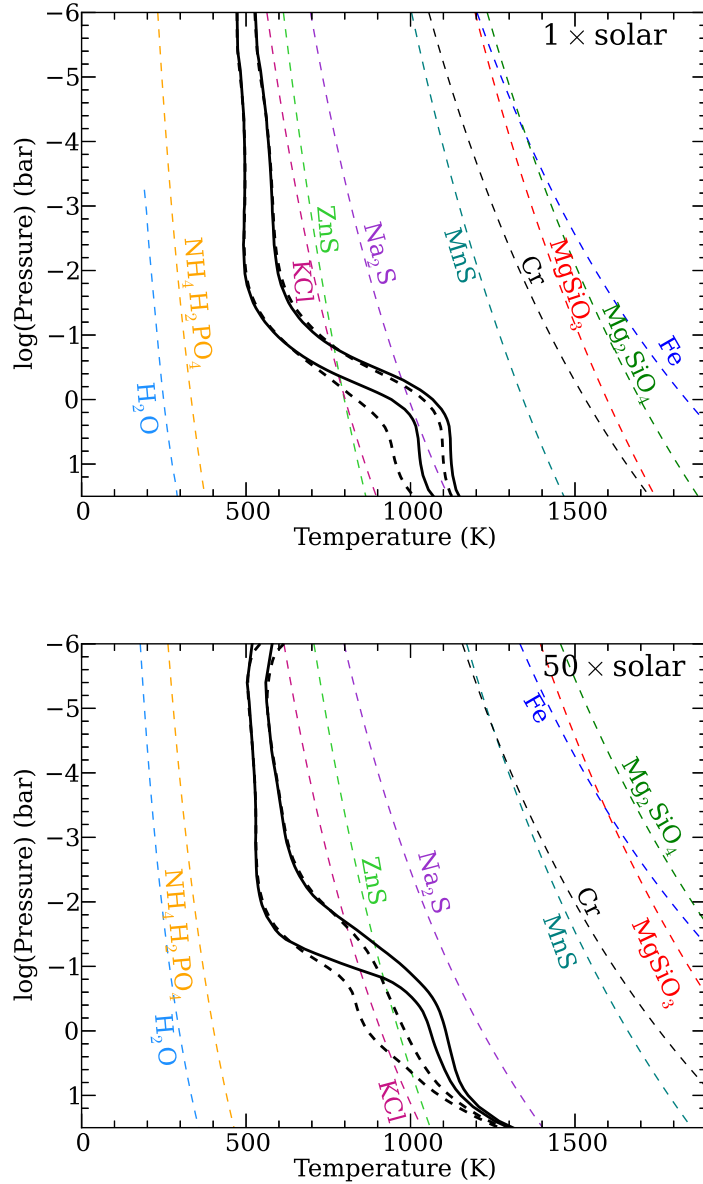
Figure 3.1: Pressure–temperature profiles of GJ 1214b with condensation curves. Top: solar composition models and condensation curves. Bottom: 50× solar models and condensation curves. Cloud-free *P–T* profiles are shown as solid black lines; cloudy (KCl and ZnS clouds) models are shown as dashed lines. The cooler (left) models in each panel assume that the absorbed radiation from the star is redistributed around the entire planet, the warmer (right) ones assume that the radiation is redistributed over the dayside only. Condensation curves of all relatively abundant materials that will condense in brown dwarf and planetary atmospheres are shown as dashed colored lines. See §2.5 for a description of the models.
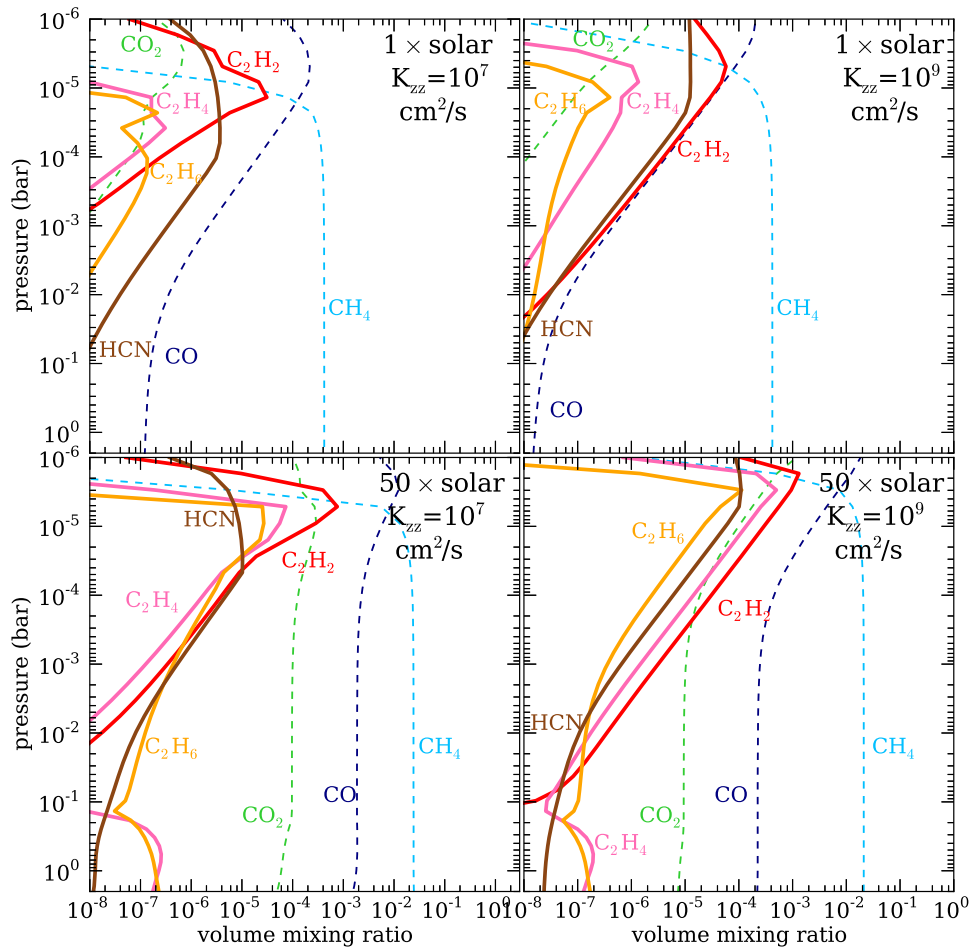
Figure 3.2: Results from photochemical calculations for C-bearing species at $1\times$ (top) and $50\times$ (bottom) solar metallicity. The volume mixing ratio at each pressure level of the atmosphere is shown for the major C-bearing species. The left and right panels shows the results using an eddy diffusion coefficient of $K_{zz} = 10^7$ and $K_{zz} = 10^9$ cm^2 s^{-1}, respectively. A fraction of the C_2H_2, C_2H_4, and C_2H_6 and HCN formed are assumed in this study to form the photochemical haze layer; CO, CO_2, and CH_4 do not readily form haze material.
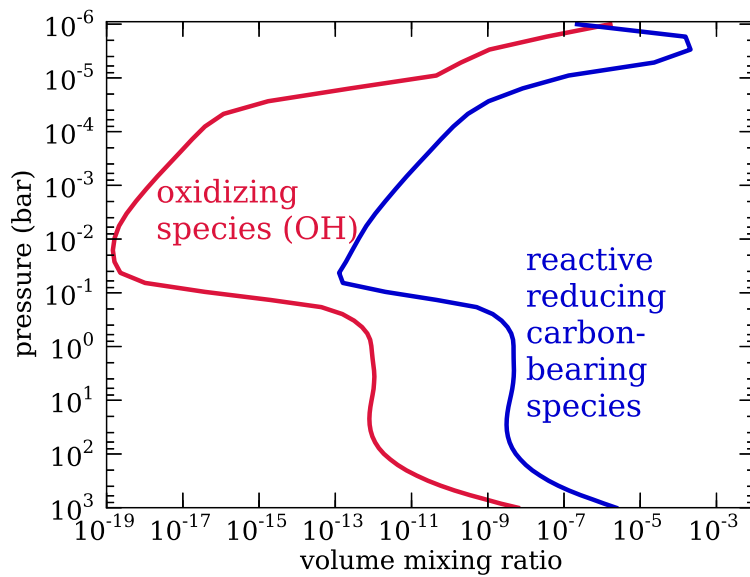
Figure 3.3: Comparison of reducing and oxidizing species for 50× solar, $K_{zz}=10^9$ cm^2 s^{-1} photochemical model. The volume mixing ratio of the major oxidizing species (OH) and summed mixing ratio of all the major reactive reducing species (C$_2$H, C$_2$H$_3$, CH, CH$_2$, CH$_3$, CN) are plotted. There is significantly more reducing material at the pressure levels where we form hazes, so we assume that higher-order hydrocarbons will continue to grow to potentially form condensed hydrocarbon soot-like particles.
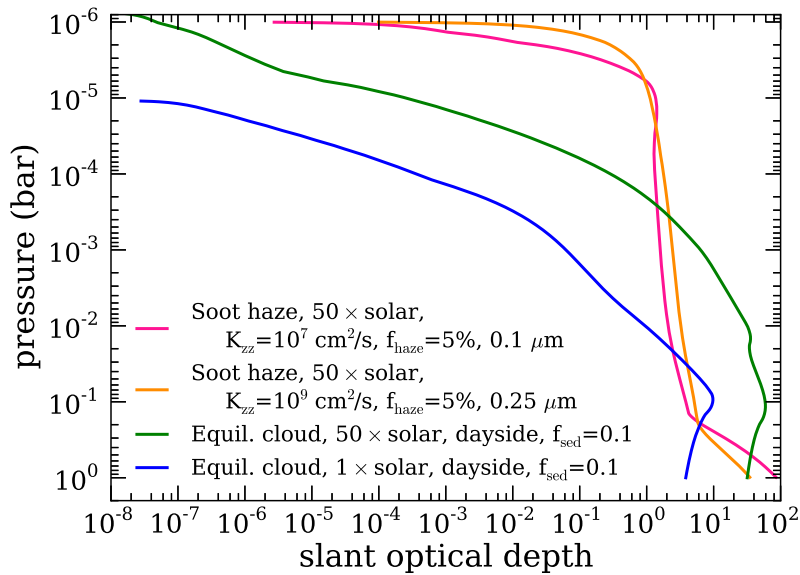
Figure 3.4: Slant optical depth. The slant optical depth at 1 μm in four representative atmosphere models are shown. Two models include equilibrium clouds (KCl and ZnS) within the Ackerman and Marley (2001) framework; the other two models include a hydrocarbon (soot) haze as described in Section 3.2.4. The three models with enhanced (50$\times$ solar) metallicity generally match the observations (see spectra in Figures 3.6 and 3.10) and have similar slant optical depths between 10^{-3} and 10^{-4} bar. The solar metallicity model has a lower optical depth and does not match observations.
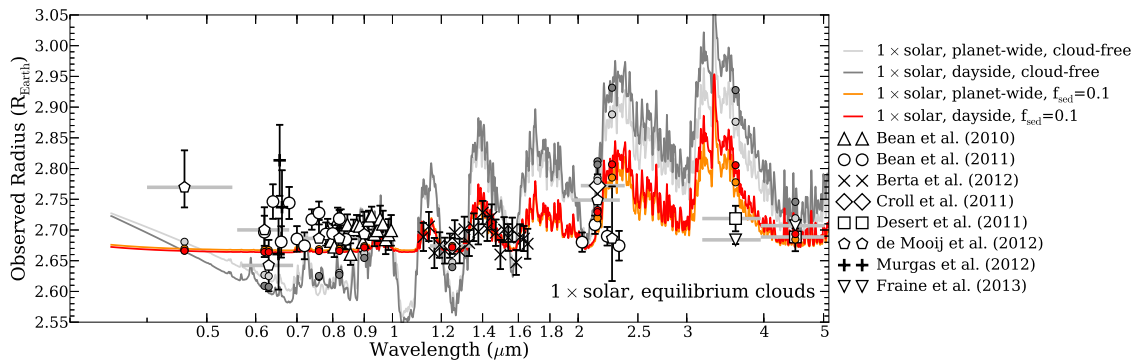
Figure 3.5: Reported transmission spectrum data compared to equilibrium cloud models of solar composition atmospheres. Data from a variety of sources are shown; the horizontal error bars show the width of the photometric band. Model spectra for cloud-free and cloudy solar atmospheres are plotted with corresponding model photometric points for the bands with data. We plot both 'dayside' models, which assume no redistribution of heat to the nightside of the planet, and 'planet-wide' models that assume that the heat is fully redistributed. Cloud-free models have features in the optical and near-IR that are inconsistent with data; cloudy models have somewhat smaller features in the near-infrared, but the features are not small enough to be consistent with the data.
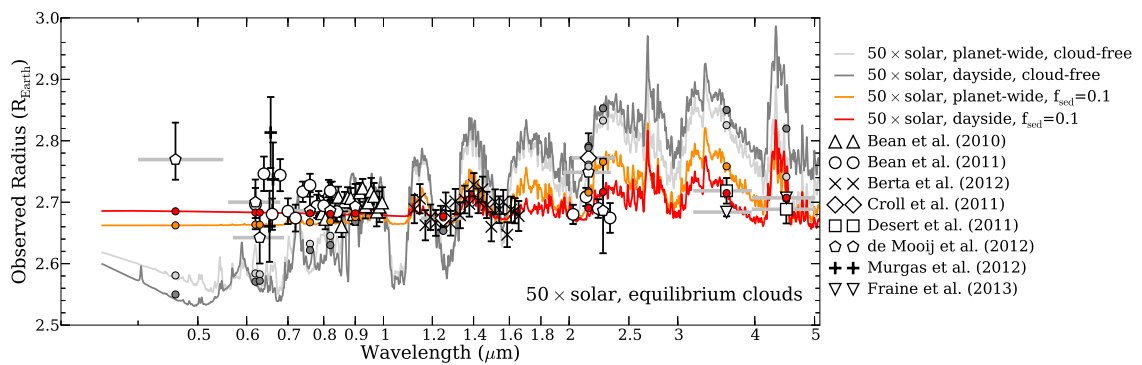
Figure 3.6: Reported transmission spectrum data compared to equilibrium cloud models of 50× solar composition atmospheres. Data and models are plotted as in Figure 3.5. Cloud-free models have features in the optical and near-IR that are inconsistent with data; the cloudy 'dayside' model has a relatively flat spectrum that is generally consistent with the data.

111
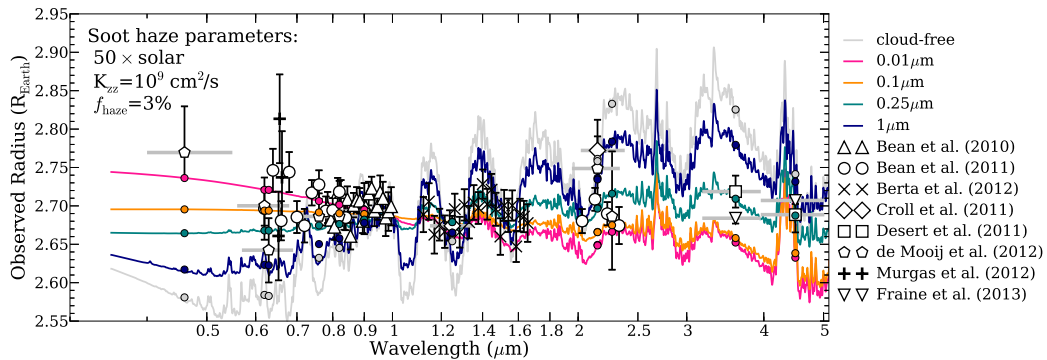
Figure 3.7: The effect of particle size on the transmission spectrum is shown. Data are compared to 50× solar composition hydrocarbon haze models. Data from a variety of sources are shown; the horizontal error bars show the width of the photometric band. The model radii integrated over the photometric band are shown for each photometric data point. All models have 50× solar composition and use the photochemical results for $K_{zz}=10^9$ cm^2 s^{-1} models. All models use a 3% soot-forming efficiency (f_{haze}) so the mass of haze particles in each layer is the same. Particle size has a strong effect on the cloud opacity. The smallest particles are the most optically thick in the optical; large particles are fairly optically thin because, given the same amount of cloud mass, their number density is significantly lower.
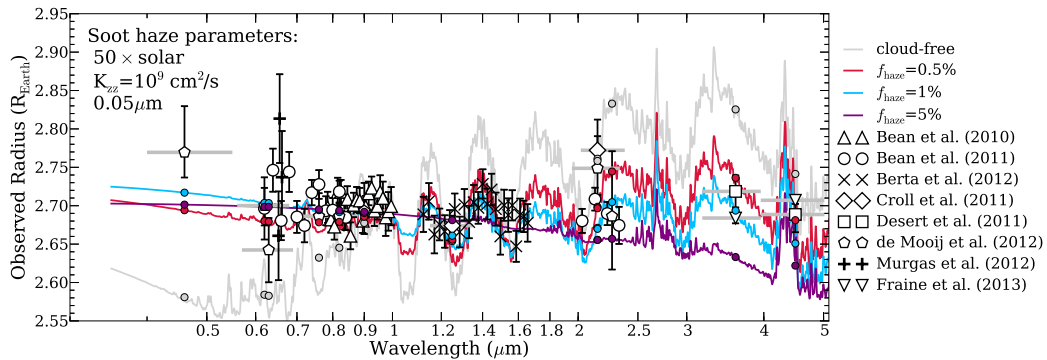
Figure 3.8: The effect of f_{haze} on the transmission spectrum is shown. Data are compared to solar composition hydrocarbon haze models. Data from a variety of sources are shown; the horizontal error bars show the width of the photometric band. The model radii integrated over the photometric band are shown for each photometric data point. All models have solar 50× solar composition, a 0.05μm mode particle size, and $K_{zz}=10^9$ cm^2 s^{-1}. Higher values of f_{haze} lead to optically thicker clouds and a more obscured transmission spectrum.
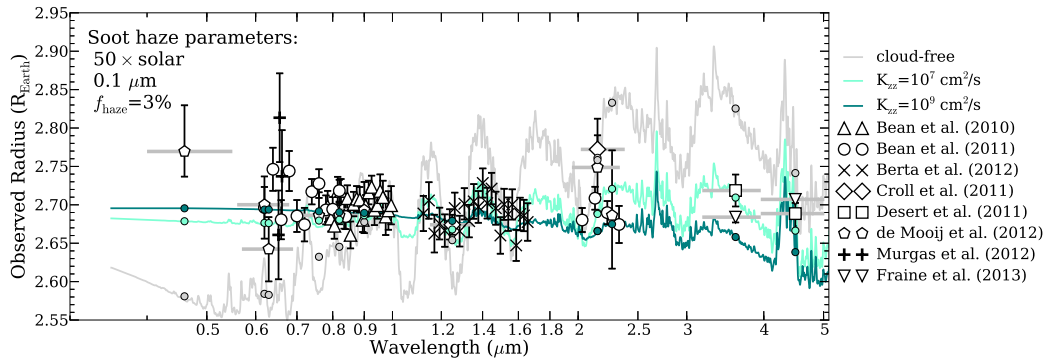
Figure 3.9: The effect of vertical mixing on the transmission spectrum is shown. Data are compared to solar composition hydrocarbon haze models. Data from a variety of sources are shown; the horizontal error bars show the width of the photometric band. The model radii integrated over the photometric band are shown for each photometric data point. All models have solar $50\times$ solar composition, a 0.1μ mode particle size, and a soot-forming efficiency f_{haze}=3%. The eddy diffusion coefficient K_{zz}, which parametrizes the strength of vertical mixing, is varied between K_{zz}=10^7 to 10^9 cm^2 s^{-1}. K_{zz} has a strong effect on the cloud opacity. More vertical mixing lofts more soot-forming material high in the atmosphere; the cloud is therefore most optically thick in the near infrared for K_{zz}=10^9cm^2 s^{-1}.
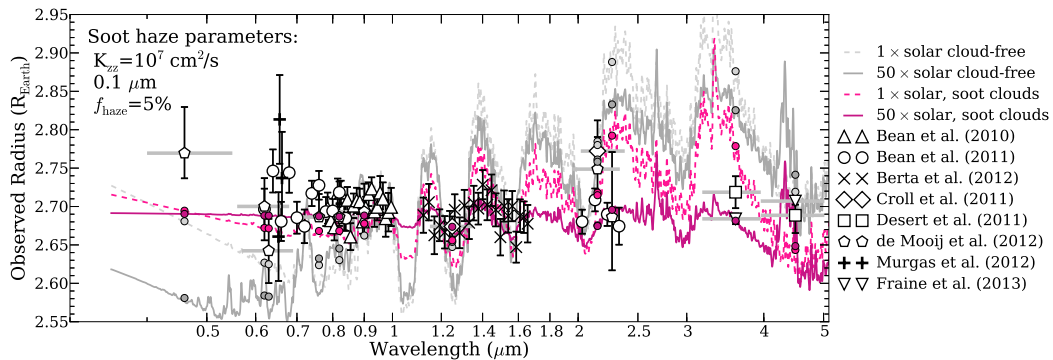
Figure 3.10: The effect of both metallicity and hazes on the transmission spectrum is shown. Data are compared to solar composition and $50\times$ solar models, with and without hydrocarbon hazes. Data from a variety of sources are shown; the horizontal error bars show the width of the photometric band. The model radii integrated over the photometric band are shown for each photometric data point. All models have a 0.1μ mode particle size, and a soot-forming efficiency of 5%. The eddy diffusion coefficient K_{zz}, which parametrizes the strength of vertical mixing, is K_{zz}=10^7 cm^2 s^{-1}. Solar composition models with hazes generally are generally not flatted enough to become consistent with the data.

113
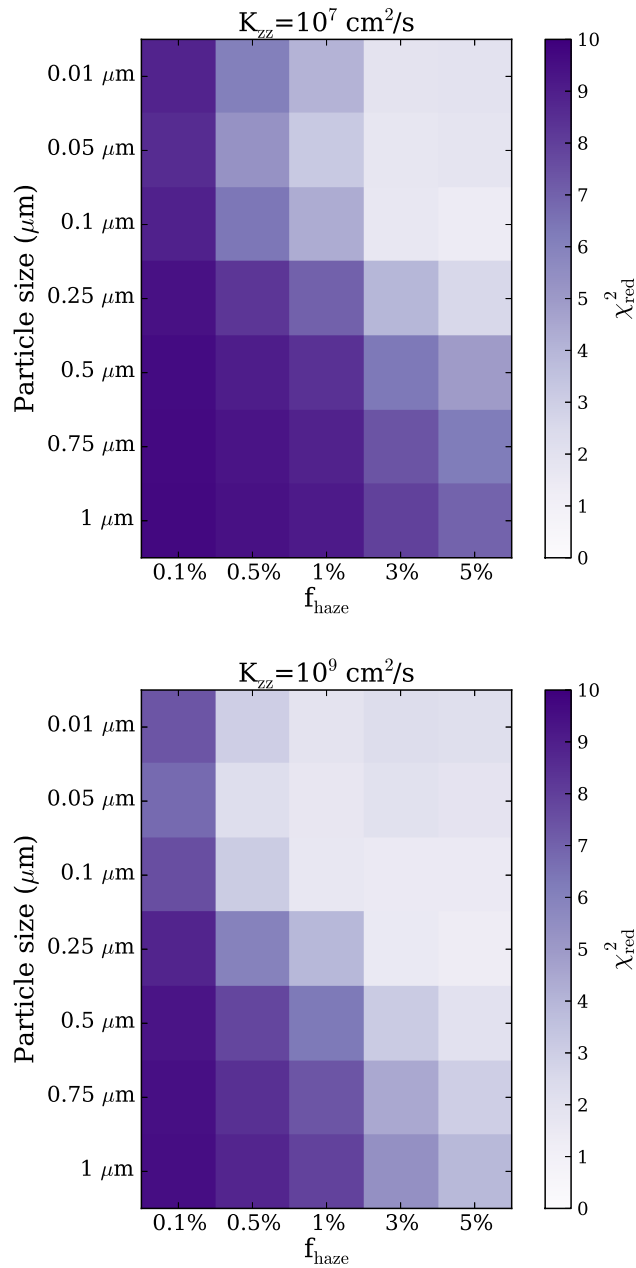
Figure 3.11: χ^2_{red} for 50× solar models with hazes. The goodness-of-fit parameter χ^2_{red} for each of the 50× solar hydrocarbon haze models is plotted. $K_{zz}=10^7$ cm^2 s^{-1} is on the left and $K_{zz}=10^9$ cm^2 s^{-1} is on the right. At each particle size and f_{haze} value, the shading indicates the goodness of the fit with lighter shades indicating a better fit. It is clear that small particles and moderate to high f_{haze} is necessary to reproduce the majority of the observed transmission spectrum. The range of well-fitting models is larger for the more vigorous ($K_{zz}=10^9$ cm^2 s^{-1}) vertical mixing.

114
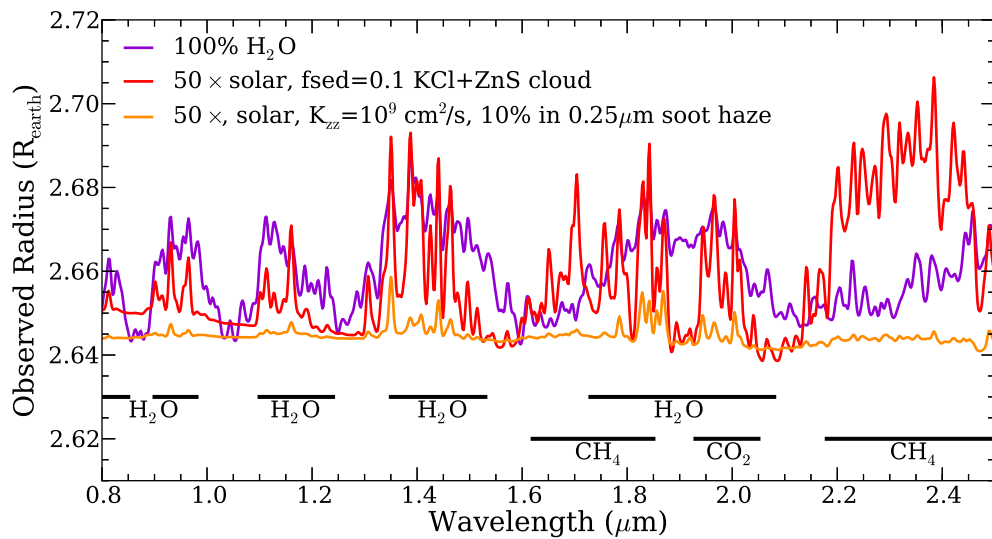
Figure 3.12: Comparison of steam and cloudy H-rich atmosphere models. A 100% water atmosphere is compared to two cloudy H-rich models in the near-infrared. With a higher-fidelity near-infrared spectrum, these models could be easily distinguished. Locations of strong absorption features from H_2O, CH_4, and CO_2 are noted. The Hubble Space Telescope G141 grism has a maximum resolving power of 130 in the range 1.1–1.7 μm.
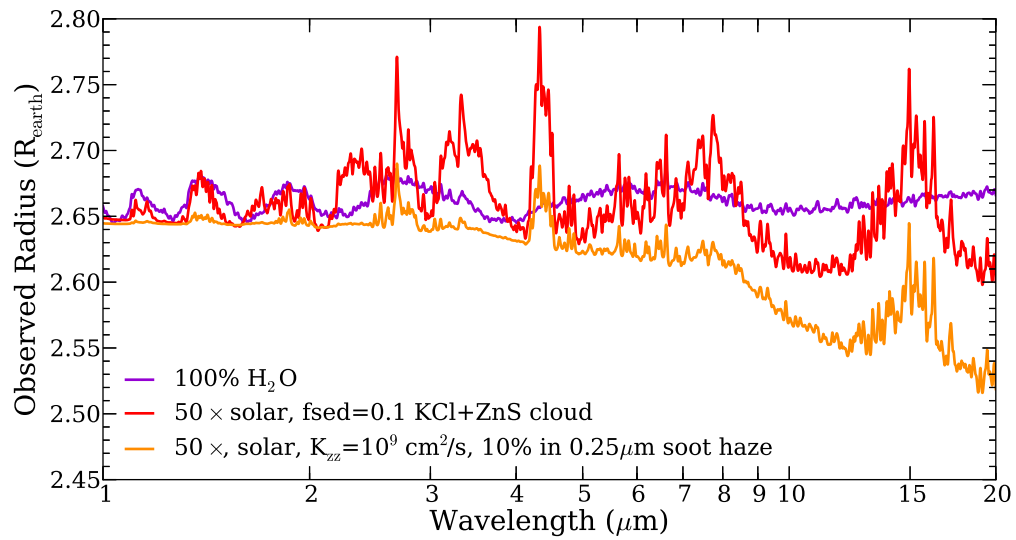
Figure 3.13: Comparison of steam and cloudy H-rich atmosphere models in the mid-infrared. The models from Figure 3.12 are shown for a wider wavelength range. The 100% water atmosphere model shows water vapor features of a similar amplitude from 1–20μm. However, for both of the cloudy models, the clouds become significantly less optically thick at longer wavelengths than they are in the near-infrared where current data exists. This means that in the mid-infrared, the features are much larger.

Chapter 4

Water Clouds in Y Dwarfs and Exoplanets

4.1 Introduction

Brown dwarfs link planetary and stellar astrophysics, with compositions like stars but the temperatures of planets. They form the tail of the initial mass function and, too low in mass to have core temperatures high enough to fuse hydrogen, they cool over time through the brown dwarf spectral sequence. As they cool, different molecules and condensates form and carve their spectra.

With the discovery of very cool brown dwarfs we are able to investigate for the first time the physical and chemical processes that occur in atmospheres with effective temperature ranges that would be suitable for a warm beverage. While brown dwarfs are free-floating, they should share many of the same physical processes as the giant planets that will be uncovered by future surveys.

4.1.1 Discovery and Characterization of Y Dwarfs

The proposed spectral class Y encompasses brown dwarfs that have cooled below $T_{\mathrm{eff}} \sim 500$ K. About 17 objects have been classified as Y dwarfs to date. Many of those have now been found using the Wide-field Infrared Survey Explorer (WISE) (Cushing *et al.*, 2011; Kirkpatrick *et al.*, 2012; Liu *et al.*, 2012; Tinney *et al.*, 2012; Kirkpatrick *et al.*, 2013). Additional objects have been discovered as wide-separation companions. Liu *et al.* (2011) found a very cool ($\sim$Y0) companion to a late T dwarf; Luhman *et al.* (2012) discovered a $\sim$300–350 K object orbiting a white dwarf. At these temperatures, NH_3 absorption features begin to appear in their near-infrared spectra, and sodium and potassium wane in importance in the optical as they condense into clouds.

Recent follow-up studies have aimed to characterize the Y dwarf population. There has been a large effort to measure parallaxes of Y dwarfs: Marsh *et al.* (2013) present results for 5 Y dwarfs and 3 late T dwarfs using a compilation of data from the ground and space. Dupuy and Kraus (2013) present results using only the *Spitzer* Space Telescope for 16 Y and T dwarfs. Beichman *et al.* (2014) present results from a compilation of data from Keck II, the *Spitzer* Space Telescope, and the *Hubble* Space telescope for 15 Y and T dwarfs. Groups have also been collecting followup observations to better understand the spectral energy distributions of Y dwarfs. Leggett *et al.* (2013) present followup near-infrared photometry for six Y dwarfs and a far-red spectrum for WISEPC J205628.90+145953.3. Lodieu *et al.* (2013) observed 7 Y dwarfs in the *z* band using the Gran Telescopio de Canarias.

4.1.2 Previous Models of Y dwarfs

A number of available models for brown dwarfs include models cold enough to represent Y dwarfs (Allard *et al.*, 2012; Saumon *et al.*, 2012; Morley *et al.*, 2012), but do not yet treat the effects of water clouds. The first models to incorporate the effects of water clouds into a brown dwarf atmosphere are those of Burrows *et al.* (2003b). These models generally find that water clouds do not strongly affect the spectrum of Y dwarfs, but there have been few followup studies. Hubeny and Burrows (2007) also includes simple water clouds with a fixed mode particle size of 100 μm. In Section 4.6.2 we will discuss how our results compare to these early models.

A number of studies have included water clouds in exoplanetary atmospheres; Marley *et al.* (1999) and Sudarsky *et al.* (2003) both modeled the effect of water clouds on the albedos of giant exoplanets; they find the formation of water clouds significantly increases the planetary albedos. Burrows *et al.* (2004) also consider water clouds in exoplanets, using a similar approach as Burrows *et al.* (2003b) but for irradiated planets; Sudarsky *et al.* (2003) and Sudarsky *et al.* (2005) calculate the thermal emission of exoplanets that include water clouds and find that they have a strong effect on the emergent spectrum.

4.1.3 Clouds in L and T dwarfs

Clouds have posed the greatest challenge for brown dwarf modeling since the first L dwarfs were discovered. As brown dwarfs cool along the L sequence from 2500 K to 1300 K, refractory materials like corundum, iron, and silicates condense to form thick dust layers (Lunine *et al.*, 1986; Fegley and Lodders, 1996; Burrows and Sharp, 1999; Lodders and Fegley,

2002; Lodders, 2003; Lodders and Fegley, 2006; Helling and Woitke, 2006; Visscher *et al.*, 2010) which thicken as the brown dwarf cools. These dust clouds shape the emergent spectra of L dwarfs (see, e.g. Tsuji *et al.*, 1996; Allard *et al.*, 2001; Marley *et al.*, 2002; Burrows *et al.*, 2006; Helling *et al.*, 2008a; Cushing *et al.*, 2008; Witte *et al.*, 2011).

For field brown dwarfs these clouds clear over a very small range of effective temperature around 1200–1300 K and around the same temperature, methane features begin to appear in the near-infrared. The brown dwarf is then classified as a T dwarf and, for many years, mid to late T dwarfs were considered to be cloud-free. However, it has long been recognized that other somewhat less refractory materials such as sulfides and salts should condense in cooler T dwarfs (Lodders, 1999). As late T dwarfs (500–900 K) were discovered and characterized, a population of objects redder in the near-infrared (e.g. $J-K$, $J-H$ colors) than the predictions of cloud-free models emerged. Morley *et al.* (2012) included the clouds predicted to form by condensation of the sulfides and alkali salts and showed that by including thin layers of these clouds, the colors and spectra of these redder observed T dwarfs can be matched. As these T dwarfs are further characterized, variability has been observed in mid-late T dwarfs (Buenzli *et al.*, 2012); the sulfide clouds may play a role in this variability.

4.1.4 Directly-imaged Exoplanets

Spectra of directly-imaged planets are also strongly influenced by the opacity of clouds. The first multi-planet directly-imaged system, HR 8799, has four planets, all of which have infrared colors that indicate cloudy atmospheres, much like L dwarfs (Marois *et al.*, 2008). Other planetary-mass objects also appear to have spectral properties similar to L dwarfs includ-

ing β Pictoris b (Bonnefoy *et al.*, 2013) and 2M1207b (Barman *et al.*, 2011b). In fact, at similar effective temperatures planetary-mass objects appear to be even more cloudy than their brown dwarf counterparts (Madhusudhan *et al.*, 2011a; Barman *et al.*, 2011a), which has been used to suggest that the breakup of the iron and silicate clouds at the L/T transition may be gravity dependent (Metchev and Hillenbrand, 2006; Marley *et al.*, 2012).

Nonetheless the transition to a methane-dominated atmosphere and cloud-depleted near-infrared spectrum must happen at some effective temperature, with the resulting objects appearing as low-gravity 'T' and 'Y' dwarfs. The first such object discovered is GJ 504b (Kuzuhara *et al.*, 2013) which is currently the coldest directly-imaged planet ($T_{\mathrm{eff}} \sim 500$ K) and has colors very similar to T dwarfs; followup observations probing the methane feature at 1.6 μm suggest that, as expected from thermochemical equilibrium calculations, methane is present in the atmosphere (Janson *et al.*, 2013).

4.1.5 Water clouds

In a cold solar composition atmosphere, water clouds will be a massive cloud and an important opacity source. Unlike the refractory clouds which have been extensively studied by a number of groups (Ackerman and Marley, 2001; Helling and Woitke, 2006; Allard *et al.*, 2001; Tsuji *et al.*, 1996; Burrows *et al.*, 2006; Helling *et al.*, 2008a), the same attention has not been paid to volatile clouds in brown dwarfs. In this work, we aim to predict the effects that water clouds will have on brown dwarf atmospheres. We calculate pressure–temperature profiles, spectra, and colors for the coolest brown dwarfs. We study the signatures of the water clouds and their optical properties, estimate their likely particle sizes, and determine at which

effective temperatures the cloud will become optically thick in the photosphere. We end by considering the observability of Y dwarfs with the four major instruments being built for the *James Webb Space Telescope (JWST)* and the detectability of cool giant planets with new and upcoming ground-based instruments.

4.2 Methods

4.2.1 Atmosphere Model

We calculate 1D pressure–temperature profiles, which are self-consistent with both the chemistry and clouds, of atmospheres in radiative–convective equilibrium. The thermal radiative transfer is determined using the "source function technique" presented in Toon *et al.* (1989). The gas opacity is calculated using correlated-k coefficients to increase calculation speed; our opacity database incorporates published data from both laboratory experiments and first-principles quantum mechanics calculations and is described extensively in Freedman *et al.* (2008). The opacity database includes two significant updates since Freedman *et al.* (2008), which are described in Saumon *et al.* (2012): a new molecular line list for ammonia (Yurchenko *et al.*, 2011) and an improved treatment of the pressure-induced opacity of H_2 collisions (Richard *et al.*, 2012). The cloud opacity is included as Mie scattering of spherical cloud particles in each atmospheric layer. The atmosphere models are more extensively described in McKay *et al.* (1989); Marley *et al.* (1996); Burrows *et al.* (1997); Marley and McKay (1999b); Marley *et al.* (2002); Saumon and Marley (2008); Fortney *et al.* (2008b).

4.2.2 Cloud Model

The cloud model calculates the vertical locations, heights, and mode particle sizes of clouds as they condense in the atmosphere. The calculation is coupled with the radiative transfer calculations, so a converged model will have a temperature structure that is self-consistent with the clouds.

The cloud code is a modification of the Ackerman and Marley (2001) cloud model. This model has successfully been used to model the effects of the iron, silicate, and corundum clouds on the spectra of L dwarfs (Saumon and Marley, 2008; Stephens *et al.*, 2009) as well as the sulfide and chloride clouds that likely form in the atmospheres of T dwarfs (Morley *et al.*, 2012). Here, we modify it to include the effects of water clouds. The Ackerman and Marley (2001) approach avoids treating the highly uncertain microphysical processes that create clouds in brown dwarf and planetary atmospheres. Instead, it aims to balance the advection and diffusion of each species' vapor and condensate at each layer of the atmosphere. It balances the upward transport of vapor and condensate by turbulent mixing in the atmosphere with the downward transport of condensate by sedimentation. This balance is achieved using the equation

$$-K_{zz}\frac{\partial q_t}{\partial z} - f_{\text{sed}}w_*q_c = 0, \tag{4.1}$$

where K_{zz} is the vertical eddy diffusion coefficient, q_t is the mixing ratio of condensate and vapor, q_c is the mixing ratio of condensate, w_* is the convective velocity scale, and f_{sed} is a parameter that describes the efficiency of sedimentation in the atmosphere.

Solving this equation allows us to calculate the total amount of condensate in each layer of the atmosphere. We calculate the modal particle size using the sedimentation flux and by prescribing a lognormal size distribution of particles, given by

$$\frac{dn}{dr} = \frac{N}{r\sqrt{2\pi}\ln\sigma}\exp\left[\frac{\ln^2(r/r_g)}{2\ln^2\sigma}\right] \tag{4.2}$$

where N is the total number concentration of particles, r_g is the geometric mean radius, and σ is the geometric standard deviation. We fix σ at 2.0 for this study (see discussion in Ackerman and Marley (2001)). We calculate the falling speeds of particles within this distribution assuming viscous flow around spheres (and using the Cunningham slip factor to account for gas kinetic effects). We calculate the other parameters in equation 6.1 (K_{zz} and w_*) using mixing length theory and by prescribing a lower bound for K_{zz} of 10^5 cm^2/s, which represents the residual turbulence due to processes such as breaking gravity waves in the radiative regions of the atmosphere.

This process allows us to calculate the mode particle size in each layer of the atmosphere using calculated or physically motivated values for all parameters except for the free parameter f_{sed}. In general, we find larger particles (which have higher terminal velocities) in the bottom layers of a cloud and smaller particles (which have lower terminal velocities) in the upper layers.

A high sedimentation efficiency parameter f_{sed} results in vertically thinner clouds with larger particle sizes, whereas a lower f_{sed} results in more vertically extended clouds with smaller particles sizes. As a result, a higher f_{sed} corresponds to optically thinner clouds and a

lower f_{sed} corresponds to optically thicker clouds.

The Ackerman and Marley (2001) cloud model code computes the available quantity of condensible gas above the cloud base by comparing the local gas abundance (accounting for upwards transport by mixing via K_{zz}) to the local condensate vapor pressure p_{vap}. In cases where the formation of condensates does not proceed by homogeneous condensation we nevertheless compute an equivalent vapor pressure curve.

4.2.3   Challenges of water clouds

The condensation of water vapor into water ice clouds poses some unique problems for our self-consistent equilibrium approach. Water vapor is the most dominant source of opacity in a Y dwarf atmosphere. After it condenses, if the cloud opacity is somehow removed, there is very little gas opacity left in the atmosphere and the layers beneath can radiate efficiently. However, the cloud opacity cannot just be removed from the atmosphere; it must condense into a cloud, and because oxygen is one of the most abundant elements, the water cloud that forms is quite massive and optically thick. This means that the dominant vapor opacity source condenses into a dominant solid opacity source.

In practice, when aiming to calculate a solution in radiative–convective and chemical equilibrium that is self-consistent with the water cloud, we find that we are not able to find a self-consistent solution for a range of model effective temperatures from $\sim$225–450 K. As the water cloud forms in the model, it significantly warms the atmosphere below it because it prevents flux from escaping. This warming causes the cloud to evaporate, removing the opacity source, and allowing flux to escape and cool the atmosphere again; a cloud forms again. An

equilibrium solution is not found.

To solve this problem, we borrow phenomenological ideas from our own solar system. When water clouds are observed in the solar system on Earth, Jupiter, and Saturn, they never form in a globally homogeneous layer. Instead, they form into patchy clouds. For example, on Jupiter, there are 5 μm hot spots though which flux emerges from deep within the atmosphere; these are believed to be "holes" or thin areas of the deep Jovian water cloud (Westphal, 1969; Westphal *et al.*, 1974; Orton *et al.*, 1996; Carlson *et al.*, 1994). Saturn has similar mid-infrared heterogeneity (Baines *et al.*, 2005).

Because water clouds *never* appear to form globally homogeneous, uniform clouds in the solar system planets, models that include clouds for these planets do not attempt to find a 1D steady-state equilibrium solution in a self-consistent way. Instead, for clouds in Earth's atmosphere, the evolution of clouds is either modeled over time using a time-stepping model or the clouds are modeled in 2D or 3D. In fact a method sometimes used in 3D circulation models on Earth inspires our approach, described below. In these circulation models, clouds form on scales smaller than the grid scale; cloud opacity is implemented using a two-column sub-grid approach. Other previous efforts for exoplanets and brown dwarfs either did not iterate or used a highly specified cloud parametrization for particle size and cloud height (e.g Marley *et al.*, 1999; Sudarsky *et al.*, 2003; Hubeny and Burrows, 2007). Our approach here is not to include a specified cloud, but instead to iteratively solve for a cloud profile that is self-consistent with the atmosphere structure. We rely on a model which successfully reproduces cloud particle sizes and distributions on Jupiter and Earth (Ackerman and Marley, 2001). Perhaps fortuitously, the particular cloud model employed by Burrows *et al.* (2003b), who also solve the problem self-

126

consistently, produced somewhat large particles with small infrared optical depth. More general cases in which some clouds have smaller particle sizes have a far greater optical depth and are more challenging to converge.

In this work, we make the assumption that patchy water clouds also form in brown dwarfs. Theoretical motivation for this patchiness has not yet been well-developed, but recent highly idealized models suggest that the rotation and internal heating of brown dwarfs could drive jet-like or vortex-like circulation (Zhang and Showman, 2014). Such weather patterns in the atmosphere may create rising and sinking parcels of air and maintain inhomogeneous clouds.

Other evidence for cloud patchiness in the silicate cloud decks of warmer brown dwarfs has been seen in the variability observations by, e.g., Radigan *et al.* (2012) and the spatial mapping of the L/T transition brown dwarf Luhman 16B (Crossfield *et al.*, 2014).

In this model, even though the water cloud layer forms a thick opacity source, the flux can emerge from holes in the cloud deck. This assumption allows us to calculate a temperature structure in radiative–convective equilibrium that is self-consistent with the clouds because flux is able to emerge through the holes even when the clouds become optically thick. This means that the temperature structure can remain cool enough to have a condensed water cloud layer.

4.2.4 Implementing patchy clouds

We calculate patchy clouds following the approach of Marley *et al.* (2010), who implemented patchy clouds in an attempt to understand a mechanism that could reproduce the L/T transition, in which clouds break up progressively and more flux emerges from holes in the

$$\mathbf{F_{total}} = h\mathbf{F_{clear}} + (1\text{-}h)\,\mathbf{F_{cloudy}}$$

$h=1.0$

$h=0.5$

$h=0.0$
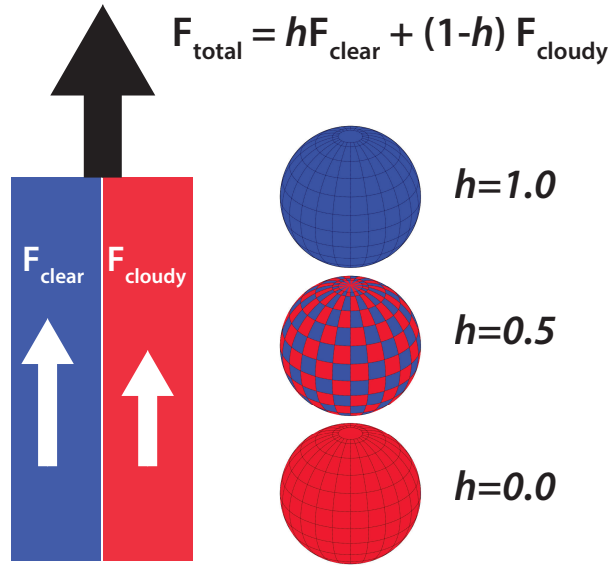
Figure 4.1: Partly cloudy model atmospheres. This cartoon illustrates our approach to calculating pressure–temperature profiles in radiative–convective equilibrium for partly cloudy atmospheres. We calculate the flux separately through two columns: one that does not include cloud opacity and one that does. We then sum these fluxes to calculate the total flux, according to the fraction of the surface we assume to be covered by holes, h. $h = 1$ represents a fully clear atmosphere; $h = 0$ represents a fully cloudy atmosphere. For the models in the grid presented here, $h = 0.5$.

clouds. Following this prescription, we calculate flux separately through both a cloudy column

(with the cloud opacity included) and a clear column (with the cloud opacity not included) with

the same pressure–temperature profile. This calculation is shown schematically in Figure 4.1.

We can change the cloud-covering fraction by varying h, the fractional area of the atmosphere

assumed to be covered in holes:

$$F_{\text{total}} = hF_{\text{clear}} + (1-h)F_{\text{cloudy}} \tag{4.3}$$

Using this summed flux F_{total} through each atmospheric layer, we iterate as usual

until we find a solution in radiative–convective equilibrium. Using $h \gtrsim 0.4$–0.5 greatly improves convergence. With a hole fraction of at least 40–50%, flux escapes from warm, deep layers through the cloud-free column and a consistent $P - T$ profile with water clouds can be calculated.

4.2.5 Cloud properties

To model clouds and their radiative effect in the atmosphere, we need three pieces of information about the material. The first is the optical properties—the real and imaginary parts of the refractive index—of the condensed solid or liquid. In Y dwarfs, water always condenses in the solid phase (Burrows *et al.*, 2003b), so we use the optical properties of water ice (Warren, 1984). The second property is the material's density; we use 0.93 g/cm^3 for water ice. Lastly, we need the saturation vapor pressure of water ice, which tells us where the cloud will form and how much material is available to form it. We assume that all material in excess of the saturation vapor pressure condenses to form a cloud. We use the equation from Buck (1981) to describe the saturation vapor pressure of water ice:

$$p_{\mathrm{vap}} = a \exp \left[\frac{(b - T_c/d)T_c}{T_c + c} \right] \tag{4.4}$$

where T_c is the temperature in degrees Celsius and a, b, c, and d are constants (6.1115×10^3, 23.036, 279.82, and 333.7, respectively).

The other clouds included in these models are Cr, MnS, Na$_2$S, KCl, and Zns. The thermochemical models that describe the formation of these clouds are described in Visscher *et al.* (2006). Using these models, fits to the saturation vapor pressure as a function of pressure,

temperature, and metallicity were presented in Morley *et al.* (2012), Section 2.4. Sources of the optical properties used in the Mie scattering calculations are also presented in Table 1 of Morley *et al.* (2012).

4.2.6 Model grid

Our grid of models encompasses the full range of Y dwarfs and extends the grid from Morley *et al.* (2012) to lower temperatures. This grid includes models from 200–450 K in increments of 25–50 K. We include surface gravities that range from giant planets to brown dwarfs, from log g of 3.0 to 5.0 in increments of 0.5. We run all models on this main grid with f_{sed}=5 and h=0.5.

Of course, it is likely that h and f_{sed} vary, and could in fact be different for the underlying sulfide/salt clouds and the higher altitude water clouds. In fact, models at the L/T transition generally need to include non-uniformity in cloud properties across the transition to match its shape (Marley *et al.*, 2010). We do not aim to fully model all parts of this parameter space here. However, we do explore some parts of this space; we run additional models in which we vary f_{sed} from 3–7 at a single surface gravity (log g=4.0) and in which we vary h from 0.2 to 1.0 (see Figure 4.11). We assume solar metallicity composition for all models, using elemental abundances from Lodders (2003).

The grid was deliberately chosen to be square, but includes some unphysical combinations of temperature and surface gravity, because higher mass brown dwarfs cannot have cooled enough during the age of the universe to reach very low temperatures. For the coolest models in our grid, T_{eff}=200 K, the maximum expected log g (that of a 10 Gyr brown dwarf)

is ~ 4.2. For 300 K, maximum log g is ~ 4.5–4.6; for 450 K, $\sim$4.7–5.0 (Saumon and Marley, 2008). The ranges come from using a cloudy or cloud-free atmospheric boundary condition for the evolution models, see Figures 4 and 5 from Saumon and Marley (2008).

4.2.7 Evolution models

Absolute fluxes and magnitudes are calculated from our model spectra by applying the evolutionary radii of Saumon and Marley (2008). Those cooling sequences provide the radius of the brown dwarf as a function of T_{eff} and log g. Here we have used the radii from the evolution sequences computed with cloudless atmospheres as the surface boundary condition. A fully self-consistent calculation of the evolution would use a surface boundary condition defined by the corresponding model atmospheres. This is becoming increasingly difficult for brown dwarfs as the evolution of clouds during the long cooling time of the very cool objects considered here is rather complex. The sequence of transitions from cloudy L dwarfs to mainly clear mid-T dwarfs, to late-T dwarfs veiled with sulfide clouds (MnS, Na$_2$S, ZnS, Cr, KCl), which may also clear out in early Y dwarfs before water clouds appear, has yet to be understood properly, both empirically and theoretically. The use of a uniform, cloudless surface boundary condition has the virtue of simplicity. We can estimate the uncertainty in the radius thus obtained by comparing the surface boundary condition extracted from the present atmosphere models to those used by Saumon and Marley (2008). We find that for our nominal $f_{\mathrm{sed}} = 5$, $h = 0.5$ partly cloudy sequence, the entropy at the bottom of the atmosphere (which gives the entropy of the matching interior model) is quite close to the cloudless case at $T_{\mathrm{eff}} = 450\,\mathrm{K}$. As the object cools the entropy decreases, and for $T_{\mathrm{eff}} = 200\,\mathrm{K}$ the entropy is close to the entropy

of cloudy atmospheres used in Saumon and Marley (2008). This nicely corresponds to the transition of the partly cloudy models from optically thin to optically thick water clouds. Figures 4 and 5 of Saumon and Marley (2008) show that for given T_{eff} and $\log g$, the radii between the cloudless and cloudy evolution sequences vary by at most 1–2% below 500 K. Thus, the inconsistency between the surface boundary condition used in the evolution sequences and the model atmospheres presented here causes at most a 4% error in the absolute fluxes.

4.3 Results

We present results for the grid of models discussed in Section 4.2.6. Where appropriate, we incorporate warmer models of T dwarfs from previous studies (Saumon *et al.*, 2012; Morley *et al.*, 2012) for comparison. In Section 4.3.1, we present the model cloud properties. In Section 4.3.2 we present the temperature structures of the models. In Section 4.3.3 we present the model spectra, including effects of disequilibrium chemistry. In Section 4.3.4 we present model photometry and compare to the growing collection of very cool objects with known distances (Dupuy and Kraus, 2013; Beichman *et al.*, 2014). Lastly, in Sections 6.5.5 and 4.5 we will make predictions for the characterizability of Y dwarfs with *JWST* and the detectability of cool planets with new instruments like GPI, SPHERE, and the LBT.

4.3.1 Cloud properties

The models presented here include the effects of both sulfide/chloride clouds (first included in model atmospheres in Morley *et al.* (2012)) and of water clouds. We will mainly fo-
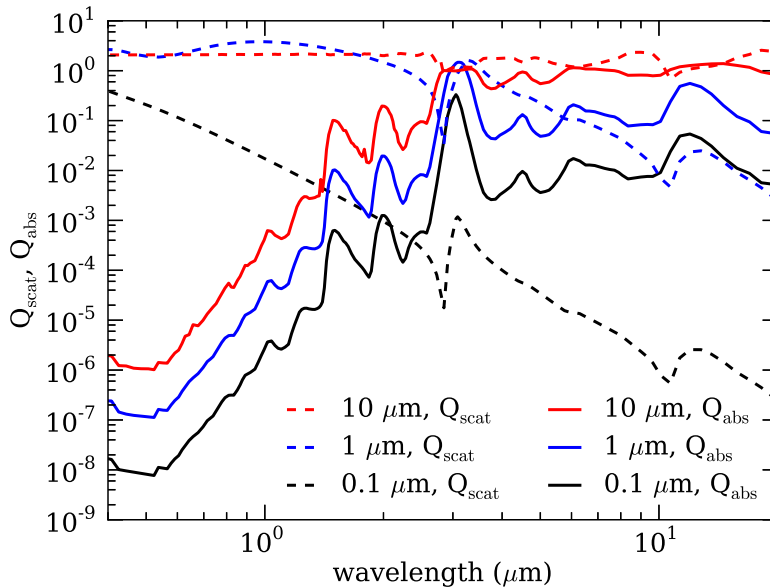
Figure 4.2: Absorption and scattering efficiencies. The results of the Mie scattering calculation (Q_{scat} and Q_{abs}) for water clouds of three particle sizes are shown. These results are for single particle sizes, not a distribution of sizes. All three show similar general properties, with low Q_{abs} in the optical rising into the infrared and the strongest absorbing feature around 3 μm. Larger particles are more efficient at both absorbing and scattering for most wavelengths.

cus on the properties of water clouds as the former set of clouds are more thoroughly examined

in Morley *et al.* (2012).

4.3.1.1 Scattering and absorption efficiencies of water ice

Figure 4.2 shows the optical properties calculated using Mie theory for water ice particles with sizes of 0.1, 1, and 10 μm. The scattering efficiency, Q_{scat}, is the ratio of the scattering cross section of the particle to the geometric cross section. The absorption efficiency, Q_{abs}, is the ratio of the absorbing cross section to the geometric cross section. In general, the larger particle sizes both scatter and absorb more efficiently than smaller particles for most
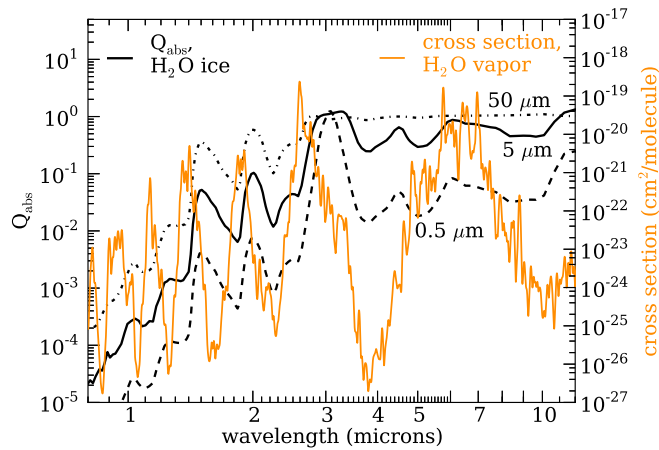
Figure 4.3: Absorption efficiency of water ice particles and absorption cross section of water vapor. The absorption efficiency Q_{abs} of water ice particles of three particle sizes (0.5, 5, and 50 μm) is shown (left axis). These results are for single particle sizes, not a distribution of sizes. The absorption cross section of water vapor is shown on the right axis. The phase change of water substantially changes the wavelengths at which it strongly absorbs, filling in many of the regions where water vapor is transparent.

wavelength ranges. The locations of features are similar for different particle sizes with the strongest feature in Q_{abs} at 3 μm. In general, Q_{abs} rises from optical to infrared wavelengths and remains fairly high through the infrared. The persistence of these features over a large range in particle sizes suggests that water ice features may be observable for a relatively optically thick cloud even if it contains a range of particle sizes.

Figure 4.3 shows both the absorption efficiency of water ice and the cross section of water vapor; the wavelength range at which water absorbs shifts as it condenses from vapor to solid phase. In particular, water ice absorbs strongly within the major water vapor opacity windows in the mid-infrared.

134

4.3.1.2 Particle sizes and optical depths of water clouds

Water clouds form in brown dwarfs cooler than T_{eff}=400 K, but initially in thin, tenuous layers. They first become relatively optically thick in the photospheres of brown dwarfs cooler than $\sim$350–375 K. Figure 4.4 shows the cloud properties (mode particle size and geometric column optical depth) of a representative set of cloudy models. Geometric column optical depth is the equivalent optical depth of particles that scatter as geometric spheres; since water clouds are very much non-gray absorbers, this is a poor approximation at wavelengths where the particles scatter much more strongly than they absorb.

T_{eff}=400 K model atmospheres have sulfide and salt clouds in the photosphere and a thin water cloud in the upper atmosphere. The cloud properties for an example T_{eff}=400 K, log g=4.5 model is shown in the upper panel of Figure 4.4. The water cloud does forms at a pressure level of 4×10^{-2} bar, in the upper atmosphere, in an optically thin layer. The sodium sulfide cloud becomes optically thick ($\tau = 2$) at 20 bar, near the bottom of the photosphere. Mode particle sizes of this dominant Na_2S cloud are around 20–30 μm.

As a brown dwarf cools below T_{eff}=400 K, the water cloud forms deeper in the atmosphere and more material is available to condense, making the water cloud much more optically thick. The middle panel shows a cooler model, T_{eff}=275 K, in which the cloud has become geometrically optically thick near the top of the photosphere. Mode particle sizes in this high cloud layer are fairly small—around 1–5 μm. The feature in the column optical depth around 10^{-2} bar is caused by the fact that the pressure–temperature profile becomes warmer than the water condensation curve at that pressure. In this model, the sulfide and chloride clouds become

135

optically thick much deeper in the atmosphere, around 100 bar, which is below the photosphere.

For a brown dwarf that has cooled to $T_{\rm eff}$=200 K, the water cloud is very optically thick and forms within the photosphere. The bottom panel shows a $T_{\rm eff}$=200 K model; the base of the water cloud is at 2 bar and the column optical depth is ∼60. Mode particle sizes of water ice in the photosphere are 4–20 μm. The cloud opacity is the dominant opacity source through cloudy columns of the model atmosphere.

Overall, and in agreement with Marley *et al.* (1999) and Burrows *et al.* (2003b), we see that water clouds begin to form with small particle sizes high in the atmospheres of objects around 400 K. They become marginally optically thick for objects cooler than 350–375 K. For very cold objects, ∼200–250 K, the water cloud is a dominant opacity source through cloudy columns of the atmosphere.

4.3.1.3 Single scattering albedos

However, even if a cloud is geometrically optically thick, depending on the optical properties of the absorbing and scattering particles, the cloud may not dramatically affect the spectrum. If the absorption efficiency is very low at a given wavelength, photons from layers below the cloud will have a very low probability of being absorbed by the cloud; thus the spectrum will appear essentially as it would in a cloud-free atmosphere at that wavelength.

The single scattering albedo quantifies the importance of scattering and absorption by cloud particles. It is the ratio of the scattering coefficient to extinction coefficient (including both scattering and absorption) at a given wavelength. A single scattering albedo of 1.0 indicates that the cloud particles are entirely scatterers; a single scattering albedo of 0.0 indicates that the

cloud particles are entirely absorptive.

Figure 4.5 shows the single scattering albedo for the clouds in the T_{eff}=200 and 275 K models also shown in Figure 4.4. We show both the single scattering albedo for the sodium sulfide cloud, which is deep within the atmosphere at ~ 100 bar, and the water ice cloud, which is in the photosphere around 0.1–1.0 bar. The single scattering albedo of the sulfide cloud is almost identical for each of these two model atmospheres; it rises from 0.6 in the optical to 0.95 at 12 μm, indicating that the cloud becomes less efficient at absorbing as the wavelength increases. In contrast, the single scattering albedo of the water ice cloud has strong absorption features throughout the near and mid-infrared. The two models have slightly different features because the particle sizes are different, and the scattering and absorption properties depend fairly strongly on particle size (see Figure 4.2). For the 200 K object, the water ice mode particle size at 2 bar is about 20 μm. For the warmer 275 K model, the mode particle size at 0.03 bar is about a factor of four smaller, $\sim$5 μm.

However, the strongest features are evident for both models. The most obvious is the sharp decrease in single scattering albedo at 2.8 μm, indicating that the cloud becomes more strongly absorbing at that wavelength. The feature at 10 μm is very evident for the warmer model, and much more muted in the cooler model. The presence of features indicates that water ice is not a mostly gray absorber (like many of the more refractory clouds are) and, when present and optically thick, may cause spectral features, including ones that depend on particle size.

4.3.2 Pressure–temperature structure

Examples of model pressure–temperature profiles for the model grid are shown in Figure 5.3. In general, cloud opacity in a brown dwarf increases the temperature of the atmosphere at all points in the atmosphere. This is because in a cloudy atmosphere, the overall opacity is slightly higher, so the temperature structure of a converged model with the same outgoing flux will be slightly warmer.

For a cloud-free model atmosphere, once the water has condensed out of the atmosphere, there are very few opacity sources left: mainly CH_4, NH_3, and collision-induced absorption from molecular hydrogen. This means that the brown dwarf is quite transparent in those layers and flux is able to emerge from deeper layers. In contrast, if we assume, as we do in our cloudy models, that water in excess of the saturation vapor pressure condenses to form a water ice cloud, that cloud provides a large opacity source, preventing the brown dwarf from efficiently emitting from layers underneath the cloud, and significantly warming the atmosphere.

For model atmospheres between 400 and 500 K, even though the cloud-free P–T profile may cross the water condensation curve, the converged cloudy models (including the effect of sulfide clouds) are somewhat warmer and do not cross the water condensation curve, so the model water cloud does not form.

For the warmest effective temperature brown dwarfs in which we find that water clouds form and can exist in radiative equilibrium, ($\lesssim$400 K), the water clouds are at low pressures within the radiative upper atmosphere. They remain above the photosphere and optically thin. This means that the clouds affect the spectra very little, but the converged cloudy model's

138

P–T profile is warmer by ∼20-50 K in the upper atmosphere than a corresponding cloud-free model.

Figure 5.3 shows the models of pressure–temperature profiles of brown dwarfs (log g=5.0, upper panel) and planet-mass objects (log g=3.5, lower panel), with effective temperatures of 200, 300, and 450 K. The photospheres, shown as thick black lines, show that the observable region of the atmospheres tends to be below the radiative upper atmospheres which are prone to numerical challenges in the models. The convective regions are also shown as colored shaded regions; higher gravity objects at these temperatures have multiple convection zones. This well-known result is because their P–T profiles cross regions of parameter space where the opacity of a solar composition equilibrium gas is low, and radiative energy transport becomes efficient. In lower pressure regions in the atmosphere, the opacity increases and radiative transport is once again inefficient and the model becomes unstable to convection (e.g. Marley *et al.*, 1996; Burrows *et al.*, 1997).

Note that the coolest models (T_{eff}=200 K) also cross the NH_3 condensation curve, indicating that for very cold Y dwarfs we will also need to consider the effects of the ammonia cloud. Like the H_2O cloud, it will first form as a thin cloud high in the atmosphere, and become more optically thick as the object cools further. The opacity of this cloud is not currently included in the models.

4.3.3 Spectra

The spectra of Y dwarfs are dramatically different from blackbodies at the same effective temperatures, with strong molecular absorption features where the thermal emission would

peak and opacity windows at shorter wavelengths where a blackbody would be faint. A 450 K object is 6 orders of magnitude brighter in J band than its blackbody counterpart; a 300 K object is 10 orders of magnitude brighter; a 200 K object is 15 orders of magnitude brighter.

4.3.3.1   Molecular absorption bands

The spectra of Y dwarfs are dominated by the opacity of H_2O, CH_4, NH_3, and H_2 collision-induced absorption (CIA). Figure 4.7 shows the molecular opacity and collision induced absorption at representative locations in the photospheres of objects with effective temperatures of 900 (T6.5), 450 (Y0), and 200 K (Y2+). This progression from mid-T to late-Y is marked by the increase in ammonia absorption relative to water and methane.

Features from CO and CO_2 have been found in T dwarfs (Yamamura *et al.*, 2010; Tsuji *et al.*, 2011). The strongest band of CO is the dominant opacity source at 4.5–5 μm, even assuming equilibrium chemistry, for a mid-T dwarf. CO_2 is also an important opacity source in the mid-infrared for warmer objects, especially if its mixing ratio is increased by vertical mixing. As an object cools, CO and CO_2 are strongly disfavored in equilibrium, but vertical mixing could increase their abundance in the atmosphere by several orders of magnitude, so the strongest absorption bands may still prove to be important for late T and early Y dwarfs. For very cold objects, the effects of disequilibrium carbon chemistry should become less important.

Species such as PH_3 (phosphine) and H_2S, which have been observed in Jupiter's atmosphere (Prinn and Lewis, 1975), will also be present in Y dwarfs. Phosphine is likely observable in the mid-infrared; the strongest PH_3 feature is at 4.3 μm and is the dominant opacity source at that wavelength in the photosphere of a T_{eff}=450 K Y dwarf. While equilibrium mod-

els find little phosphine in the photospheres of T_{eff}=200 K objects, Visscher *et al.* (2006) predict that phosphine will be in disequilibrium in giant planet and T dwarf atmospheres and could be orders of magnitude more abundant than equilibrium models predict. The effect of phosphine on Y dwarf spectra may therefore be underestimated in these models and even more pronounced in real Y dwarfs. H_2S affects the spectra mostly in *H* band, where it acts largely as a continuum absorber, depressing the *H* band peak, and to a smaller degree the *Y* band peak.

4.3.3.2   Model spectra

Model spectra of objects at two different representative gravities (log g=5.0, 4.0) from T_{eff}=450 to 200 K are shown in Figure 4.8. The models shown assume f_{sed}=5 and $h = 0.5$, as described in Section 4.2.4, and include both the salt/sulfide clouds (Na_2S, KCl, ZnS, MnS, Cr) and water ice clouds. As a brown dwarf cools over the Y dwarf sequence, the near-infrared flux dramatically declines. By the time the object has cooled to 200 K, almost all flux emerges in the mid-infrared, between strong molecular absorption features.

Figure 4.8 also shows the locations of the dominant absorption bands. For objects at these temperatures, absorption is dominated by water, methane, and ammonia, with contributions from PH_3 in the mid-infrared, including the feature at 4.3 μm for the 450 K model spectrum. Features from CO and CO_2 are not present here due to the low mixing ratios of these molecules at these temperatures in chemical equilibrium. Minor differences exist between models at the two shown gravities. We explore the gravity-dependence of features more in the discussion of Figure 4.15.

Figure 4.9 shows how the changes in molecular abundances and absorption changes

the shape of the near-infrared spectra over the T to Y sequence. The wide spectral windows in the water absorption, typical of warmer brown dwarfs, narrow as ammonia and methane increase in abundance in the near-infrared photosphere. As ammonia increases in abundance, the weaker ammonia feature between 1 and 1.1 μm begins to carve away the center of Y band. For the 300 K model shown in Figure 4.9, the Y band is bifurcated into two peaks by this absorption band. The appearance of this split Y band will depend on the nitrogen chemistry; if ammonia is less abundant due to disequilibrium chemistry, this change may occur at a lower temperature. The decline of the alkali absorption with temperature (see Figure 4.14) will also affect the underlying continuum absorption in Y band and therefore the appearance of this split.

4.3.3.3 The effect of sulfide and water clouds

Figure 4.8 shows the summed flux through the cloudy and clear columns of the model atmosphere. However, the flux through each of those columns is not equal; since the opacity of the cloud increases the total opacity through the column, less flux always emerges through the cloudy column than through the clear column.

Figure 4.10 shows models at the same effective temperatures, now showing the flux from the cloudy and clear columns. At effective temperatures above 400 K, the water cloud has not yet formed or is extremely thin, so the cloudy and cloud-free columns look quite similar; they differ only substantially in the Y and J bands, which is the region that the deep sulfide clouds affect. At effective temperatures between 300–375 K, the water cloud gradually becomes more optically thick. It first forms quite high in the atmosphere, and influences the mid-infrared from 2.8–5 μm where water ice particles absorb most efficiently (see Figure 4.5).

For cold Y dwarfs—between 200-300 K—the water cloud thickens as the object cools. At effective temperatures of 200 K, it has become quite optically thick: most regions of the near- and mid-infrared have significantly less flux emerging from the cloudy column. In fact, about 10^4 times less flux emerges at 4.5 μm from the cloudy column than the cloud-free column. This picture, where flux is emitted almost entirely through clearer columns of the atmosphere, is similar to Jupiter and Saturn's deep water clouds, which appear to have holes in the clouds (the so-called '5-micron hot spots' in Jupiter) through which most of the mid-infrared flux emerges.

Interestingly, water ice particles of this size (1–20 μm) are very inefficient at absorbing photons with wavelengths shorter than 1.4 μm, so the J and Y bands are not strongly affected, even in a column with a geometrically optically thick cloud.

It is also instructive to look at models that have the same total amount of flux emitted through model atmospheres with different cloud-covering fraction h and different sedimentation efficiency f_{sed}, to understand the sensitivity of our results to our choice of those parameters. The models presented in Figure 4.11 are separate from our main grid, which was run with $h = 0.5$ and f_{sed}=5 for all models; these models instead are run with h=1.0, 0.7, 0.4, 0.3, and 0.2 and with f_{sed}=3, 5, and 7 respectively. All models have the same amount of total flux emitted as a 200 K blackbody.

In both panels, the models look very similar to each other at wavelengths shorter than about 2 μm, where the water clouds do not strongly absorb. As we increase the cloud fraction (decrease h), more flux emerges between 2 and 3.6 μm and beyond 5.5 μm. This additional flux comes at the expense of the peak flux at $\sim$ 4.5 μm. In essence, increases in cloudiness

redistribute this peak flux to other wavelengths. When we vary f_{sed}, as expected, lower values of f_{sed} have somewhat more cloud opacity; this effect is largest in K band.

4.3.3.4 Disequilibrium chemistry

Disequilibrium carbon chemistry was predicted by Fegley and Lodders (1996) and confirmed in spectra by Noll *et al.* (1997) and Saumon *et al.* (2000). It is known to be important for brown dwarfs of many temperatures (Saumon *et al.*, 2006; Hubeny and Burrows, 2007) and may be even more significant for young planets (Konopacky *et al.*, 2013). The atmospheres of cool brown dwarfs should be methane-dominated. However, the chemical reaction that leads to methane formation is strongly temperature sensitive and becomes very slow at cold temperatures. If the timescale of mixing in the atmosphere is faster than the timescale for this reaction to occur, carbon will remain in CO instead of being converted to the CH_4 favored by equilibrium chemistry; for very cold objects this will become less important as the region where methane is thermochemically favored will extend very deeply into the atmosphere. This process has been explored in detail in a number of papers (Saumon *et al.*, 2006; Hubeny and Burrows, 2007; Visscher and Moses, 2011; Moses *et al.*, 2011).

Disequilibrium chemistry also affects other abundant molecules, such as the conversion of N_2 to NH_3 and CO_2 to CH_4. Other elements such as phosphorous are also out of chemical equilibrium in cold planets like Jupiter; in equilibrium, phosphorous would be in the form P_4O_6 but it is instead observed as PH_3 because the pathways for forming P_4O_6 are kinetically inhibited (Visscher *et al.*, 2006).

Here, we use the approach developed in Smith (1998) and techniques presented in

Saumon *et al.* (2006) to approximate the effect of CO/CH$_4$ and N$_2$/NH$_3$ disequilibrium in the atmospheres of Y dwarfs. Using this approach, we calculate a quench point in the atmosphere where the mixing timescale is equal to the chemical reaction timescale, which is governed by the slowest step of the fastest pathway of the reaction. Above the quench point, we assume that the mixing ratio of the molecule is constant. This has been shown using full kinetics models to be a good approximation in substellar atmospheres (Visscher and Moses, 2011). Note that in the disequilibrium chemistry calculation we calculate K_{zz} in the convective zone using mixing length theory and vary K_{zz} in the radiative zone as a free parameter, between 10^2–10^6 cm^2/s. In contrast, in the cloud code, we calculate K_{zz} using mixing length theory with a minimum K_{zz} of 10^5 cm^2/s; the clouds and chemistry are thus not strictly self-consistent in the radiative region.

The results of these calculations are shown in Figure 4.12 for three test cases. For the 450 K model, the disequilibrium model is generally slightly brighter across the near-infrared than the equilibrium model. This is because in equilibrium, ammonia is strongly thermochemically favored; out of equilibrium, there is slightly more N$_2$, which is not a strong absorber, and slightly less NH$_3$, which absorbs strongly across the near-infrared (see Figure 4.7). In the mid-infrared, the disequilibrium model is slightly brighter around 4 μm and slightly fainter around 4.6 μm. This is due to the increase in CO and decrease in CH$_4$; this shift increases absorption from the most prominent CO band at 4.5 to 4.9 μm and decreases absorption from both CH$_4$ and NH$_3$ between 3 and 4.4 μm. The increase in flux beyond 8 μm is because of the decrease in NH$_3$ which is the strongest absorber at those wavelengths.

For the 300 K and 200 K objects shown in Figure 4.12, disequilibrium chemistry of these particular gases becomes less important as the objects cool. The atmospheres of these

colder objects favor CH_4 and NH_3 strongly in equilibrium over a progressively wider proportion of their atmospheres. This means that even if deeper layers were mixed upwards to the photosphere, those layers would still be dominated by CH_4 and NH_3.

The shape of the *H* band has been used as an indicator of the increased abundance in ammonia through the T sequence to the Y dwarfs as they cool (see Figure 5 from Cushing *et al.* (2011)). We show a modeler's version of the same sequence in Figure 4.13 with the three sets of spectral indices used to classify T dwarfs (Burgasser *et al.*, 2006; Delorme *et al.*, 2008). The blue side of *H* band narrows as the object cools, due largely to increased ammonia absorption from 1.5 to 1.6 μm. In equilibrium, the shape changes from 900–450 K as the ammonia absorption increases. Disequilibrium chemistry changes the progression somewhat because the ammonia appears more gradually from 900–300 K. The shape of the disequilibrium *H* band at 450 K is very similar to the shape of the equilibrium *H* band at 600 K.

4.3.3.5 Decline in the alkali absorption

Because of the high densities in brown dwarf atmospheres, sodium and potassium bands at optical wavelengths are extremely pressure-broadened in brown dwarf spectra (Tsuji *et al.*, 1999; Burrows *et al.*, 2000; Allard *et al.*, 2005, 2007). There are few other optical absorbers in brown dwarf atmospheres, so these strong pressure-broadened features shape the optical spectra of most brown dwarfs, but for Y dwarfs these atoms begin to wane in abundance. As is shown in Figure 4.14, as sodium and potassium condense into Na_2S and KCl solid condensates, the depths and widths of the alkali features decrease. Because the slope of the optical spectrum for warmer objects is largely controlled by the pressure-broadening of these

features, as they decrease in strength, the overall slope of the optical also decreases, making Y dwarfs somewhat bluer in these colors.

4.3.3.6   Gravity signatures

Of great interest to the community in the coming years is the detection of cold planetary mass objects, either orbiting stars or free-floating (Marois *et al.*, 2008; Liu *et al.*, 2013).

Figure 4.15 shows potential gravity signatures for 450 K objects predicted by our models in the near-infrared (Y, J, H, K) and from 3–12 μm. For the near-infrared bands, the inset figure shows the shapes of the bands with the peak flux in the bands normalized to the same relative height. These broad gravity signatures are largely caused by the higher pressure photospheres of higher gravity objects.

In Y and J bands, the wings of the alkali bands, especially potassium, extend into these bands. These broad wings are due to the extreme pressure-broadening of the alkali lines. The higher pressures probed in the higher gravity photosphere cause less flux to emerge in both Y and the blue side of J band.

As opacity sources change due to increased pressure, the temperature profile of the atmosphere adjusts; for Y dwarfs, this brightens H band, causing more flux to emerge from that window.

In K band, the collision-induced absorption of H_2 is a major opacity source. This feature is quite pressure-dependent, so much like the broadened alkali bands in Y and J bands, the higher gravity atmosphere with the higher pressure photosphere has more total opacity in K band. This decreases the amount of flux that emerges and broadens the K band shape.

The major gravity dependent feature at wavelengths longer than 3 μm is between 3.5 and 4.7 μm. At these wavelengths, the lower gravity objects have an additional absorber which changes the shape of that mid-infrared feature. This region of the spectrum is in a window between major methane and water absorption features and is the brightest peak in the near-mid-infrared spectra. PH_3 is a strong absorber from 4–4.6 μm and somewhat gravity dependent at those wavelengths, absorbing more strongly in the lower gravity models. Additionally at these wavelengths, due to the different P–T profile at high gravity, we probe somewhat deeper, hotter layers, allowing more flux to emerge from the higher gravity model.

4.3.4   Model Photometry

In order to compare to observations of the Y dwarf population, we calculate model photometry. The radii used to calculate absolute magnitudes were interpolated using the cloud-free evolution models from Saumon and Marley (2008).

Color–magnitude diagrams (CMDs) of the model photometry are shown for two different gravities (log g=5.0 and log g=4.5) in Figures 4.16 and 4.17 respectively. Each set of CMDs shows L and T dwarfs as open grey circles and Y dwarfs as green points with error bars. Models from this work and models from Saumon *et al.* (2012) and Morley *et al.* (2012) are shown.

The first panel ($Y-J$ vs. M_Y) shows that Y dwarfs are significantly bluer in this color than the slightly warmer T dwarfs, with a 0.25 magnitude gap in color between the coolest T dwarfs and warmest Y dwarfs. This bluer $Y-J$ color is expected and indeed predicted by the models, and is due to the condensation of the alkalis into Na_2S and KCl clouds. As they

condense out of the gas phase, the broadened alkali lines decrease in strength (Marley *et al.*, 2002; Burrows *et al.*, 2003b). Since those lines had been suppressing Y band flux more than J band flux, as they decrease the effect is to make $Y - J$ appear bluer. However, three of the six Y dwarfs with measured Y and J photometry are appreciably bluer than even the bluest models predict, and cloudy models are significantly redder.

The second CMD shows $J - H$ vs. M_J. These colors are most sensitive to the sulfide and chloride clouds, which suppress the Y and J band flux. Since clouds tend to suppress the flux in J band, the clouds make these colors redder, matching the observations of the redder Y dwarfs. The sulfide/chloride clouds wane in importance as objects cool from 450 to 325 K. For objects cooler than 325 K, the water clouds become increasingly important. Counterintuitively, the water clouds tend to make $J - H$ colors bluer; this is because of water ice is strongly scattering (and a poor absorber) in J band but becomes absorbing in H band (see single scattering albedo plot, Figure 4.5). Around 325 K, the cloudy color and cloud-free colors are the same.

On the $J - H$ CMD, a line showing the effect of disequilibrium chemistry is also shown. Interestingly, this also makes the $J - H$ colors redder, mostly due to decreased absorption from NH_3 across the near-infrared. In reality, a combination of condensates and disequilibrium may be affecting Y dwarf spectra.

The third panel shows $H - K$ vs. M_K. Somewhat puzzlingly, all the Y dwarfs except one cluster around a color of 0.0 and M_H of 20.5. This behavior is quite different from the late T dwarfs, which have a large spread in $H - K$ colors. The location of this cluster is somewhat redder and brighter in H band than the models predict. This could be due to a number of factors; a major contributor is the incompleteness of the methane line list used in the current study. We

expect from preliminary results that the new line list from Yurchenko and Tennyson (2014) will redden these colors.

The last panel shows the Y dwarfs where they emit the most energy: the mid-infrared. Brown dwarfs get quickly redder in $H - [4.5]$ color as they cool and the peak of the Planck function moves redward. Generally the colors of the objects seem to match the model colors relatively well, with the exception of the two reddest objects, which appear to be brighter than the models at 4.5 microns by up to 2 magnitudes.

4.4 Observing Y dwarfs with *JWST*

Y dwarfs emit most of their flux in the mid-infrared. This will make their characterization from the ground extremely challenging, especially for the coldest objects. No Y dwarfs had yet been discovered during the *Spitzer* Space Telescope's cryogenic mission, which ended in 2009, so the coolest brown dwarf to have a mid-infrared IRS spectrum is spectral type T7.5 (Saumon *et al.*, 2006). *JWST* will have unprecedented sensitivity in the near-infrared, and it will be the main tool with which we can study the coldest brown dwarfs. The two most important instruments for spectroscopic characterization will be the Near-Infrared Spectrograph (NIRSpec) and the Mid-Infrared Instrument (MIRI).

4.4.1 NIRSpec

NIRSpec is the most sensitive near-infrared spectrograph on *JWST* and will be capable of moderate resolution spectroscopy (R∼1000 or R∼2700) from 1–5 μm in 3 bands

(1.0–1.8, 1.7–3.0, and 2.9–5.0 μm respectively). Figure 4.18 shows the sensitivity for each of these channels; these sensitivity lines represent the faintest continuum flux observable with an integration time per channel of 10^5 seconds (27.8 hours) and a signal-to-noise ratio (SNR) of 10. We also show example spectra of brown dwarfs spanning a full range of Y dwarf temperatures and located 5 pc from the Earth. In the bottom panel we zoom into the band 3 spectral region, where even our coolest models ($T_{\rm eff}$=200 K) would be observable. The dotted lines show models with no clouds from Saumon *et al.* (2012); the solid lines show the models from this work including water and sulfide/salt clouds.

The warmer Y dwarfs discovered to date, $T_{\rm eff}$=400–500 K, will be observable across the near-infrared bands, with the exception of the deepest absorption bands. We will be able to detect the presence or absence of strong features from water, ammonia, methane, phosphine, carbon monoxide, and carbon dioxide using this instrument, allowing us to constrain disequilibrium carbon, nitrogen, and phosphorous chemistry in Y dwarf atmospheres.

The Y dwarfs cooler than 300 K will be too faint to observe at wavelengths from 1–3.5 μm, as the flux from the near-infrared collapses. However, we will be able to detect these objects at high SNR between 3.5 and 5.0 μm. The shape of this region is controlled by a variety of absorbers: ammonia and methane on the blue side, water on the red side, and possibly H_2S, PH_3 (if phosphorous chemistry is in disequilibrium), and CO and CO_2 (if carbon chemistry is in disequilibrium). The prominent feature at 4.2 μm is an ammonia absorption feature and could be useful for determining the effective temperatures of cold brown dwarfs. This window region of the opacity will likely provide the most information about these otherwise very faint objects.

4.4.2 MIRI

MIRI will be capable of low (R∼100) resolution spectroscopy from 5–14 μm and moderate resolution (R∼3000) spectroscopy from 5–28.3 micron. It is the only *JWST* instrument that will observe wavelengths longer than 5 μm and will be 50 times more sensitive than the *Spitzer* Space Telescope. The MIRI moderate resolution spectrograph has four channels: channel 1 from 5.0–7.7 μm, channel 2 from 7.7–11.9 μm, channel 3 from 11.9–18.3 μm, and channel 4 from 18.3–28.3 μm. Figure 4.19 shows the sensitivity for each of these bands; like the NIRSpec sensitivity limits, these sensitivity lines represent the faintest continuum flux observable with an integration time per channel of 10^5 seconds (27.8 hours) and a signal-to-noise ratio (SNR) of 10, and we show example spectra of the same brown dwarf models located 5 pc from Earth. The MIRI sensitivity at 6.4 μm is about 10 times less sensitive than the NIRSpec sensitivity at 5 μm. This is due to a combination of instrumental effects, including MIRI's higher dark current, higher intrinsic spectral resolution, finer spatial sampling, lower quantum efficiency, and additional optics. To obtain the full 5–28 μm spectrum without gaps, three separate observations (using three different settings of the MRS spectrograph) are needed, so the actual observing time to acquire these spectra is three times as long.

Many of the current suite of Y dwarfs discovered to date using the *WISE* data will be easily observable using this instrument. Most of these objects have temperatures between 400–500 K and are within 10 pc of the Earth (Dupuy and Kraus, 2013; Beichman *et al.*, 2014). The T_{eff}=450 K model shown in Figure 4.19 is well above the sensitivity limit for 5–18.3 μm. This will allow us to probe parts of the spectrum where the opacity is dominated by different

molecules: water from 5–7.2 μm, methane from 7.2–8.5 μm, and ammonia from 8.5–18 μm. Channel 4 is much less sensitive so a 450 K object is only marginally detectable from 18–28.3 μm with a SNR of 10.

The coldest brown dwarfs will push the sensitivity limits for this instrument. No objects colder than 300 K have been discovered to date, but if we find such objects, they will be quite challenging to observe. The highest SNR spectra will be from channels 2 and 3, from 7.7–18.3 μm. This wavelength range is shaped by methane, ammonia, and H_2 CIA. Objects below 300 K will be only marginally detectable in channel 1 and not detectable in channel 4 at R$\sim$1000. Binning the spectra to R$\sim$300 would improve sensitivity by a factor of $\sim$3, improving the detection limit for T_{eff}=250 K objects and still providing adequate resolution for identifying prominent molecular bands.

4.4.3 NIRCam and NIRISS

The two other main science instruments on *JWST* are the Near-Infrared Camera (NIRCam) and Near-InfraRed Imager and Slitless Spectrograph (NIRISS). These instruments are somewhat less well-suited to the spectral characterization of the coolest brown dwarfs. NIRISS is optimized for high contrast imaging, high resolution imaging of extended sources, and transiting exoplanet measurements; it also has a wide-field R$\sim$150 slitless spectroscopy mode designed for detecting high redshift emission lines. However, for the characterization of cool brown dwarfs, sensitivity is the most important feature.

NIRCam does have a grism mode that will be capable of 2.4–5 μm R$\sim$2000 slitless spectroscopy. However, its sensitivity at those wavelengths will be somewhat lower than NIR-

Spec's sensitivity. The lower sensitivity is because NIRCam uses a slitless grism that is sensitive to sky background across a large field. This mode is more optimized for precision photometry and stability, making it a powerful instrument for, e.g., exoplanet transmission spectra and secondary eclipses. For the sensitivity-limited work needed to characterize Y dwarfs, NIRSpec will be a more suitable instrument.

4.5 Observing cold directly-imaged planets

Observing directly-imaged giant planets at the temperatures of Y dwarfs (200–450 K) will push the limits of current technology. Nonetheless, some current or soon forthcoming instruments specialized for high-contrast imaging will be capable of detecting such planets. If planets with masses between 1 and 10 M_J are quite common, systems of a variety of ages will have planets with these temperatures. Depending on the mechanism of formation, a 10 M_J planet will reach $T_{\rm eff}$=450 K at an age of 1–2 Gyr. A 5 M_J planet will reach $T_{\rm eff}$=450 K in 300–600 Myr; a 1 M_J planet in 20–30 Myr (Fortney *et al.*, 2008b). The current and forthcoming instruments most capable of detecting such planets are the Gemini Planet Imager (GPI), the Spectro-Polarimetric High-contrast Exoplanet Research (SPHERE), and the Large Binocular Telescope Adaptive Optics System (LBTAO).

4.5.1 GPI and SPHERE

GPI (Macintosh *et al.*, 2006) and SPHERE (Beuzit *et al.*, 2006) are instruments designed for 8-meter class telescopes and optimized for studying young hot giant planets around bright stars. Both will have advanced adaptive optics systems and hope to achieve planet-star flux contrasts between 10^{-6} and 10^{-8}. They will target young stars to find self-luminous planets and expect to find up to dozens of planets in their initial campaign surveys (McBride *et al.*, 2011).

Predicted GPI contrast curves suggest that it will be capable of 5×10^{-8} contrast for very bright stars ($I = 5$) and 10^{-6} contrast for fainter ($I = 9$) targets. In Figure 4.20, a representative value of 1.9×10^{-7} is shown, which is the predicted contrast at 1 arcsec separation from a 7th magnitude G0 dwarf. The models shown are binned to the resolution of GPI in *H* band, $R \sim 45$ at 1.65 μm and are shown as the flux ratio compared to a blackbody with the temperature and radius of a G0 dwarf. The T_{eff}=450 K planet is detectable above the contrast limits in the spectral regions where the planet is bright. Cooler planets (T_{eff}=350, 250 K) will be too faint to observe around a G dwarf.

4.5.2 LBTAO

The LBTAO system includes a high-contrast imaging instrument optimized for the mid-infrared. It is capable of 4.8×10^{-6} contrast in *L'* band (Skemer *et al.*, 2014) for a bright star and has six narrow band filters spanning 3.04 to 3.78 μm. This spectral region is particularly useful for two reasons: first, the planet-star flux ratio is much higher for cool planets in *L* and *M* bands. Second, this spectral region spans the most prominent methane feature at 3.3 μm,

allowing for the characterization of a prominent atmospheric component. For example Skemer *et al.* (2013) used this instrument to observe the HR 8799 system and find that the planets do not have strong methane absorption, inferring that methane must be in disequilibrium.

Similar to GPI, a 450 K planet around a G dwarf would be detectable with LBTAO but a 350 or 250 K planet around a G dwarf would not be. Note that, because it operates in the mid-infrared where the sky is bright, the LBTAO system is also background limited; it can only observe objects brighter than $\sim$18th magnitude in L$'$. This limit approximately corresponds to a 350 K object at 10 pc. More distant objects will therefore be background limited; closer objects will be contrast limited. The LEECH campaign is currently using this instrument to survey stars in the solar neighborhood and discover new planets (Skemer *et al.*, 2014).

4.6   Discussion

4.6.1   Outstanding Issues

Discrepancies between models and observations may indicate that the physics or ingredients in the model are either incorrect or incomplete. For example, there are many sources of uncertainty in the molecular opacity databases.

Alkali opacity uncertainties may affect the optical and near-infrared. The handful of Y dwarfs that have observed $Y - J$ color suggest that these objects are bluer in this color than the models. This spectral region is controlled in part by the decline of the strongly pressure-broadened alkali opacity, so this mismatch could be due to the treatment used for the alkali opacity. For these calculations, we use the line broadening treatment outlined in Burrows *et al.*

([2000](#)), which is somewhat *ad hoc* and potentially creates some inaccuracies in the model flux in Y and J bands. A calculation of the molecular potentials for potassium and sodium in these high pressure environments, as is carried out in Allard *et al.* ([2005](#), [2007](#)), would improve the accuracy of these models. Subsolar metallicities also make $Y-J$ colors bluer (Mace *et al.*, [2013](#); Burrows *et al.*, [2006](#)), so it is important to model the opacity correctly to interpret metallicity measurements using this spectral region.

Another known source of opacity uncertainty is in the methane line list; the list used in this study is known to be incomplete. The new line list from Yurchenko *et al.* ([2013](#)) and Yurchenko and Tennyson ([2014](#)) has over nine billion lines and will vastly improve accuracy of the treatment of methane.

It is possible that we may be missing important physical processes in our models that occur in actual Y dwarfs. For example, an assumption we make when calculating the spectra is that the atmospheres are in radiative–convective equilibrium. It is inevitable that real brown dwarf atmospheres have higher levels of complexity than these simple assumptions. The upper atmospheres of brown dwarfs could be heated by a similar mechanism to that which creates Jupiter's thermosphere, in which energy is deposited high in the atmosphere by dissipation of gravity waves (Young *et al.*, [1997](#)). If indeed the upper atmosphere is hotter than radiative–convective equilibrium models, this would change the observed spectrum. Using mid-infrared spectra of L dwarfs, Sorahana *et al.* ([2014](#)) show that several L dwarf spectra can be fit significantly better using a model that allows for this upper atmospheric heating. In fact, in our equilibrium models the [3.6]–[4.5] color is redder by ~ 1 magnitude at some T_{eff}; simple preliminary models in which we change the P–T profile of the upper atmosphere show that heating

157

high in the atmosphere increases the flux within the methane band centered at 3.3 μm, which makes the [3.6]–[4.5] color bluer, and closer to the observed colors.

Another limitation of this study is that the models here include only solar abundances. We expect Y dwarfs and exoplanets to have a range of metallicities and potentially a range of other abundance ratios such as non-solar C/O ratios. Future work will be needed to analyze the effect of abundances on Y dwarf spectra and colors.

We consider disequilibrium chemistry of N_2/NH_3 and CO/CH_4, but other molecules such as PH_3 and CO_2 may also be out of chemical equilibrium. Such unmodeled chemistry could change abundances of molecules we do include, or create additional molecules that we do not include in the calculations.

As 1D models, these calculations naturally do not include the effect of 3D dynamics on the cloud structure. The breakup of the iron and silicate clouds at the L/T transition is a source of continued study; due to dynamical processes, those clouds dissipate at higher temperatures than 1D cloud settling models predict. As the sulfide and salt clouds sink more deeply into the atmosphere as the brown dwarf cools, they may also break up and disappear from spectra at higher temperatures than our treatment predicts. Further study, including dynamical effects, will be necessary to understand this phenomenon across the brown dwarf spectral sequence.

4.6.2 Comparison with Burrows et al. 2003 models

To our knowledge, the only previous comprehensive set of models analyzed and published for Y dwarfs including water clouds using a cloud model were those in Burrows *et al.* (2003b). Our approaches and results are overall very similar; we assume chemical equilibrium,

radiative–convective equilibrium, incorporate a cloud model, and publish spectra and colors of the coolest brown dwarfs. Like Burrows *et al.* (2003b), we predict the growing importance of methane and ammonia absorption over the T to Y sequence, the weakening of the alkali absorption, and a reversal in the blueward trend in near-IR colors of the T dwarfs around 400 K. Our spectra differ in details due largely to changes in the line lists over the past decade; we have continuously improved our opacity database over the last ten years (Freedman *et al.*, 2008). Most relevant here, we are using updated treatments for both ammonia (which becomes very important for Y dwarfs) and H_2 collision-induced absorption.

One of the conclusions presented in Burrows *et al.* (2003b) is that the water clouds do not significantly affect the spectra of Y dwarfs and it is on this point that we differ most significantly. The differences lie in our treatment of the cloud model for the water clouds. Burrows *et al.* (2003b) uses the cloud model presented in Cooper *et al.* (2003), which results in a uniform distribution of very large particles (20–150 μm) within a single pressure scale height. Since our cloud particles are much smaller ($\sim$1-20 μm), we have far more particles to create a cloud of the same mass. This means that when our water cloud forms, it is much more optically thick. For a more detailed comparison of the cloud models themselves see Marley *et al.* (2003) which describes the challenges of modeling clouds in brown dwarfs and the problems inherent to different approaches.

4.6.3 WISEPA J182831.08+265037.8

WISEPA J182831.08+265037.8 (hereafter WISEP J1828+2650) is a particularly interesting object. Its near-infrared colors are inconsistent with the models and with the other Y

dwarfs. The peculiarities of the near-infrared colors and comparisons to models led Cushing *et al.* (2011) and Kirkpatrick *et al.* (2012) to classify it as a >Y0 and >Y2 respectively; comparisons to models gave Cushing *et al.* (2011) a temperature estimate of $T_{\mathrm{eff}} \leq 300$ K. However, for a brown dwarf that cold to have the measured mid-infrared luminosity, it would need to have an unphysically large radius, leading Leggett *et al.* (2013) to suggest that it is an unresolved binary.

Dupuy and Kraus (2013) revised the parallax measurement and found that based on its luminosity, WISEP J1828+2650 likely has a temperature closer to the late T dwarfs, 500–600 K, and that even if it is a binary, those components must still be 400–500 K.

Using the models presented here, it is not possible to fit all of the near-infrared colors of WISEP J1828+2650 using a lower gravity model. For example, the models predict that a brighter J band flux and corresponding bluer $J - H$ color at lower gravity, due to the decreased strength of the alkali absorption in a lower gravity photosphere, whereas for this object we observe an extremely red $J - H$ color.

Additional spectroscopic data at near- and mid-infrared wavelengths will be required to determine whether WISEP J1828+2650 is indeed a prototypical $T_{\mathrm{eff}} \leq 300$ K Y dwarf, or a peculiar version of the T8–Y0 spectral classes.

4.7 Conclusions

As brown dwarfs approach the effective temperatures of the solar system's planets, volatile clouds will form in their atmospheres. The first and most massive type of volatile cloud

that forms is water ice clouds. Water ice clouds form in objects cooler than effective temperatures of ∼400 K. In order to converge atmospheric temperature structures self-consistently with both clouds and chemistry, we calculate models in which, like water clouds in the solar system planets, the clouds heterogeneously cover the surface ("patchy" clouds). Our model grid covers the Y dwarf spectral class as well as giant planets with the same effective temperatures, from T_{eff}=200–450 K and log g=3.0–5.0.

Our main results include:

1. While water condenses high in the atmospheres of all objects below T_{eff}∼400 K, these clouds do not become optically thick until the object has cooled to 350–375 K. This result means that for the current set of Y dwarfs warmer than 400 K, water clouds will not strongly effect their spectra.

2. Water clouds, unlike other clouds in brown dwarf atmospheres, are very much nongray absorbers. Using the Ackerman and Marley (2001) cloud model, water ice particle sizes range from ∼1–20 μm. For these particle sizes, the ice particles are strongly scattering in the optical through J band and do not change the spectra significantly at those wavelengths. The ice particles absorb strongly in the infrared with prominent features, the strongest of which is at 2.8 μm.

3. H_2O, NH_3, CH_4, and H_2 CIA are the dominant opacity sources in Y dwarf atmospheres. Less abundant species such as PH_3 may also be observable at 4–4.6 μm, as well as H_2S in H and Y bands and the alkalis in the optical.

4. JWST's MIRI and NIRSpec instruments will be well-suited to characterizing cool brown dwarfs. T_{eff}=400–500 K objects will be observable across their near- and mid-infrared

161

spectra, and even T_{eff}=200 K objects will be observable in the spectral window region between 3.8 and 5.0 μm and at some wavelengths between 8 and 17 μm. Existing and upcoming ground-based instruments such as GPI, SPHERE, and LBTAO will be capable of directly-imaging T_{eff}=400–500 K planets around nearby G dwarfs.
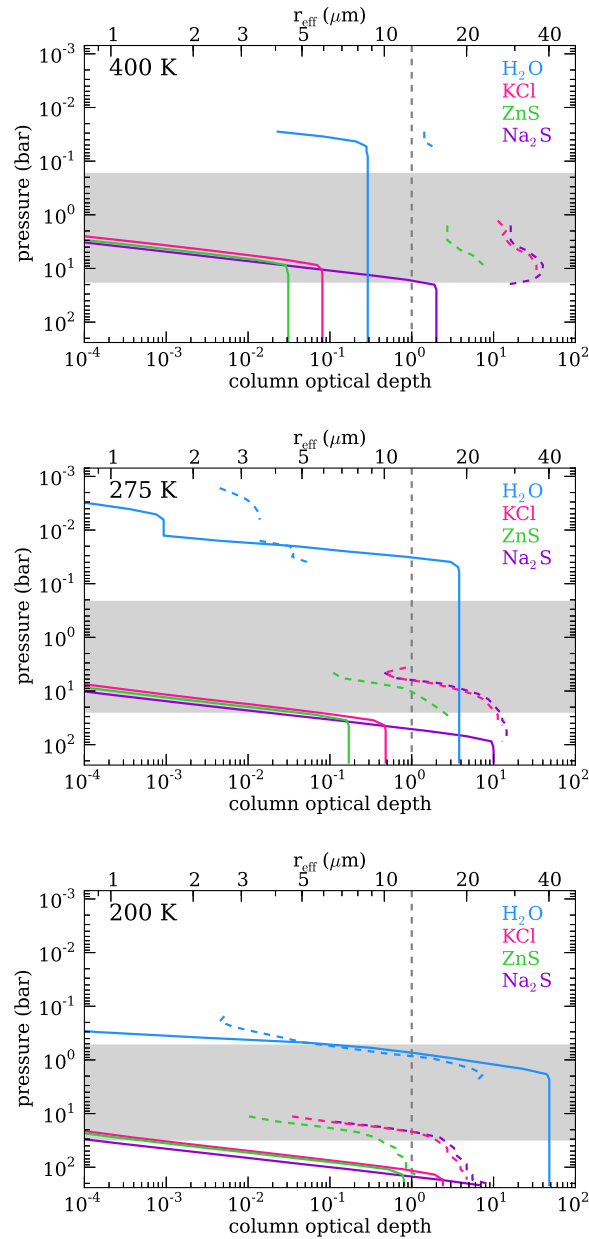
Figure 4.4: Cloud properties for sulfide/salt and water clouds at three temperatures. The geometric column optical depth is shown as solid lines. The effective (area-weighted) mode radius of the cloud particles at each pressure is shown as dashed lines. The 1–6 μm photosphere is shown as the shaded gray region, and the $\tau = 1$ line is shown to guide the eye. Thin water clouds form in all three models, but only become optically thick in the two coolest models. Mode particle sizes are small (3–5 μm) for T_{eff}=275 K and larger (5–20 μm) for the 200 K model. The sulfide/salt clouds form and become optically thick in the photosphere of the 400 K model but are optically thick below the photospheres of the cooler two models as they form more deeply.

163
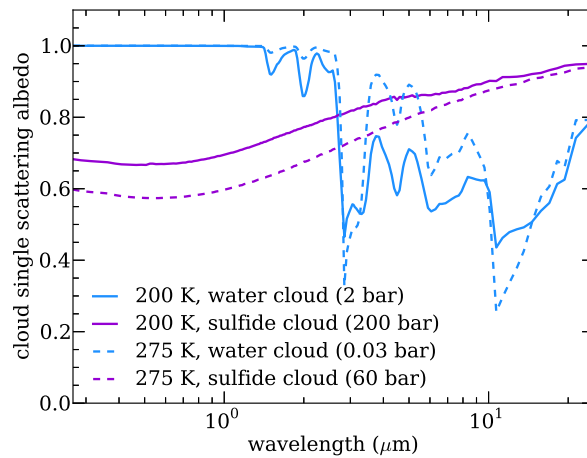
Figure 4.5: Single Scattering Albedo for water and Na$_2$S cloud. For models with T_{eff}=200 K and 275 K, the single scattering albedos of both the water and Na$_2$S cloud are shown for a single atmospheric layer. The water cloud forms high in the atmosphere (2 bar and 0.03 bar for the layers shown from the 200 and 275 K models, respectively) and the Na$_2$S cloud forms deeper (200 and 60 bar, respectively). The sulfide cloud single scattering albedo is relatively uniform, rising from ∼0.6 in the optical to 0.9 at 10 μm. The water cloud single scattering albedo has many more features, which vary with particle size (the mode particle size is ∼20 μm for the 200 K model and ∼5 μm for the 275 K model; the single scattering albedo is calculated for the distribution of particle sizes calculated using the cloud code). In the optical the single scattering albedo is 1.0, which means that the water clouds do not absorb efficiently at short wavelengths.
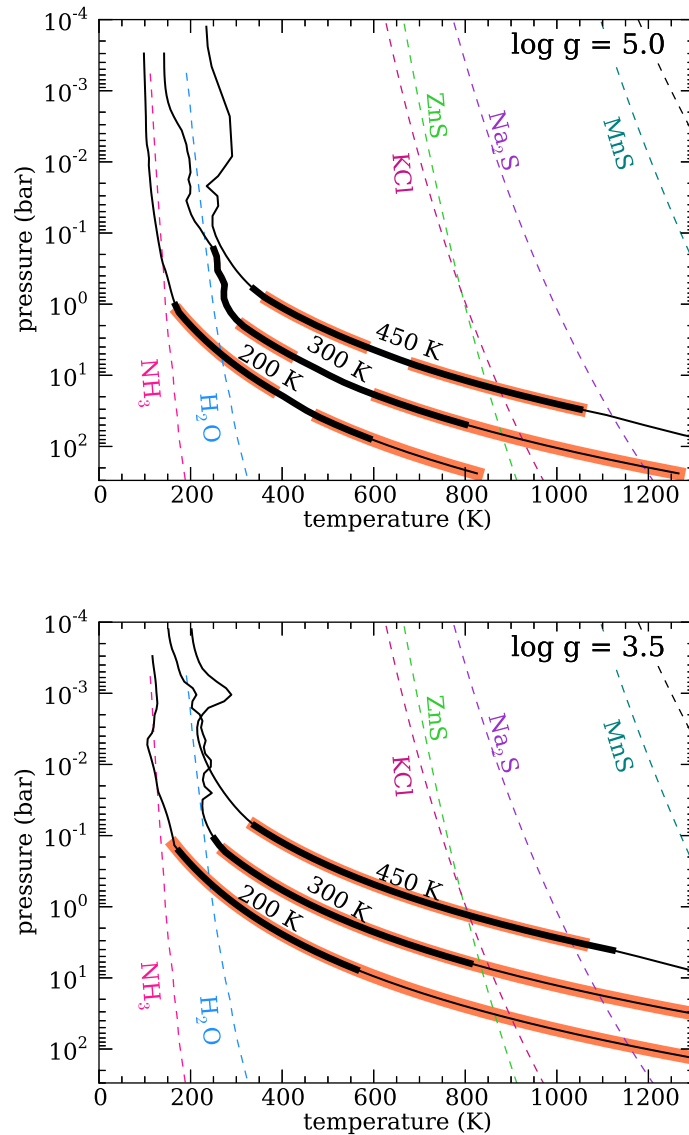
Figure 4.6: Pressure–temperature profiles for three representative temperature and two gravities are shown. The thicker black line indicates the location of the 1–6 μm photosphere. The shaded salmon region shows where the atmosphere is convective. The dashed lines show condensation curves for each substance expected to condense in thermochemical equilibrium. The curve represents the pressure–temperature points at which the partial pressure of the gas is equal to the saturation vapor pressure; to the left of the curve, the partial pressure of each gas is higher than the saturation vapor pressure and the excess vapor will form a cloud. The kinks in the profile in the upper atmosphere are numerical and do not represent 'real' features in the atmospheres of Y dwarfs. Fortunately, the kinks lie above the regions of the atmosphere from which flux emerges and so they do not pose a problem for this work.
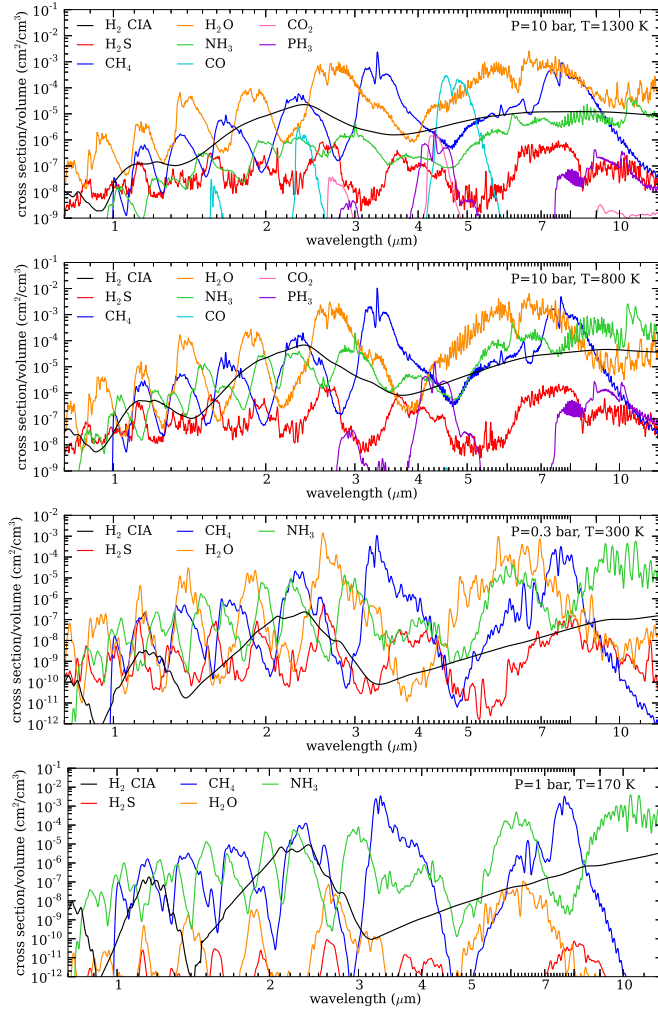
Figure 4.7: Opacities of the major constituents of Y and T dwarfs. We choose four representative P–T points in the photospheres of models at three different temperatures (all with log g=5.0): T_{eff}=900 K (P=10 bar, T=1300 K), T_{eff}=450 K (P=10 bar, T=800 K and P=0.3 bar, T=300 K), and T_{eff}=200 K (P=1 bar, T=170 K). We multiply the molecular opacities (cm^2/molecule) by the number density of that molecule in a solar metallicity atmosphere in thermochemical equilibrium to get a opacity per volume of atmosphere. In this temperature range, the abundances of CO and CO$_2$ drop by orders of magnitude. Water vapor remains an important opacity source in the top three panels, but drops significantly in the bottom panel because of water condensation. NH$_3$ and CH$_4$ gradually become more important as objects cool. PH$_3$ may also be an important absorber for the Y dwarfs in the mid-infrared.

166
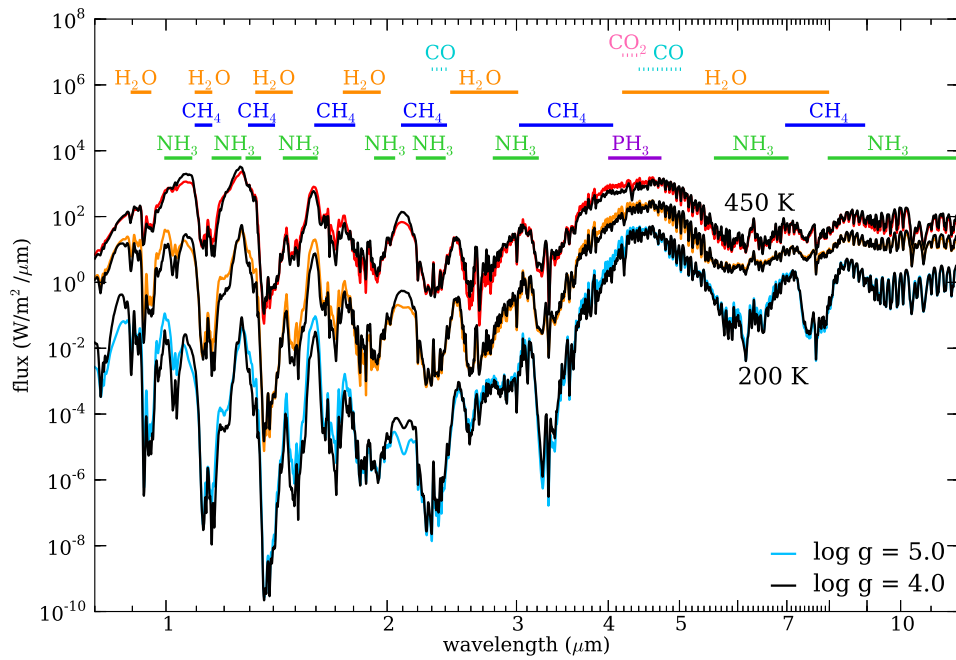
Figure 4.8: Model spectra of three effective temperature (450, 300, 200 K) at two gravities (log g=4.0, 5.0) and cloud parameters f_{sed}=5, h=0.5. Locations where each of the major molecules in the atmosphere peak in absorption are marked by the bands along the top. The near- and mid-infrared are carved by overlapping bands of water, methane, and ammonia absorption. The mid-infrared is also affected by PH_3.
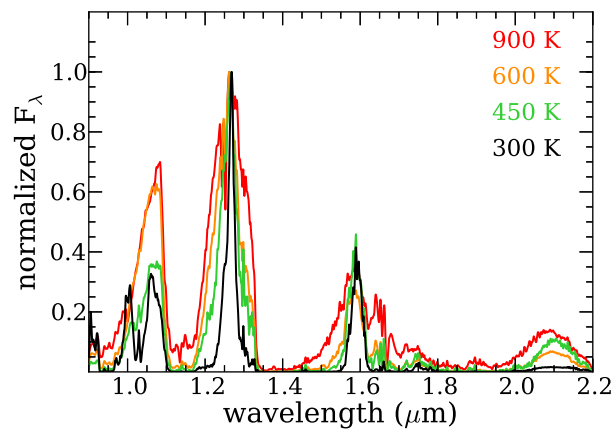
Figure 4.9: Model spectra at four effective temperature spanning mid-T to Y dwarfs (900, 600, 450, 300 K), log g=4.5, and cloud parameters f_{sed}=5, h=0 (900, 600 K) and h=0.5 (450, 300 K). Spectra are rescaled such that the flux at the peak of J band is the same for all models. Note the change in the shape of the near-IR spectral windows. J and H bands narrow as ammonia and methane increase in abundance. Ammonia absorption in Y band causes the band shape to bifurcate for the coolest model.
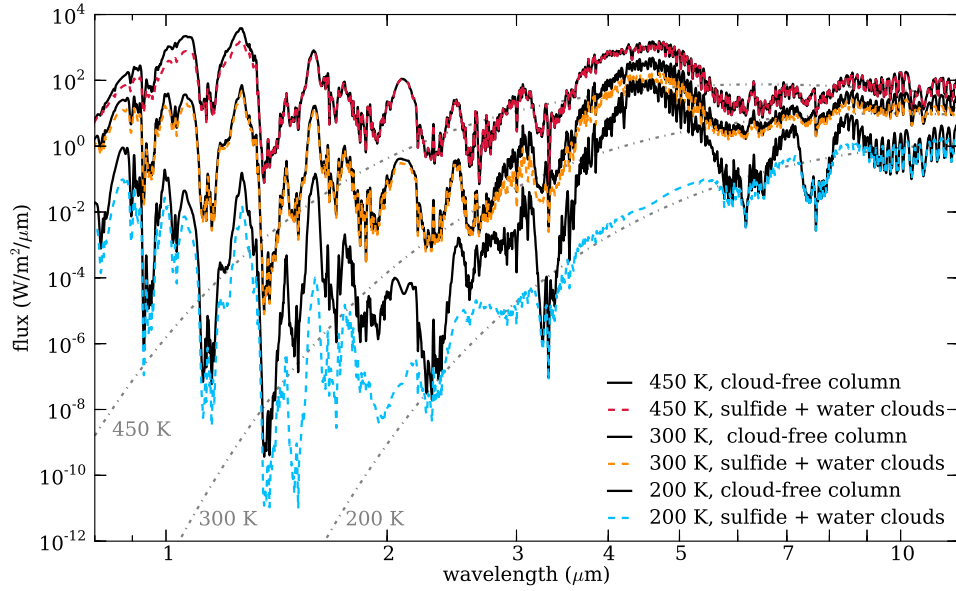
Figure 4.10: Clear and cloudy spectra of models of three effective temperature (450, 300, 200 K) with log g=5.0 and cloud parameters f_{sed}=5, h=0.5. Blackbodies of equivalent effective temperatures are shown as dashed gray lines. Each of the models shown for a given temperature has the same P–T profile; the cloud-free spectrum is the flux calculated through the clear column and the cloudy spectrum is the flux calculated through the cloudy column. Summed together, they have the correct effective temperature. More flux is able to emerge from the clear column because the opacity is lower. For the 450 K model, the greatest flux difference between the cloud-free and cloudy models is in Y and J bands. In the 300 K model, the greatest flux difference is at the flux peak at 4.5 μm where the water clouds absorb strongly. For the 200 K model, the water cloud is very optically thick and within the photosphere, so at all the wavelengths where the water cloud absorbs, the flux emerging from the cloudy column is significantly limited.

169
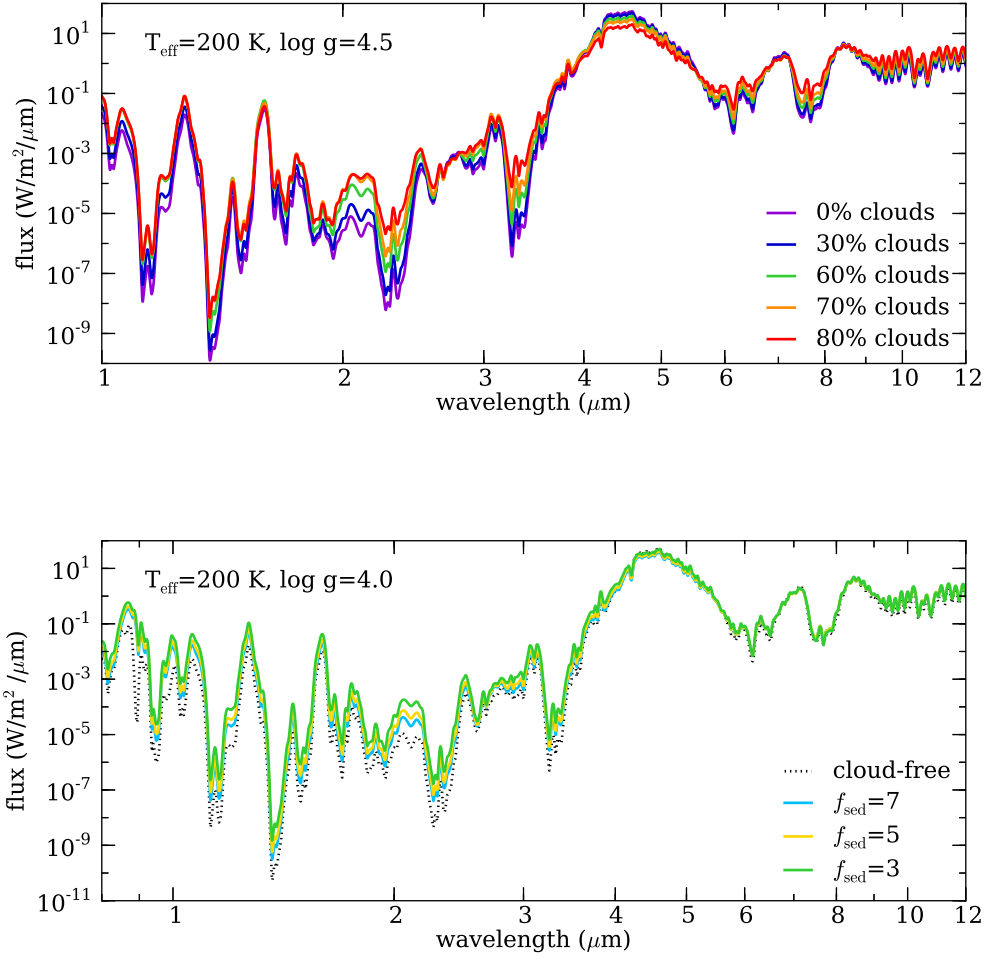
Figure 4.11: Spectra of models in which we vary the two free parameters of the patchy cloud model, h and f_{sed}. All the models shown have T_{eff}=200 K. In the upper panel, h is varied from 1.0 (cloud-free) to 0.2 (80% of the surface covered in clouds) and f_{sed}=5. In the lower panel, f_{sed} is varied from 3 to 7 and h=0.5. The flux is redistributed when an atmosphere is cloudy; all models have the same total amount of energy emerging. Most prominently, clouds decrease the flux in the major flux peak at 4–5 μm and redistribute that energy from the flux peak into other parts of the spectrum. For example, the cloudiest model is significantly brighter at the K band peak than the cloud-free model.
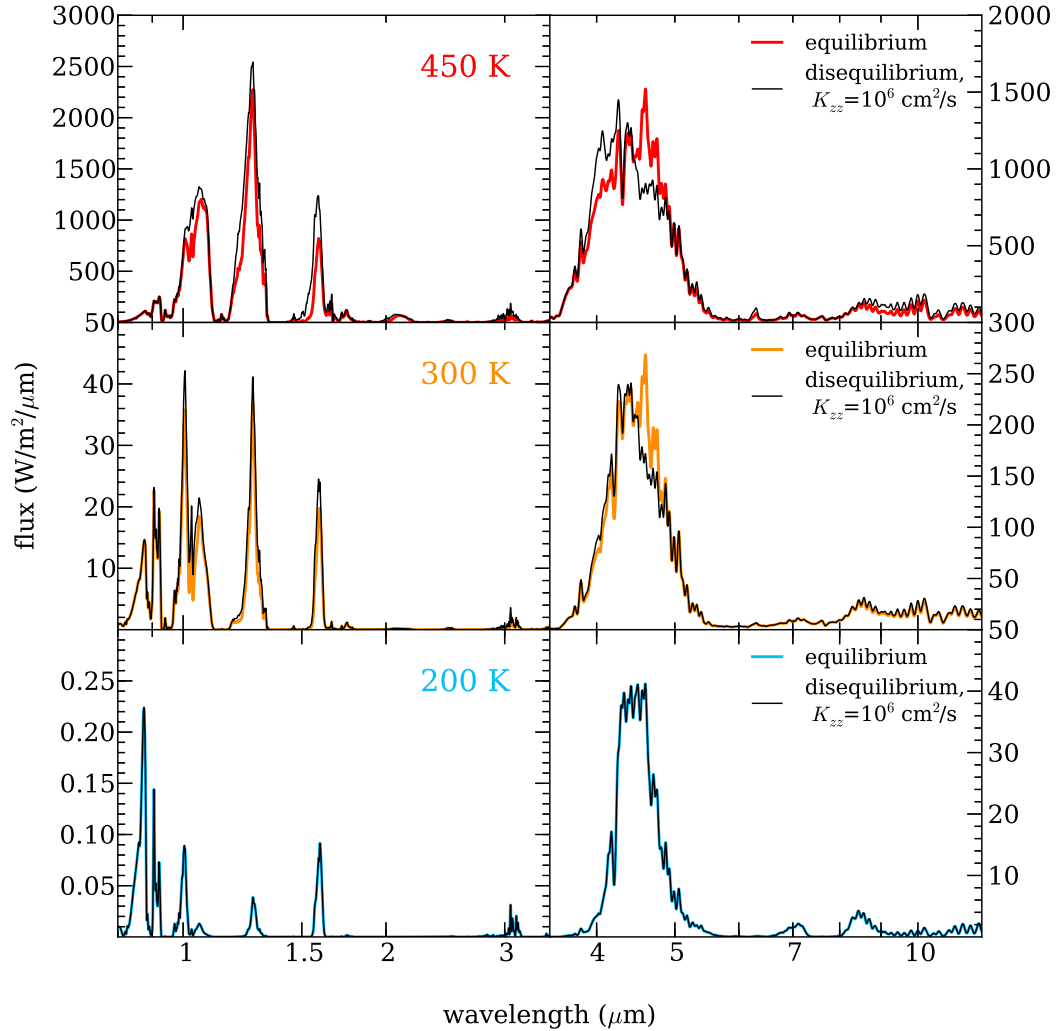
Figure 4.12: Spectra of models including disequilibrium chemistry at T_{eff}=450, 300, and 200 K and log g=5.0. All disequilibrium models use eddy diffusion coefficient K_{zz}=10^6 cm^2/s and include CO/CH$_4$ and N$_2$/NH$_3$ disequilibrium. Near- and mid-infrared spectra are shown on axes with different linear scales to facilitate viewing small changes in spectra. At 450 K, in disequilibrium slightly more flux emerges from Y, J, and H bands, the shape of the 4.5 μm peak changes, and slightly more flux emerges from 8–12 μm. At 300 K, the equilibrium and disequilibrium models do not differ as strongly, though the shape of the 4.5 μm peak changes. At 200 K, the equilibrium and disequilibrium models are indistinguishable.
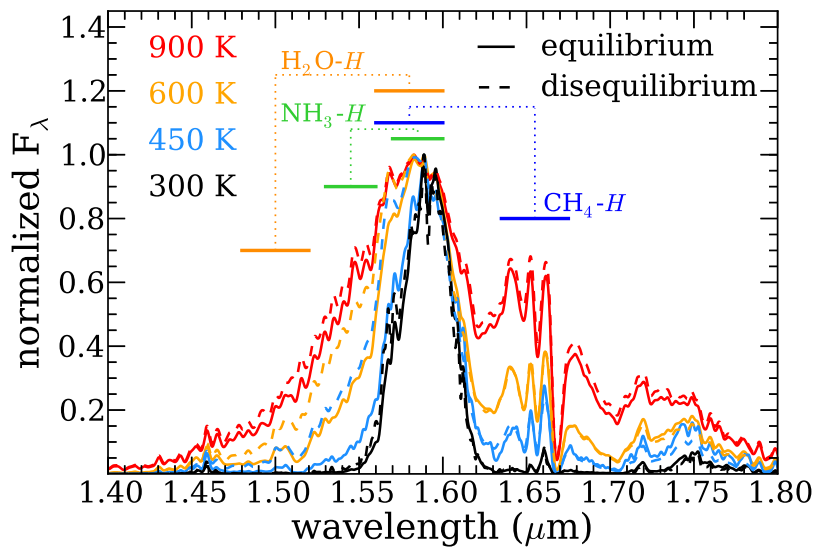
Figure 4.13: Shape of the *H* band over the late T to Y sequence. As ammonia and methane absorption on the blue and red sides of the *H* band, the peak narrows. The disequilibrium models (K_{zz}=10^4 cm²/s) narrow more slowly on the blue side where ammonia absorbs because disequilibrium chemistry decreases the amount of NH_3 and increases the amount of N_2. The locations of spectral indices used to classify T dwarfs are shown (Burgasser *et al.*, 2006; Delorme *et al.*, 2008).
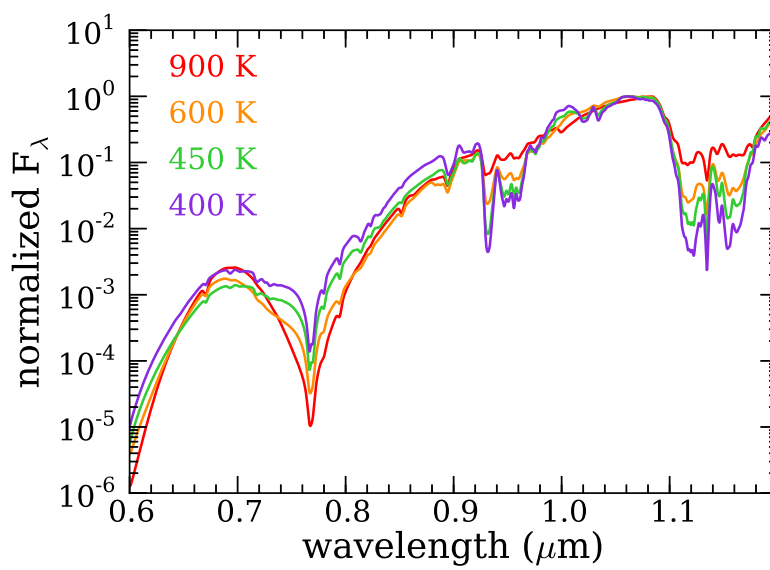
Figure 4.14: Shape of the red optical and *Y* band over the late T to Y sequence. The spectra are normalized to the same peak flux in *Y* band. The strength of the potassium feature at 0.77 μm decreases as the brown dwarf cools.
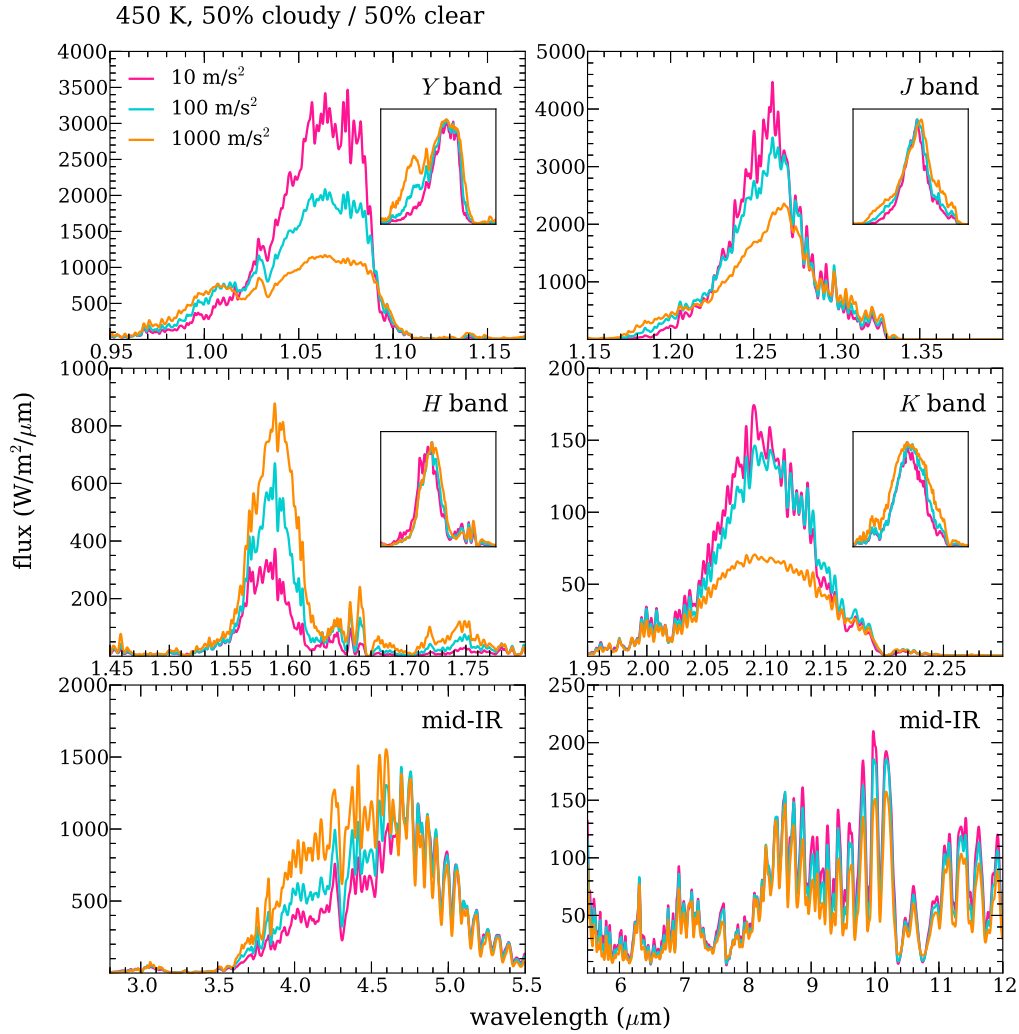
Figure 4.15: Gravity signatures in near- and mid-infrared. Each panel shows a wavelength range centered on a prominent molecular window, from top left, *Y*, *J*, *H*, *K*, 3–4.5 μm, and 6–12 μm. The inset panels for the near-IR bands show normalized version of the feature to show how the shape changes. In *Y*, *J*, and *K*, high gravity broadens the shape of the window; between 3.5–4.6 μm, the lower gravity spectra are more strongly influenced by absorption by PH_3, changing the shape of the feature.
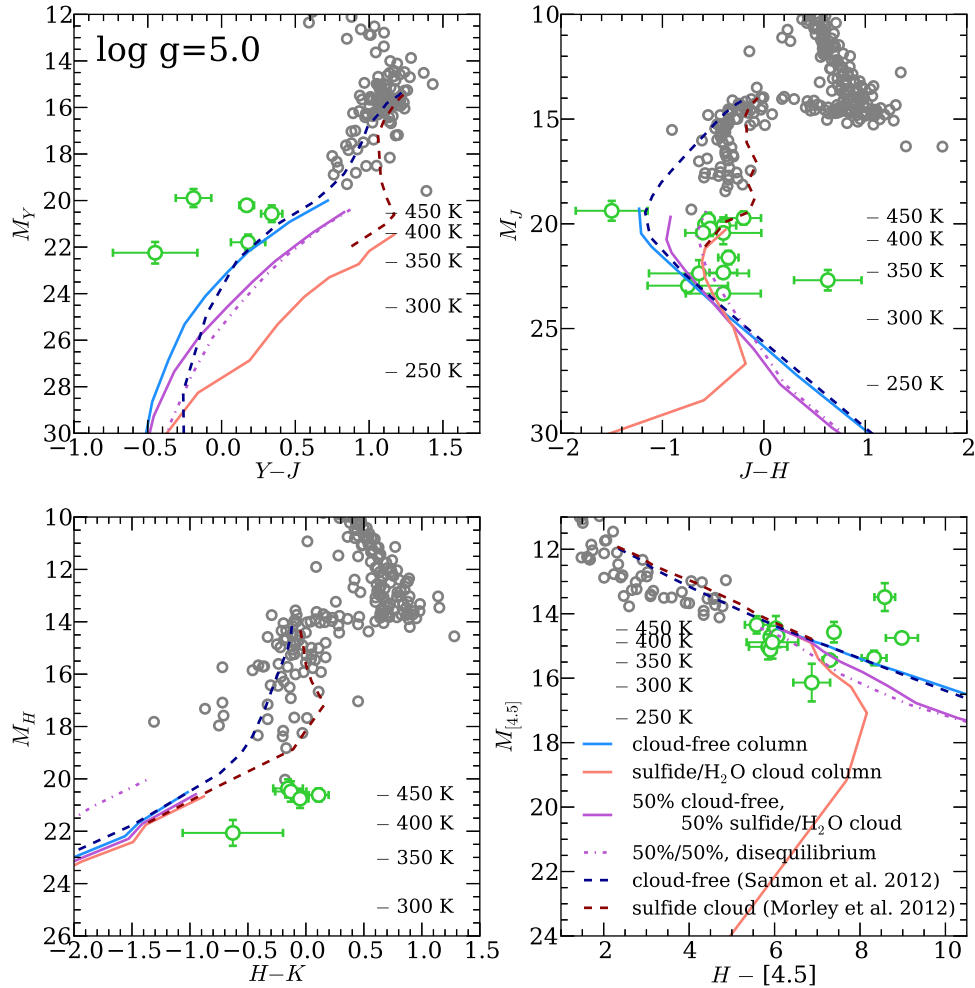
Figure 4.16: Color–magnitude diagrams at log g=5.0. L and T dwarfs are shown in gray, Y dwarfs are shown in green with error bars. Y dwarf parallax data is from Dupuy and Kraus (2013); Beichman *et al.* (2014). L and T dwarf photometry is from Dupuy and Liu (2012). The top left panel shows $Y-J$ vs. M_Y; the top right panel shows $J-H$ vs. M_J; the bottom left panel shows $H-K$ vs. M_H; the bottom right panel shows $H-[4.5]$ vs. $M_{[4.5]}$. The temperatures along the side show the magnitude at which the 50% cloud-free/50% cloudy model has that temperature (solid purple line).
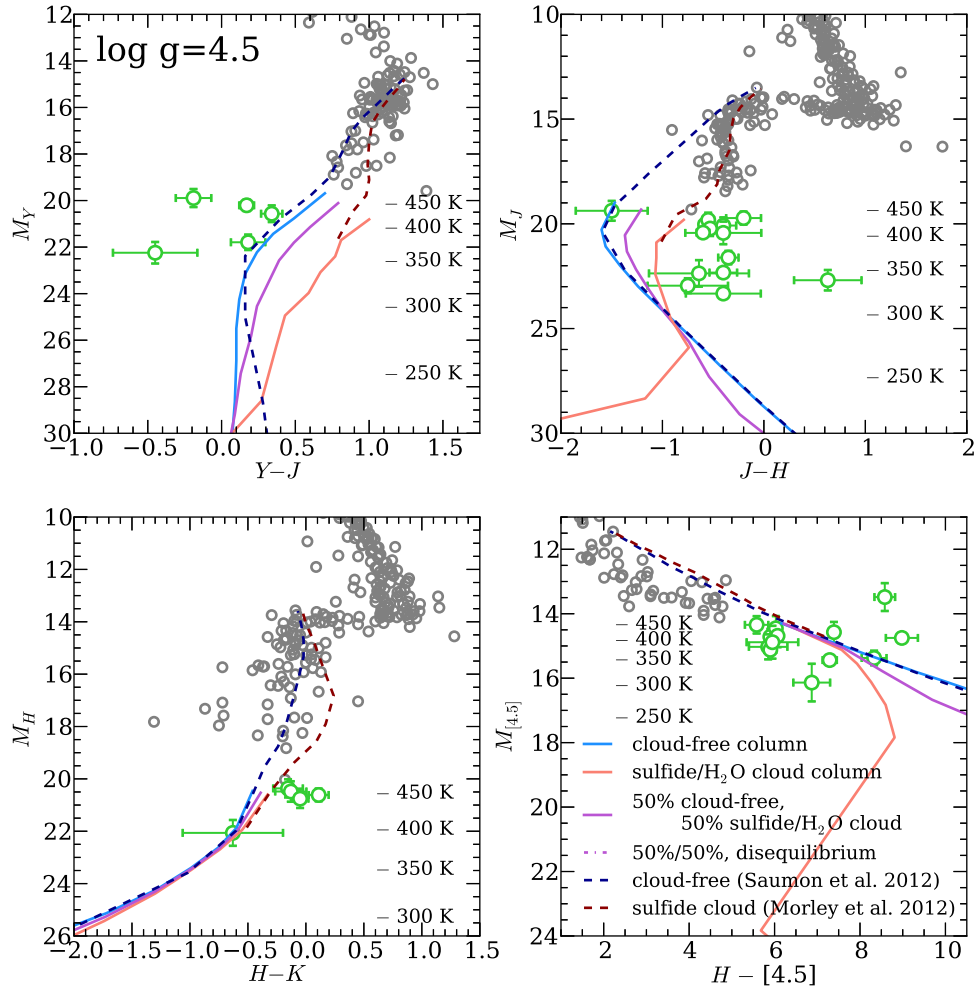
Figure 4.17: Color–magnitude diagrams at log g=4.5. L and T dwarfs are shown in gray, Y dwarfs are shown in green with error bars. Y dwarf parallax data is from Dupuy and Kraus (2013); Beichman *et al.* (2014). L and T dwarf photometry is from Dupuy and Liu (2012). The top left panel shows $Y-J$ vs. M_Y; the top right panel shows $J-H$ vs. M_J; the bottom left panel shows $H-K$ vs. M_H; the bottom right panel shows $H-[4.5]$ vs. $M_{[4.5]}$. The temperatures along the side show the magnitude at which the 50% cloud-free/50% cloudy model has that temperature (solid purple line).
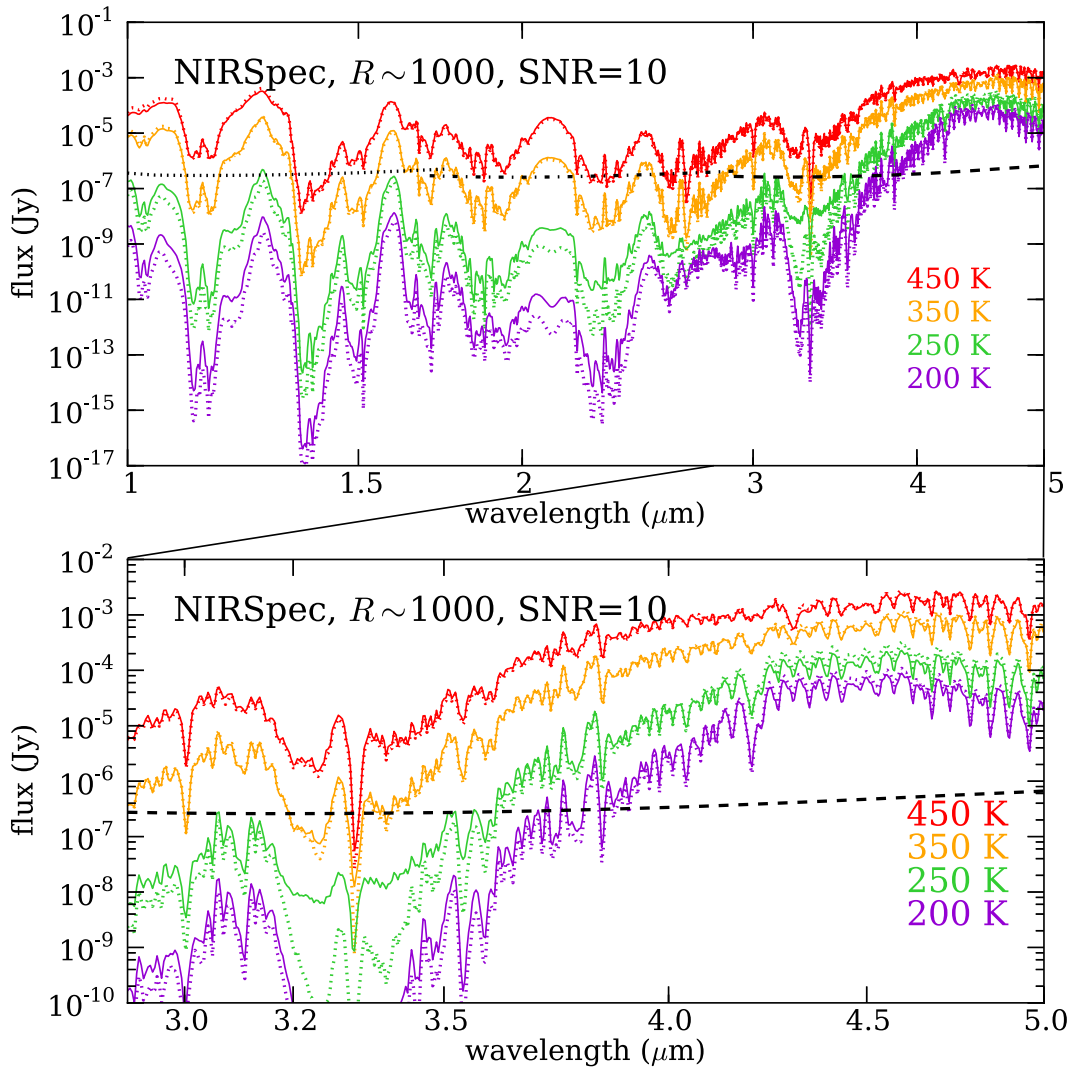
Figure 4.18: Model brown dwarf spectra with NIRSpec sensitivity limits. The brown dwarf spectra are scaled to represent objects 5 pc away from Earth and smoothed and binned to R~1000. All models have log g=4.5. Solid lines are the converged 50% cloud coverage models from this work. Dotted lines are cloud-free models with the same temperature and gravity from Saumon *et al.* (2012). The top panel shows the sensitivity limits assuming 10^5 seconds of observation time in each of the three NIRSpec channels to observe a spectrum with a SNR of 10. The bottom panel zooms into the spectral region between 2.9 and 5.0 μm.
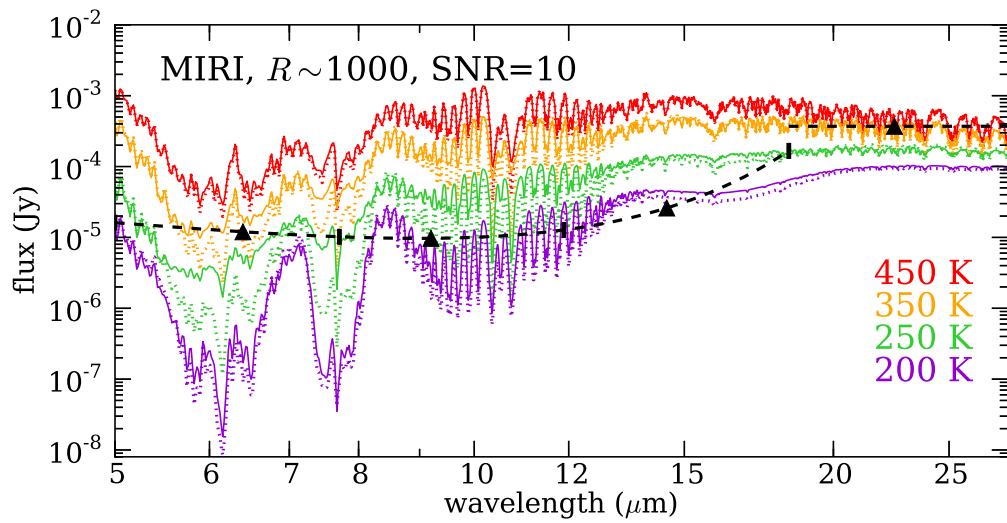
Figure 4.19: Model brown dwarf spectra with MIRI sensitivity limits. The brown dwarf spectra are scaled to represent objects 5 pc away from Earth and smoothed and binned to R~1000. All models have log g=4.5. Solid lines are the converged 50% cloud coverage models from this work. Dotted lines are cloud-free models with the same temperature and gravity from Saumon *et al.* (2012). The sensitivity limits represent 10^5 seconds of observation time in each of the four MIRI channels to observe a spectrum with a SNR of 10.
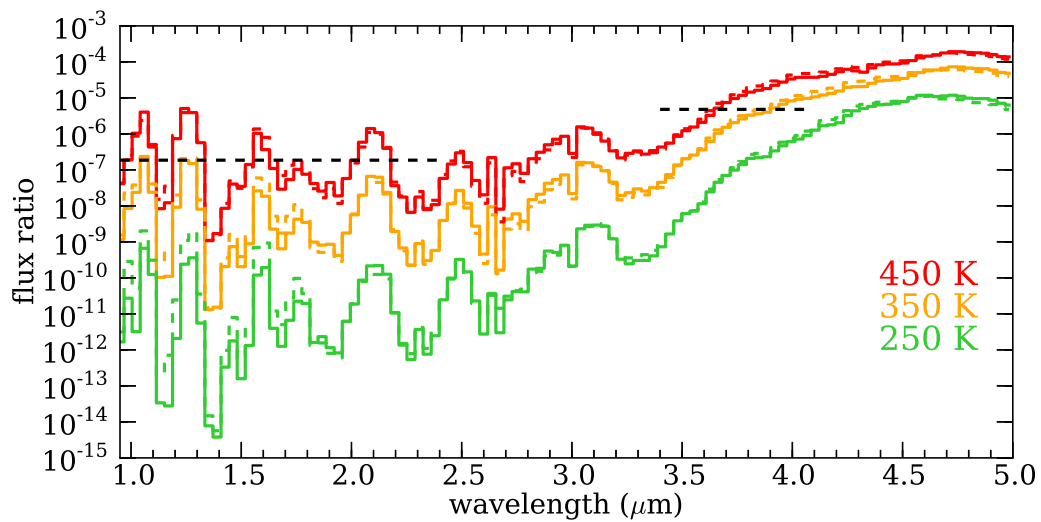
Figure 4.20: Spectra of model planets with T_{eff}=450, 350, 250 K, smoothed to $R \sim 45$ at 1.65 μm. Spectra are shown as contrast ratio to a blackbody with the temperature and radius of a G0 dwarf. The black dashed lines show expected contrast around a G0 star for GPI (near-IR) and LBTAO (mid-IR) for a moderately bright star (I=7). Solid colored lines show low gravity (log g=3.0) and dashed lines show moderate gravity (log g=4.0) for directly-imaged planets.

Chapter 5

Spectral Variability from the Patchy

Atmospheres of T and Y Dwarfs

5.1 Introduction

Brown dwarfs, the lowest-mass product of star formation, lack sustained hydrogen fusion and cool continuously, passing through the same temperature ranges as planets. Easier to observe than exoplanets, they are the first extrasolar substellar objects on which we have observed weather on other worlds, creating time-varying spectral features.

Clouds form in brown dwarfs of most spectral types; if regionally heterogeneous, they cause photometric variability as cloudier hemispheres rotate in and out of view. L dwarf clouds are dusty layers of iron and silicates (Tsuji *et al.*, 1996; Allard *et al.*, 2001; Marley *et al.*, 2002; Burrows *et al.*, 2006; Cushing *et al.*, 2008). At the L/T transition, these clouds form holes or dissipate, leaving the early T dwarfs relatively cloud-free (Ackerman and Marley, 2001;

Burgasser *et al.*, 2002; Kirkpatrick, 2005). In the mid-late T dwarfs, alkali salts and sulfides solidify, reddening late T dwarfs which are otherwise quite blue in the near-infrared (Lodders, 1999; Visscher *et al.*, 2006; Morley *et al.*, 2012).

In the coolest brown dwarfs, the Y dwarfs, volatile species condense; the first to condense is water, below effective temperatures (T_{eff}) of $\sim$400 K. Morley *et al.* (2014) presented a new grid of model atmospheres for objects from 200–450 K including water ice clouds which become optically thick in Y dwarfs cooler than 350–375 K.

5.1.1 Observed Variability in L and T Dwarfs

Early searches for ultracool dwarf variability focused on the L dwarfs and found evidence for low-amplitude variability (e.g Bailer-Jones and Mundt, 2001; Gelino *et al.*, 2002; Clarke *et al.*, 2008). A turning point in the field occurred with the discovery of high amplitude variability in the near-infrared in two L/T transition objects (Artigau *et al.*, 2009; Radigan *et al.*, 2012). Today, with a combination of higher precision ground- and space-based data, the study of variability in brown dwarfs is reaching maturity. Brown dwarfs of spectral types from L to Y have been observed to be variable using photometry (Artigau *et al.*, 2009; Radigan *et al.*, 2012; Gizis *et al.*, 2013; Biller *et al.*, 2013) or spectroscopy (Buenzli *et al.*, 2012; Apai *et al.*, 2013; Buenzli *et al.*, 2014; Burgasser *et al.*, 2014). The shape of observed light curves is not always sinusoidal and repeated observations days apart show evolution (Artigau *et al.*, 2009; Gillon *et al.*, 2013; Biller *et al.*, 2013).

Different wavelengths probe different layers of a brown dwarf; by observing spectral variability we can understand both the causes of variability and the vertical structure. For ex-

ample, Buenzli *et al.* (2012) observed phase lags between variability at different wavelengths and found a correlation between pressure probed and phase lag. The complex, evolving nature of variability suggests that many physical processes are involved.

5.1.2 Two mechanisms that cause variability

There are two classes of physical processes that would cause variability in T and Y dwarfs. One class is heterogenous opacity sources in the atmosphere, either caused by non-uniform chemical abundances or cloud cover. We will focus on the role of clouds. The second class is non-uniform temperature structure, either "hot spots" or "cold spots," and may be caused by effects of 3D circulation or radiative interaction between deeper patchy clouds and the over-lying atmosphere (Showman and Kaspi, 2013; Robinson and Marley, 2014). Here, we present models in each of these categories and make predictions for photometric and spectroscopic variability.

5.2 Variability from Patchy Clouds

If one hemisphere has a larger fraction of the surface covered by clouds than the other, as the brown dwarf rotates, the cloudier hemisphere comes in and out of view, and we observe variable brightness.

We estimate the spectral variability using 1D models that include patchy sulfide/salt and water clouds; briefly, these models follow the approach of Marley *et al.* (2010); Morley *et al.* (2014); we calculate flux separately through both a cloudy column and a cloud-free (clear)

column and sum these columns together to calculate the total emergent flux. We can change the cloud-covering fraction by varying h, the fractional area assumed to be covered in holes:

$$F_{\text{total}} = hF_{\text{clear}} + (1-h)F_{\text{cloudy}} \qquad (5.1)$$

Using this summed flux F_{total} through each atmospheric layer, we iterate to find a solution in radiative–convective equilibrium. Thus the total flux is the area-weighted sum of the flux from the clear and cloudy columns. Neither column alone carries the flux associated with the combined effective temperature.

The cloud properties for water ice and sulfide/salt clouds are presented in Morley *et al.* (2014) and Morley *et al.* (2012) respectively. The atmosphere models are presented in detail in McKay *et al.* (1989); Marley *et al.* (1996); Marley and McKay (1999b); Saumon *et al.* (2012).

5.2.1 Partly Cloudy Spectra

To calculate the pressure–temperature (P–T) structures used here, h=0.5 (50% cloudy). However, both hemispheres do not necessarily have the same cloud-covering fraction. When the clouds/holes are distributed non-uniformly, variability will be observed; the hemisphere with more holes is brighter and has a higher apparent T_{eff}. The amplitude of variability is calculated by summing the flux through the clear and cloudy columns in different proportions which must sum to a net cloud-cover of 50% to match the P–T profile.

One strength of this method is that using a single, global P–T profile isolates the effect

of the cloud opacity. Furthermore, the entropy deep within the atmosphere's convective zone must meet the interior entropy; a given pressure should be horizontally uniform in temperature. Our method captures that fact, instead of modeling cloudy and clear regions with the same T_{eff} but very different internal entropy. This approach implicitly assumes that the columns are interacting with each other dynamically, an assumption that breaks down for very large, hemispheric patches.

Example spectra from T_{eff}=1000 to 200 K are shown in Figure 5.1. The black lines show the flux emitted from a 30% cloudy hemisphere; the colored lines show flux emitted from a 70% cloudy hemisphere. Less flux emerges through the cloudier hemisphere because clouds increase the total opacity.

The flux ratio between hemispheres is shown in the bottom panels of Figure 5.1; the flux ratio shows quantitatively the predicted spectral variability. The highest amplitude is within spectral windows, between the major molecular opacity sources in the atmosphere. For T_{eff}=700–1000 K models, the strongest variability is in Y, J and H bands with lower-amplitude variability in K band, between 3.6 and 5 μm, and within the water absorption features.

In the 400 K model, the variability is largest in Y and J bands with lower level variability at other wavelengths. Flux at longer wavelengths emerges from higher altitudes than the sulfide and salt clouds, so cloud opacity alone does not change the spectra.

The predicted variability at T_{eff}=200 K looks fundamentally different from the warmer models; this is because by 200 K, the water cloud is thick and dominates the cloud opacity. The flux ratio is nearly uniform from 0.7 to 5.5 μm, with dips within the major methane absorption features at 2.3 and 3.3 μm. At this temperature range, significant hemispheric differences in

cloud cover cause large amplitude variability at most wavelengths.

5.2.2 Partly Cloudy Color–Magnitude Diagrams

Model photometry for the partly cloudy models are calculated using radii from the cloud-free Saumon and Marley (2008) evolution models. The photometry is calculated for the 50% cloudy converged models and the cloudy and clear columns of each model separately. Two sample color–magnitude diagrams (CMDs) are shown in Figure 5.2. The clear, 50% cloudy, and fully cloudy photometry are shown as large, medium, and small dots connected with a line.

A near-infrared CMD ($J-H$ vs. M_J) is shown in the top panel of Figure 5.2. If variability in T and Y dwarfs were due solely to heterogenous clouds, the brown dwarf would move from the center dot along the line that connects the column photometry. For brown dwarfs with $T_{\text{eff}}>300$ K, the object would become redder and somewhat fainter as the cloudier side rotates into view; the sulfide/salt clouds that dominate have the largest impact on J (and Y) bands. The impact of the sulfide/salt clouds peaks at $T_{\text{eff}}=500$–600 K.

For brown dwarfs below $T_{\text{eff}}\sim 300$ K, increasing the cloud covering fraction tends to make the brown dwarf bluer in $J-H$. This new behavior is because those objects have thick water ice clouds, which are extremely nongray absorbers. Water ice particles predominantly scatter in J band, but absorb more strongly in H band and longer wavelengths (see Morley *et al.* (2014)). The water clouds become extremely thick for 200–250 K objects, causing almost all the flux emerging from those objects to emerge through the clear column of the atmosphere; the cloudy point on the CMD becomes extremely blue and faint.

Likewise, in the mid-infrared CMD ([3.6]–[4.5] vs. $M_{[4.5]}$) shown in the bottom

panel of Figure 5.2, the models separate into two groups. In objects with $T_{\text{eff}} \geq 400$ K, sulfide/salt clouds dominate. However, the sulfide/salt clouds minimally affect the mid-infrared wavelengths (see also Figure 5.1) so $M_{[4.5]}$ and $M_{[3.6]}$ stay nearly constant. Changes in cloud opacity do not cause significant variability in the mid-late T dwarfs in *Spitzer* observations. In contrast, for models with $T_{\text{eff}} < 400$ K, water clouds start to have appreciable optical depth in the mid-infrared where they absorb strongly. The cloudy column becomes fainter in [4.5] and somewhat bluer in [3.6]−[4.5].

5.3 Variability from Hot Spots

Clouds are not the only likely driver of variability; atmospheric dynamics may drive perturbations to the temperature structures. Dynamical effects may create rising and sinking parcels of air on timescales faster than the parcel can equilibrate, causing cold or hot regions. The upper atmosphere may react radiatively to changes in the deep atmosphere, such as heterogenous cloud opacity or dynamically driven perturbations. Robinson and Marley (2014) show that temperature perturbations at ∼10 bar can be communicated to the overlying parts of the atmosphere through radiative heating, potentially generating complex time-dependent behaviors, including phase shifts.

We incorporate heterogeneous temperature profiles by adding energy at specified pressure levels of static cloud-free model atmospheres from 400–1000 K as we calculate the P–T structure in radiative–convective equilibrium. The perturbations have the shape of a Chapman function, which is often used to represent heating by incident flux within molecular bands

(e.g. Chamberlain and Hunten, 1987; Marley *et al.*, 1999). This provides a reasonable approximation of energy added by, e.g., heating from thermal flux from below through holes in the clouds. We use a Chapman function with a width of a single pressure scale height and amplitude to give total emergent flux $F_{new} = 1.5 F_{baseline}$. We inject energy at pressure levels from 0.1–30 bar. The *P–T* profiles of the warmest and coldest model in the grid (T_{eff}=400 and 1000 K) are shown in the top left panel of Figure 5.3; the location of the heating function is shown in the right panel. The bottom panel of Figure 5.3 shows the location of the $\tau = 2/3$ pressure level as a function of wavelength; the colored bands indicate the perturbed pressure levels shown in the top panel.

5.3.1 Hot Spot Spectra

Representative spectra of models with perturbed *P–T* profiles are shown in Figure 5.4 from T_{eff}=400–1000 K; for each perturbed model, 5% of the surface is assumed to be covered by the hot spot.

The flux ratios look quite different from those due to patchy clouds in Figure 5.1. For these models, the greatest flux ratio is within absorption features instead of within spectral windows. Especially prominent is the methane feature at 3.3 μm.

The spectral dependence of variability is controlled by the layer at which the *P–T* profile is perturbed. Heating high in the atmosphere increases flux emerging from higher altitudes, in the mid-infrared. Heating deep within the atmosphere increases flux more uniformly. By observing variability across many wavelengths, we can distinguish between patchy cloud variability and heating at different levels of the atmosphere.

5.3.2 Hot Spot Color–Magnitude Diagrams

Near- and mid-infrared CMDs for the models with hot spots are shown in Figure 5.5. In the top panel ($J-H$ vs. M_J), heating high in the atmosphere causes a minimal color and brightness change. The greatest color change occurs when we heat the near-infrared photosphere, around 3–10 bar. Deep heating leads to less chromatic changes.

In the bottom panel ([3.6]–[4.5] vs. $M_{[4.5]}$), heating high in the atmosphere causes a very chromatic change, due to significant brightening within the methane band captured in the [3.6] filter. Deeper heating causes less dramatic brightening in both *Spitzer* filters.

5.4 Discussion

5.4.1 Simultaneous multi-wavelength observations

This study suggests that the most illustrative types of observations for understanding the physical processes underlying brown dwarf variability are simultaneous, multi-wavelength observations that probe both inside and outside of molecular absorption features. These measurements are best done from space to avoid the strong molecular absorption of water vapor in Earth's atmosphere.

Several objects have been observed in such a way to date. Two L/T transition objects, 2M2139 and SIMP0136, were observed using the *Hubble Space Telescope* from 1.1–1.7 μm, which probes J and H bands and the water features surrounding those windows. The spectral dependence of the variability observed looks qualitatively similar to the top panel of Figure 5.1, in which the variability within the spectral windows is larger than the variability within the

absorption features. Buenzli *et al.* (2012) present observations of 2MASS J22282889–431026 from partially simultaneous *HST* and *Spitzer* Space Telescope observations. In that object, there are hints that there is larger variability within absorption features: the largest amplitude variability (5.3±0.6%) is measured in the 1.35–1.43 μm range. However the other absorption features show similar amplitude variability ($\sim$2%) as the spectral windows.

5.4.2 Time and length scales for atmospheric heterogeneity

A number of physical timescales compete in T and Y dwarf atmospheres. The radiative time constant

$$\tau_{\mathrm{rad}} \sim \frac{P}{g} \frac{c_P}{4\sigma T^3} \tag{5.2}$$

describes the relaxation timescale towards radiative equilibrium following a temperature perturbation (Goody and Yung, 1989; Fortney *et al.*, 2008a). In mid T photospheres, $\tau_{\mathrm{rad}} \sim$1–10 hours, increasing to $\tau_{\mathrm{rad}} \sim$100 hours for Y dwarf photospheres. The timescale for mixing in convective regions can be approximated using mixing length theory; the mixing timescale is 1–2 orders of magnitude faster than τ_{rad}. The timescale for mixing in radiative regions is more uncertain and controlled by the interaction of the stable upper atmosphere with the turbulent convective zone, which generates a wide spectrum of atmospheric waves including gravity waves and Rossby waves (Freytag *et al.*, 2010; Showman and Kaspi, 2013). Analytical estimations in Showman and Kaspi (2013) suggest that typical timescales for parcels of air to rise or fall one scale height are tens to hundreds of hours. The timescale for radiative relaxation and vertical advection are comparable, creating a complex interplay between atmospheric dynamics and radiative feed-

back. In addition, the condensation timescale for $\sim$5 μm Na_2S particles (Carlson *et al.*, 1988, equation 1) is of the same order of magnitude. Cool brown dwarfs likely have heterogeneous atmospheres in which rising and falling parcels of air move vapor which condenses on comparable timescales to both the motion and radiative cooling.

It is challenging to estimate the spatial scales of these heterogeneities from models without better understanding the horizontal wind speeds of brown dwarfs. The sizes of jets in the solar system giant planets generally scale with the Rhines scale, $L_{Rh} \sim (U/2\Omega R\cos\phi)^{1/2}$ where U is wind speed, R is the radius, Ω is $2\pi/P$, P is the rotation period, and ϕ is the latitude (Rhines, 1970; Showman *et al.*, 2008). Showman and Kaspi (2013) estimate a typical brown dwarf Rhines scale to be 10,000–20,000 km, or roughly 5-10% of a hemisphere, with typical temperature perturbations on isobars of 5–50 K, even ignoring the effect of heterogeneous clouds. Cloud opacity may increase the apparent T_{bright} differences. For example, the 5 μm hot spots on Jupiter are observed to have a $\sim$50 K difference in T_{bright} due to non-uniform cloud and gas opacity (Carlson *et al.*, 1992).

5.4.3   Role of high resolution spectral mapping

High resolution Doppler spectral mapping has been used by Crossfield *et al.* (2014) to create a brightness map of the surface of the nearby brown dwarf Luhman 16B. Such techniques are currently limited to the brightest brown dwarfs. Although powerful, these techniques probe limited wavelength ranges and thus a limited pressure level in the atmosphere; the generated map is a map only of that particular level. In addition, they are most sensitive to a single molecule (e.g. CO), which means that abundance variations could also cause the observed

brightness map. This technique is most powerful when combined with the simultaneous multi-wavelength observations that probe a much larger part of the brown dwarf atmosphere and are affected by a number of absorbing species.

5.4.4   Giant Planets: Effect of gravity on variability

Further study is necessary to understand the effect of gravity on spectroscopic variability. There is evidence that warm planet-mass objects of a given temperature have thicker clouds than higher mass brown dwarfs (Currie *et al.*, 2011; Barman *et al.*, 2011b; Madhusudhan *et al.*, 2011a; Liu *et al.*, 2013). Marley *et al.* (2012) suggest that the apparent thickness naturally emerges as a result of low gravity and that the process that may break up clouds at the L/T transition may be gravity-dependent, causing lower-gravity objects to become mostly clear T dwarf-like objects at lower T_{eff}. The interplay of gravity, T_{eff}, and atmospheric dynamics is currently not well-understood. Observations of variability in planets or low-gravity brown dwarfs and comparisons with higher mass brown dwarfs could shed light on these physical processes. Kostov and Apai (2013) conclude that 1% amplitude photometric variability will be detectable with next-generation AO systemics such as the Gemini Planet Imager, while the James Webb Space Telescope and 30-meter class telescopes will provide spectral mapping data. Snellen *et al.* (2014) suggest that using 30-m class telescopes, high-resolution Doppler mapping will be possible for the brightest directly imaged planets such as beta Pictoris b.

5.5 Summary

We present models of brown dwarfs that include two drivers of spectroscopic variability: patchy clouds and hot spots. We find that the two mechanisms have different spectral dependence, with patchy clouds driving the highest amplitude variability within spectral windows and hot spots driving larger variability within absorption features.

From patchy sulfide and salt clouds in objects over 300 K, the largest amplitude variability is within near-infrared opacity windows; objects become redder in near-infrared colors (e.g. $J - H$) as the cloudy side rotates into view. Variability in the mid-infrared would be significantly smaller. In objects below 375 K, water clouds are important and affect the spectrum strongly in the mid-infrared, especially within the 4.5 μm window. Water clouds cause a blueward shift in the near-infrared ($J - H$) as the cloudier side rotates into view because water clouds do not absorb as strongly in J as they do in H or K.

From heating in the atmosphere at different pressure levels, the spectrum changes predominantly within the absorption features. The highest amplitude variability occurs at the wavelengths that probe the pressure levels where the perturbation is centered. For example, the methane feature at 3.3 μm probes high in the atmosphere; heating at high altitudes ($\sim$0.1 bar) causes the highest amplitude variability within that feature. Heating deeper within the atmosphere warms the whole atmosphere more uniformly and causes the brown dwarf to look like a warmer object.

By analyzing simultaneous multi-wavelength spectral variability, we can disentangle the physical processes causing brown dwarf variability. By observing these processes over

long time periods for a larger sample of objects, we can study atmospheric dynamics and the

evolution of weather on substellar extrasolar objects.
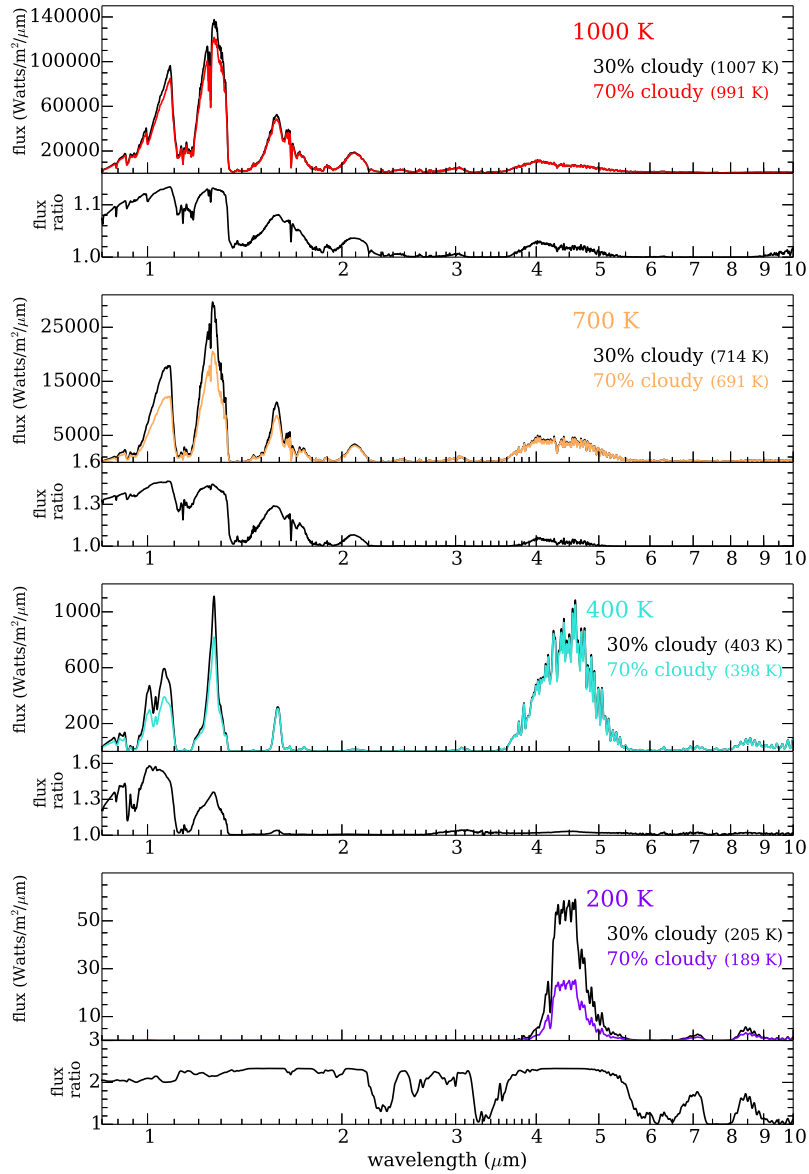
Figure 5.1: Spectra of partly cloudy models from T_{eff}=1000 K to 200 K. Each pair of panels shows a different summed T_{eff}. Spectra for each T_{eff} are calculated using a single 50% cloudy model with the cloud parameter f_{sed}=5 in radiative–convective equilibrium. The spectra represent two heterogeneous hemispheres of a 50% cloudy brown dwarf. Apparent T_{eff} of each hemisphere is shown in parentheses. The flux ratio (the ratio of the plotted spectra) is shown in the bottom panel of each pair.
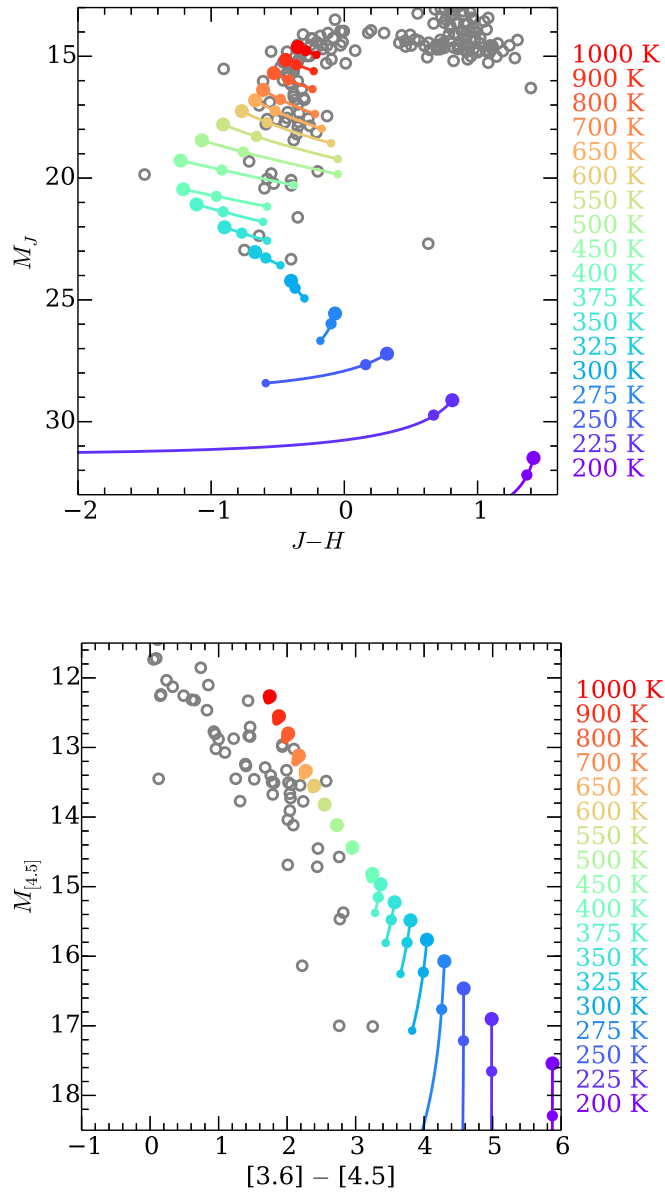
Figure 5.2: Color–magnitude diagrams for partly cloudy models. The center medium-sized dot represents the 50% cloudy model in radiative–convective equilibrium. The connected large and small dots show the photometry of the clear and cloudy columns respectively. The T_{eff} corresponding to each color is shown on the right of each panel. The observed brown dwarfs with distance measurements are shows as gray open circles (Dupuy and Liu, 2012). The top panel shows $J-H$ vs. M_J; the bottom panel shows $[3.6]-[4.5]$ vs. $M_{[4.5]}$.
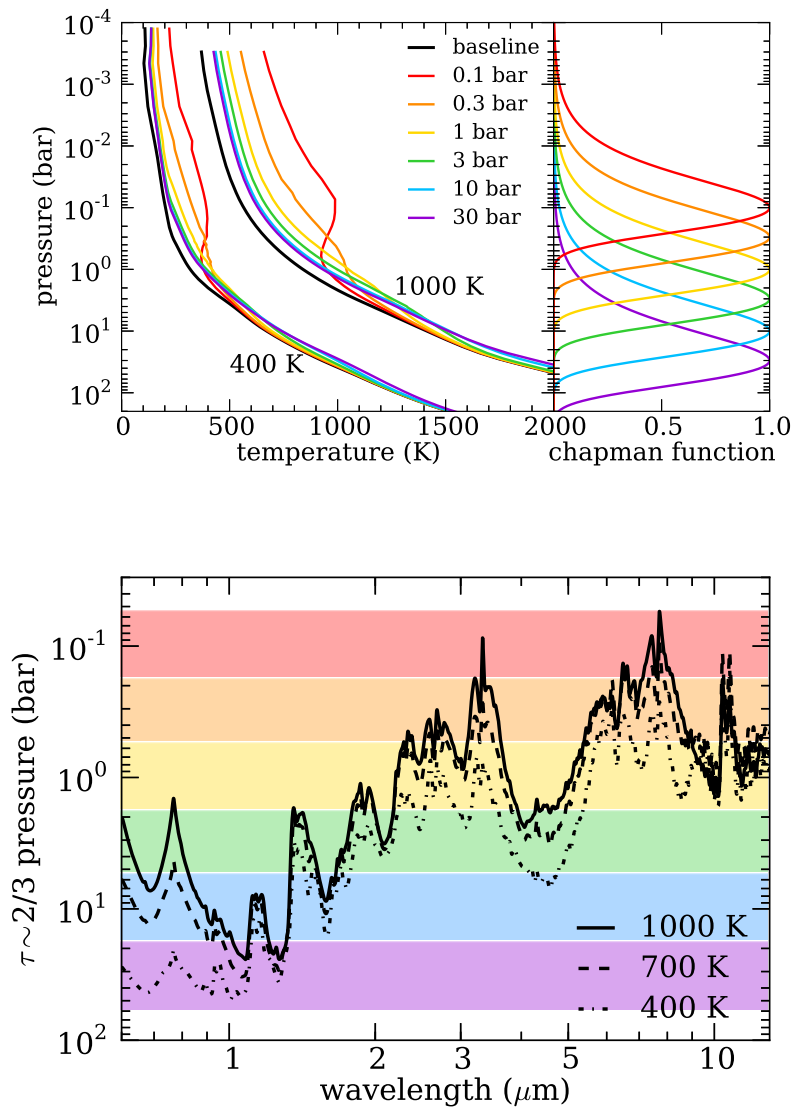
Figure 5.3: Top panel: Perturbed and unpeturbed pressure–temperature profiles (left) and heating functions (right). The baseline models at $T_{\rm eff}$=400 and 1000 K are shown in black. The colored lines show models with P–T profiles calculated including an additional energy source with the shape of the heating function in the right panel. Bottom panel: the 'pressure spectrum' of models with $T_{\rm eff}$=1000, 700, and 400 K. The colored bars show the same pressure levels as the top panel, at which the perturbations to the profiles are centered. The black lines show the approximate location of the $\tau = 2/3$ pressure level as a function of wavelength for the unperturbed models.
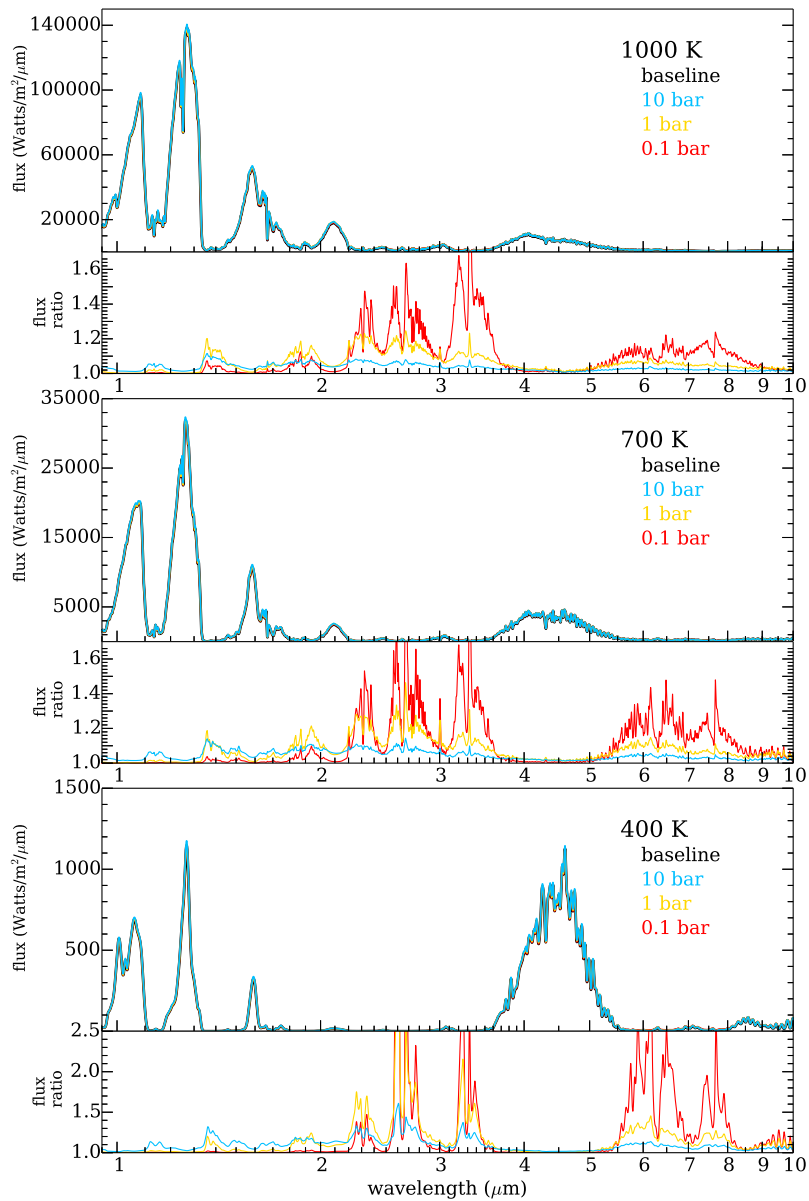
Figure 5.4: Spectra of models with heated *P–T* profiles from baseline T_{eff}=1000 K to 400 K. Each pair of panels shows a different T_{eff}. The baseline model is shown as a black line. The red, gold, and blue lines show models with 5% of the surface covered in a hot spot, with heating at 0.1, 1, and 10 bar, respectively. The flux ratio (the ratio of the heated model divided by the baseline model) is shown in the bottom panel of each pair.
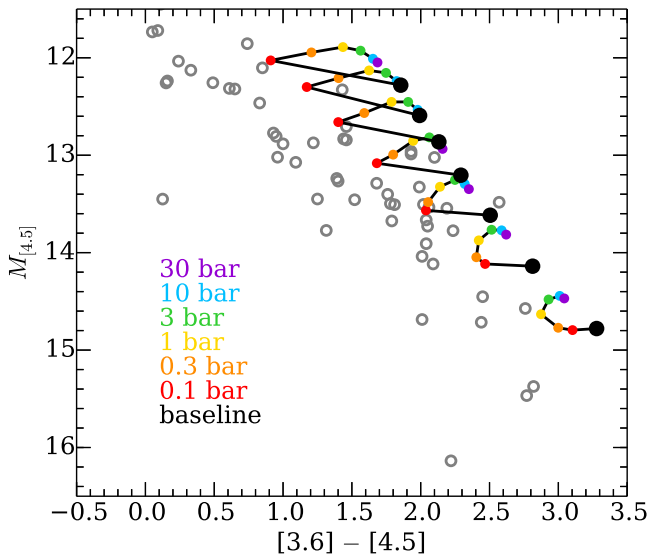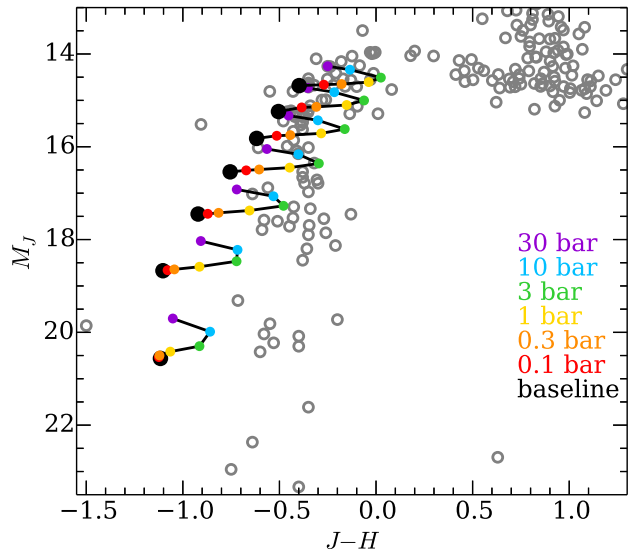
Figure 5.5: Color–magnitude diagrams for models with perturbed *P–T* profiles. The larger black point shows the photometric point of the 'baseline' model for T_{eff}=400–1000 K (in 100 K increments). The colored points show photometry for *P–T* profiles with added energy at each of the specified pressure levels. The observed brown dwarfs with distance measurements are shows as gray open circles (Dupuy and Liu, 2012). The top panel shows $J-H$ vs. M_J; the bottom panel shows [3.6]–[4.5] vs. $M_{[4.5]}$.

198

Chapter 6

Thermal Emission and Albedo Spectra of Super Earths with Flat Transmission Spectra

6.1 Introduction

Since its launch in 2008, the *Kepler* mission has revealed a population of planets with radii between that of Earth and Neptune, which make up a substantial fraction of the planets in the galaxy (Borucki *et al.*, 2011; Howard *et al.*, 2012). No planet of that size exists in our own solar system as an archetype for these "super Earths."[1] This population likely has a range of compositions from rocky, to water-rich, to gas-rich (Rogers, 2015; Wolfgang and Lopez, 2015), but we have not yet probed their compositions directly. A critical part of the puzzle to understand the nature of super Earths is to measure the abundances of molecules in their atmospheres.

---

[1] We use the term 'super Earth' here to mean planets larger than Earth and smaller than Neptune, but recognize these planets are diverse in their compositions and many may be more accurately considered 'sub Neptunes.'

One powerful tool that has been used to probe the atmospheres of transiting planets is transmission spectroscopy. During a transit, the transit depth is measured simultaneously at multiple wavelengths. At wavelengths of strong absorption features, the planet's atmosphere will become optically thick at a higher altitude and we will observe a deeper transit; at wavelengths outside these absorption features, the planet's atmosphere is optically thinner and the transit depth is shallower. The depth of the features we observe in a cloud-free atmosphere scales linearly with the pressure scale height H (Seager and Sasselov, 2000; Hubbard $et\ al.$, 2001). The scale height is defined as $H = kT/\mu g$, where k is Boltzmann's constant, T is temperature, g is gravity, and μ is the mean molecular weight. In the absence of clouds, low gravity, low density targets have the largest amplitude features and many have been targeted for characterization.

By measuring the amplitude of features in a planet's transmission spectrum we can both probe the composition of absorbers like sodium, potassium, methane, water, and carbon monoxide and also measure the bulk composition of the atmosphere by measuring the mean molecular weight. If the observed mean molecular weight is low ($\mu \sim 2.3$) the planet is H/He-rich like a scaled down Neptune; if it is high, it may be water, nitrogen, or carbon dioxide rich, more akin to a terrestrial planet (Miller-Ricci $et\ al.$, 2009).

6.1.1   Observations of Super Earths

Hundreds of orbits of Hubble Space Telescope (HST) time have been dedicated to characterizing these small planets, as well as hundreds of hours of ground-based observations. Despite this dedication of resources, super Earths and sub-Neptunes have proved extremely

challenging to characterize with this technique because their features are more muted than predicted using cloud-free models.

By far the most-studied super Earth to date is GJ 1214b, the first planet discovered by the MEarth survey (Charbonneau *et al.*, 2009). GJ 1214b is a 6.16 $\pm 0.91 M_\oplus$ and 2.71$\pm$0.24$R_\oplus$ planet, and, critically, orbits a fairly bright mid M dwarf (M4.5). Its transit depth of over 1% and a short orbital period of 38 hours make it an ideal target for high signal-to-noise followup observations.

Early observations from both ground and space were inconclusive: they showed no features, but were not sensitive enough to detect the small features predicted for a high mean molecular weight atmosphere (Bean *et al.*, 2010; Désert *et al.*, 2011; Crossfield *et al.*, 2011; Croll *et al.*, 2011; Berta *et al.*, 2012; de Mooij *et al.*, 2012; Murgas *et al.*, 2012; Teske *et al.*, 2013; Fraine *et al.*, 2013). In 2014, Kreidberg *et al.* (2014a) measured 15 additional transits of GJ 1214b with *HST* Wide Field Camera 3 (WFC3) grism spectroscopy (1.1–1.7 μm) and detected, at high signal to noise, a featureless transmission spectrum. Unlike the previous observations, these observations were sensitive enough to detect features in a high mean molecular weight atmosphere. They concluded that the predicted molecular features are obscured by a high altitude cloud or haze layer.

Other planets close to GJ 1214b's size have also been observed with this technique, with somewhat lower signal-to-noise than the Kreidberg *et al.* (2014a) observations. Knutson *et al.* (2014b) present observations of the super Earth HD 97658b and show that its spectrum is consistent with a flat line. Likewise, the Neptune-sized GJ 436b and GJ 3470b also have featureless spectra measured with WFC3 within their measurement uncertainties (Knutson *et al.*,

2014a; Ehrenreich *et al.*, 2014). In fact, the only planet in the super-Earth to Neptune mass range with a statistically significant spectral feature is HAT-P-11b; water vapor absorption was detected using WFC3 with an amplitude of 250 parts per million (Fraine *et al.*, 2014). This measurement is consistent with a metal-enhanced H/He dominated atmosphere with a several hundred times solar metallicity composition or a less enriched atmosphere with features muted by clouds or hazes.

The observing efforts to date have revealed that small, cool planets have relatively featureless transmission spectra. If features are muted in the transmission spectra of all small planets, it will be extremely challenging to characterize their compositions using transmission spectroscopy.

6.1.2 Understanding Super Earths Despite the Clouds

While these featureless near-infrared transmission spectra are informative—they inform us that there is an optically thick, gray absorber in the measured wavelength range—they do not allow us to measure the composition of the atmosphere. To understand the compositions of super Earths—perhaps the most abundant planets in the galaxy—we need to probe their atmospheres with other techniques. A number of pathways will help to accomplish this goal, including transmission spectra of hotter targets, thermal emission spectra, and reflected light spectra.

In this paper, we use models of super Earths to understand how we can characterize super Earths as a class. We move beyond modeling GJ 1214b itself and run models of its cousins, with the same gravity and host star but different incident flux. Cloud and haze forma-

tion depends strongly on incident flux (and resulting equilibrium temperature) so spanning a range of irradiation levels allows us to make predictions about a diverse set of planets.

We quantify properties of clouds or hazes thick enough to flatten transmission spectra at the signal-to-noise of the Kreidberg *et al.* (2014a) observations for a variety of different incident flux levels. Using these cloud properties, we generate both thermal emission spectra and reflected light spectra. With the upcoming *JWST* mission, thermal emission of selected super Earths will be observable over a wide wavelength range (Gardner *et al.*, 2006); we show how optically thick clouds and hazes will shape that thermal emission. In the more distant future, missions to detect reflected light from exoplanets using a space-based coronagraph are being planned (Spergel *et al.*, 2015). We show that reflected light spectra will be a promising technique to understand very cloudy super Earths, especially for colder objects.

6.1.3   Format of this Paper

In Section 6.2, we describe the extensive set of modeling tools used to model the effects of clouds and hazes on super Earth spectra. In Section 6.3, transmission, emission, and reflection spectra for planets with equilibrium clouds (both salt/sulfide in warm planets and water ice in cold planets) are presented. In Section 6.4, transmission, emission, and reflection spectra for planets with photochemical hazes are presented. In Section 6.5, we discuss implications of this work for future studies and in Section 6.6 we conclude. The Appendix discusses the new, flexible radiative transfer tool developed for this work.

6.2 Methods

In order to predict spectra of small planets with clouds and hazes, we use a comprehensive suite of atmosphere modeling tools. We use a 1D radiative–convective model to calculate the pressure–temperature structure, a photochemical model to calculate the formation of soot precursors (hydrocarbons that may form hazes), and a cloud model to calculate cloud altitudes, mixing ratios, and particle sizes. We then calculate spectra in different geometries and wavelengths using a transmission spectrum model, a thermal emission spectrum model, and an albedo model. In the following subsections we discuss each of these calculations.

We run a grid of radiative-convective models of GJ 1214b analogs (g=7.65 m/s^2, M4.5 host star). We vary the distance from the host star to encapsulate a range of super Earths from temperatures of 190–1400 K (0.01–30× GJ 1214b's incident flux). In one set of models, we include "equilibrium clouds". These, in this work, are considered to be clouds that form when the pressure of a condensible gas exceeds the saturation vapor pressure; we assume that all material in excess of the saturation vapor pressure condenses into cloud material. For these objects, the clouds include water ice (for the coldest models), and salts and sulfides (for the warmer models). In the other set of models, we include a photochemical haze using a photochemical model.

Given the number steps involved for each set of models, we will first outline the modeling process performed for every set of parameters. We follow a slightly different set of steps for the equilibrium clouds and the photochemical hazes.

Equilibrium clouds

1. Generate a cloud-free pressure–temperature (P–T) profile at high metallicity (100–1000×

solar metallicity) using a modified 1D radiative–convective model

2. Using that P–T profile (1), calculate cloud locations, particle sizes, and optical properties using a stand-alone version of the Ackerman and Marley (2001) cloud code

3. Using that P–T profile (1), calculate the equilibrium chemistry along the profile using Chemical Equilibrium with Applications (CEA).

4. Using the P–T profile, cloud output, and equilibrium chemistry (1,2,3), calculate the model transmission spectrum and compare it to the flat (Kreidberg *et al.*, 2014a) spectrum of GJ 1214b.

5. Using the P–T profile, cloud output, and equilibrium chemistry (1,2,3), calculate the thermal emission spectrum

6. Using the P–T profile, cloud output, and equilibrium chemistry (1,2,3), calculate the reflected light spectrum

Photochemical hazes

1. Using a pre-computed pressure–temperature profile, calculate the disequilibrium chemistry caused by vertical mixing and photochemistry

2. Using the abundances and locations of soot precursors from (1), calculate a pressure–temperature profile consistent with haze using a 1D radiative–convective atmosphere model

3. Using the P–T profile and haze properties (2), calculate the model transmission spectrum and compare to the flat (Kreidberg *et al.*, 2014a) spectrum of GJ 1214b.

4. Using the P–T profile and haze properties (2), calculate the thermal emission spectrum

5. Using the P–T profile and haze properties (2), calculate the reflected light spectrum

6.2.1 1D Radiative–Convective Model

For objects with and without clouds, we calculate their temperature structures assuming 1D atmospheres in radiative–convective equilibrium. Our approach has been successfully applied to objects ranging in size from moons to brown dwarfs; the models are described in McKay *et al.* (1989); Marley *et al.* (1996); Burrows *et al.* (1997); Marley and McKay (1999b); Marley *et al.* (2002); Fortney *et al.* (2005); Saumon and Marley (2008); Fortney *et al.* (2008b).

We use the radiative transfer techniques described in Toon *et al.* (1989) and use Mie theory to calculate the absorption and scattering of cloud particles in each layer of the atmosphere. The opacity database for gases is described extensively in Freedman *et al.* (2008). In this work, the opacity database includes two significant updates since Freedman *et al.* (2008), which are described in Saumon *et al.* (2012): a new molecular line list for ammonia (Yurchenko *et al.*, 2011) and an improved treatment of collision induced H_2 absorption (Richard *et al.*, 2012). Optical properties for salts and sulfides are as described in Morley *et al.* (2012); for ZnS and KCl they are obtained from Querry (1987) and for Na_2S we combine laboratory and numerical measurements from Montaner *et al.* (1979) and Khachai *et al.* (2009).

The opacities, using the k-coefficient technique for computational speed and accuracy, are pre-calculated and pre-summed at multiples of solar metallicity ranging from [M/H]=0.0 to 1.7 (1–50× solar), but super Earths potentially have much higher metallicity atmospheres (see Fortney *et al.* (2013) and discussion in Section 6.5.1). Higher metallicity opacities have not been calculated, so in order to calculate the temperature structures at higher metallicities (100-1000×
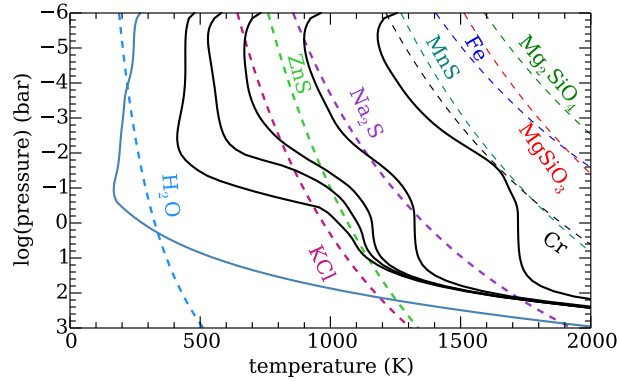
Figure 6.1: Pressure–temperature profiles of models at 300× solar metallicity with cloud condensation curves. P–T profiles are shown as solid curves; black indicates models with salt/sulfide clouds and blue indicates models with water ice clouds. From left to right, these profiles are at 0.01, 0.3, 1, 3, 10, and 30 × GJ 1214b's incident flux. Condensation curves are shown as dashed lines for individual cloud species; a cloud forms where the P–T profile crosses the condensation curve.

solar), we approximate the gas opacity by multiplying the [M/H]=1.7 pre-summed opacities by the appropriate factor. For example, for 300× solar metallicity, we multiply the 50× solar summed molecular gas opacities by 6. We decrease the abundance of hydrogen and helium by the same proportion and calculate the collision induced absorption separately from the other molecular gas opacities. This approximation is appropriate for the qualitative results explored here; for future work, e.g. comparing models to data, new k-coefficients at 100–1000× solar metallicity should be used.

Examples of calculated P–T profiles are shown in Figure 6.1, for models from 0.01 to 30× GJ 1214b's incident flux.

6.2.2 Equilibrium Chemistry

After we calculate the pressure–temperature profiles of models with greater than $50\times$ solar metallicity, we calculate the composition, assuming chemical equilibrium, along that profile. To be clear, this isn't strictly self-consistent. However, tests run using $10\times$ solar and $50\times$ solar compositions—both of which we calculate self-consistently with the chemistry—show that the effect on emergent spectra is very small.

For this calculation, we use the Chemical Equilibrium with Applications model (CEA, Gordon & McBride 1994) to compute the thermochemical equilibrium molecular mixing ratios (with applications to exoplanets see, Visscher *et al.* (2010); Line *et al.* (2010); Moses *et al.* (2011); Line *et al.* (2011); Line and Yung (2013a)). CEA minimizes the Gibbs Free Energy with an elemental mass balance constraint of a parcel of gas given a local temperature, pressure, and elemental abundances. We include species that contain H, C, O, N, S, P, He, Fe, Ti, V, Na, and K. We account for the depletion of oxygen due to enstatite condensation by removing 3.28 oxygen atoms per Si atom (Burrows and Sharp, 1999). When adjusting the metallicity all relative elemental abundances are rescaled equally relative to H while ensuring that the elemental abundances sum to one.

6.2.3 Cloud Model

We use a modified version of the Ackerman and Marley (2001) cloud model which includes sulfide and salt clouds (Morley *et al.*, 2012, 2013). The Ackerman and Marley (2001) approach balances the upward transport of vapor and condensate by turbulent mixing in the atmosphere with the downward transport of condensate by sedimentation using the equation

$$-K_{zz}\frac{\partial q_t}{\partial z} - f_{\text{sed}}w_*q_c = 0, \tag{6.1}$$

where K_{zz} is the vertical eddy diffusion coefficient, q_t is the mixing ratio of condensate and vapor, q_c is the mixing ratio of condensate, w_* is the convective velocity scale, and f_{sed} is a parameter that describes the efficiency of sedimentation in the atmosphere. f_{sed} is the only tunable free parameter in this cloud mode. It represents the ratio of the sedimentation velocity to the convective velocity. Higher f_{sed} values result in larger particles in a vertically compact layer; lower f_{sed} values result in smaller particles in a more lofted cloud layer. Typical f_{sed} values for brown dwarfs, for which this model was first developed, are 1–5 (Saumon and Marley, 2008; Morley *et al.*, 2012), while planets may have clouds best fit with smaller f_{sed} (<1) (Ackerman and Marley, 2001; Morley *et al.*, 2013).

Cloud material in excess of the saturation vapor pressure of the limiting gas is assumed to condense into cloud particles. We extrapolate the saturation vapor pressure equations from Morley *et al.* (2012) to high metallicites, which introduces some uncertainties but serves as a reasonable first-order approximation for the formation of these cloud species.

We prescribe a lognormal size distribution of particles given by

$$\frac{dn}{dr} = \frac{N}{r\sqrt{2\pi}\ln\sigma}\exp\left[-\frac{\ln^2(r/r_g)}{2\ln^2\sigma}\right] \tag{6.2}$$

where N is the total number concentration of particles, r_g is the geometric mean radius, and σ is the geometric standard deviation. σ is fixed (2.0) for this study and falling speeds of particles within this distribution are calculated assuming viscous flow around spheres (and using the

209

Cunningham slip factor to account for gas kinetic effects). We calculate the other parameters in equation 6.1 (K_{zz} and w_*) using mixing length theory to relate turbulent mixing to the convective heat flow (Gierasch and Conrath, 1985). Rigorously the convective heat flow becomes zero well above the radiative-convective boundary. However for purposes only of computing K_{zz} we impose a very small convective heat flux through the radiative stratosphere, causing K_{zz} to increase with altitude at the top of the atmosphere. A lower bound for K_{zz} of 10^5 cm^{2}s^{-1} represents the residual turbulence from processes such as breaking gravity waves in radiative regions. K_{zz} values for representative models are shown in Figure 6.3; the values we calculate qualitatively match the values found by recent 3D modeling efforts (Charnay *et al.*, 2015, their Figure 13), and are generally between 10^8 and 10^9 cm^{2}s^{-1} in the upper atmosphere. The good agreement with the Charnay *et al.* (2015) K_{zz} profiles validates our approach.

Examples of the calculated cloud properties (cloud optical depth and particle size) are shown in Figure 6.2 as a function of a free parameter in this prescription, f_{sed}. The top panel of Figure 6.2 shows the resulting column optical depth of the cloud material at λ=1 and 5 μm. Note that the only f_{sed} value shown that results in optically thick clouds at high altitude is f_{sed}=0.01. The lower panel of Figure 6.2 shows the particle sizes for each cloud for three different f_{sed} values. f_{sed}=0.01 results in very small particles (0.01–0.1 μm) at the cloud top; larger f_{sed} values result in larger particles (0.1–100 μm).

Two versions of the Ackerman and Marley (2001) code are frequently used. One version is coupled self-consistently to the calculation of radiative–convective equilibrium; the other is a stand-alone version which calculates the clouds along a given P–T profile without recalculating the profile self-consistently. Note that the convective heat flow for a cloud-free model

is used in the calculation of K_{zz} in the stand-alone version. Here we use the uncoupled, stand-alone version for higher metallicity calculations (100–1000× solar) for which the convergence for self-consistent models is numerically challenging. The pressure–temperature profiles for the models with photochemical haze are calculated self-consistently with the opacity of the hazes, but the haze properties are not calculated within the Ackerman and Marley (2001) framework.

6.2.4 Photochemistry

We calculate the abundances of soot precursors in the upper atmosphere using the photochemical model described extensively in Miller-Ricci Kempton *et al.* (2012), which is based on the methods published in Zahnle *et al.* (2009a). Briefly, the models use a chemical kinetics model to calculate disequilibrium chemistry due to both vertical mixing and photochemistry in the planetary atmosphere. The eddy diffusion coefficient, which parameterizes vertical mixing in the atmosphere, is taken as a free parameter that can be varied. We use the 50× solar metallicity results first published in Fortney *et al.* (2013), at five different irradiation levels (0.3, 1, 3, 10, 30× the true irradiation of GJ 1214b) and two eddy diffusion coefficients ($K_{zz}= 10^8$ and 10^{10} cm^2 s^{-1}). We use the UV stellar spectrum measured by France *et al.* (2013).

Figure 6.4 shows the carbon chemistry in a single model as an example, at GJ 1214b's irradiation level and 50× solar composition. Because it is cool (∼600 K), the atmosphere is dominated by methane at most altitudes. At the top of the atmosphere, methane is dissociated by UV flux from the host star. The chemistry that proceeds generates a variety of soot precursors (C_2H_2, C_2H_4, C_2H_6, C_4H_2, and HCN). These are the highest order hydrocarbons that can be generated with this particular model, as reactions to form higher-order hydrocarbon

molecules in these environments are incompletely understood (see, e.g., Moses *et al.*, 2011). Nonetheless, unsaturated hydrocarbons like these soot precursors will continue to react and will likely form complex molecules (see, e.g. Yung *et al.* (1984) and discussion of photochemical haze production in Morley *et al.* (2013)).

Figure 6.5 illustrates how both K_{zz} and incident flux affect the formation of these soot precursors. The mixing ratios of C_2H_2, C_2H_4, C_2H_6, C_4H_2, and HCN are summed at each layer of the model. As found in Fortney *et al.* (2013) using the same models, we find that models with 1–3× GJ 1214b's irradiation have the most soot precursors at high altitudes. In the hotter, high irradiation models (20–30×), the atmosphere is dominated by CO instead of CH_4; the chain of chemistry that begins with methane dissociation cannot start in a CO dominated atmosphere, as CO's bond is less easily broken with UV light. The lower production of soot precursors at low irradiation levels is because the rate of methane dissociation is lower. The production of soot precursors can also be a strong function of the eddy diffusion parameter K_{zz}; this is especially true at temperatures that are close to the boundary between CO and CH_4 dominated atmospheres (20×, ∼1200 K), because the vigor of vertical mixing changes the bulk carbon chemistry.

Figure 6.6 shows the haze column optical depth for three example models, each with 50× solar metallicity, f_{haze}=10%, and GJ 1214b's incident flux. Three different particle sizes spanning our model grid are shown, and the column optical depth is calculated for two wavelengths spanning the infrared (1 and 5 μm). We find that 1 μm particles have the lowest optical depth and relatively constant optical depth across the infrared. 0.1 and 0.01 μm particles have more wavelength dependent optical depth, as expected for small particles.

Figure 6.7 summarizes these findings. We calculate the column density of the soot

precursors in high altitude layers of the model (above 10^{-5} and 3×10^{-6} bar). We find that the largest quantity of soot precursors are in models with high K_{zz} and $1-3\times$ GJ 1214b's irradiation level.

GJ 1214's stellar spectrum is used for all photochemical calculations, so we note that the results will depend on the UV spectrum of the host star, even with the same total incident flux.

6.2.4.1 Photochemical hazes

We follow the approach developed in Morley *et al.* (2013) to calculate the locations of soot particles based on the results from the photochemical models. We sum the densities of the five soot precursors (C_2H_2, C_2H_4, C_2H_6, C_4H_2, and HCN) to find the total mass in soot precursors. We assume that the soots form at the same altitudes as the soot precursors exist: we multiply the precursors' masses by our parameter f_{haze} (the mass fraction of precursors that form soots) to find the total mass of the haze particles in a given layer. For each layer,

$$M_{haze} = f_{haze} \times (M_{C_2H_2} + M_{C_2H_4} + M_{C_2H_6} + M_{HCN} + M_{C_4H_2}) \qquad (6.3)$$

where f_{haze} is the efficiency, M_x is the mass of material in each species within each model layer from the photochemical model, and M_{haze} is the calculated mass of haze particles in each layer.

We vary both f_{haze} and the mode particle size (assuming a log-normal particle distribution); we calculate the number of particles by summing over the distribution for each of our chosen particle sizes. Soot optical properties (the real and imaginary parts of the refractive

index) from the software package OPAC (Optical Properties of Aerosols and Clouds) (Hess et al. 1998), were used and linearly extrapolated in wavelength for wavelengths longer than 40 μm.

6.2.5 Transmission Spectra

We calculate the transmission spectrum for each converged P–T profile, including the effect of clouds. The optical depths for light along the slant path through the planet's atmosphere are calculated at each wavelength, generating an equivalent planet radius at each wavelength. The model is extensively described in Fortney *et al.* (2003) and Shabram *et al.* (2011). Cloud layer cross-sections generated from the model atmosphere are treated as pure absorption, and are added to the wavelength-dependent cross-sections of the gas.

6.2.6 Thermal Emission Spectra

A new model to calculate the thermal emission of a planet with arbitrary composition and clouds was developed for this work. The model includes absorption and scattering from molecules, atoms, and clouds. We use the C version of the open-source radiative transfer code disort (Stamnes *et al.*, 1988; Buras *et al.*, 2011) which uses the discrete-ordinate method to calculate intensities and fluxes in multiple-scattering and emitting layered media. We describe this new calculation in more detail in the Appendix.

6.2.7 Albedo Spectra

We calculate reflected light spectra of each model atmosphere using the methods developed for planets and described in detail in Toon *et al.* (1977, 1989); McKay *et al.* (1989); Marley *et al.* (1999); Marley and McKay (1999a); Cahoy *et al.* (2010). Here, we use the term geometric albedo to refer to the albedo spectrum at full phase (α=0, where the phase angle α is the angle between the incident ray from the star to the planet and the line of sight to the observer):

$$A_g(\lambda) = \frac{F_p(\lambda, \alpha = 0)}{F_{\odot,L}(\lambda)} \tag{6.4}$$

where λ is the wavelength, $F_p(\lambda, \alpha = 0)$ is the reflected flux at full phase, and $F_{\odot,L}(\lambda)$ is the flux from a perfect Lambert disk of the same radius under the same incident flux.

The absorption and scattering properties of clouds are calculating using Mie theory, assuming homogeneous, spherical particles.

6.3   Results: Equilibrium Clouds

A grid of 96 models with salt and sulfide clouds (ZnS, KCl, Na$_2$S) are calculated, with irradiations of 0.3, 1, 3, and 10$\times$ GJ 1214b's, metallicities of 100, 150, 200, 250, 300, and 1000$\times$ solar, and f_{sed} of 1, 0.1, 0.01, and cloud-free. A smaller grid of cold models with water clouds are calculated, with 0.01, 0.03, and 0.1$\times$ GJ 1214b's incident flux, 50, 300, and 1000$\times$ solar metallicity, and f_{sed} of 1, 0.1, 0.01, and cloud-free. For each of these sets of parameters, we calculate the transmission spectrum, thermal emission, and albedo spectrum; a

representative sample of these models are shown in this section as well as summaries of their properties. The spectra are all available online at the lead author, Caroline Morley's, website, currently at http://www.ucolick.org/∼cmorley.

6.3.1 Transmission Spectra

The top panel of Figure 6.8 shows examples of models at $1\times$ GJ 1214b's irradiation and with metallicities of 100 and $1000 \times$ solar, both with and without cloud opacity. The full grid also includes models at different temperatures (irradiation) and with intermediate and lower metallicities.

For cloud-free models, transmission spectra have visible features from various atoms and molecules; the prominence of those features changes with both temperature (irradiation) and metallicity. For example, the alkali metals (Na, K) create the strongest features in the warmest ($10\times$ GJ 1214b's irradiation) models. As they condense into clouds in cooler planets, they become significantly less prominent. Other visible features include the major absorbers H_2O, CH_4, and CO. The size of features decreases at higher metallicities because the mean molecular weight increases, decreasing the scale height. As discussed in the introduction, the size of features is proportional to the scale height. The temperature of the atmosphere also controls the carbon chemistry; CO and CO_2 features dominate the mid-infrared spectrum at $10\times$ GJ 1214b's irradiation, whereas CH_4 dominates at $0.3\times$.

We find that all clouds flatten the transmission spectrum, reducing the size of the features caused by molecules and atoms. The lowest f_{sed} values (indicating lofted clouds of small particles, as shown in Figure 6.2) flatten the spectrum the most because they become

optically thick above the gas absorbers. Higher metallicity models have flatter spectra both because they have smaller scale heights (as seen in the cloud-free spectra as well) and a larger abundance of metals to form clouds, leading to optically thicker clouds.

6.3.1.1   Comparing to the Kreidberg et al. 2014 data

We compare all of the synthetic transmission spectra to the observations published in Kreidberg *et al.* (2014a). These data are the highest signal-to-noise (SNR) spectra that have been obtained for this planet. A chi-squared analysis allows us to assess the relative goodness-of-fit for each model. We compare the hotter and colder models to the same observed data; since the data is consistent with a flat line, it represents our fiducial high SNR "flat" spectrum to explore the range of parameter space that is likely to have planets with featureless spectra. We note that we are not suggesting that GJ 1214b has a different incident flux than reality; we are using the observed data as a generic dataset representing a featureless spectrum.

Examples of these fits are shown in the lower panel of Figures 6.8. It is clear both by eye and using a chi-squared analysis that neither of the f_{sed}=1 models (thinner clouds) fit the data; the features in the models are significantly larger than the error bars or scatter in the data points. For the thicker clouds (f_{sed}=0.01) only the highest metallicity model matches the data well.

These results are summarized across the entire modeled parameter space in Figure 6.9. We calculate reduced χ^2 assuming 20 degrees of freedom (22 data points $-$ 2 fitted parameters). We consider acceptable fits to be those with $\chi^2_{\text{red}} < 1.14$, corresponding to P=0.3 of exceeding χ^2 assuming 20 degrees of freedom (Bevington and Robinson, 2003). In Figure 6.9, the dark

red regions represent the lowest reduced χ^2. We find that only models at low f_{sed} and very high metallicity ($\sim$1000 $\times$ solar) can flatten the transmission spectrum enough to match the data. We assess whether this corner of parameter space is likely in Sections 6.5.1 and 6.5.2.

6.3.2 Thermal Emission Spectra

Figure 6.10 shows thermal emission spectra for models with thin and thick clouds. The cloud-free models are dominated by features from water, methane, and carbon monoxide. As in the transmission spectra, warmer objects have deeper CO features and cooler objects have deeper CH_4 features. Note that at 3$\times$ GJ 1214b's irradiation ($\sim$800 K) the amount of methane is strongly metallicity dependent. Lower metallicity models (100$\times$ solar) show a deep methane features between 2 and 4 μm, whereas higher metallicity models have a shallower feature.

Thin (f_{sed}=1) clouds marginally change the thermal emission. The difference is very small at 3–10$\times$ GJ 1214b's irradiation. For the cooler two sets, the clouds decrease the flux in the near-infrared (0.8–2 μm) but leave longer wavelengths unchanged.

Thick clouds (f_{sed}=0.01)—the value of f_{sed} needed to flatten the spectrum to match observations—dramatically change the thermal emission. At all temperatures, the planet has fewer features and a smoother spectrum. This difference is because the clouds create an optically thick layer, blocking the passage of photons from deeper, hotter layers in the atmosphere. Essentially, we are seeing an optically thick, relatively gray, cloud layer.

6.3.3 Albedo Spectra

Albedo spectra at each irradiation level are shown in Figure 6.11. As in hot Jupiter models (e.g. Sudarsky *et al.*, 2003), at these high metallicities and warm temperatures, the albedo spectra of these objects will be very dark, especially at wavelengths beyond 0.6 μm. In particular, the alkali metals create strong absorption features that carve away the reflected light.

For models with thin clouds (f_{sed}=1) at 0.3–1$\times$ GJ 1214b's irradiation, the clouds brighten the albedo spectra at most wavelengths. Absorption features from methane, alkalis, and water are visible. A feature from the reflection of spherical ZnS particles is clearly visible in the models at 0.53 μm. This reflection feature depends on the particle size distribution in the cloud: larger particles ($>$3–5 μm) create a larger feature. Warmer models (3–10$\times$ GJ 1214b's irradiation) with thin clouds lack these interesting cloud features and have lower albedos; the clouds are too deep in the atmosphere to change the albedo spectra significantly.

Reflection spectra of models with thick clouds (f_{sed}=0.01) look significantly different. The scattering properties and locations of the clouds substantially change reflected light from a planet. For these models with thick clouds, they are made of small particles highly lofted in the atmosphere (see Figure 6.2). They absorb efficiently at wavelengths from 0.3–0.5 μm and scatter more efficiently beyond 0.5 μm, creating a spectrum that slopes upward to red wavelengths. Some absorption from water vapor between 0.9 and 1.0 μm are visible, but most of the gas absorption features seen in less cloudy models are muted.

6.3.4 Cold Planets with Water Clouds

Measuring reflected light using optical secondary eclipse depths will be extremely challenging for small, cool planets like GJ 1214b. A set of small planets that may actually be more accessible for reflected light spectroscopy will be directly-imaged distant companions, observed with telescopes like the Wide-Field Infrared Survey Telescope (*WFIRST*) or another dedicated space-based coronagraphic telescope (Spergel *et al.*, 2015). These planets will be colder, more like the planets in our own solar system ($\sim$50–300 K).

These planets may be more accessible in part because many of them will have condensed volatile clouds in their atmospheres, like water, ammonia, and methane. These volatile clouds have higher single scattering albedos in the optical compared to refractory clouds like salts, sulfides, and silicates. The importance of clouds in increasing the albedo at red and far red wavelengths was noted by Marley *et al.* (1999) and Sudarsky *et al.* (2003).

Cold ($\sim$200 K) reflected light spectra for small planets with enhanced metallicity atmospheres are shown in Figure 6.12. In the absence of clouds, planets are predicted to be bright at short wavelengths ($\sim$0.3–0.6 μm) due to efficient Rayleigh scattering at short wavelengths and fainter from 0.6 to 1 μm. The features are mostly caused by methane absorption.

Spectra with ice clouds are significantly brighter at all wavelengths. The f_{sed}=1 models (thinner clouds) have large features caused mostly by methane absorption bands of varying strengths. Some water absorption features are also visible from 0.9–1 μm. In our parameterization, an f_{sed} value of 1–3 is consistent with Jupiter's ammonia clouds (Ackerman and Marley, 2001), so it is reasonable to imagine that cold, old exoplanets will have similar clouds.

For thicker clouds (f_{sed}=0.1 and 0.01) the planet becomes more uniformly bright; this change is because the clouds reflect light at higher altitudes than photons are absorbed by molecules, except within the strongest methane bands (e.g. at 0.88 μm). Bright high altitude clouds would make planets detectable, but challenging to characterize since they have fewer molecular features.

6.4   Results: Photochemical Hazes

We consider a grid of 100 models with irradiation of 0.3, 1, 3, 10, and 30× GJ 1214b's, f_{haze} of 1, 3, 10, and 30%, and mode particle sizes of 0.01, 0.03, 0.1, 0.3, and 1 μm, and optical properties of soot, as described in Section 6.2.4.1. All models have compositions of 50× solar metallicity.

6.4.1   Temperature Structure and Anti-greenhouse Effect

Unlike the equilibrium cloud models, for the models with photochemical hazes, the temperature structure is calculated self-consistently with the haze opacity (though the photochemistry to calculate the abundance of soot precursors is calculated using a constant haze-free temperature profile, see Section 6.2).

For models that contain dark soot particles at high altitudes, these particles are efficient optical absorbers and heat the upper layers of the atmosphere. This phenomenon is called the "anti-greenhouse effect" and has been well-documented in solar system atmospheres. For example, Titan's atmosphere is exactly analogous: a photochemical haze at high altitudes cre-

ates a temperature inversion and cools Titan's surface (McKay *et al.*, 1991, 1999).

Figure 6.13 shows this effect for our grid of hazy models. The gray lines show haze-free temperature profiles of GJ 1214b analogs from 0.3 to 30 × GJ 1214b's irradiation. The black lines show models with hazes in their upper atmospheres. The haze particles absorb more efficiently at optical wavelengths than they do in the infrared; this means that they absorb stellar flux but allow the thermal flux from deeper layers to escape. The absorption from hazes means that less stellar flux reaches deeper parts of the atmosphere. Since the upper atmosphere has a low infrared emissivity, in order to radiate the energy from the absorbed stellar flux, the upper layers must reach higher temperatures.

6.4.2 Molecular Size of Condensible Hydrocarbons

The temperatures at which various hydrocarbons evaporate are also shown in Figure 6.13. These boiling temperatures (T_{evap}) are calculated using the lab-measured values of the boiling point at standard temperature and pressure (T_{STP}) and the enthalpy of vaporization (ΔH_{vap}). These are related by the Clausius-Clapeyron relationship for a phase change at constant temperature and pressure,

$$T_{\text{evap}} = \left[\frac{1}{T_{\text{STP}}} - \frac{R \ln \frac{P}{P_{\text{STP}}}}{\Delta H_{\text{vap}}} \right]^{-1} . \tag{6.5}$$

These curves look similar to condensation curves (as shown in Figure 6.1), but are physically not the same. The boiling temperature here represents the boundary where it is possible to have solid or liquid material in the atmosphere. This value is not the same as the

condensation curve, which represents the point in temperature and pressure at which an atmosphere with a certain composition (usually assuming equilibrium chemistry) has a vapor pressure of that material equal to the saturation vapor pressure.

Boiling temperatures are calculated for polycyclic aromatic hydrocarbons (PAHs) that range in size from two aromatic rings to ten. Specifically we include Azulene, 1-Methylnaphthalene (2 rings), Anthracene, Acenaphthene, Acenaphthylene, Phenanthrene, Fluorene (3 rings), Chrysene, Benz[a]anthracene, Fluoranthene, Pyrene, Triphenylene (4 rings), Dibenz[a,h]anthracene, Benzo[k]fluoranthene, Benzo[a]pyrene (5 rings), Benzo[ghi]perylene, Coronene (7 rings), and Ovalene (10 rings). The laboratory data for these PAHs were found using the NIST database (http://webbook.nist.gov/).

We find that, as expected, larger hydrocarbons boil at higher temperatures than smaller hydrocarbons. As noted in Liang *et al.* (2004), small hydrocarbons (including many of the PAHs shown here) will not be able to condense in warm planetary atmospheres.

This conclusion has a few implications. To have condensed haze material in a ∼600 K atmosphere like GJ 1214b's, the 2–4 carbon soot precursors (produced in the photochemistry model) must react many more times to make 10 or more ring PAHs, or other equivalently large hydrocarbons. We can expect that some of these intermediate materials—which must be vapor at these temperatures—are likely to be present in these atmospheres. If we could characterize the composition of vapor PAHs—the building blocks of hazes—in a hazy atmosphere, we could constrain the chemical pathways to form the condensed hazes.

6.4.3 Transmission Spectra

Figure 6.14 shows examples of model transmission spectra at GJ 1214b's incident flux. We summarize our results for a wider set of parameters in Figure 6.15.

We find a few key results:

1. A photochemical haze thick enough to flatten the near-infrared transmission spectrum only forms in models with 0.3–3× GJ 1214b's irradiation. Models at 10–30× GJ 1214b's irradiation are warmer and therefore have less methane (and more CO) resulting in overall less soot precursor material (see also Figures 6.5 and 6.7). In addition, these warmer models have somewhat larger scale heights which means more soot material is needed to flatten the spectrum.

2. Haze-forming efficiencies (f_{haze}) values of 10–30% are necessary to flatten the spectrum for the assumed 50× solar composition. The value of f_{haze} is essentially unconstrained in the literature due to the challenges of modeling all possible kinetics pathways to long chain hydrocarbons.

3. Small particles ($r \leq 0.1 \mu m$) have optical properties that cause them to absorb more efficiently at the shortest wavelengths. However, the hazes in this model become optically thick over a small range of height z, resulting in only a minor slope to the transmission spectrum even for particle sizes of 0.01 μm.
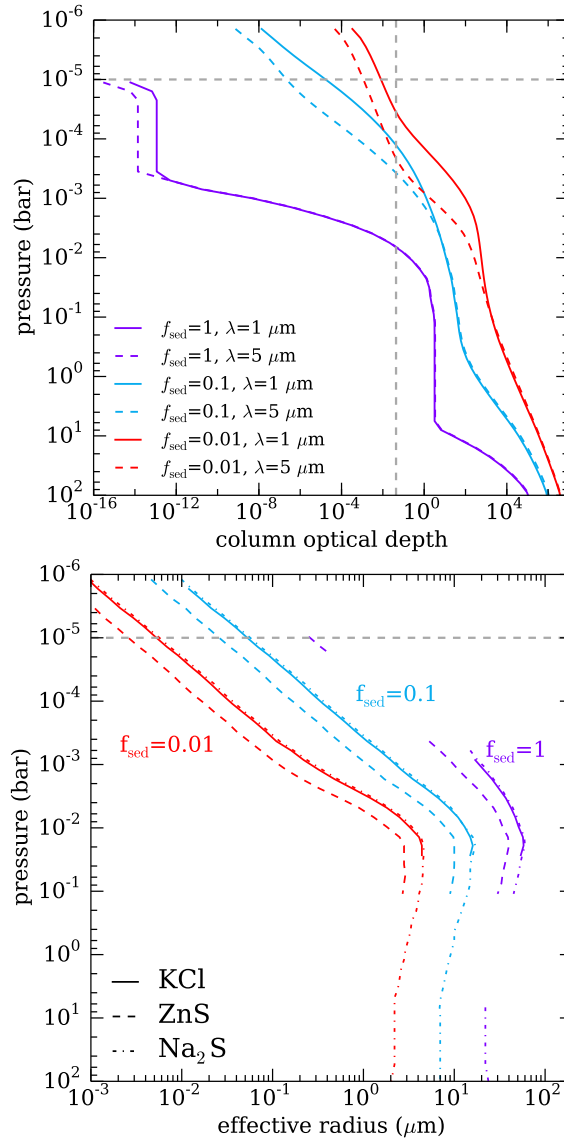
Figure 6.2: Column optical depth and mode particle sizes of clouds with varied sedimentation efficiency f_{sed}, $300\times$ solar metallicity composition, and GJ 1214b's incident flux. Top panel shows the column optical depth at two wavelengths (1 and 5 μm) as a function of pressure for Na_2S, KCl, and ZnS clouds (summed), with f_{sed} from 0.01 to 1. Note that lower f_{sed} values result in optically thicker clouds at higher altitudes. The dashed vertical gray line shows the $\tau = 1$ line for slant viewing geometry using equation 6 from Fortney (2005). The bottom panel shows the mode particle size of each cloud species for 3 values of f_{sed}; note that lower f_{sed} values result in very small particles. The dashed horizontal gray line in both panels shows the approximate altitude of GJ 1214b's cloud to cause a flat transmission spectrum.

225
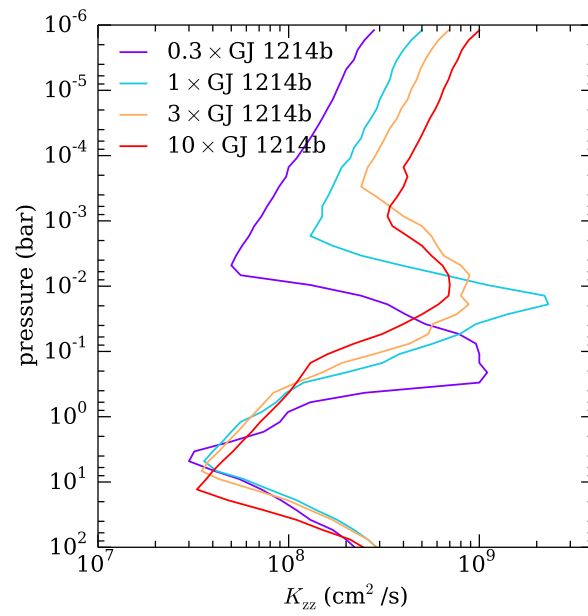
Figure 6.3: Eddy diffusion coefficients (K_{zz}) calculated within the Ackerman and Marley (2001) cloud code for models with $300\times$ solar composition and 0.3–$10\times$ the incident flux of GJ 1214b.
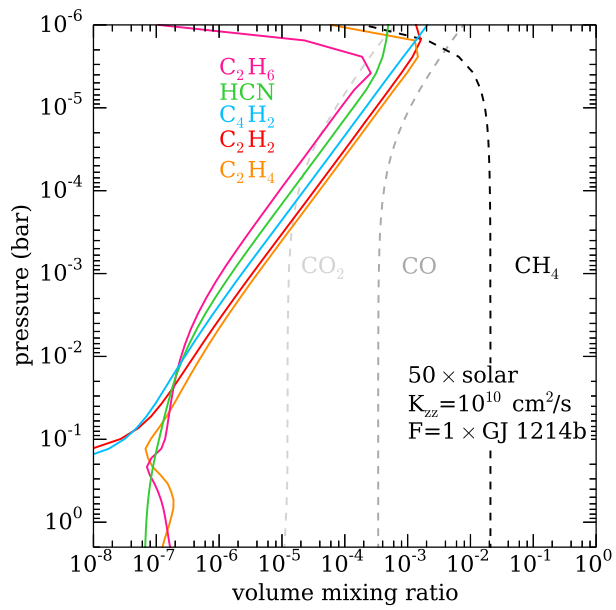
Figure 6.4: Carbon photochemistry for a $50\times$ solar metallicity model with GJ 1214b's incident flux and $K_{zz}=10^{10}$ cm^2 s^{-1}. Soot precursors (solid lines) like C_2H_2, C_2H_4, C_2H_6, C_4H_2, and HCN form in the upper layers of the atmosphere where methane is dissociated by UV flux from the star. Other major carbon-bearing species are shown as dashed lines.
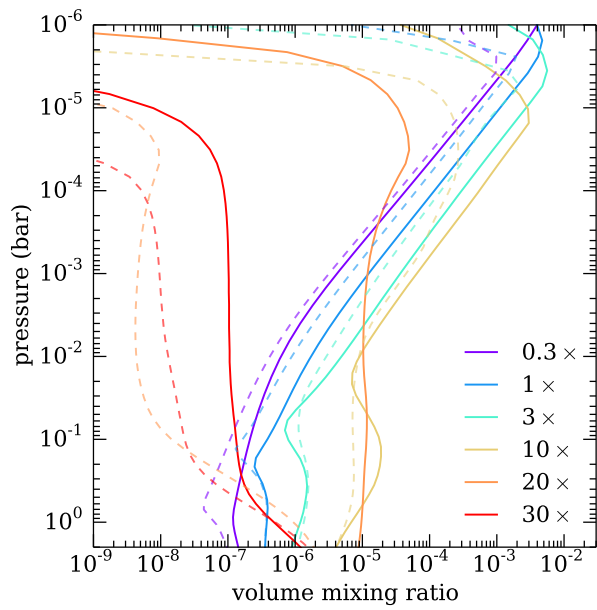
Figure 6.5: Carbon photochemistry for a set of $50\times$ solar metallicity models with varied incident flux. Lines show sum of mixing ratios of all soot precursors. Solid lines show $K_{zz}=10^{10}$ cm^2 s^{-1}; dashed lines show $K_{zz}=10^{8}$ cm^2 s^{-1}. Note that soot precursor production peaks at 1–$3\times$ the irradiation of GJ 1214b.
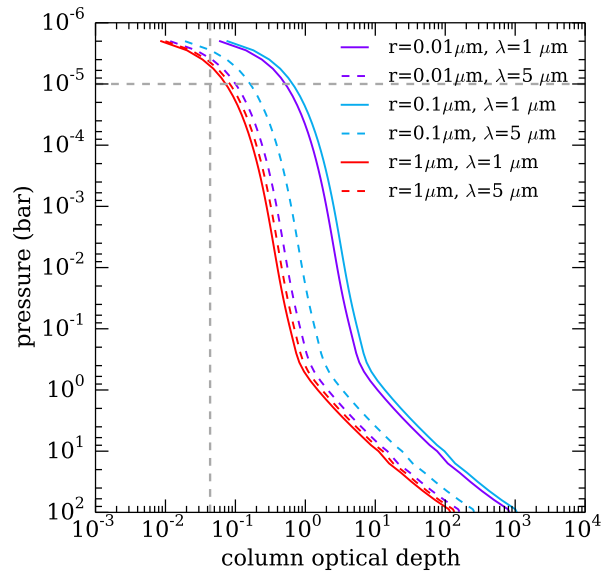
Figure 6.6: Column optical depth for hazes with varied radii (0.01 to 1μm), 50× solar metallicity composition, f_{haze}=10%, and GJ 1214b's incident flux. Column optical depth is shown for two wavelengths (1 and 5 μm) as a function of pressure. Note that smaller particles result in more wavelength-dependent optical depth. The dashed vertical gray line shows the $\tau = 1$ line for slant viewing geometry using equation 6 from Fortney (2005). The dashed horizontal gray line shows the approximate altitude of GJ 1214b's cloud to cause a flat transmission spectrum.
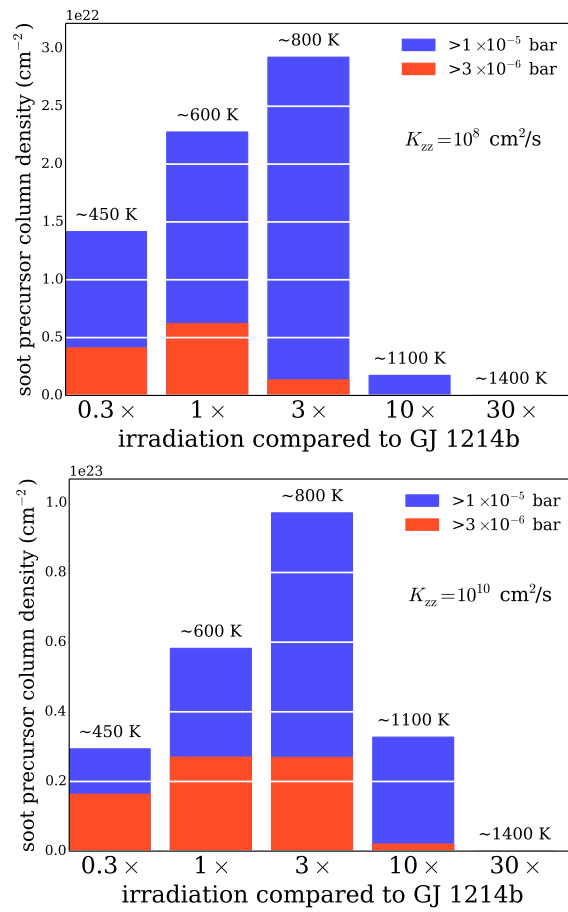
Figure 6.7: Summary of soot precursor production at high altitudes at $50\times$ solar composition. The blue and red bars show the total mixing ratio of soot precursors above 10^{-5} and 3×10^{-6} bar respectively. Top panel shows $K_{zz}=10^8$ cm^2 s^{-1}; bottom panel shows $K_{zz}=10^{10}$ cm^2 s^{-1}. Models with high K_{zz} and 1–3$\times$ the irradiation of GJ 1214b have the most soot precursors.
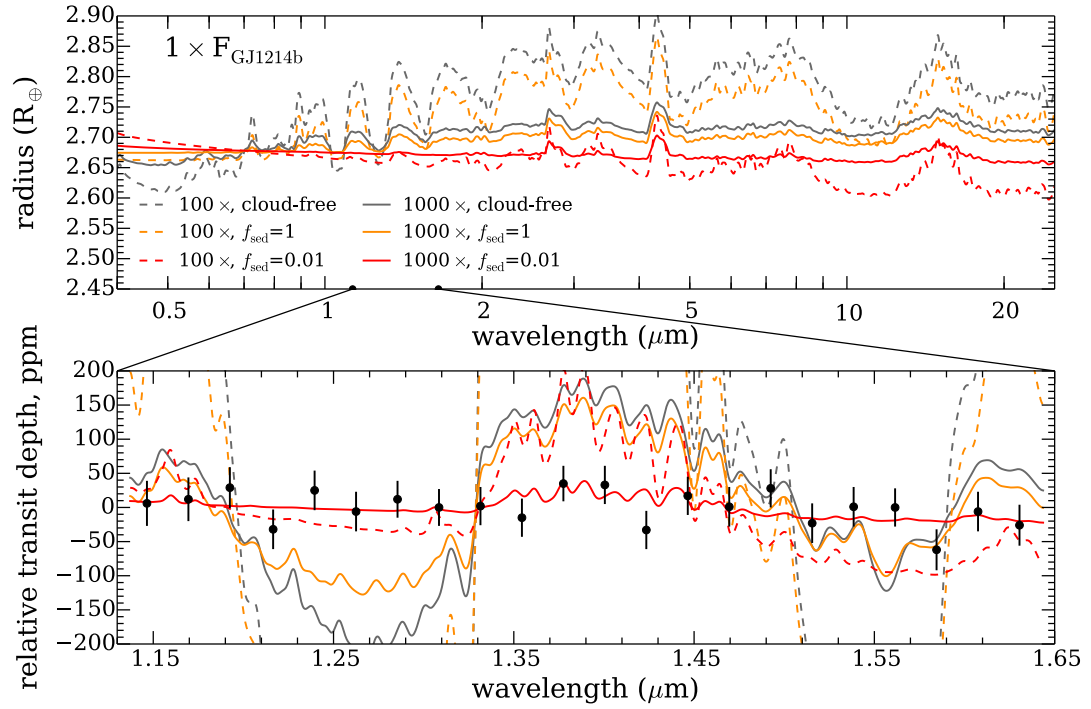
Figure 6.8: Example high metallicity (100 and 1000× solar) transmission spectra with and without clouds. The top panel shows the optical and infrared transmission spectra. The bottom panel shows the same spectra, zoomed in to focus on the Kreidberg *et al.* (2014a) data in the near-infrared. Cloud-free transmission spectra are shown as light and dark gray lines and cloudy spectra are shown as colored lines. Note that the only model that fits the data is the 1000× solar model with f_{sed}=0.01 (lofted) clouds.
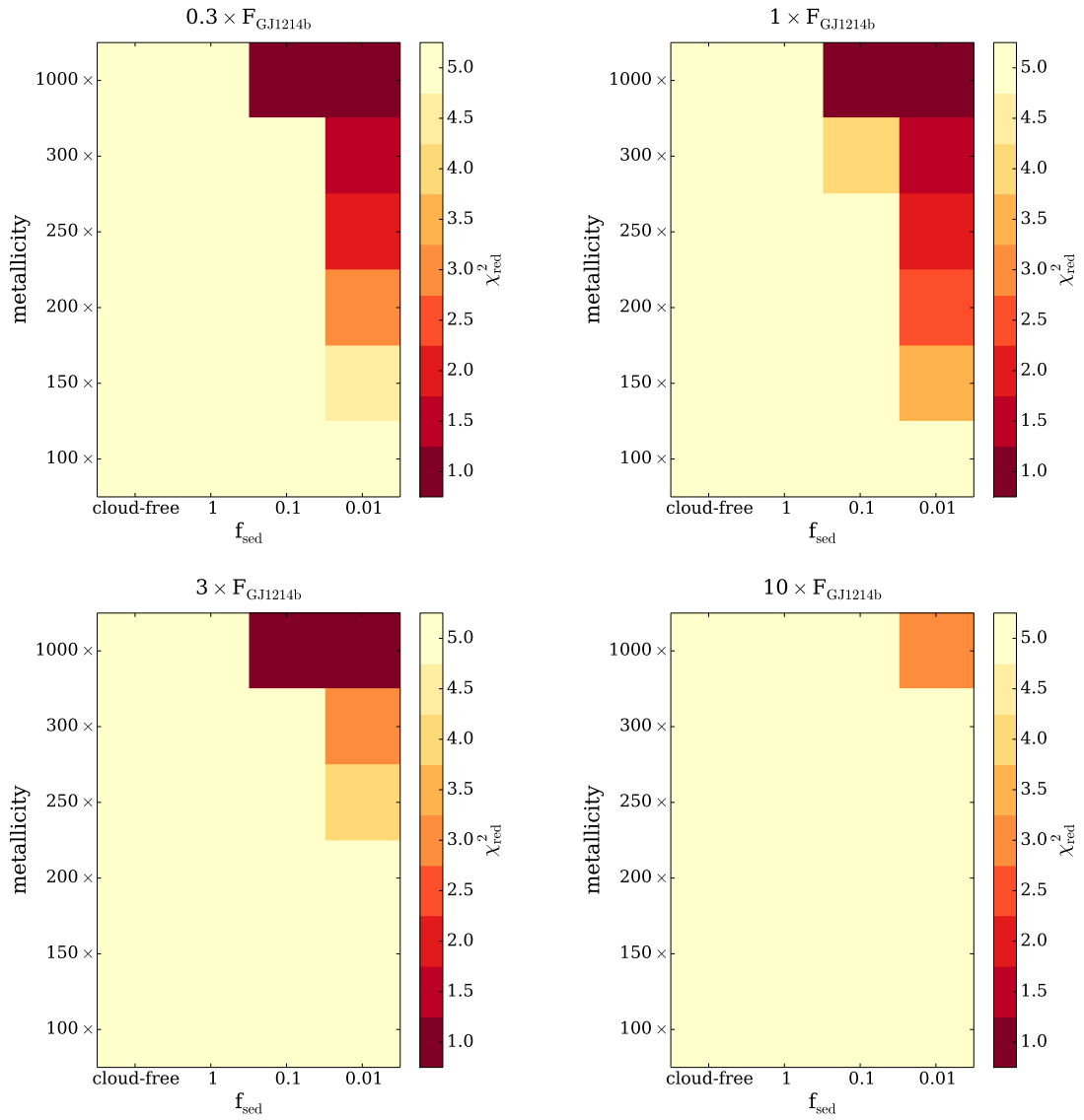
Figure 6.9: Chi-squared maps showing quality of fit to Kreidberg *et al.* (2014a) data for transmission spectra with equilibrium clouds, with varied irradiation levels, metallicities, and cloud sedimentation efficiency $f_{\rm sed}$. Starting in the top left panel, models with 0.3, 1, 3, and 10 $\times$ GJ 1214b's irradiation are shown. Dark red sections show acceptable fits (reduced χ^2 close to 1.0). Note that high metallicity and low $f_{\rm sed}$ (lofted clouds) are simultaneous requirements for these clouds to generate a flat enough transmission spectrum to be consistent with the data.
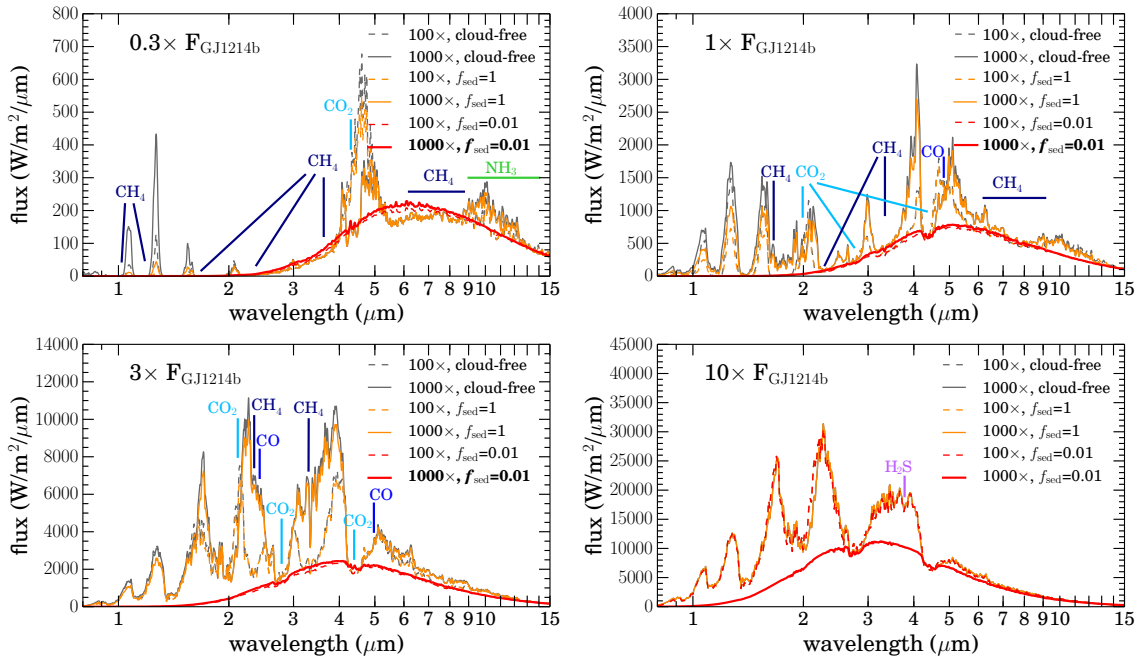
Figure 6.10: Thermal emission spectra of models with sulfide and salt clouds. Each panel shows models with a different incident flux. Gray lines show cloud-free models and colored lines show cloudy models. The fonts in the captions are bolded if the transmission spectrum with those parameters fits the Kreidberg *et al.* (2014a) data. For the cooler models, the cloud opacity decreases the near-infrared flux. For the warmer models, the clouds are optically thinner. Major molecular features are labeled. Unlabeled major features are predominantly H_2O.
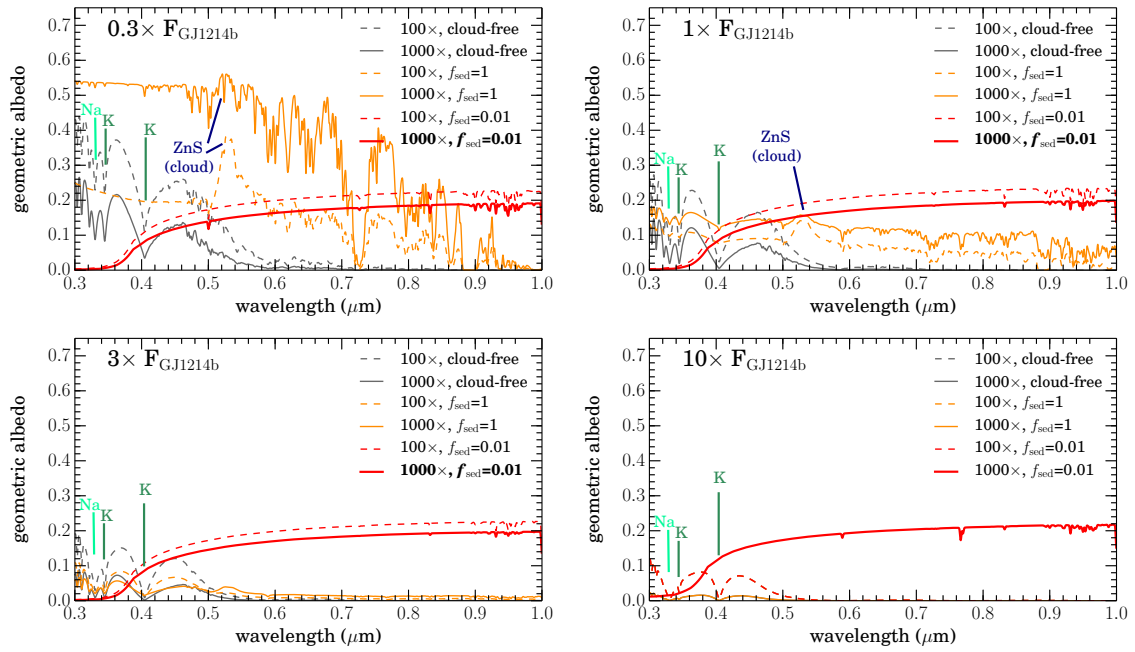
Figure 6.11: Albedo spectra for models with salt/sulfide clouds. The top set of panels show thinner clouds (f_{sed}=1) and the bottom set of panels show thicker clouds (f_{sed}=0.01). Bolded legend text indicates models that fit the transmission spectrum data. Each panel shows a different incident flux compared to GJ 1214b.
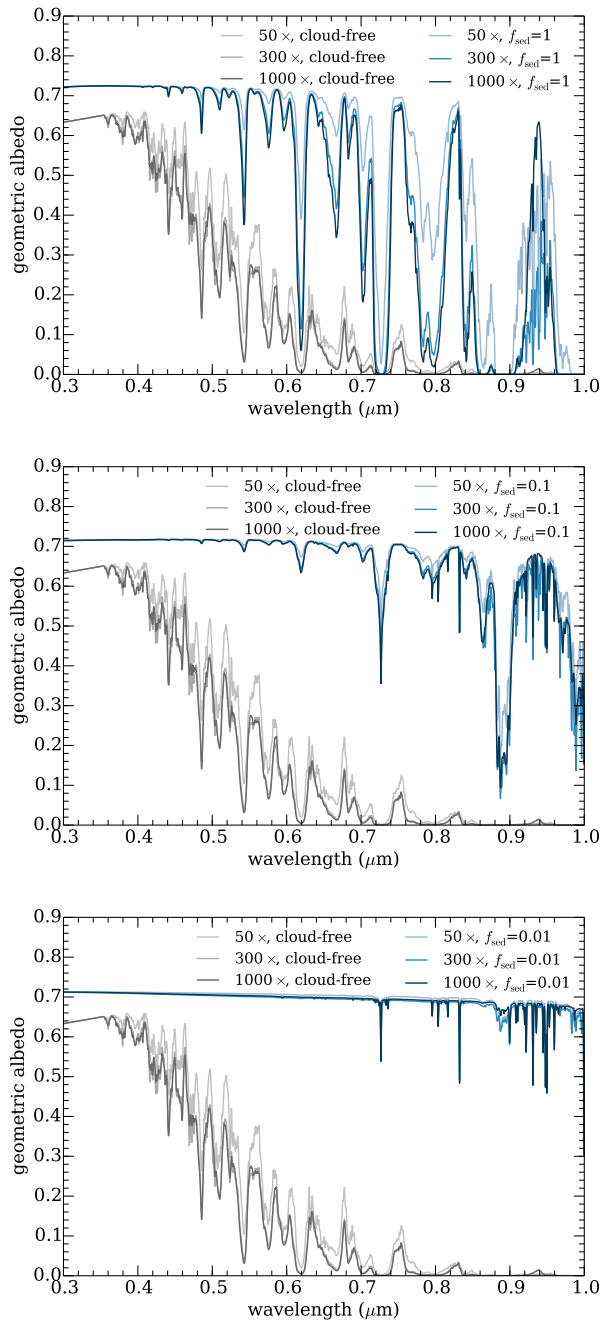
Figure 6.12: Albedo spectra for cold models (T_{eff}=190 K) with water clouds at 50–1000× solar metallicity. The top, middle, and bottom panels show models with f_{sed}=1, 0.1, and 0.01 respectively. Note that water clouds create bright albedo spectra with strong features from methane.
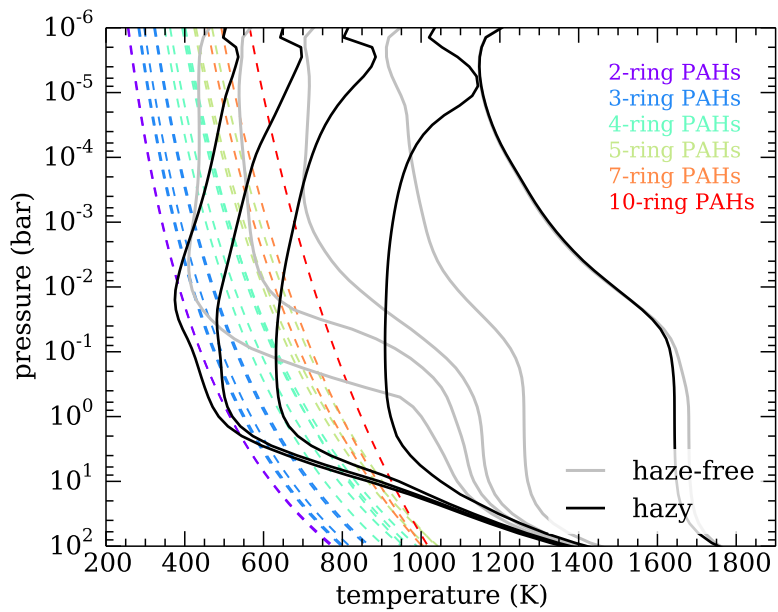
Figure 6.13: Pressure–temperature profiles of clear and hazy models are shown as gray and black lines, respectively. From left to right, these models have irradiation levels of 0.3, 1, 3, 10, and 30 times GJ 1214b's. The hazy models have particle sizes of 0.1 μm and f_{haze}=10%. The colored dashed lines show the condensation temperatures of a number of different polycyclic aromatic hydrocarbons (PAHs), color-coded by the size of the molecule.
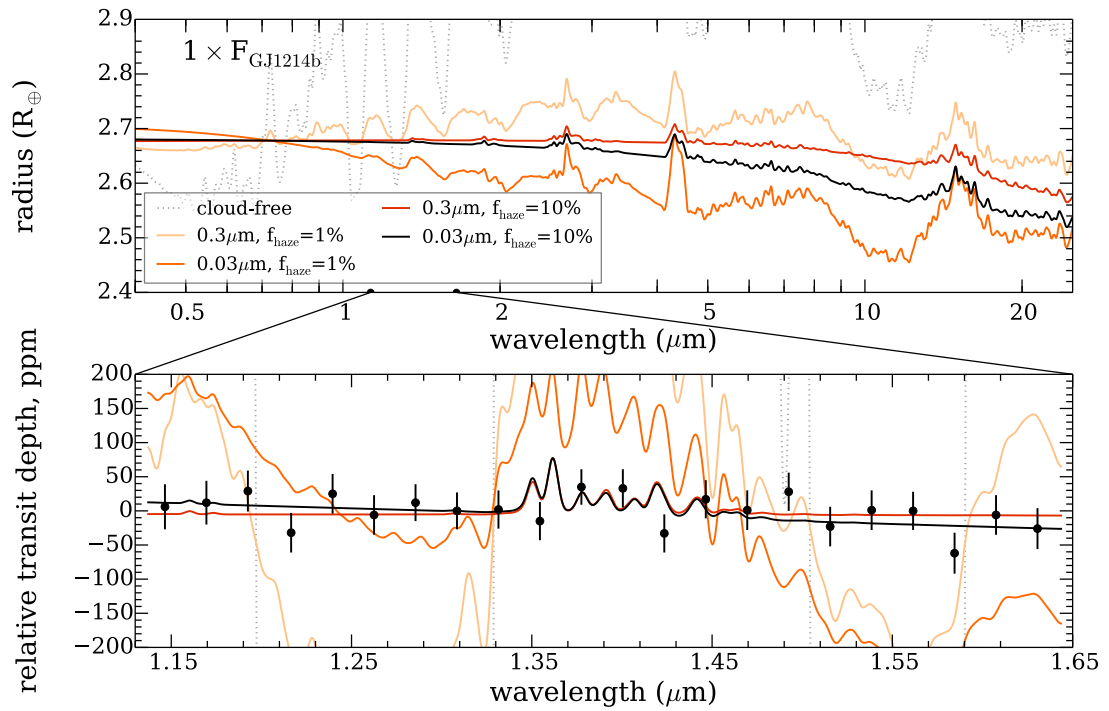
Figure 6.14: Transmission spectra of models with photochemical hazes with two different mode particle radii (0.3 and 0.03 μm) and f_{haze} values (1 and 10%). The top panel shows model planet radius from optical to mid-infrared wavelengths. The bottom panel shows the wavelength region (1.1–1.7 μm) of the Kreidberg *et al.* (2014a) measurements. Note that the two models with f_{haze}=10% qualitatively match the flat spectrum.
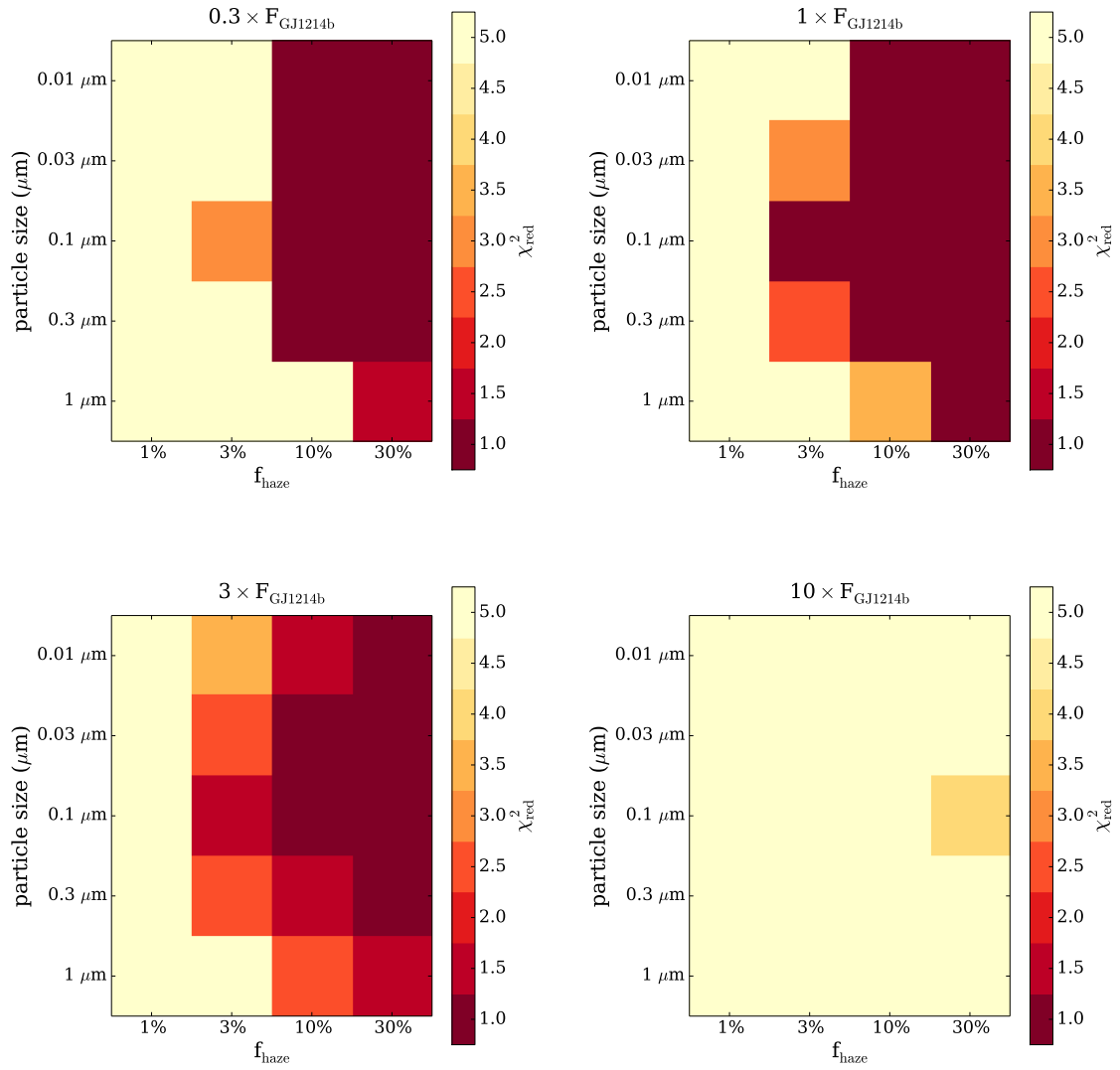
Figure 6.15: Chi-squared maps showing quality of fit to Kreidberg *et al.* (2014a) data for transmission spectra with photochemical hazes, with varied irradiation levels, mode particle sizes, and haze forming efficiency f_{haze}. Starting in the top left panel, models with 0.3, 1, 3, and 10 $\times$ GJ 1214b's irradiation are shown. Dark red sections show acceptable fits (reduced χ^2 close to 1.0). Note that a variety of models with f_{haze}=10–30% can generate a flat enough transmission spectrum to be consistent with the data, for models cooler than 10$\times$ GJ 1214b's irradiation ($T_{\text{eff}}\sim$1100 K).
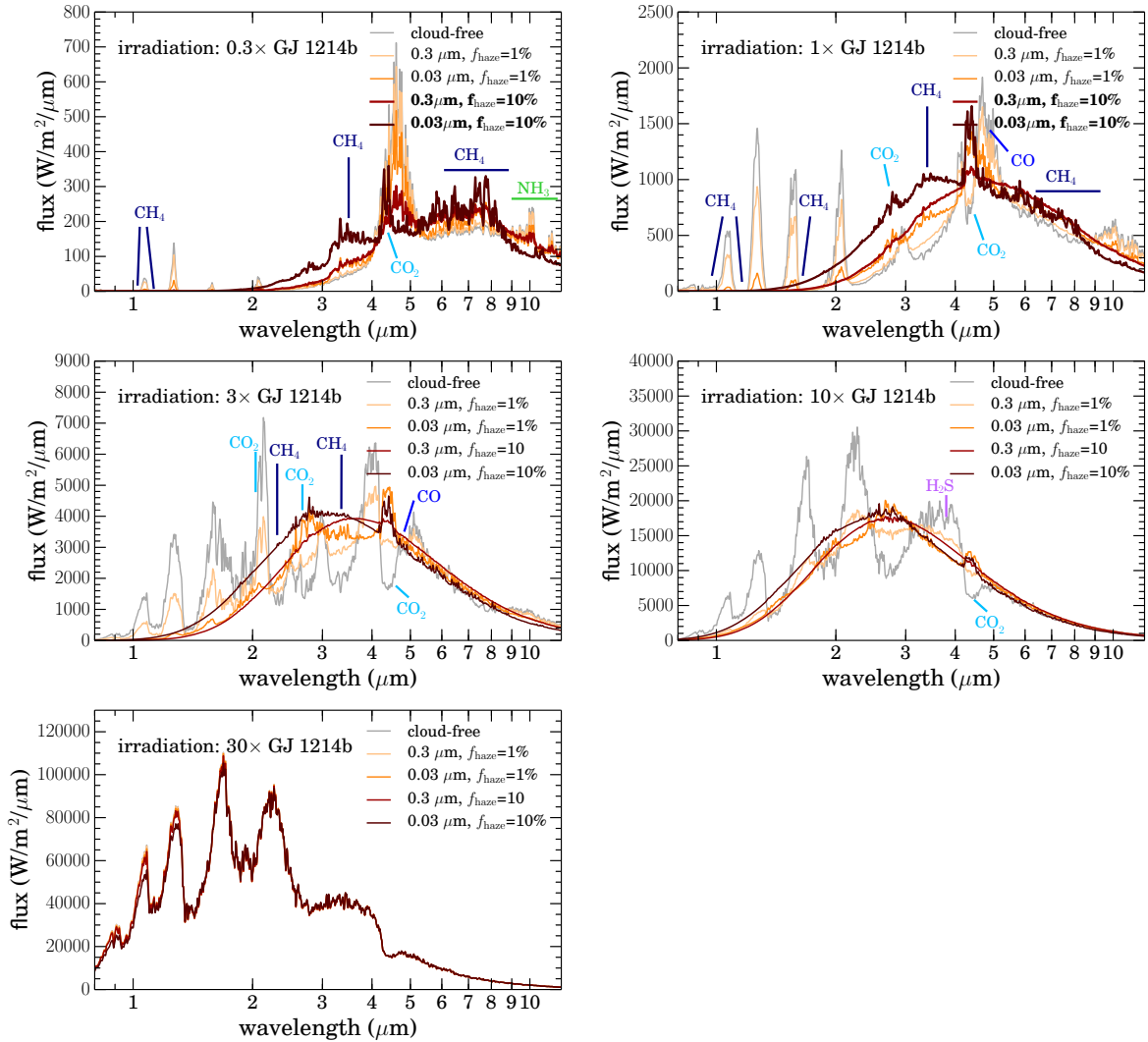
Figure 6.16: Thermal emission spectra with photochemical haze. Each panel shows a different irradiation level. Cloud-free models are shown as gray lines; models with haze particle sizes of 0.03 and 0.3 μm and f_{haze} of 1 and 10% are shown as colored lines, with hazier models in darker colors. The fonts in the captions are bolded if the transmission spectrum with those parameters fits the Kreidberg *et al.* (2014a) data.

6.4.4 Thermal Emission Spectra

Thermal emission spectra at each irradiation level are shown in Figure 6.16. The top right panel shows predictions for models with GJ 1214b's irradiation. At this temperature ($\sim$600 K), the spectrum shows absorption features from water, methane, and carbon monoxide. For thin hazes which do not flatten the transmission spectrum (f_{haze}=1%), the flux in the near-infrared peaks decreases, and the flux at absorption features, especially between 2 and 4 μm, increases. These changes are due to increased cloud opacity and increased temperature of the P–T profile due to the absorption of stellar flux by particles in the upper atmosphere. For thick hazes, the heating in the upper atmosphere is large and causes a temperature inversion (see Section 6.4.1 and Figure 6.13). This causes some molecular features to be seen in *emission* instead of absorption. Most prominent of these is CO_2, between 4 and 5 μm; at GJ 1214b's irradiation, all hazes that flatten the transmission spectrum have CO_2 in emission. This feature is potentially observable with *JWST* (see Section 6.5.5).

At 3–10$\times$ GJ 1214b's irradiation, haze-free spectra have significant features, while hazy spectra have muted features and very little flux in the near-infrared. The emission bands are weaker at higher temperatures. At 30$\times$ GJ 1214b's irradiation, the hazes are optically thin and we see very little difference between the models.

At 0.3 $\times$ GJ 1214b's irradiation, hazes decrease the flux in the near-infrared and in the 4–5 μm window between water and methane features, and increase the flux between 2 and 4 μm.

6.4.5 Albedo Spectra

Figure 6.17 shows albedo spectra for the same set of models as shown in Figure 6.16.

Haze-free models are brightest between 0.3 and 0.55 μm, with geometric albedos around 0.1 to 0.4, because Rayleigh scattering is most efficient at short wavelengths. At these short wavelengths, the hotter models have lower albedos than cooler models. From 0.6–1 μm, the albedo spectra are quite faint, with geometric albedo <1–4% because atoms and molecules absorb photons at higher altitudes than Rayleigh scattering reflects them. In particular, the pressure-broadened lines of the alkali metals absorb strongly at green and red optical wavelengths.

Soot hazes cause dark reflected light spectra. This result is not surprising given the strongly absorbing optical properties of black soots and their high altitudes; the soots absorb visible light photons at higher altitudes would be scattered. Thin hazes decrease the reflected flux at all wavelengths, to 5–70% of the haze-free albedos. For very thick hazes, the albedo becomes more uniformly dark, around 2%. At longer wavelengths (0.6–1.0 μm) the thick hazy model spectra are somewhat brighter than the very dark haze-free spectra; at wavelengths between 0.3–0.55 μm, the thick hazy model spectra are darker than haze-free spectra, because the soot layer absorbs the visible photons at higher altitudes than photons would scatter by Rayleigh scattering.

6.4.6 Effect of Optical Properties of Photochemical Haze

An important assumption made in the nominal photochemical haze grid is that haze particles have the same optical properties as soots (Hess *et al.*, 1998). Real hazes likely have

diverse optical properties that depend on the environment in which they form. Here, we show how key spectral features change if different optical properties are used. We change the optical constants to those of tholins, a material created in lab experiments to simulate hazes. Tholins are similar to the materials that form hazes in Titan's atmosphere, which form due to photochemistry at high altitudes. In a simulated transmission spectrum measured using a solar occultation with the Cassini spacecraft, this hydrocarbon haze produces a distinct slope from near- to mid-infrared wavelengths (Robinson *et al.*, 2014). Titan's haze particles are made of fractal aggregates of large hydrocarbons (McKay *et al.*, 2001). We use tholin indices of refraction from the experimentally derived values in Khare *et al.* (1984) and calculate absorption and scattering coefficients using Mie scattering assuming spherical particles. We hold all other properties constant—particle sizes and f_{haze}, the haze number density, haze particle density—to isolate the effect of optical properties alone.

Figure 6.18 summarizes these results. The top left panel shows the cloud properties at a single slice in the atmosphere, where the haze becomes optically thick in the near-infrared (1.5 μm). The optical depth of the tholin haze depends strongly on wavelength for both particle sizes (higher optical depth at shorter wavelengths) and features are visible, especially for the smaller particle size. More dramatically, the single scattering albedo of the small tholin particles is high in the near-infrared ($\sim$1 from 1–2.5 μm) with strong features in the optical and mid-infrared. In contrast, soot particles of both sizes have low, feature-poor single scattering albedo.

The top right panel shows examples of transmission spectra; note that small tholin particles absorb strongly at optical but not infrared wavelengths, unlike soots which absorb more uniformly across the infrared. Because they are much less efficient infrared absorbers,

none of the models with tholin optical properties adequately fit the Kreidberg *et al.* (2014a) data.

The bottom left panel shows examples of thermal emission spectra. The most profound difference from the soot models is that, because the tholins absorb much less of the stellar irradiation, the upper atmospheres do not warm and form a temperature inversion. [2]. Without a temperature inversion, none of the emission features seen in the spectra with soot haze are seen in spectra with tholin haze. In addition, more of the spectral features at near-infrared wavelengths are preserved.

The bottom right panel shows albedo spectra. The first obvious change is that tholin hazes scatter much more efficiently, making the albedo spectra overall much brighter (15–30% between 0.7 and 1 μm). The tholin hazes absorb more efficiently at blue wavelengths (0.3–0.6 μm), causing the spectrum to be darker at blue wavelengths and brighter at red wavelengths. Features from methane are easily visible around 0.9 μm.

6.4.7 Photochemistry At Higher Metallicities

All of the hazy models presented here assume compositions of 50× solar metallicity; however, the metallicities of low mass, low density planets may be higher (see Section 6.5.1). There are several competing effects that control the formation of hazes in higher metallicity atmospheres and the amplitude of features in their transmission spectra. Higher metallicity atmospheres ($> 50\times$ solar) have higher mean molecular weights and therefore smaller scale heights, reducing the amplitude of features. The amount of carbon available increases (by def-

---

[2]This finding of course differs from Titan's actual atmosphere which does have a haze-caused temperature inversion (McKay *et al.*, 1991)

inition) uniformly at higher metallicities. However, the abundance of soot precursors available

to form hazes does not necessarily follow, due to the complex interactions of kinetic pathways

to make and destroy soot precursors.

To create soot precursors, an atmosphere must be methane-rich. High metallicity

tends to favor the production of CO and CO_2 over CH_4, which can potentially inhibit soot pre-

cursor production. In a methane-dominated atmosphere, vigorous mixing (high K_{zz}) increases

soot precursor production (see Figures 6.5 and 6.7). However, vigorous mixing can also in-

crease the abundance of CO and CO_2 and decrease the abundance of CH_4, which decreases soot

precursor production.

Examples of high metallicity models are shown in Figure 6.19. We find that for less

vigorous mixing ($K_{zz}=10^8$ cm^2/s), the column density of soot precursor formed at high altitudes

increases with increased metallicity, at a rate higher than would be predicted by the increase in

carbon abundance alone. In contrast, with more vigorous mixing ($K_{zz}=10^{10}$ cm^2/s) the column

density of soot precursor formed is largest at $100\times$ solar.

More work should be done in the future to fully understand the differences in kinetics

pathways at high metallicity, but, generally, we find that planets with a variety of metallicities

can have similarly rich photochemistry that likely allows for the formation of hazes.

6.5 Discussion

6.5.1 High Metallicity Super Earth Atmospheres

There are several lines of reasoning that suggest that small, gas-rich planets may have high metallicities.

The first is purely empirical. In the solar system, there is a power law relationship between planet mass and metallicity, with lower mass planets being significantly more enhanced in heavy elements. Based on carbon abundance derived from methane, Jupiter (318 $M_\oplus$) is 3.3–5.5×, Saturn (95 $M_\oplus$) is 9.5–10.3×, Uranus (14.5 $M_\oplus$) is 71–100×, and Neptune (17 $M_\oplus$) is 67–111× solar metallicity (Wong *et al.*, 2004; Fletcher *et al.*, 2009; Karkoschka and Tomasko, 2011; Sromovsky *et al.*, 2011). Kreidberg *et al.* (2014b) extend this comparison to a more massive exoplanet, WASP-43b, which has a mass of $2M_J$ and a metallicity (based on the measured water abundance) of 0.4–3.5 × solar.

Extrapolating this power law to GJ 1214b's mass ($\sim 6M_\oplus$) results in a predicted metallicity of 200–300× solar. Of course, nature need not continue to follow this particular power law if, for example, the formation mechanism for extrasolar small planets differs significantly from the gas and ice giants in our own solar system, but this line of reasoning provides a testable prediction.

The other line of reasoning is based on population synthesis models of super Earths. Fortney *et al.* (2013) show that, based on models that follow the accretion of gas and planetesimals to form planets, objects in the super Earth mass range may have a wide diversity of envelope enrichments. They predict that a portion of the population will have highly enriched

245

atmospheres of several hundreds of times solar composition (see Figure 5 from Fortney *et al.* (2013)).

Together these lines of evidence show that high metallicities may be quite common, and that a measurement of atmosphere enrichment for a planet smaller than Uranus would be valuable for our understanding of planet formation.

6.5.2   Is $f_{\rm sed}$=0.01 Reasonable?

For a cloudy planet to have a flat transmission spectrum, the atmosphere must both have high metallicity and inefficient cloud sedimentation ($f_{\rm sed} \ll 1$). This low inferred $f_{\rm sed}$ is much less than the inferred $f_{\rm sed}$ for brown dwarfs ($f_{\rm sed} \approx 1$–5).

However, clouds flattening GJ 1214b's spectrum need not behave the same as the deep convective iron and silicate clouds of brown dwarfs. In fact, we might expect them to behave more like stratospheric clouds on Earth. When parameterized with this model, terrestrial stratocumulus clouds have $f_{\rm sed} < 1$ at the top of the cloud, with increasing $f_{\rm sed}$ with distance below the cloud top. Clouds studied over the North Sea, for example, have been measured to have $f_{\rm sed} \sim 0.2$ (Ackerman and Marley, 2001). It is possible that GJ 1214b differs enough in circulation patterns from Earth, as a tidally locked planet around an M dwarf, that clouds in the upper atmosphere could be more vigorously lofted to create even lower $f_{\rm sed}$ clouds.

Further study is needed to determine whether these values are reasonable (e.g. 3D circulation models with radiatively-interacting cloud tracer particles would inform us about where the clouds are likely to form).

6.5.3   Vertical Mixing to Loft Small Particles

Our results for photochemical hazes suggest that they may provide a viable way to flatten the transmission spectra of small planets. However, the models were not run with a self-consistent cloud model that governs how fast particles can sink out of the atmosphere. In particular, can particles with sizes from 0.01–0.3 μm, which allow us to fit the data, stay lofted for long enough timescales for new particles to form?

We do not attempt to address these questions here, without a complete model for cloud formation in a planetary atmosphere, nor a model for 3D atmospheric circulation, both of which would be necessary to address this question. We can however show that, for our assumed vertical mixing values in the photochemical model (K_{zz}=10^{10} cm^{2}s^{-1}), which are based on upper limits from circulation models (Kataria *et al.* (2014) and T. Kataria, private communication), mixing should be vigorous enough to loft $\sim$1 μm particles.

In Figure 6.20, we show the timescale for a cloud particle to fall one pressure scale height (H/v_{fall}) where H is the scale height and v_{fall} is the particle falling velocity. We calculate falling velocities assuming viscous flow, following the approach of Ackerman and Marley (2001) (their Appendix B). We also show lines that represent constant K_{zz} of 10^8 cm^{2}s^{-1} and 10^{10} cm^{2}s^{-1}, which were the values used in the photochemical models.

We find that for particles smaller than 1 μm, the falling timescale is longer than the lofting timescale assuming K_{zz}=10^{10} cm^{2}s^{-1}. Given these conditions, it should therefore be possible to have particles of this size in the upper regions of GJ 1214b's atmosphere. However, if the mixing is less vigorous, it will be significantly harder to keep particles in the size range

from 0.01–1 μm lofted at 10^{-5} bar.

6.5.4 Need for Laboratory Studies at Super Earth Conditions

One path forward to understand photochemical hazes is the same that has been used for decades to study Titan's complex atmospheric chemistry: laboratory measurements. The conditions present in super Earths like GJ 1214b, including the moderately high temperature ($\sim$600 K) and the H_2-rich composition, are quite different from that of any solar system planets or moons, and therefore require new laboratory studies.

Lab experiments are crucial because theoretical modeling of full chemical kinetic pathways from 2-carbon hydrocarbons to complex PAHs and long-chain hydrocarbons poses a huge challenge. The information provided by laboratory measurements would provide empirical constrains on these reactions. For example, we could determine whether reactions necessary to create condensible hydrocarbons do indeed proceed at low pressures in a GJ 1214b-like atmosphere, and whether, like on Titan's these hydrocarbons form with the help of ion chemistry (Lavvas *et al.*, 2011). The types of condensed materials could be predicted and their optical properties would allow us to make predictions for future observations. The concentrations of other gases formed in the chemical reactions could be determined and testable predictions could be made. In addition, lab experiments could allow us to make predictions, beyond the predictions we make here, about which conditions create the most obscuring haze material, allowing us to better target planets.

6.5.5 Planning Future Observations of Super Earths

The *Kepler* results demonstrably show that super Earths are incredibly common. To understand planets as a population, we must be able to measure properties of super Earths. The flat transmission spectra of super Earths that have been observed over the last few years have shown that this is not as easy a task as originally perceived (e.g., Miller-Ricci *et al.*, 2009). We suggest several directions that may allow us to move forward to understand the compositions of super Earth atmospheres.

6.5.5.1 Transmission Spectra of Hotter Targets

One avenue for advancement is to observe warmer super Earth targets. If photochemical hazes are indeed obscuring the transmission spectra of cool targets such as GJ 1214b, these hazes, according to our models, should decrease in abundance significantly between 3 and $10\times$ GJ 1214b's irradiation (around $\sim$1000 K), at the transition between CO and CH_4 dominated compositions (see Figures 6.5 and 6.7). We note that we do not consider hazes derived from other elements such as sulfur, which may exist at warmer temperatures (Zahnle *et al.*, 2009b).

This idea has also been discussed in Fortney *et al.* (2013) (see their Figure 6), and one of the best targets, since it is $\sim$2000 K and around a bright star, is 55 Cnc e. A handful of *Kepler* planets are also >1000-1100 K, but orbit faint stars that make the observations challenging. In addition, many small planets in this temperature range may have experienced significant mass loss (Lopez *et al.*, 2012; Lopez and Fortney, 2013; Fortney *et al.*, 2013, their Figure 1). The current K2 mission (using the repurposed *Kepler* telescope) (Howell *et al.*, 2014) and upcoming Transiting Exoplanet Survey Satellite (TESS) mission (Ricker *et al.*, 2014) may reveal

additional hot super Earths around the stars they target, which are on average closer and brighter than the *Kepler* targets.

Mapping out the parts of parameter space with flat transmission spectra will provide information about the types of clouds and hazes that exist in these atmospheres. Temperature (incident flux) is the most important parameter that likely controls clouds and hazes; unfortunately most of the targets observed so far have been in the same 600–900 K range that we predict to have significant methane-derived photochemical hazes.

6.5.5.2 Thermal Emission Spectra with JWST

Looking to the future, one path that will be opened with the launch of the James Webb Space Telescope (*JWST*) will be observing the thermal emission spectra of warm and hot super Earths. These will be challenging measurements that will likely take several secondary eclipses to achieve the necessary signal-to-noise to detect features (Greene et al., in prep.).

Several instruments will be capable of observing secondary eclipses of super Earths. In the near-infrared, both the Near-Infrared Camera (NIRCam) and Near-InfraRed Imager and Slitless Spectrograph (NIRISS) will be able to observe transits and eclipses. In particular, NIRCam has a grism mode that will be capable of 2.4–5 μm R$\sim$2000 slitless spectroscopy. It uses a slitless grism that is sensitive to sky background across a large field, which is optimized for the precision photometry and stability needed to make these observations of exoplanets. NIRISS has a single object slitless spectroscopy mode with wavelength coverage from 0.6–2.5 μm spectral resolution of $\sim$700, and optimized for spectroscopy of transiting planets. Lastly, The Near-Infrared Spectrograph (NIRSpec), offers slit spectroscopy in the 0.6 to 5.0 μm wave-

length range with a wide variety spectral resolutions ($30 < R < 3500$), which may be particularly useful for targeted observations of specific spectral features.

For longer wavelengths, the Mid-Infrared Instrument (MIRI) will be capable of low ($R\sim100$) resolution spectroscopy from 5–14 μm and moderate resolution ($R\sim3000$) spectroscopy from 5–28.3 μm. It is the only *JWST* instrument that will observe wavelengths longer than 5 μm and will be 50 times more sensitive than the Spitzer Space Telescope.

Figure 6.21 shows the planet-star flux ratio (i.e. the depth of secondary eclipse) for three different representative models. Given high signal-to-noise observations across a wide wavelength range, it should be possible to determine the differences between these models. However, piecing together an infrared spectrum will be an expensive endeavor that requires multiple observations, each taking many hours. As a community, targets for this treatment must be carefully considered.

Of concern is that many models with thick clouds (that match the transmission spectrum observations) have spectra that appear nearly identical to blackbodies. If these models indeed represent reality, thermal emission will not allow us to determine the compositions of gases in the planetary atmosphere. However, the models that include optically thick photochemical hazes in the upper atmosphere have strong temperature inversions that create observable emission bands in the mid-infrared. Discovering a spectrum like this would strongly indicate that hazes are indeed the cause of flat transmission spectra; constraining the strength of the temperature inversion would allow us to constrain the optical properties of the hazes, since this inversion indicates that the particles are strong optical and weaker infrared absorbers.

6.5.5.3 Albedo Spectra from Space-based Coronagraph

Further in the future, a space-based mission with a coronagraph, such as the *WFIRST-AFTA* mission, will allow us to measure the reflected light from old, giant planets, just as we have observed the solar system planets for centuries. Current predictions for the performance of the *WFIRST-AFTA* coronagraph suggest that for favorable configurations, super Earths and small Neptunes may also be viable targets (Spergel *et al.*, 2015). These objects will be easily observable with a larger space-based telescope designed to be capable of characterizing habitable-zone Earth-like planets (e.g. Advanced Technology Large-Aperture Space Telescope (ATLAST), Terrestrial Planet Finder (TPF), or High Definition Space Telescope (HDST)).

Figure 6.22 shows the relative sizes of the features we might observe in reflected light compared to in transmission. In transmission, the radius of the planet changes by tiny amounts due to absorption by gases through the limb of the planet's atmosphere. The observable—the transit depth—changes by only a few percent. In contrast, in reflected light, the size of features may be large. Within deep absorption bands, the planet may disappear nearly completely (100% change in reflected flux) compared to its average flux. At brighter-than-average wavelengths, it can be 100–200% brighter.

Reflected light from cold planets will be a rich source of information. Cold planets likely have thick layers of volatile clouds such as water and ammonia. Unlike in transmission spectra, where clouds tend only to damp spectral features, in reflected light, clouds actually make many features larger. Without clouds, only blue wavelengths have efficient scattering (from Rayleigh scattering by H_2 gas). At longer wavelengths, very little starlight is scattered,

and the planet just appears uniformly dark. With clouds, especially volatile clouds which scatter very efficiently, light will scatter from the cloud layers. If layers above the cloud have gases with strong absorption bands, wavelengths within those bands will appear dark. The depth of the cloud, the composition of gas above it, and the strength of the band itself all affect the size of these molecular features. By measuring the depths of several features, we can therefore extract these pieces of information. Solar system scientists have been applying these techniques for decades, and we can draw on this knowledge base as we observe exoplanets in reflected light.

6.5.5.4   High Resolution Spectra from Large Ground-based Telescopes

Another fruitful path forward to measure the compositions of hazy planets may be to observe them at very high spectral resolution ($R \geq 10^5$). Within the cores of spectral lines, the opacity is significantly higher than the average opacity across a molecular band. This means that, even with an obscuring haze, features may still be visible from absorption at the cores of these lines from the tenuous atmosphere above the haze (Kempton *et al.*, 2014). In the next decades, these observations may be possible using the thirty meter class telescopes currently planned, such as the Thirty Meter Telescope (TMT), Giant Magellan Telescope (GMT), and E-ELT (European Extremely Large Telescope).

6.6   Conclusions

We have presented models of low mass, low density planets to explore the effect of clouds and hazes which are known to be present in super Earth atmospheres such as GJ 1214b. The grids of models are GJ 1214b analogs in their gravity, radius, and host star, and span a wide

range of incident flux, metallicity and cloud properties. Key insights of this study include:

1. For cloudy atmospheres to have featureless transmission spectra, they must have both very high metallicities ($\sim 1000\times$ solar) and very inefficient cloud sedimentation compared to other clouds ($f_{\mathrm{sed}}\sim 0.01$). These characteristics seem possible but not the most probable scenario.

2. Photochemical hazes likely form at high altitudes in planets like GJ 1214b. Assuming $50\times$ solar composition, a variety of different haze particle sizes (<1 μm) and haze forming efficiencies ($f_{\mathrm{haze}}\geq 10\%$) can create featureless transmission spectra over a wide range in wavelength.

3. Methane-derived photochemical hazes will not form in planets with $T_{\mathrm{eff}}\gtrsim 1000$ K. Determining the prevalence of small planets with featureless transmission spectra over a range of incident flux will test this prediction.

4. Thermal emission spectra of these planets will be possible to attain with dedicated *JWST* time, and cloudy and hazy models may have distinct thermal emission. Cloudy thermal emission spectra have muted features and blackbody-like spectra. Photochemical hazes, depending on their optical properties, may cause mid-infrared emission features due to haze-caused temperature inversions.

5. Analysis of reflected light can distinguish between cloudy and hazy planets. Salt and sulfide clouds cause brighter albedos and potentially have features from optical properties of the clouds themselves such as ZnS at 0.53 μm. Albedos of soot-rich planets will be

very dark ($A_g \sim 2\%$).

6. Spectra of cold planets ($\sim$200 K) with ice clouds, potentially accessible to space-based coronagraphic telescopes like *WFIRST-AFTA*, will have high albedos and information-dense molecular features, and may be a key population to study to measure super Earth compositions.

Despite the challenges presented by clouds and hazes in super Earth atmospheres, there are many paths forward for understanding super Earths in the next decades. At the present, we predict that observing warmer targets (>1000 K) with *HST* will allow us to measure spectral features, because these objects should have a much less significant photochemical haze. Regardless of whether this prediction is correct, these measurements will allow us to determine which clouds and hazes are important. In the next decade, *JWST* will measure thermal emission spectra of these small planets for the first time, and potentially place constraints on the optical properties of an optically thick haze. In future decades, observing reflected light from cold planets will be a leap in information content in our spectra and will allow us to better understand this population of super Earths.

6.7   New Radiative Transfer Using `disort`

To model the thermal emission emerging from atmospheres of arbitrary composition, we developed a flexible new tool using the C version of the open-source radiative transfer code `disort` (Stamnes *et al.*, 1988; Buras *et al.*, 2011). The code `disort` is a numerical implementation of the discrete-ordinate method for radiative transfer and is a powerful tool

for monochromatic (unpolarized) radiative transfer, including absorption, emission, and scattering, in non-isothermal, vertically inhomogeneous media. It has been used for a variety of atmospheric studies in Earth's atmosphere and beyond, and here we apply it in a way that is applicable to self-luminous or irradiated exoplanets and brown dwarfs.

In this calculation, `disort` takes as inputs arrays of optical depth (τ), single scattering albedo (ω), asymmetry parameter (g), and temperature (T). The flux and intensities are returned for a given wavenumber. For multiple scattering media, several treatments of the phase function are possible within `disort`'s framework; we implement the Henyey-Greenstein phase function.

The bulk of the new calculations are written in the Python programming language. The radiative transfer scheme `disort` is in C and is called as a shared library from the main Python code.

In order to calculate the emergent spectrum, we calculate τ, ω, g, and T using the outputs of our 1D radiative–convective equilibrium code. We calculate spectra using models with 60 layers (though arbitrary numbers of layers are trivial to implement) and specify the temperatures at the 61 intersections between layers. Here we use molecular abundances calculated assuming equilibrium chemistry (though arbitrary compositions are also trivial to implement).

Our opacity database is based on Freedman *et al.* (2008) with significant updates described in Freedman *et al.* (2014), including methane (Yurchenko and Tennyson, 2014), phosphine (Sousa-Silva *et al.*, 2015), and carbon dioxide (Huang *et al.*, 2013, 2014) . We include line lists of 17 molecules: H_2, He, CO_2, H_2O, CH_4, CO, NH_3, PH_3, H_2S, Na, K, TiO, VO, FeH, CrH, Rb, and Cs. It is very easy to add additional molecules to the model if we have line lists

for their opacities. We include collision-induced opacity of H_2–H_2, H_2–He, H_2–H, and H_2–CH_4 using Richard *et al.* (2012). Rayleigh scattering is calculated for H_2, He, and CH_4 and is assumed to be isotropic (Rages *et al.*, 1991). We calculate line lists at 1060 pressure–temperature pairs from 10^{-6} bar to 300 bar and 75 K to 4000 K at $10\times$ the desired resolution (in this case, 1 cm^{-1} resolution for a final resolution of 10 cm^{-1}). We interpolate the opacities bilinearly in $\log(P)$ and $\log(T)$ space to the pressures and temperatures of the P–T profile. We use Mie scattering (within the Ackerman and Marley (2001) cloud code described in the Methods section) to calculate the single scattering albedo ω and asymmetry parameter g of the clouds for each layer at each wavenumber. We sum all opacity sources, multiplying by the appropriate abundances, and convert opacities into optical depth τ by assuming hydrostatic equilibrium,

$$\tau = \frac{\Delta P}{\mu g}\sigma \tag{6.6}$$

where ΔP is the change is pressure across a layer, μ is the mean molecular weight, g is the gravity, and σ is the opacity (cm^2 per atom or molecule).

Using the calculated values of τ, ω, g, and T, we call `disort` to calculate the flux at each wavenumber.

A comparison between this radiative transfer calculation and the forward model from a published atmospheric retrieval code `CHIMERA` (Line *et al.*, 2013) is shown in Figure 6.23. These two particular calculations use the same line lists, so this represents a test of just the radiative transfer and associated calculations. Note that the agreement is very good. `CHIMERA` calculates only absorption and emission, not scattering, so only cloud-free models can be di-

rectly compared. We have compared models that include clouds against previous similar calculations by Saumon and Marley (2008); Morley *et al.* (2014) and the agreement is also very good in regions where the line lists have not changed. Other tests comparing to other groups with different line lists and radiative transfer methods are beyond the scope of this work but would be important for understanding model uncertainties.
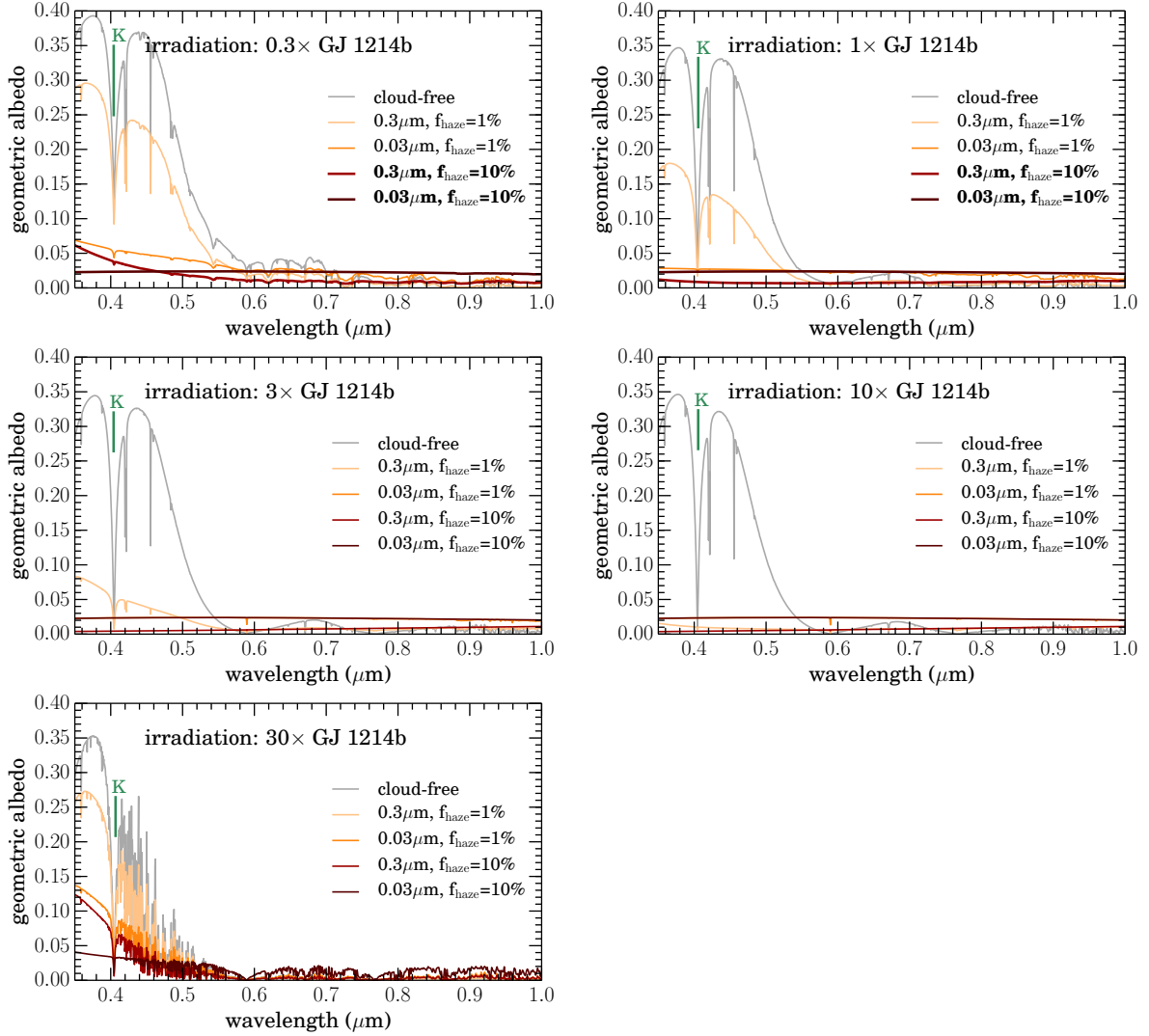
Figure 6.17: Albedo spectra with photochemical haze. Haze-free models are shown as gray lines; models with haze particle sizes of 0.03 and 0.3 μm and f_{haze} of 1 and 10% are shown as colored lines, with hazier models in darker colors. The fonts in the captions are bolded if the transmission spectrum with those parameters fits the Kreidberg *et al.* (2014a) data. Note that the scale on these plots is different from the previous albedo spectra in Figures 6.11 and 6.12.
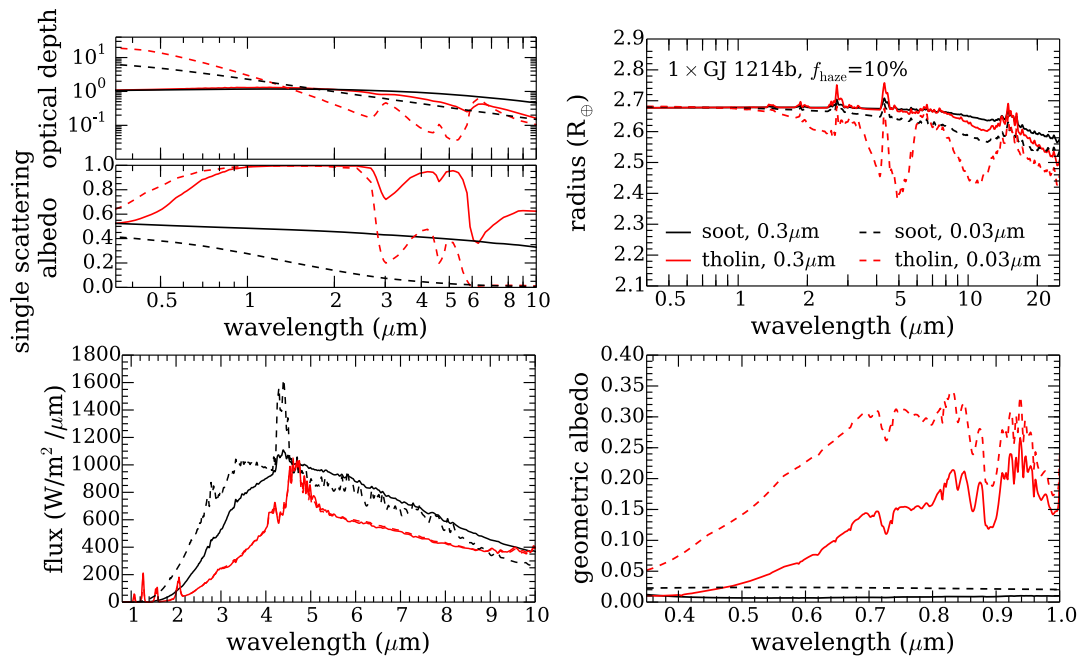
Figure 6.18: Effect of optical properties of photochemical haze on spectra. Each panel includes models with soot optical properties (black lines) and tholin optical properties (red lines) with two different particle sizes (0.3 and 0.03 μm) as solid and dashed line styles. Top left: cloud optical depth and single scattering albedo; top right: transmission spectra; bottom left: thermal emission spectra; bottom right: geometric albedo spectra.
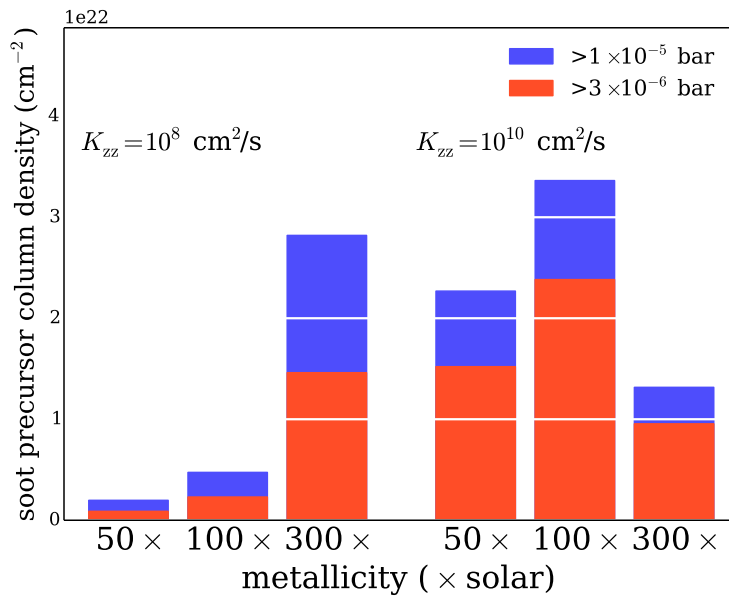
Figure 6.19: Effect of K_{zz} and metallicity on column density of soot precursors, at incident flux of GJ 1214b. Photochemical models with K_{zz}=10^8 cm^2/s are on the left and K_{zz}of10^{10} cm^2/s are on the right. At lower K_{zz}, the column densities of high altitude soot precursors increase substantially with increased metallicity. At higher K_{zz}, there is a peak at $100\times$ solar metallicity and no clear trend.
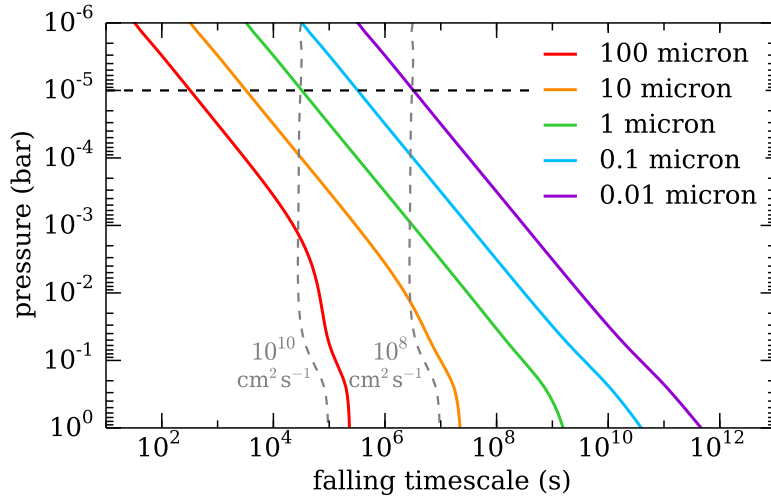
Figure 6.20: Cloud particle falling timescales. The dashed horizontal line is at 10^{-5} bar, the approximate height of GJ 1214b's haze. Solid lines show the timescale for particles to fall one pressure scale height as a function of particle size. The dashed vertical lines show the pressure scale height divided by constant K_{zz} (10^8 and 10^{10} cm^{2}s^{-1}), giving the "lofting timescale" for that K_{zz}.
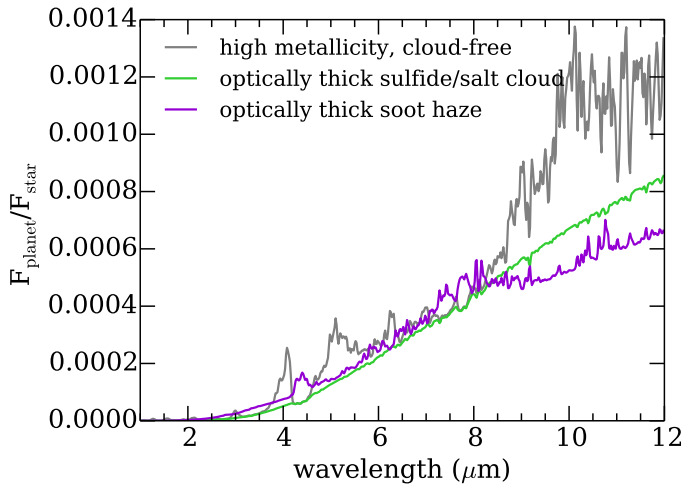
Figure 6.21: Planet star flux ratio of cloud-free, cloudy, and hazy GJ 1214b analogs. Thermal emission spectra are divided by a blackbody representing the GJ 1214b host star. Models are smoothed to R~200. All models are at GJ 1214b's incident flux. Cloud-free and cloudy model are 1000× solar metallicity, and the cloudy model has cloud parameter f_{sed}=0.01 (Na$_2$S, KCl, and ZnS clouds). The hazy model has mode particle size of 0.03 μm and f_{haze}=10%.

262
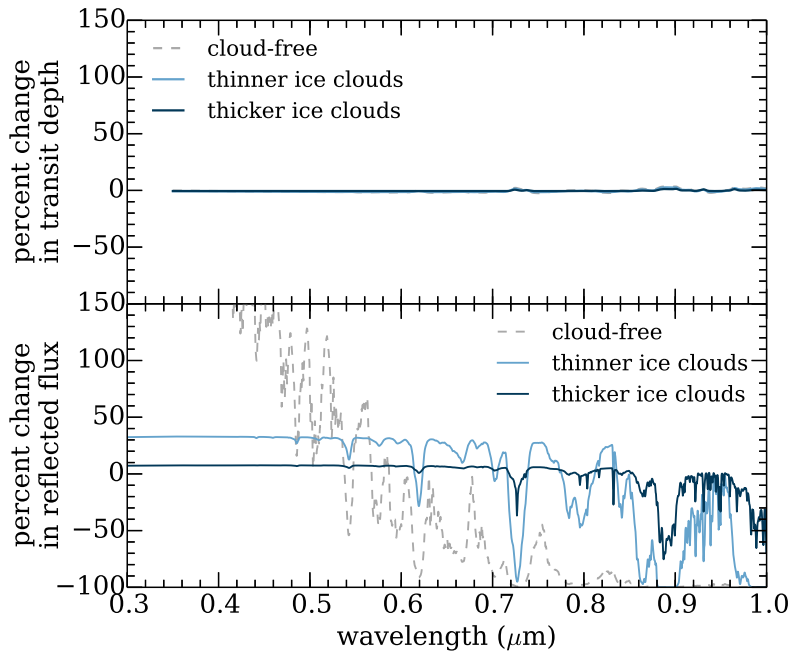
Figure 6.22: Relative amplitude of measurement compared to mean for transmission spectra (top) and reflected light spectra (bottom) for a planet with 1% GJ 1214b's incident flux, $50\times$ solar composition, and f_{sed}=1 and 0.1 for the thinner and thicker clouds respectively. The percent change in transit depth in transmission is very small, regardless of the molecules present (the cloud-free and thinner clouds lines plot are covered by the thicker clouds line). The percent change in reflected light will be up to several hundred percent, with the planet disappearing at wavelengths of very strong absorption features and becoming very bright at wavelengths with efficient scattering. As a caveat, note that the precision achievable during a transmission spectrum observation is much higher than the precision achievable in a reflected light measurement.
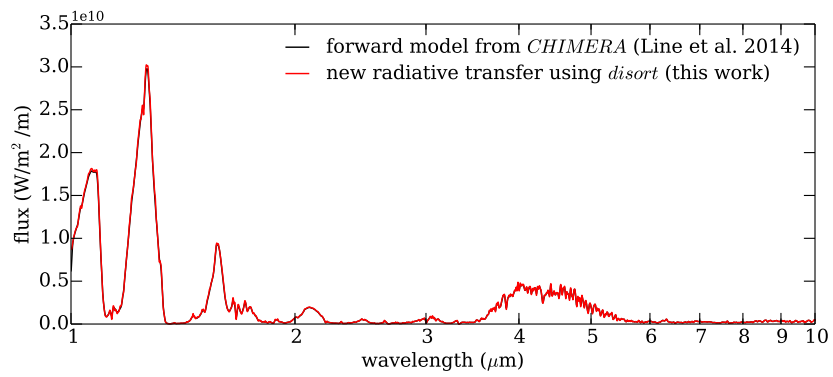
Figure 6.23: Comparison between radiative transfer methods at T_{eff}=700 K, g=3000 m s^{-2}, cloud-free. Our test model from this work is shown in red; a spectrum using identical inputs (line lists, abundances, pressure, temperature) calculated using CHIMERA is shown in black. Note the excellent agreement at all wavelengths.

Chapter 7

Forward and Inverse Modeling of the Emission and Transmission Spectrum of GJ 436b: Investigating Metal Enrichment, Tidal Heating, and Clouds

7.1   Introduction

Determining the compositions of exoplanets ranging from Earth-mass to Jupiter-mass in different environments is a key goal of exoplanetary research. Planetary compositions are shaped by the details of planet formation and altered by atmospheric physics and chemistry. Over a decade after its discovery by Butler *et al.* (2004), GJ 436b remains the planet in its Neptune-mass class for which we have obtained the most detailed observations of its atmosphere.

GJ 436b was discovered to transit by Gillon *et al.* (2007b) and, as the smallest transiting planet in 2007 and a favorable target for observations, immediately became a target for atmospheric characterization studies with the *Spitzer Space Telescope* and *Hubble Space Telescope*. It remains one of the most favorable and interesting targets for followup spectroscopic studies: to date a total of 18 secondary eclipses and 8 transits have been observed with *Spitzer*, along with 7 transits with *HST* (Deming *et al.*, 2007; Demory *et al.*, 2007; Gillon *et al.*, 2007a; Stevenson *et al.*, 2010; Beaulieu *et al.*, 2011; Knutson *et al.*, 2011, 2014a).

The atmosphere of GJ 436b has been a perennial challenge to understand. Previous observations and modeling efforts, which we describe below, have suggested high metallicity compositions with strong vertical mixing. Many of these conclusions rest on the robustness of the *Spitzer* 3.6 and 4.5 μm eclipses. Here, we move forward to study this planet using both its thermal emission photometry and its transmission spectrum, adding three new eclipse observations at these two wavelengths and analyzing the dataset with a powerful dual-pronged approach of self-consistent and retrieval modeling.

7.1.1 Observations and Interpretation of Thermal Emission

Secondary eclipse measurements allow us to infer the planet's brightness, and therefore temperature, as a function of wavelength when the planet passes behind the host star. A planet will appear fainter, and therefore create a shallower occultation, at wavelengths of strong absorption features, and appear brighter at wavelengths of emission features.

The first secondary eclipse measurements of GJ 436b were observed at 8 μm, while *Spitzer* was still operating cryogenically (Deming *et al.*, 2007; Demory *et al.*, 2007). These

observations revealed that GJ 436b has a high eccentricity, $\sim$0.15, which, given predicted tidal circularization timescales, suggests the presence of a companion and of potential tidal heating (Ribas *et al.*, 2008; Batygin *et al.*, 2009).

With an equilibrium temperature around 700–800 K, GJ 436b is cool enough that models assuming thermochemical equilibrium predict high CH_4 abundance and low CO and CO_2 abundance, which would result in a deeper occultation at 4.5 μm than 3.6 μm. However, when Stevenson *et al.* (2010) published the first multi-wavelength thermal emission spectrum of GJ 436b, measuring photometric points at 3.6, 4.5, 5.8, 8.0, 16, and 24 μm, they found that its occultation was deeper at 3.6 μm and shallower at 4.5 μm and suggested methane depletion due to photo-dissociation as an explanation. Additional studies have reanalyzed these observations and observed additional secondary eclipses (Knutson *et al.*, 2011; Lanotte *et al.*, 2014). In particular, the analysis by Lanotte *et al.* (2014) revealed a significantly shallower 3.6 μm eclipse and somewhat shallower 8.0 μm eclipse; no detailed atmospheric studies have been carried out since these revisions.

From the time of the initial observations of GJ 436b's thermal emission, it has been a major challenge to find self-consistent models that adequately explain the data. Madhusudhan and Seager (2011) found using retrieval algorithms that the atmosphere is best fit by an atmosphere rich in CO and CO_2 and depleted in CH_4. Line *et al.* (2011) used disequilibrium chemical models including the effect of photochemistry, but found that they were not able to reproduce the low observed methane abundance. Moses *et al.* (2013) found that high metallicities (230–1000$\times$ solar) favor the high CO and CO_2 abundances inferred from the observations. Agúndez *et al.* (2014), noting the high eccentricity of GJ 436b, studied the effect of tidal heat-

267

ing deep in the atmosphere on the chemistry and find that significant tidal heating and high metallicities fit the observed photometry best.

7.1.2   Observations and Interpretation of Transmission Spectrum

Wavelength-dependent observations of the transit depth of GJ 436b allow us to probe the composition of GJ 436b's day–night terminator. At wavelengths with strong absorption features, the planet will occult a larger area of the star, resulting in a deeper transit depth. Pont *et al.* (2009) observed the transmission spectrum of GJ 436b from 1.1 to 1.9 μm with NICMOS on *HST* but due to systematic effects were unable to achieve high enough precision to detect the predicted water vapor feature. Beaulieu *et al.* (2011) presented transit measurements in *Spitzer*'s 3.6, 4.5, and 8.0 μm filters that showed higher transit depths at 3.6 and 8.0 μm than at 4.5 μm, indicating strong methane absorption. However, these data were reanalyzed by Knutson *et al.* (2011) and Lanotte *et al.* (2014); the modulations in transit depth are likely due to residual instrumental effects in the light curves.

More recently, Knutson *et al.* (2014a) used WFC3 on *HST* to measure the transmission spectrum from 1.1–1.7 μm. Like Pont *et al.* (2009), they do not detect a water vapor feature, but with their higher S/N spectrum are able to rule out a cloud-free H/He-dominated atmosphere to high confidence (48σ). The spectrum is consistent with a high cloud at pressures of $\sim$1 mbar, or a H/He poor (3% H/He by mass, 1900$\times$ solar) atmospheric composition.

7.1.3 The Need for an Additional Atmospheric Study

Here, we build on this extensive history of both observations and modeling for this enigmatic warm Neptune to answer the still-outstanding questions about this planet. Do the revisions in the eclipse points from Lanotte *et al.* (2014) change the inferred composition? Is it truly ultra-high (>300× solar) metallicity? What atmospheric physics must be present for a Neptune-mass planet to have the observed spectra and inferred atmospheric composition?

To these ends, we present an additional three secondary eclipse observations (1 at 3.6 μm, 2 at 4.5 μm), demonstrating the robustness of these observations with modern *Spitzer* observational and analysis techniques. For the first time we study both the thermal emission and transmission spectra of GJ 436b in tandem, including the published dataset of *Spitzer* photometry spanning from 3.6 to 16 μm and the transmission spectrum from *HST*/WFC3. Unlike most previous studies, we investigate whether including clouds or hazes in GJ 436b's atmosphere can match both sets of observations for Neptune-like compositions (50–300 × solar), without invoking ultra-high metallicity (>1000× solar) compositions. We combine our self-consistent treatment with results from chemically-consistent retrievals that do not include clouds, and show that H/He-poor atmospheric compositions with tidal heating provide the most precise fit to GJ 436b's thermal emission spectrum, while also fitting the transmission spectrum.

7.1.3.1 Format of this work

In Section 7.2 we describe the observations and data analysis. In Section 7.3, we describe the modeling tools used to simulate the observations, including both self-consistent and retrieval models. In Section 7.4.2 we compare the data to self-consistent models; in Section

Table 7.1: *Spitzer* Observation Details

λ (μm)	UT Start Date	Length (h)	n_{img}[a]	t_{int} (s)[b]	t_{trim}[c]	n_{bin}[c]	r_{pos}[c]	r_{phot}[c]	Bkd (%)[e]
3.6	2008-01-30	5.9	163,200	0.1	1.0	192	3.0	2.8	0.05
3.6	2014-07-29	4.5	122,112	0.1	1.0	128	2.0	2.5	0.25
4.5	2008-02-02	5.9	49,920	0.4	3.0	32	2.0	2.9	0.09
4.5	2011-01-24	6.1	51,712	0.4	2.0	32	2.0	4.5	0.38
4.5	2014-08-11	4.5	122,112	0.1	0.5	128	2.0	2.7	0.11
4.5	2015-02-25	4.5	122,112	0.1	0.5	128	2.0	2.8	0.12

[a]Total number of images.

[b]Integration time.

[c]t_{trim} is the amount of time in hours trimmed from the start of each time series, n_{bin} is the bin size used in the photometric fits, r_{pos} is the radius of the aperture used to determine the position of the star on the array, and r_{phot} is the radius of the photometric aperture in pixels.

[e]Sky background contribution to the total flux for the selected aperture.

7.4.3 we use retrieval algorithms to retrieve chemical abundances and pressure–temperature profile and compare these results with the results from self-consistent modeling.

7.2 Observations and Data Analysis

7.2.1 Photometry and Instrumental Model

These observations were obtained in the 3.6 and 4.5 μm bandpasses using the Infra-Red Array Camera (IRAC) on the *Spitzer Space Telescope*. In this paper we present three new secondary eclipse observations of this planet, including a 3.6 μm observation obtained on UT 2014 Jul 29 and two 4.5 μm observations obtained on UT 2014 Aug 11 and UT 2015 Feb 25, respectively, as part of *Spitzer* program 50056 (PI: Knutson). We also re-examine three archival eclipse observations including a 3.6 μm eclipse from UT 2008 Jan 30, as well as 4.5 μm eclipses from UT 2008 Feb 2 and UT 2011 Jan 24 (Stevenson *et al.*, 2010, 2012; Lanotte *et al.*, 2014). Eclipses from 2008 were observed during *Spitzer's* cryogenic mission, while the remaining eclipses were observed during the extended warm mission. All eclipses were

observed in subarray mode, with integration times and observation durations given in Table 7.1. Our new 2014-2015 observations included a now-standard 30-minute peak-up pointing observation prior to the start of our science observations. This adjustment corrects the initial telescope pointing in order to place the star near the center of the pixel where the effect of intrapixel sensitivity variations is minimized.

We utilize BCD image files for our photometric analysis and extract BJD_{UTC} mid-exposure times using the information in the image headers. We then estimate and subtract the sky background, calculate the flux-weighted centroid position of the star on the array, and derive the corresponding total flux in a circular aperture for each individual image as described in previous studies (e.g. Lewis *et al.*, 2013; Deming *et al.*, 2015; Kammer *et al.*, 2015). We consider both fixed and time varying photometric aperture sizes in our fits but find that in all cases we obtain a lower RMS and reduced levels of time-correlated ("red") noise in our best-fit residuals using fixed apertures, in good agreement with the conclusions of Lanotte *et al.* (2014). We consider apertures with radii ranging between $2.0 - 5.0$ pixels, where we step in increments of 0.1 pixels between $2.0 - 3.0$ pixels and in 0.5 pixel increments for larger radii.

The sensitivity of individual 3.6 and 4.5 μm IRAC pixels varies from the center to the edge; when combined with short-term telescope pointing oscillations, this produces variations in the raw stellar fluxes plotted in Fig. 7.1. We correct for this effect using the pixel-level decorrelation (PLD) method (Deming *et al.*, 2015), which produces results that are comparable to or superior to those from a simple polynomial decorrelation or pixel mapping method for light curves with durations of less than ten hours (for a discussion of the PLD method applied to longer phase curve observations, see Wong *et al.*, 2015). We utilize the raw flux values in

271

a 3×3 grid of pixels centered on the position of the star, and then normalize these individual pixel values by dividing by the total flux in each 3×3 postage stamp. We then incorporate these light curves into an instrumental model given by:

$$F_{model}(t) = \frac{\sum_i w_i F_i(t)}{\sum_i F_i(t)} \tag{7.1}$$

where F_{model} is the predicted stellar flux in an individual image, F_i is the measured flux in the ith individual pixel, and w_i is the weight associated with that pixel. We leave these weights as free parameters in our fit, and solve for the values that best match our observed light curves simultaneously with our eclipse fits.

Following the example of Deming *et al.* (2015), we fit this model to binned light curves with bin sizes given in Table 7.1. After identifying the best-fit model we apply this solution to the unbinned light curves in order to generate corresponding plots. As discussed in Deming *et al.* (2015) and Kammer *et al.* (2015), we create a metric to measure the noise properties of a given version of the photometry by calculating the root mean square (RMS) variance of the residuals as a function of bin size (Fig. 7.2). We then take the difference between a Gaussian noise model with $1/\sqrt{n}$ scaling and the observed RMS as a function of bin size, square the difference, and sum over all bins. We then pick the version of the photometry that has the lowest amount of red noise as measured by our least squares metric after discarding solutions where the RMS of the best-fit residuals is more than 1.1 times higher than the lowest RMS version of the photometry. We trim a small section of data from the start of each light curve in order to remove the exponential ramp, which is another well-known feature of the

Table 7.2: Best Fit Eclipse Parameters

λ (μm)	UT Start Date	F_p/F_* (ppm)	$F_p/F_{*,avg}$ (ppm)[a]	T_{bright} (K)[a]	T_s[b]	$O-C$ (d)[c]
3.6	2008-01-30	177 ± 31	151 ± 27	879^{+29}_{-27}	4496.4888 ± 0.0012	-0.0007 ± 0.0012
3.6	2014-07-29	133 ± 35			6868.0655 ± 0.0054	-0.0006 ± 0.0054
4.5	2008-02-02	30 ± 36	29 ± 20	< 633	4499.1334[d]	
4.5	2011-01-24	37 ± 37			5585.7756[d]	
4.5	2014-08-11	64 ± 45			6881.2856[d]	
4.5	2015-02-25	1 ± 44			7079.5779[d]	

[a]We report the error-weighted mean eclipse depths at 3.6 and 4.5 μm. Brightness temperatures are calculated using a PHOENIX stellar model interpolated to match the published stellar temperature and surface gravity from von Braun *et al.* (2012).

[b]BJD$_{UTC}$ - 2,450,000.

[c]Observed minus calculated eclipse times, where we have accounted for the uncertainties in both the measured and predicted eclipse times as well as the XX s light travel time delay in the system. We calculate the predicted eclipse time using the best-fit eclipse orbital phase from Knutson *et al.* (2011).

[d]We allow the eclipse times in this bandpass to vary as free parameters in our fit, but we use the orbital phase and corresponding uncertainty from Knutson *et al.* (2011) as a prior constraint in the fit.

[e]2σ upper limit based on the error-weighted average of the four 4.5 μm eclipse measurements.

IRAC 3.6 and 4.5 μm arrays (e.g., Lewis *et al.*, 2013; Zellem *et al.*, 2014). After selecting the optimal aperture and bin sizes, we examine the normalized light curves after detector effects have been removed and trim until no ramp is visible at the start of the observations. We then re-run our previous analysis in order to ensure that our aperture and bin sizes are still optimal given this new trim duration.

7.2.2 Eclipse Model and Uncertainty Estimates

We generate our secondary eclipse light curves using the routines from Mandel and Agol (2002), where we fix the planet-star radius ratio, orbital inclination, eccentricity e, longitude of periapse ω, and ratio of the orbital semi-major axis to the stellar radius to their best-fit values from Lanotte *et al.* (2014). We allow individual eclipse depths and center of eclipse times to vary as free parameters in our fits to the 3.6 μm data. We find that the eclipse depth in individual 4.5 μm observations is consistent with zero, and therefore place a Gaussian prior on

273

the phase of the secondary eclipse in order to constrain the best-fit eclipse time. We implement this prior as a penalty in χ^2 proportional to the deviation from the error-weighted mean center-of-eclipse phase and corresponding uncertainty from Knutson *et al.* (2011). Although we also calculate the best-fit eclipse orbital phase using the e and ω values from Lanotte *et al.* (2014) and find that it is consistent with the value from Knutson *et al.* (2011), the corresponding uncertainty is substantially larger than that reported in Knutson *et al.* (2011). This is not surprising, as the measured times of secondary eclipse constrain $e\cos\omega$ while $e\sin\omega$ is typically derived from fits to radial velocity data and has larger uncertainties (e.g. Pál *et al.*, 2010; Knutson *et al.*, 2014c). The uncertainties in the values for e and ω reported in Lanotte *et al.* (2014) are therefore likely to be dominated by the $e\sin\omega$, while $e\cos\omega$ is well-measured from secondary eclipse photometry alone. As a test we repeat our 3.6 μm fits including this prior on the eclipse phase and find that the measured eclipse depths change by less than 0.1 sigma, as expected for cases where the eclipse is detected at a statistically significant level.

We fit our combined eclipse and instrumental noise model to each light curve using a Levenberg-Marquardt minimization routine with uniform priors on all parameters except the 4.5 μm eclipse time as described in the previous paragraph. Our model includes nine pixel weight parameters, two eclipse parameters, and a linear function of time in order to account for long-term instrumental and stellar trends. We show the resulting light curves and best-fit eclipse models after dividing out the best-fit instrumental noise model and linear function of time in Fig. 7.3. Uncertainties on model parameters are calculated using a Markov chain Monte Carlo (MCMC) analysis with 10^6 steps initialized at the location of the best-fit solution from our Levenberg-Marquardt minimization. We trim any remaining burn-in at the start of

the chain by checking to see where the χ^2 value of the chain first drops below the median value over the entire chain, and trim all points prior to this step. We find that in all cases our probability distributions for the best-fit eclipse depths and times are Gaussian and do not show any correlations with other model parameters. We therefore take the symmetric 68% interval around the median parameter value as our 1σ uncertainties.

7.3   Atmospheric Modeling

We use a combination of self-consistent modeling and retrieval algorithms to model the atmosphere of GJ 436b and match its spectrum. The self-consistent modeling mirrors that used in Morley *et al.* (2015); our suite of tools includes a 1D radiative–convective model to calculate the pressure–temperature structure, a photochemical model to calculate the formation of hydrocarbons that may form hazes, and a cloud model to calculate cloud mixing ratios, altitudes, and particle sizes. We calculate spectra in different geometries and wavelengths using a transmission spectrum model, a thermal emission spectrum model, and an albedo model. We also use a retrieval model, CHIMERA (Line *et al.*, 2012, 2013, 2014) to explore the thermal emission spectrum. In the following subsections we will briefly discuss each of these calculations.

7.3.1   1D Radiative–Convective Model

We calculate the temperature structures of GJ 436b's atmosphere assuming radiative–convective equilibrium. These models are more extensively described in McKay *et al.* (1989); Marley *et al.* (1996); Burrows *et al.* (1997); Marley *et al.* (1999, 2002); Fortney *et al.* (2005);

Saumon and Marley (2008); Fortney *et al.* (2008b). Our opacity database for gases is described

in Freedman *et al.* (2008, 2014). We calculate the effect of cloud opacity using Mie theory,

assuming spherical particles. Optical properties of sulfide and salt clouds and soot haze are

from a variety of sources and presented in Morley *et al.* (2012) and Morley *et al.* (2013).

To calculate P–T profiles for models with greater than $50\times$ solar metallicity, we make

the same approximation as used in Morley *et al.* (2015). We multiply the total molecular gas

opacity by a constant factor (e.g. we multiply the $50\times$ solar opacities by 6 to approximate the

opacity in a $300\times$ solar composition atmosphere). We change the abundances of hydrogen and

helium separately to calculate collision-induced absorption. This approximation is appropriate

for the results explored here; for future work, e.g. comparing models to *JWST* data, new k-

coefficients at 100–1000Œ solar metallicity should be used.

7.3.2   Equilibrium Chemistry

After calculating the pressure–temperature profiles of models with greater than $50\times$

solar metallicity, we calculate the gas abundances assuming chemical equilibrium along that

profile. We use the Chemical Equilibrium with Applications model (CEA, Gordon & McBride

1994) to compute the thermochemical equilibrium molecular mixing ratios (with applications

to exoplanets see, Visscher *et al.* (2010); Line *et al.* (2010); Moses *et al.* (2011); Line *et al.*

(2011); Line and Yung (2013b)). CEA minimizes the Gibbs Free Energy with an elemental mass

balance constraint given a local temperature, pressure, and elemental abundances. We include

molecules containing H, C, O, N, S, P, He, Fe, Ti, V, Na, and K. We account for the depletion

of oxygen due to enstatite condensation by removing 3.28 oxygen atoms per Si atom (Burrows

and Sharp, 1999). When adjusting the metallicity all elemental abundances are rescaled equally relative to H, ensuring that the elemental abundances sum to one.

7.3.3 Photochemical Haze Model

We use results from photochemical modeling in Line *et al.* (2011). Briefly, the computations use the Caltech/JPL photochemical and kinetics model, KINETICS (a fully implicit, finite difference code), which solves the coupled continuity equations for each species and includes transport via both molecular and eddy diffusion (Allen *et al.*, 1981; Yung *et al.*, 1984; Moses *et al.*, 2005). We use results for $50\times$ solar composition, $K_{zz}=10^8$ cm^2/s (Figures 5, 6 and 7 in Line *et al.* (2011)).

We follow the approach developed in Morley *et al.* (2013) and used for GJ 1214b in Morley *et al.* (2015) to calculate the locations of soot particles based on the photochemistry. We sum the number densities of the five soot precursors (C_2H_2, C_2H_4, C_2H_6, C_4H_2, and HCN) to find the total mass in soot precursors. We assume that the soots form at the same altitudes as the soot precursors exist: we multiply the precursors' masses by our parameter f_{haze} (the mass fraction of precursors that form soots) to find the total mass of the haze particles in a given layer. We vary both f_{haze} and the mode particle size as free parameters, and calculate the optical properties of the haze using Mie theory.

7.3.4 Sulfide/Salt Cloud Model

To model sulfide and salt clouds, we use a modified version of the Ackerman and Marley (2001) cloud model (Morley *et al.*, 2012, 2013, 2015). Cloud material in excess of

the saturation vapor pressure of the limiting gas is assumed to condense into spherical, homogeneous cloud particles. We extrapolate the saturation vapor pressure equations from Morley *et al.* (2012) to high metallicites, which introduces some uncertainties but serves as a reasonable first-order approximation for the formation of these cloud species. Cloud particle sizes and vertical distributions are calculated by balancing transport by advection with particle settling.

7.3.5 Thermal Emission Spectra

We use a radiative transfer model developed in Morley *et al.* (2015) to calculate the thermal emission of a planet with arbitrary composition and clouds. Briefly, this model includes the C version of the open-source radiative transfer code `disort` (Stamnes *et al.*, 1988; Buras *et al.*, 2011) which uses the discrete-ordinate method to calculate intensities and fluxes in multiple-scattering and emitting layered media.

7.3.6 Albedo Spectra

We calculate albedo spectra following the methods described in Toon *et al.* (1977, 1989); McKay *et al.* (1989); Marley *et al.* (1999); Marley and McKay (1999a); Cahoy *et al.* (2010). Here, we use the term geometric albedo to refer to the albedo spectrum at full phase (α=0, where the phase angle α is the angle between the incident ray from the star to the planet and the line of sight to the observer):

$$A_g(\lambda) = \frac{F_p(\lambda, \alpha = 0)}{F_{\odot, L}(\lambda)} \tag{7.2}$$

where λ is the wavelength, $F_p(\lambda, \alpha = 0)$ is the reflected flux at full phase, and $F_{\odot,L}(\lambda)$ is the flux from a perfect Lambert disk of the same radius under the same incident flux.

7.3.7 Retrieval Model

To more thoroughly explore the chemically plausible parameter space allowed by the emission spectrum, we employ the chemically consistent atmospheric retrieval scheme described in Kreidberg *et al.* (2015) and Greene *et al.* (2016) based on the CHIMERA (Line *et al.*, 2013, 2014) emission forward model. The retrieval uses the 6 parameter analytic radiative equilibrium temperature profile scheme of Parmentier and Guillot (2014) (see Line *et al.* (2013) for implementation within the emission retrieval) where the free parameters are the infrared opacity (κ_{IR}), the ratio of the visible to infrared opacity for two visible streams (γ_1, γ_2), the partitioning between the two visible streams (α), scaling to the top-of-atmosphere irradiation temperature (β, to accommodate for the unknown albedo and redistribution), and finally the internal temperature (T_{int}). These parameters are all free parameters, not recalculated to be consistent with the derived abundances.

The molecular abundances are initially computed along the temperature profile under the assumption of thermochemical equilibrium (using the Chemical Equilibrium with Applications routine, Gordon & McBride 1994;1996; Line *et al.* (2010); Moses *et al.* (2011); Line *et al.* (2011)) given the bulk atmospheric metallicity ([M/H]) and carbon-to-oxygen ratio (C/O). To account for possible disequilibrium chemistry we include a "quench pressure" parameter (P_{quench}) whereby the abundances of H_2O, CH_4, and CO above the quench are fixed at their quench pressure values, a valid representation of many disequilibrium models (e.g., Moses

Table 7.3: Uniform prior ranges on the retrieved parameters

parameter	range
$\log(\kappa_{IR})[\text{cm}^2/\text{g}]$	-3 to 0
$\log(\gamma_1, \gamma_2)$	-3 to 2
α	0 to 1
β	0 to 2
T_{int} (K)	100 to 400
M/H	10^{-4} to $10^4 \times$ solar
$\log(C/O)^a$	-2 to 2
$\log(P_{quench})$ [bar]	-6 to 1.5

[a]Solar $\log(C/O)$ is -0.26.

et al., 2011; Line *et al.*, 2011; Zahnle and Marley, 2014). The temperature profile and chemistry parameters result in a total of 9 free parameters. Bayesian estimation is performed using a multi-modal nested sampling algorithm (Feroz *et al.*, 2009) implemented with the PYMULTI-NEST routine (Buchner *et al.*, 2014) recently employed in Line and Parmentier (2016), with generous uniform priors on each parameter (see Table 7.3).

[b!]

7.4 Results

7.4.1 Observations

The new eclipse depths are shown in Table 7.2 and Figure 7.4. Our eclipse depths of 151 ± 27 ppm at 3.6 μm and 29^{+20}_{-16} ppm at 4.5 μm are consistent to 1-σ with those published in Lanotte *et al.* (2014) (177 ± 45 and 28^{+25}_{-18} ppm respectively), with a moderate reduction in the uncertainties in both bands. This result serves as confirmation of the high flux at 3.6 μm compared to 4.5 μm.

7.4.2 Self-Consistent Modeling

We ran a variety of models from 50–1000$\times$ solar metallicity, varied heat redistribution (planet-wide average and dayside average), internal temperatures (T_{int}) from 100–400 K, with clouds (f_{sed}=0.01–1), and hazes with particle sizes from 0.01–1 μm and f_{haze} from 1–30%. We compare each model to the thermal emission photometry from this work (3.6 and 4.5 μm) and from Lanotte *et al.* (2014) (5.6, 8.0, 16 μm), using a chi-squared analysis to assess relative goodness-of-fit between the models.

We show example pressure–temperature profiles along with cloud condensation curves in Figure 7.5. Raising the internal temperature, T_{int}, increases the temperature of the deep atmosphere (P$\gtrsim$0.1 bar). The heat redistribution of incident stellar flux controls the temperature in the upper atmosphere. GJ 436b's profile crosses condensation curves of sulfides and salts, suggesting that if the atmosphere is cloudy, those clouds may be composed of Na_2S, KCl, and ZnS.

7.4.2.1 Best-fit fiducial model

Of the 288 models in our grid of cloudy and cloud-free planets, our nominal best-fit set of parameters are:

- 1000$\times$ solar metallicity

- T_{int}=240 K

- f_{sed}=0.3 sulfide/salt clouds

- disequilibrium chemistry via quenching

- full heat redistribution (planet-wide average PT profile)

This model provides an excellent fit to the transmission spectrum ($\chi^2_{red} < 1$ assuming 3 degrees of freedom), though an inadequate fit to the thermal emission ($\chi^2_{red} \sim 11$ assuming 3 degrees of freedom). We show the thermal emission and transmission spectra in Figure 7.6.

7.4.2.2 Equilibrium and disequilibrium chemistry

As has been discussed in the literature (Stevenson *et al.*, 2010; Line *et al.*, 2011; Moses *et al.*, 2013), GJ 436b's high 3.6 μm flux and low 4.5 μm flux indicate that it likely has a high abundance of CO and CO_2 relative to CH_4. Since equilibrium chemistry for an object at GJ 436b's temperature would instead result in high abundances of CH_4 at metallicities similar to Neptune, this indicates that GJ 436b's chemistry is in disequilibrium. This disequilibrium may be due to a combination of vertical mixing, photochemistry, and other effects (Line *et al.*, 2011). Here, we approximate the effect of disequilibrium chemistry by 'quenching' the abundances of the carbon species (CO, CO_2, CH_4) in the atmosphere at deep pressures (10 bar), effectively setting the abundances of these species to be constant through the atmosphere.

The resulting effect of disequilibrium chemistry on spectra is shown in Figure 7.7. In equilibrium, the model predicts that GJ 436b would be very faint at 3.6 μm, and progressively brighter at redder wavelengths. In disequilibrium, as is observed in the data, the planet is predicted to be brighter at 3.6 μm due to decreased absorption by CH_4. In general, even the models that include disequilibrium chemistry overpredict the brightness at 4.5 μm compared to the observed flux, despite the higher abundance of CO and CO_2 in disequilibrium.

7.4.2.3 Metallicity

Increasing the metallicity of GJ 436b's atmosphere allows us to fit both the thermal emission and transmission spectrum more accurately. There are two reasons for this. As has been discussed at length in Moses *et al.* (2013), high metallicity atmospheres are predicted, in equilibrium or disequilibrium, to have higher abundances of CO and CO_2 relative to CH_4. Pushing the chemistry to CO/CO_2-rich compositions is crucial to match GJ 436b's thermal emission. We show this effect in Figure 7.8; models at high metallicities have higher flux at 3.6 and 8 μm due to the change in chemistry. We find that this effect partially saturates at metallicities greater than 300$\times$ solar.

High metallicities also make it much easier to flatten the transmission spectrum of GJ 436b sufficiently to match the featureless HST/WFC3 transmission spectrum even in the absence of clouds (Knutson *et al.*, 2014a). In Figure 7.9 we show cloud-free models for different metallicities. While at metallicities lower than 1000$\times$ solar metallicity clouds are required to sufficiently flatten the spectrum, for models above 1000$\times$ solar metallicity even cloud-free models have high enough mean molecular weights that the size of the features, which scale according to the scale height of the atmosphere, are small enough that they appear featureless at the S/N of the data.

7.4.2.4 Tidal heating

As a Neptune-sized planet orbiting an old star, without an additional energy source, GJ 436b's interior temperature T_{int} would be $\sim$60 K, slightly warmer than Neptune which has a $T_{int} \sim$50 K (Fortney *et al.*, 2007). However, GJ 436b is on an eccentric orbit (e$\sim$0.15) despite

orbiting its star at a semi major axis where it is predicted to have a tidally circularized orbit, indicating that its interior may still be heated by tidal dissipation. Moses *et al.* (2013) and Agúndez *et al.* (2014) both considered the effect of tidal heating, noting that a hotter interior changes the chemistry of the deep interior and therefore the resulting emission spectrum.

Increasing T_{int} tends to move the deep P–T profile (see Figure 7.5) to regions with high CO/CO_2 and lower CH_4 abundances, which allows us to better match the observed spectrum. Heating the deep atmosphere also increases the effective temperature of the atmosphere by changing the P–T profile, increasing flux at all *Spitzer* wavelengths. This effect is shown in Figure 7.11 for three different T_{int} values (100, 240, and 400 K). Best-fit models cluster around T_{int}=240 K, a temperature that allows us to match the 3.6, 5.6, and 8.0 μm points relatively well, while over predicting the 4.5 μm flux somewhat.

We note that this is the first indication that the internal temperature of a planet has an important and observable effect on the emission spectrum of a transiting planet.

7.4.2.5 Clouds

Clouds increase opacity across all wavelengths as (relatively) gray absorbers. This means that including clouds decreases flux between absorption features (e.g. at 3.6 and 8.0 μm for GJ 436b's composition) and somewhat less significantly at the locations of absorption features where the planet is already dark. Thinner clouds (f_{sed}=0.3–1 in our parameterization) alter the spectrum slightly, while thicker clouds ($f_{sed} \leq 0.1$) create a blackbody-like spectrum with the temperature of the top of the cloud. Comparing this to the observed photometry of GJ 436b, these thick clouds significantly under predict the flux at 3.6 μm especially.

In transmission, clouds flatten the spectrum without increasing the mean molecular weight of molecular gas in the atmosphere. As discussed above, for metallicities $\sim1000\times$ solar, no additional cloud opacity is needed to match the featureless spectrum ($\chi^2_{\mathrm{red}}\sim1$ for all models). At $300\times$ solar metallicity, thin clouds (f_{sed}=1) adequately obscure the spectral features, whereas for a Neptune-like $100\times$ solar composition, f_{sed}=0.3 clouds are required. In the Ackerman and Marley (2001) prescription, lower f_{sed} values indicate less efficient sedimentation, causing smaller particles sizes and more lofted clouds.

7.4.2.6 Photochemical Hazes in GJ 436b

We investigate the effect of photochemical hazes on the thermal emission spectrum of GJ 436b. Morley *et al.* (2015) showed that it is possible for optically thick photochemical hazes (such as those postulated to exist in GJ 1214b) to cause a temperature inversion in the upper atmospheres of planets. This can change the spectrum such that molecules that would normally be seen in absorption in a planet without a temperature inversion such as methane are actually seen in emission in an atmosphere with a temperature inversion. We tested whether this process could be happening on GJ 436b and causing the observed thermal emission.

The results of this investigation are summarized in Figure 7.13. The top panel shows the thermal emission of the planet alone. We find that it is possible to create a temperature inversion with dark soot-like photochemical haze in GJ 436b, especially for relatively small particle sizes. As expected, methane is seen in emission, significantly brightening the model spectrum at 3.6 μm compared to a haze-free model. As in Morley *et al.* (2015), CO_2 at 4.3 μm is also predicted to be seen in emission at Neptune-like metallicities (in this case $50\times$ solar

metallicity). In the bottom panel, we show the planet-star flux ratio; here it becomes clear that the hazy model does not fit the observations significantly better than the haze-free model. In particular, the model spectrum is much fainter than the planet's 3.6 μm photometric point. The 4.5 μm flux, despite the significant changes to the shape of the spectrum across the bandpass, remains nearly identical across the range of hazy models tested.

In general, we find that even though a temperature inversion in a methane-rich atmosphere can increase the 3.6 μm flux, it is not a significant enough effect to match the observed flux, and, furthermore, the flux within the 4.5 μm region can also increase due to emission in the CO_2 bandpass. We conclude that photochemical hazes cannot erase the need for an atmosphere with significant CO and CO_2 and a low abundance of CH_4. This required low-CH_4 atmospheric composition, in turn, reduces the likelihood that carbon-based photochemical hazes will be significant in the atmosphere (Fortney *et al.*, 2013).

7.4.3 Retrievals

We have shown in Section 7.4.2 that we favor models at high metallicity, with both disequilibrium chemistry and tidal heating; these three properties combine to maximize the CO/CO_2 abundances and minimize CH_4 abundance, allowing the models to match approximately with the measured photometry. Retrieval models provide a quantitative way to test these conclusions and fully explore parameter space beyond our self-consistent model grids.

We find that retrieval methods draw similar conclusions to the self-consistent modeling; GJ 436b appears to be very high metallicity, with evidence for both deeply-quenched disequilibrium chemistry and thermal heating of the deep interior. For the dayside thermal

emission spectrum, the best-fit retrieved solution has a goodness-of-fit divided by number of data points χ^2/N=2.02, compared to χ^2/N=4.54 for the best self-consistent thermal emission spectrum, indicating a significantly improved fit.

7.4.3.1 Retrieved Posterior Probability Distributions

Retrieved posterior probability distributions and correlations are shown in the stair-pair plot in Figure 7.14 for 5 of the 9 free parameters in the retrieval: β, T_{int}, [M/H], log(C/O), log(P_{quench}). The best-fit models have:

- High metallicity. The maximum likelihood model has a metallicity of $\sim$6000$\times$ solar metallicity, with a 3-σ lower limit on the metallicity of 106$\times$ solar.

- Disequilibrium chemistry. The maximum likelihood model has a quench pressure around 9 bar (with a wide range of values for P_{quench} allowed).

- Enhanced internal temperature. The maximum likelihood T_{int} is 336 K (with large uncertainties), indicating that tidal heating may be increasing GJ 436b's internal temperature, in agreement with the tidally heated self-consistent models.

- Solar C/O ratio. The maximum likelihood C/O ratio is 0.70, with a sharp cut-off at higher C/O ratios and a long tail to lower C/O ratios.

In Figure 7.15 we compare the retrieved P–T profile to self-consistent models at 300 $\times$ solar metallicity. We find that retrieved profile is in remarkable agreement with self-consistent models that include the effect of tidal heating in the deep interior. Our best-fit T_{int} from the self-consistent modeling approach (240 K) falls within the 2-σ range of the retrieved profile.

The contribution functions for each of the *Spitzer* bandpasses are also shown in Figure 7.15. 3.6 μm probes the deepest pressures, probing pressures as high as 1 bar. As expected, comparing the contribution functions to the range of P–T profiles found by the retrieval, the spread in allowed P–T profiles increases for pressures deeper than 1 bar. The other wavelengths probe lower pressures of the atmosphere, with 5.8 and 8.0 μm centered around 0.05 bar and 16 μm centered around 0.003 bar. The 4.5 μm bandpass has the largest range of pressures, with a peak at deep pressures (0.2 bar) and a long tail to low pressures, unsurprising given that the band covers the spectrum where the modulation is the greatest.

Figure 7.16 shows the best-fit retrieved range of spectra compared to both the data and the best-fit self-consistent model. The retrieved best-fit is statistically and by-eye a somewhat better fit to the data than the self-consistent models. In particular, it has higher flux at 3.6 μm and lower flux at 4.5 μm. Both the retrieved and self-consistent models fit the 5.6 and 8.0 μm points well; the 16 μm photometry is underestimated by both models, though the error bar is large.

7.5   Discussion

7.5.1   Predictions for Reflected Light Spectra

Cloud properties have the strongest effect on the predicted reflected light spectrum of GJ 436b. Cloud-free models are dark from 0.6–1μm (A_g<1%) and somewhat brighter (up to $A_g \sim$10%) at bluer wavelengths, as is generally true for cloudless giant planets (Marley *et al.*, 1999; Sudarsky *et al.*, 2000). Thinner clouds (f_{sed}=0.3–1) are brighter with albedos between a

few percent and tens of percent. Thicker clouds (f_{sed}=0.1) have the brightest albedos from 0.6 to 1μm, up to nearly 30%. Some example cloudy spectra are shown in the top panel of Figure 7.17.

Other properties have weaker effects on the reflected light spectrum for this planet. For example, models with metallicities from 100–300× solar metallicity are shown in the bottom panel of Figure 7.17. Increasing the metallicity (which also changes the cloud) increases the geometric albedo across the spectrum.

7.5.2 Is [M/H]>1000× Solar Reasonable?

We find that the best-fit atmospheric models have high metallicities, but it remains to be seen whether these values are physically realistic. GJ 436b has a different host star, equilibrium temperature, and orbit than the ice giants in our own solar system, so it likely formed and evolved in very different conditions. The maximum metal-enrichment of the envelope of a Neptune-mass exoplanet is not yet known. Studies of this to date, including Fortney *et al.* (2013), have suggested that a diverse range of outcomes might be expected for planets in this intermediate mass regime between Earth and Saturn, with potentially high atmospheric enrichments in some cases.

Furthermore, because of the uncertainty in the internal entropy of GJ 436b, its mass and radius do not provide strong limits on the metal-enrichment of the envelope. Nettelmann *et al.* (2010) find that a minimum H/He fraction of 10^{-3} M_p is necessary to match the radius. This very low H/He fraction would require a warm planetary interior, as is favored by the best-fit thermal emission spectra in this work.

These very high metallicities are only possible if accretion and subsequent enrichment is dominated by rocky rather than icy materials. Fortney *et al.* (2013) show that if the majority of accretion is from icy material, the hydrogen in those ices is also accreted and the maximum metal-enrichment is about $\sim$600$\times$ solar metallicity. If GJ 436b is indeed >1000$\times$ solar composition, it likely formed in a region with more refractory than volatile materials available.

7.5.3   Role of JWST Spectral Observations

JWST will amplify our understanding of warm Neptunes like GJ 436b by providing spectra instead of photometry, breaking some of the current degeneracies. For example, examining the spectra in Figure 7.16, it is clear that models with very different spectra can have very similar photometry. *JWST* may also allow us to detect molecules that are not currently included in most models; for example, Shabram *et al.* (2011) showed that if species such as C_2H_2 and HCN exist in the atmosphere of GJ 436b, their abundances could be constrained by measuring the widths of features at 1.5, 3.3, and 7 μm.

Greene *et al.* (2016) quantify our ability to constrain planet properties of a wider variety of atmospheres including hot Jupiters, warm Neptunes, warm sub-Neptunes, and cool super Earths with *JWST* and find that the mixing ratios of major species in warm Neptunes like GJ 436b can be constrained to within better than 1 dex with a single secondary eclipse observation for each wavelength region from 1–11 μm.

7.5.4 Measuring Internal Dissipation Factor Using T_{int}

Measuring T_{int} of GJ 436b using atmospheric models allows us to approximate the dissipation factor in GJ 436b's interior, Q'. Q' is defined as $3Q/2k_2$, where Q is the quality factor and k_2 is the Love number of degree 2 (Goldreich and Soter, 1966). Our best-fit T_{int} from the retrieval analysis is 336 K. Agúndez *et al.* (2014) calculated relations between T_{int} and Q' assuming obliquities of 0 and 15 degrees and 3 different rotation speeds (1:1 resonance, 3:2 resonance, and pseudo-synchronous). Assuming $T_{\text{int}} \sim 300$–350 K, their calculations suggest that $Q' \sim 2 \times 10^5$–10^6. These values are somewhat larger than the value of Q' that has been measured using Neptune's satellites of between 3.3×10^4 and 1.35×10^5 (Zhang and Hamilton, 2008).

7.5.5 Condensation of graphite

As has been discussed in, e.g., Moses *et al.* (2013), cool high metallicity atmospheres may have regions that are stable for the condensation of graphite. Indeed, the very high metallicity models favored by the retrieval models do indeed cross the graphite stability curve above 0.1 bar. While the effect of this condensation is beyond the scope of this work, the major effects would be twofold. First, the graphite condensation will deplete the carbon reservoir, decreasing the CO abundance in the upper atmosphere. In addition, the condensed graphite may form into cloud particles with their own opacity. Like other clouds and hazes, graphite clouds would likely decrease the size of features in transmission spectra and thermal emission spectra, and may either increase or decrease the albedo depending on the optical properties of the graphite particles.

7.6 Conclusion

We have presented new observations of GJ 436b's thermal emission at 3.6 and 4.5 μm, which are in agreement with previous analyses from Lanotte *et al.* (2014) and reduce the uncertainties of GJ 436b's flux at those wavelengths. For the first time, we combine these revised data with *Spitzer* photometry from 5.6 to 16 μm and transmission spectra from *HST*/WFC3 and compare these data to both self-consistent and retrieval models. We vary the metallicity, internal temperature from tidal heating, disequilibrium chemistry, heat redistribution, and cloud properties. We find that our nominal best-fitting self-consistent model has 1000× solar metallicity, T_{int}=240 K, f_{sed}=0.3 sulfide/salt clouds, disequilibrium chemistry, and planet-wide average temperature profile. Retrieval models find a statistically better fit to the ensemble data than the self-consistent model, with parameters in general agreement with the self-consistent approach: *all signs point to a high metallicity, with best fits above 1000× solar metallicity, and tidal heating warming its interior, with best-fit T_{int}∼300–350 K.*

While Neptune has been measured based on its methane abundance to have an atmospheric carbon enhancement of ∼100× solar, repeated observations of both the thermal emission and transmission spectra of the first exo-Neptune to be studied in detail, GJ 436b, have demonstrated that it likely has a significantly higher metallicity. Neptune itself may actually be more enhanced in other elements than it is in carbon; Luszcz-Cook and de Pater (2013) infer a 400–600× solar enhancement in oxygen from microwave observations of upwelled CO in Neptune, though this cannot be verified with infrared spectra since oxygen is frozen into clouds. Studies of warmer exoplanet atmospheres will allow us to spectroscopically measure

abundances of these molecules like oxygen that are locked into clouds in the cold ice giants of our solar system, potentially revealing unexpected patterns in the metal-enrichments of these intermediate-mass objects.

An interesting new paradigm for this class of intermediate-sized planet is now being pieced together: we suggest that Neptune-mass planets may be more compositionally diverse than previously imagined. High quality data across of range of Neptune-mass planets with different temperatures and host stars will be critical to investigate the diversity of this class of planets.
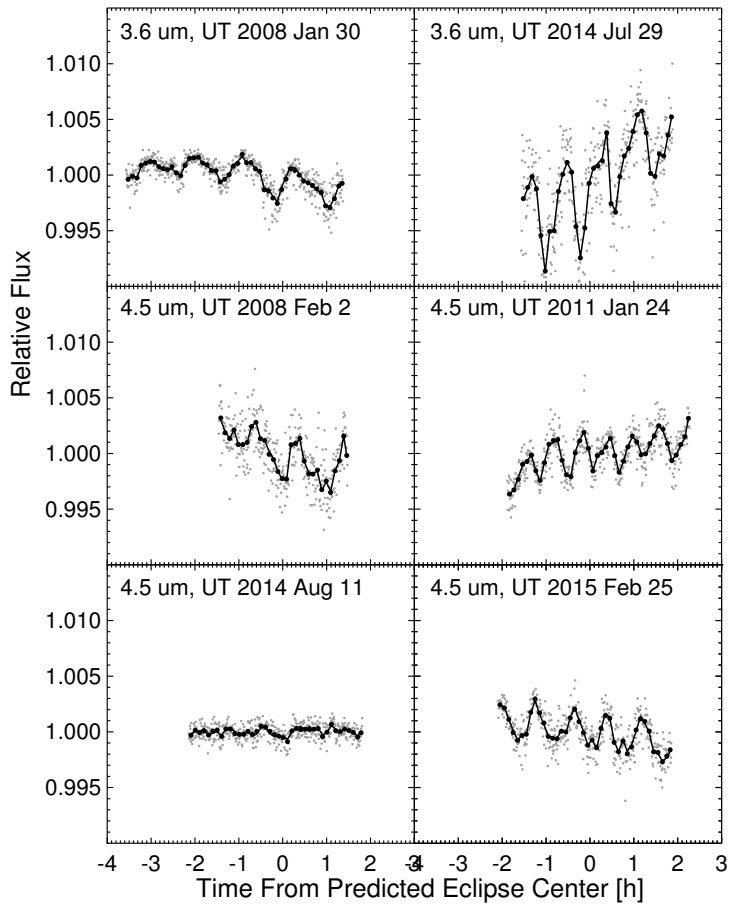
Figure 7.1: Raw *Spitzer* 3.6 and 4.5 μm photometry as a function of time from the center of eclipse phase reported in Knutson *et al.* (2011). We bin the photometry in 30 s (grey filled circles) and 5 minute (black filled circles) intervals, and overplot the best fit instrumental models binned in 5 minute intervals for comparison (solid lines).
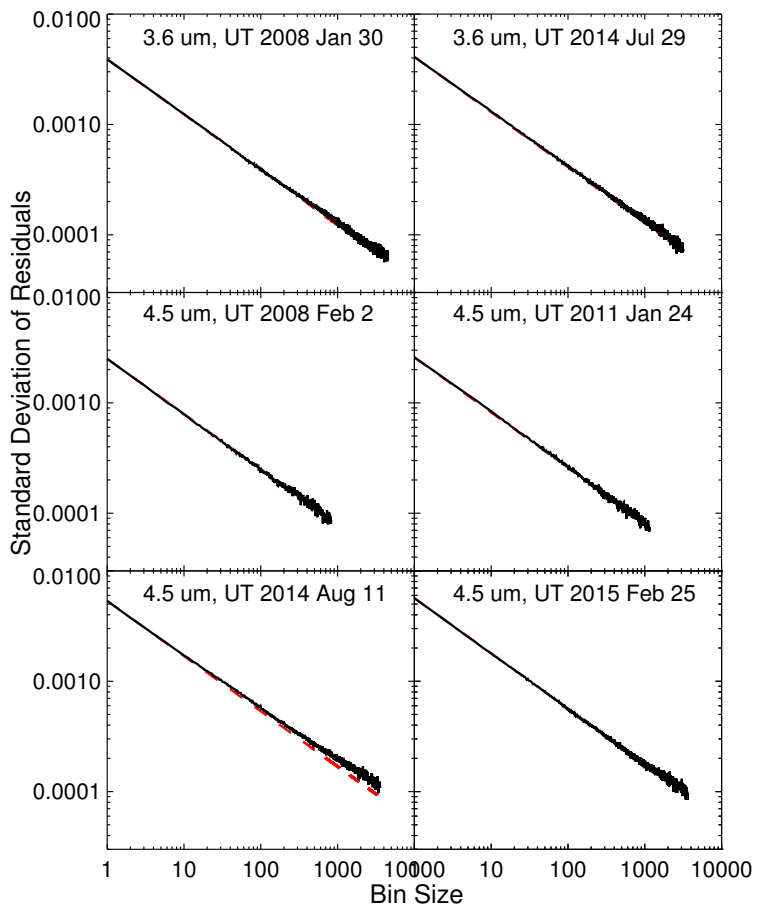
Figure 7.2: Standard deviation of the best-fit residuals as a function of bin size (black lines). We over plot the expected $1/\sqrt{n}$ scaling for Gaussian noise as red dashed lines, where we have normalized these lines to match the standard deviation of the unbinned residuals.
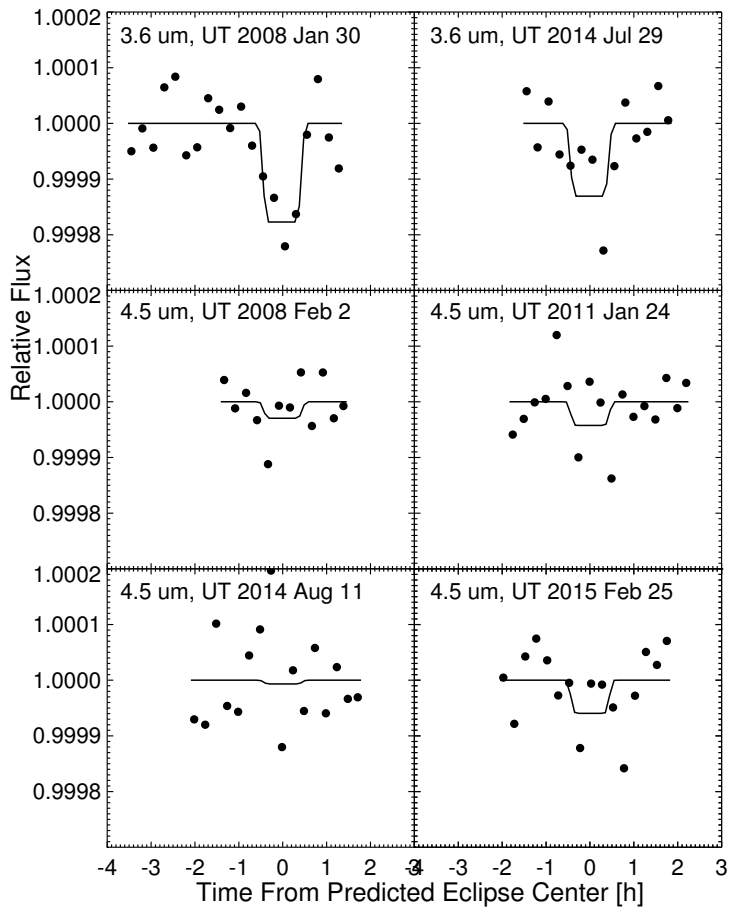
Figure 7.3: Normalized *Spitzer* 3.6 and 4.5 μm light curves as a function of time from the predicted center of eclipse, where we have divided out the best-fit instrumental model shown in Fig. 7.1. The normalized flux is binned in 10 minute intervals, and best fit eclipse model light curves are over plotted for comparison (solid lines).
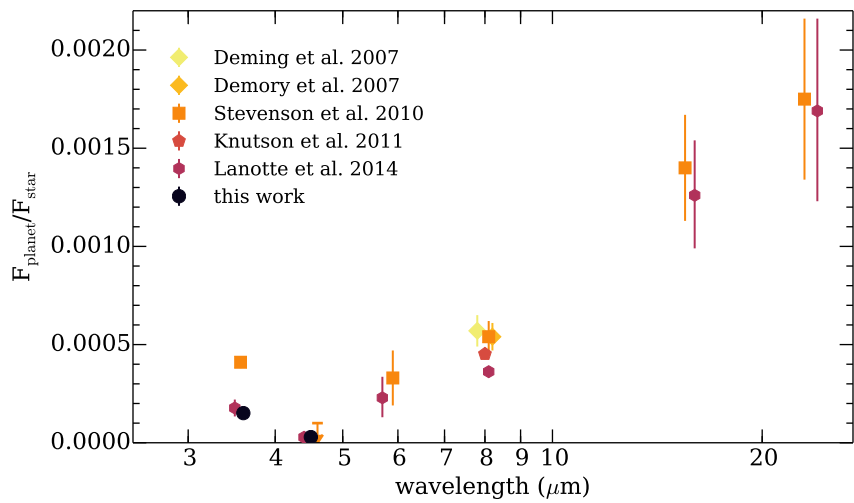
Figure 7.4: Eclipse depths in the 6 *Spitzer* bandpasses from the literature and this work. Different publications are offset slightly in wavelength for clarity; darker colors indicate later years.
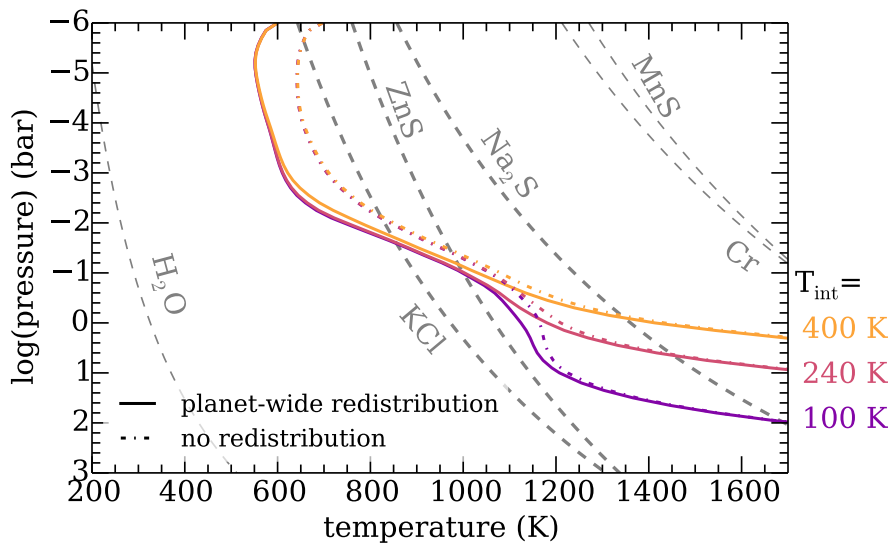
Figure 7.5: Pressure–temperature profiles with condensation curves. All models are cloud-free with 300× solar composition. Solid lines show models with T_{int}=100, 240, and 400 K and planet-wide heat redistribution. Dash-dot lines show models with the same T_{int}s but with no heat redistribution (dayside temperature). Condensation curves show where the vapor pressure of a gas is equal to the saturation vapor pressure; cloud material condenses where the P–T profile intersections a condensation curve.
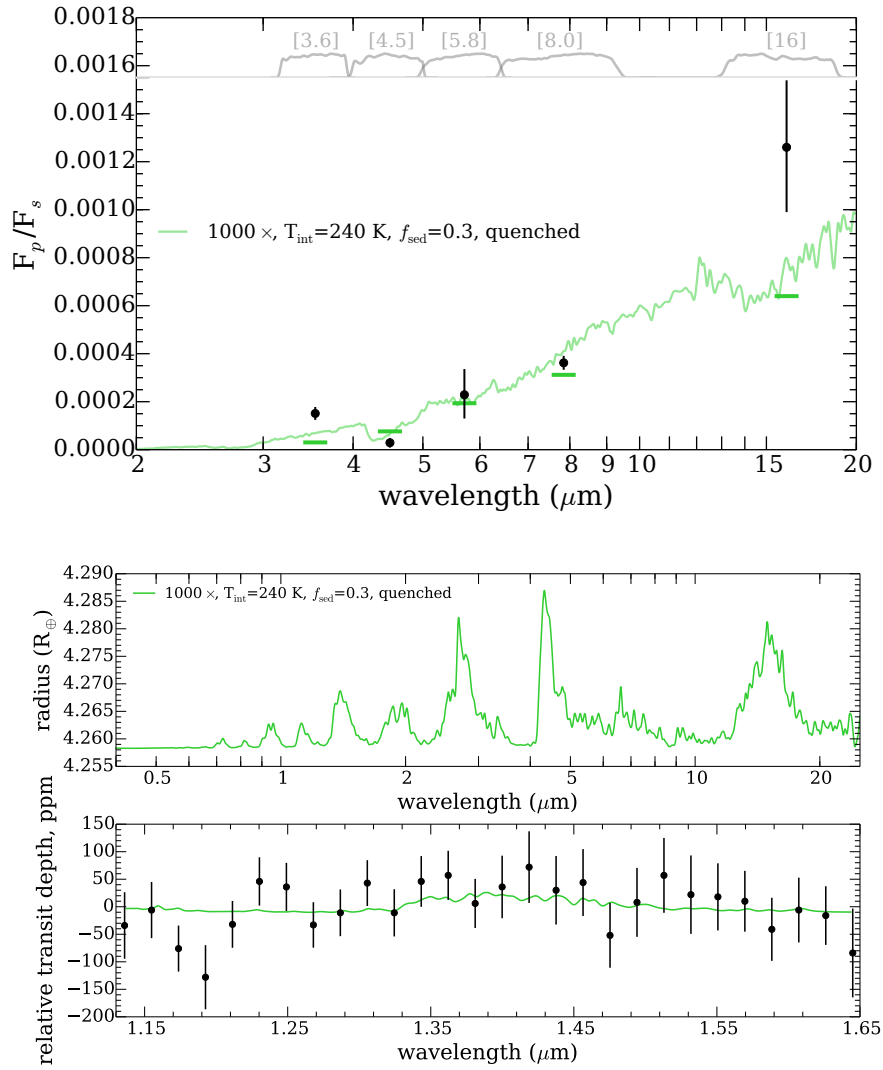
Figure 7.6: Best-fit thermal emission and transmission spectra. Top panel: Thermal emission spectrum of the best-fit model from the suite of forward models compared to the data. The model is shown as a green line, with synthetic model photometry shown as horizontal lines at the central wavelength of the filter. Data are shown as black points with 1-σ error bars. The filter functions for the photometry are shown as gray lines in the top panel. Bottom panels: Transmission spectrum of the same best-fit thermal emission model from the suite of forward models compared to the data. The model is shown as a green line in both panels. The HST/WFC3 transmission spectrum is shown as black points with 1-σ error bars in the bottom panel.

299
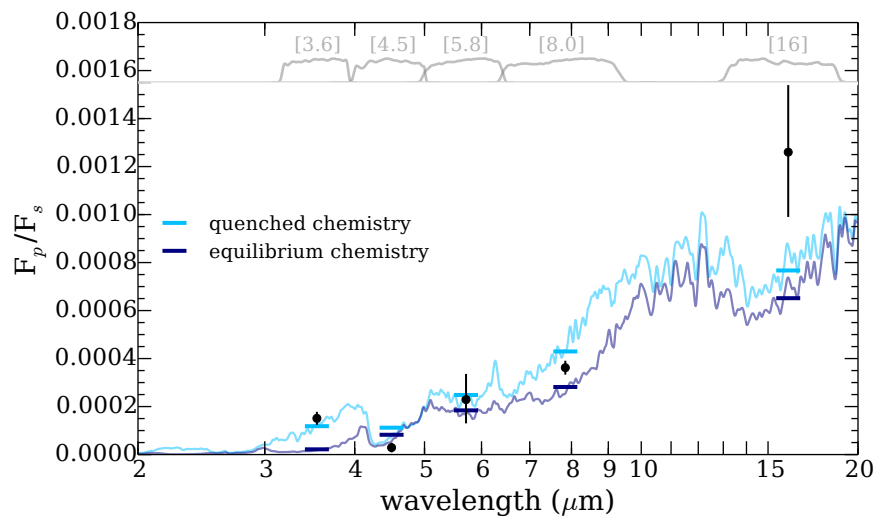
Figure 7.7: Effect of chemistry on thermal emission spectrum. Both models assume $300\times$ solar metallicity, f_{sed}=1 sulfide/salt clouds, planet-wide heat redistribution, and T_{int}=240 K. The darker blue line and horizontal bars show a model spectrum and photometry assuming equilibrium chemistry; the lighter blue line and horizontal bars show the same model, but with the chemistry quenched at the 10 bar abundances throughout the atmosphere.
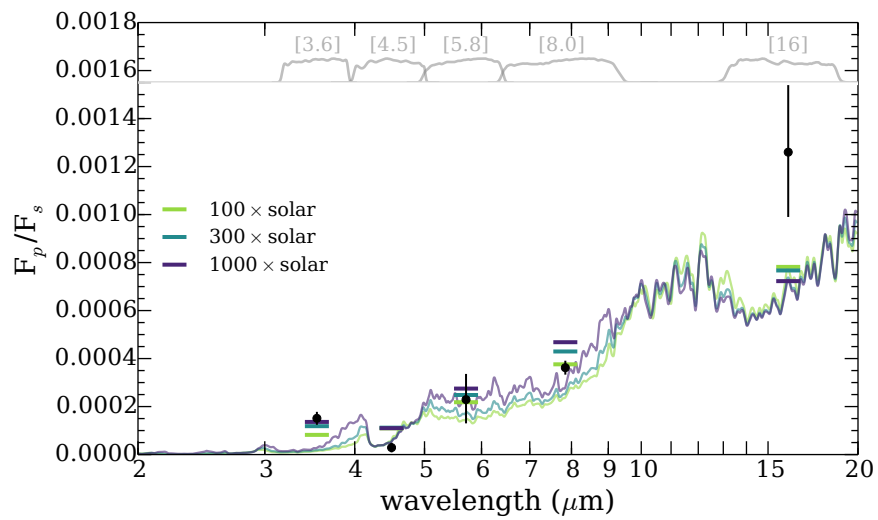
Figure 7.8: Effect of metallicity on thermal emission. Each model assumes quenched chemistry, f_{sed}=1 sulfide/salt clouds, planet-wide heat redistribution, and T_{int}=240 K. Metallicities of 100, 300, and 1000× solar metallicity are shown. Even assuming quenched (disequilibrium) chemistry, increasing the metallicity decreases the CH_4 abundance and increases CO and CO_2 abundance.
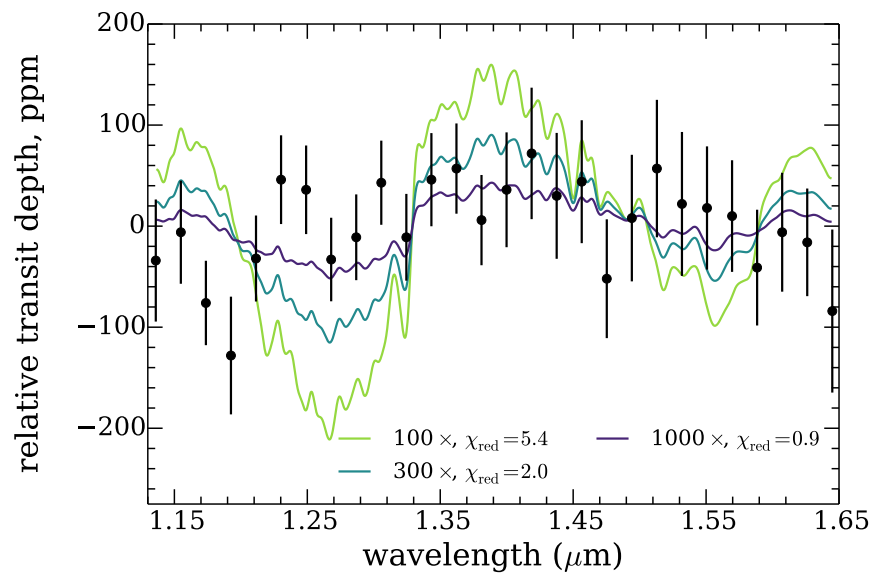
Figure 7.9: Effect of metallicity on transmission spectrum. Each model is cloud-free, with planet-wide heat redistribution, equilibrium chemistry, and T_{int}=240 K. Metallicities of 100, 200, 300, and 1000× solar metallicity are shown. Increasing the metallicity decreases the CH_4 abundance and increases CO and CO_2 abundance.
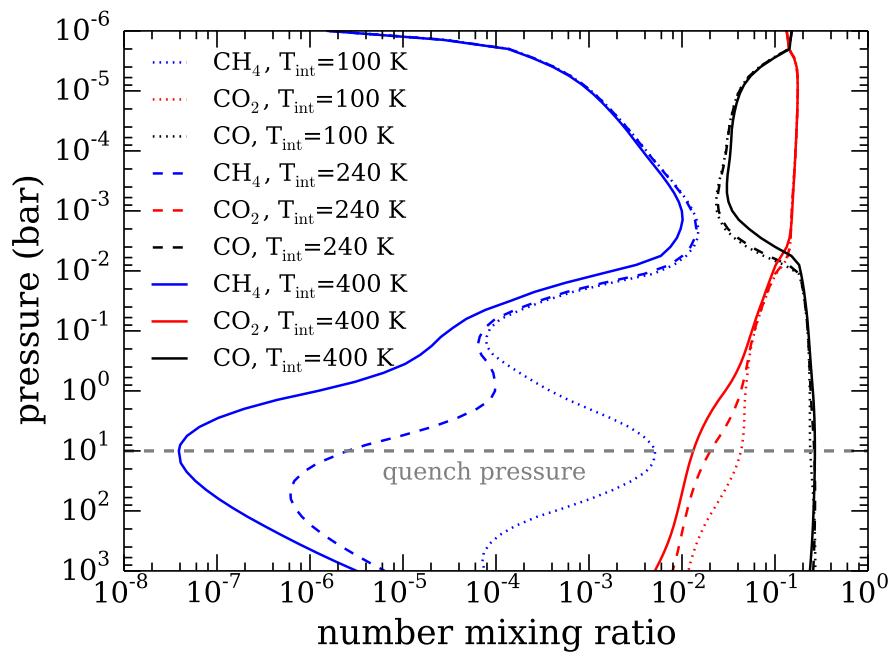
Figure 7.10: Abundances of major carbon-bearing species in chemical equilibrium. All models have a composition of $1000\times$ solar metallicity and a planet-wide average PT profile. Different T_{int} values are shown with different line styles, and each molecule (CH_4, CO, CO_2) is shown in a different color. The fiducial quench pressure used in the self-consistent modeling is shown as a horizontal dashed line. Note that increasing the internal temperature decreases the CH_4 abundance in the deep atmosphere.
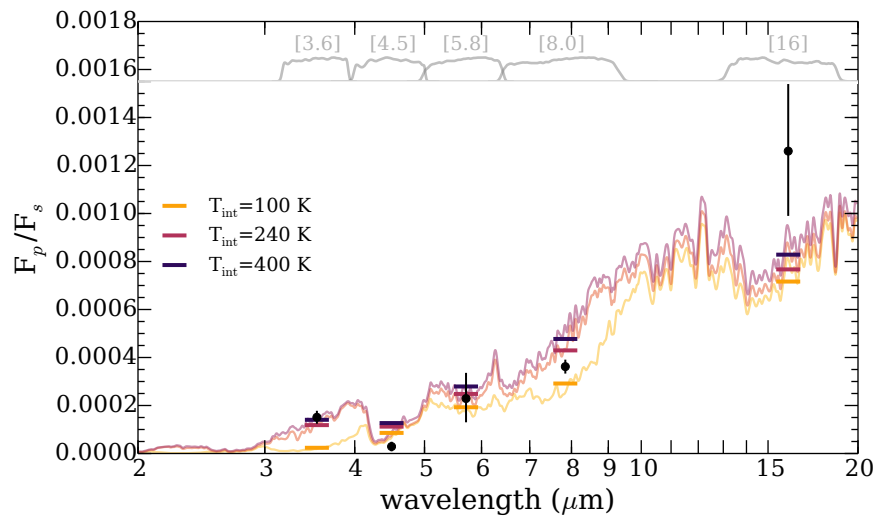
Figure 7.11: Effect of tidal heating on thermal emission. Each model assumes $300\times$ solar metallicity, quenched chemistry, f_{sed}=1 sulfide/salt clouds, and planet-wide heat redistribution. The tidally heated atmospheres (240 and 400 K) have higher abundances of CO and CO_2 and lower abundances of CH_4 due to the hotter deep atmosphere (where the chemistry is quenched). Tidal heating also increases the T_{eff} of the planet by changing the temperature profile, increasing the emergent flux at all wavelengths.
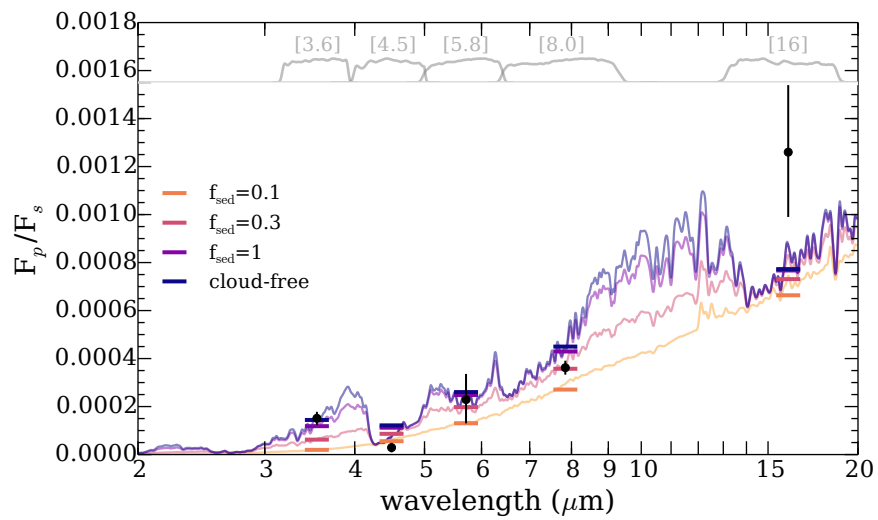
Figure 7.12: Effect of sulfide/salt clouds on thermal emission. Each model uses the same pressure-temperature profile and assumes $300\times$ solar metallicity, quenched chemistry, planet-wide heat redistribution, and T_{int}=240 K. A cloud-free model and cloudy models with f_{sed}=0.03 to 1 are shown. Cloud opacity decreases the thermal emission across the spectrum. Models with moderate clouds (f_{sed}=0.3 to 1) fit the *Spitzer* points best.
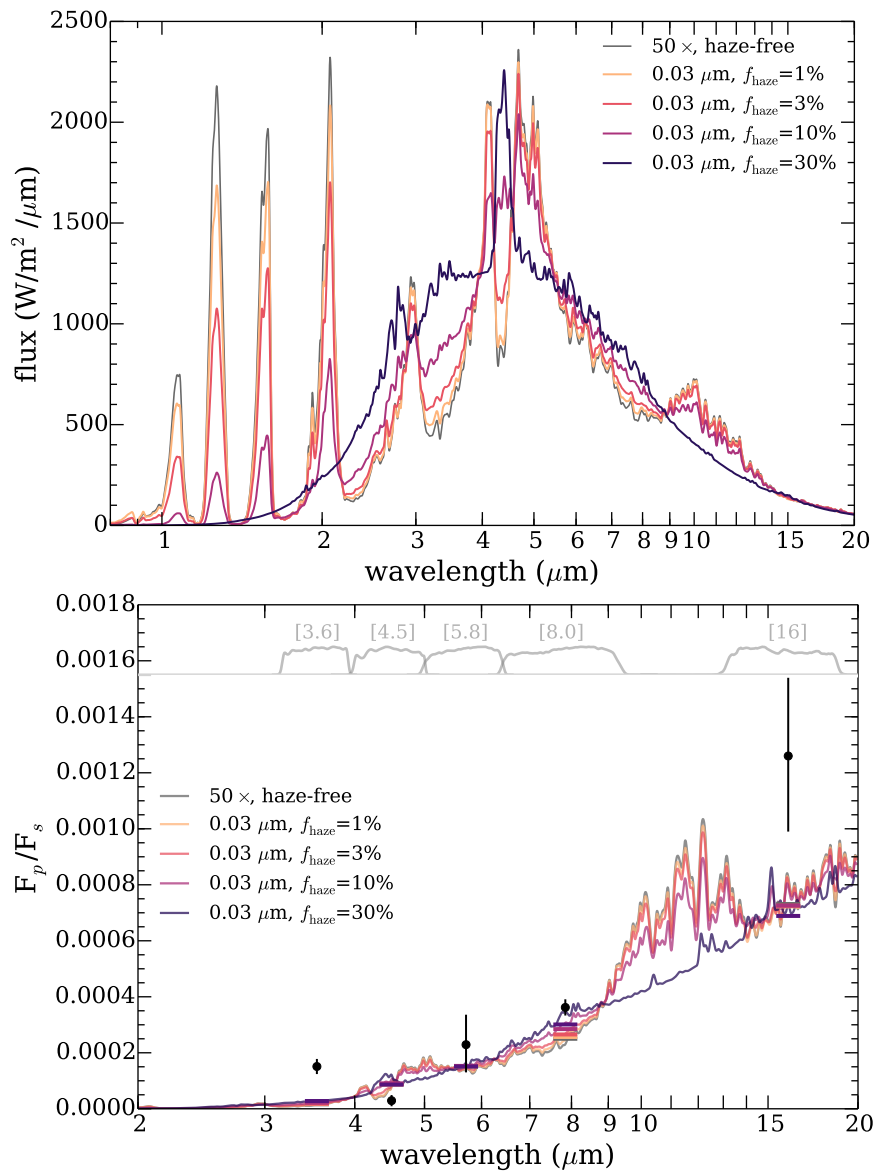
Figure 7.13: Effect of photochemical hazes on thermal emission. The top panel shows the emergent flux from the planet. All models have $50\times$ solar metallicity, equilibrium chemistry, and planet-wide heat redistribution. The gray line shows a cloud-free model, and the colored lines show a progression of hazy models with hazy-forming efficiency parameter f_{haze} varying from 1 to 30%. The bottom panel shows the same models, but dividing by the flux of the host star to compare to the measured photometry.
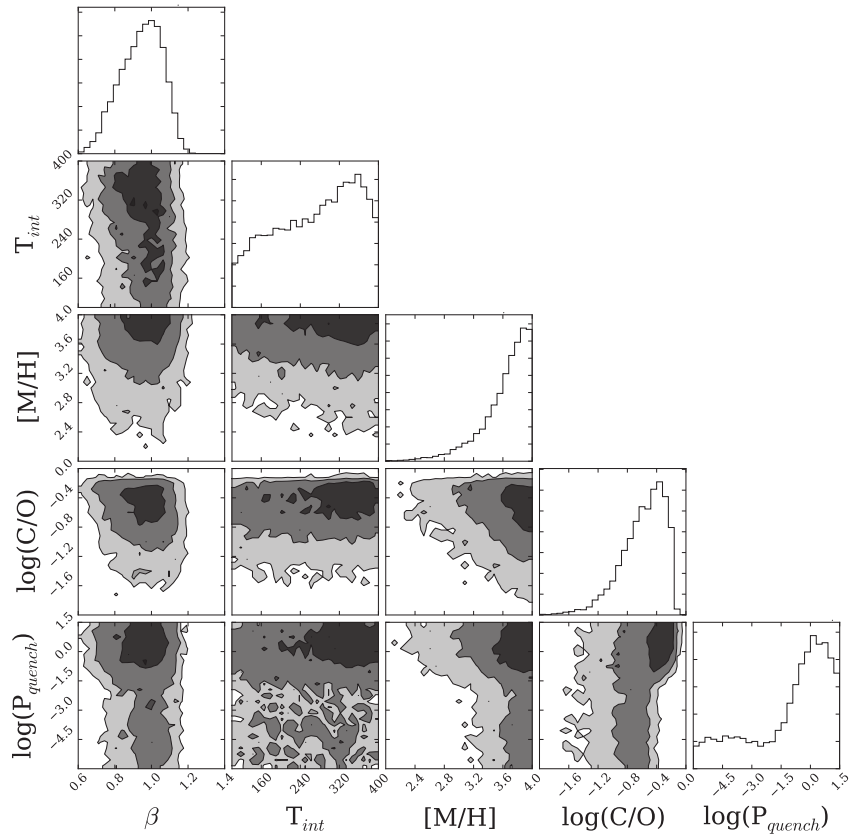
Figure 7.14: Posterior probability distributions and correlations. The top panel (histogram) shows the posterior probability distribution for each parameter, marginalized over all other parameters. The other panels show 2D contour plots that represent the correlations between each pair of parameters, where the regions from darkest to lightest represent the 1-, 2-, and 3-σ contours.
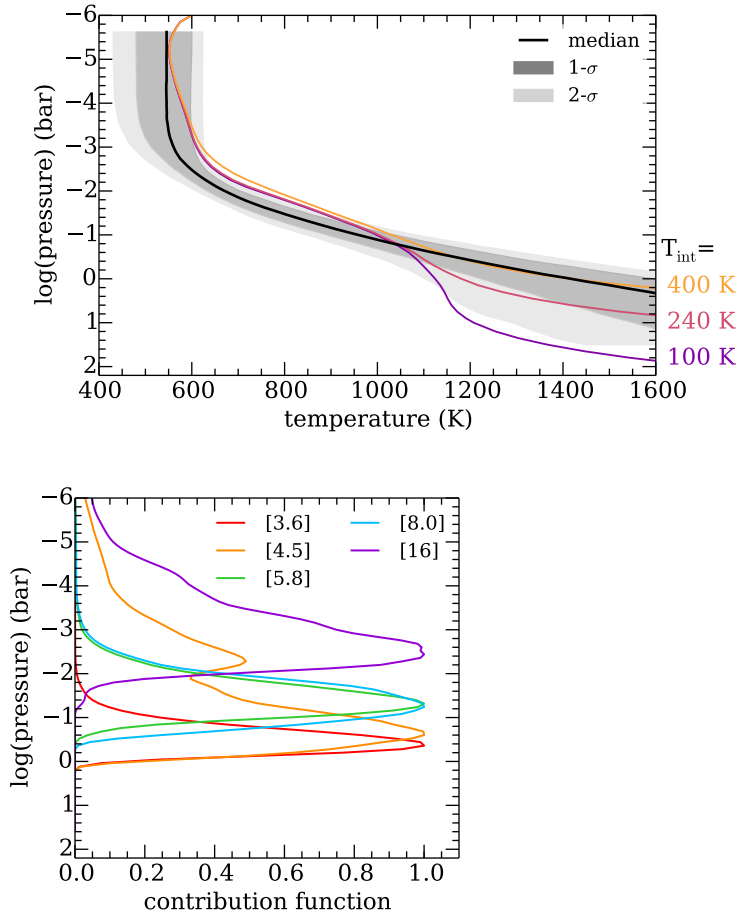
Figure 7.15: Pressure–temperature profiles and contribution functions for each bandpass. The left panel shows pressure-temperature profiles of both retrieved and self-consistent models. The black line indicates the median retrieved profile while the dark and light gray shaded regions represent the 1- and 2-σ confidence regions respectively. The colored lines show self-consistent models with planet-wide heat redistribution and T_{int} of 100, 240, and 400 K. Note the good agreement between the tidally heated (240–400 K) models and the retrieved profile. The right panel shows contribution functions for each of the five bandpasses for a representative retrieval model. The shortest wavelength 3.6 μm band probes the deepest wavelengths while the 16 μm band proves the shallowest.
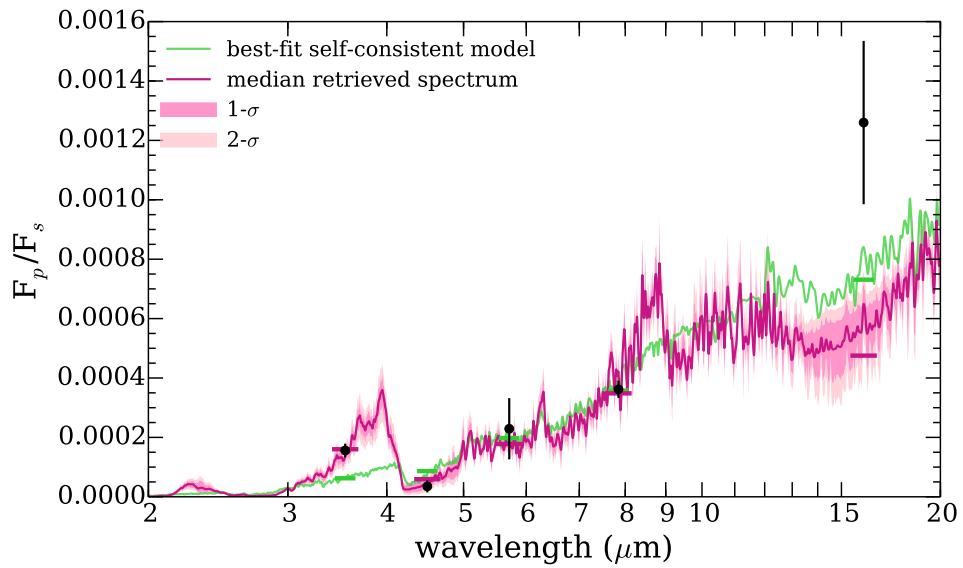
Figure 7.16: Retrieved data compared to data and best-fit self-consistent model. The pink line and shaded dark and light pink regions are the median fit, 1-σ, and 2-σ confidence intervals respectively. The green line is the best-fit self-consistent model (300$\times$ solar metallicity, T_{int}=240 K, f_{sed}=0.3, quenched disequilibrium chemistry).
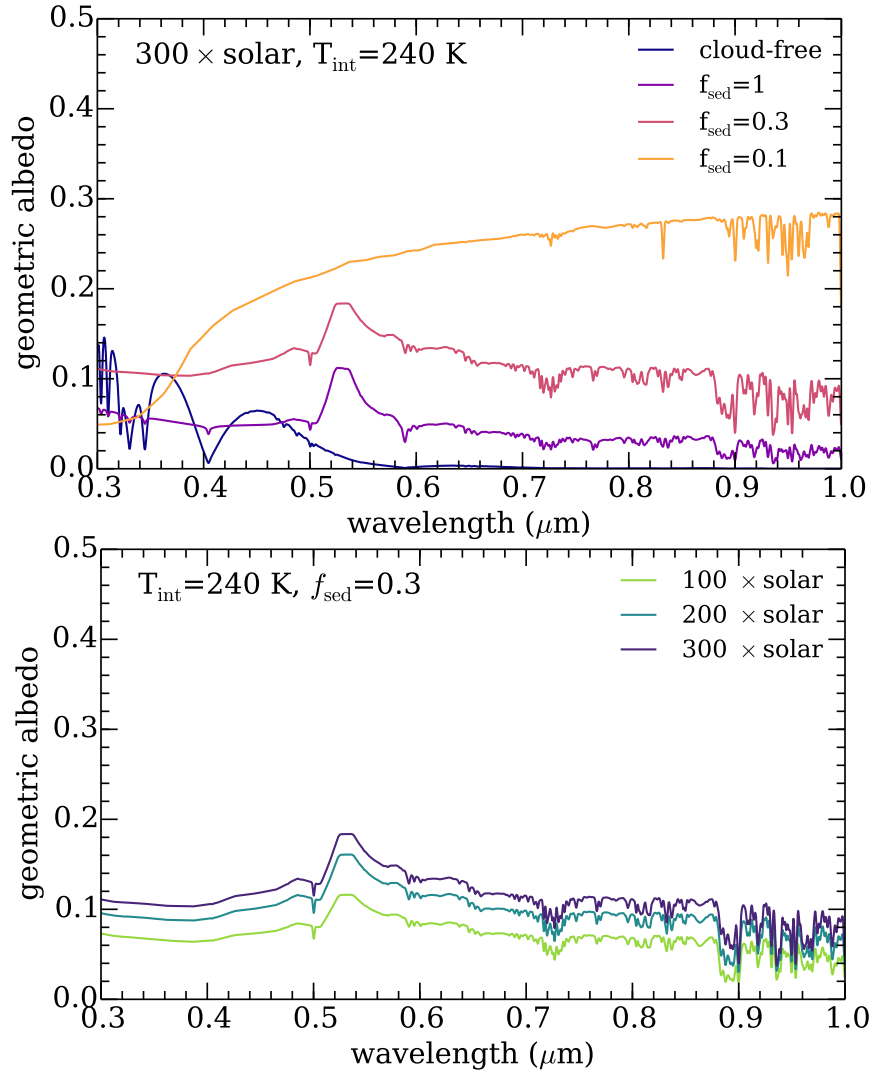
Figure 7.17: Predicted albedo spectra. Top panel shows models with 300×solar metallicity, T_{int}=240 K. A cloud-free model and models with cloud parameter f_{sed} from 0.03 to 1 are shown. Bottom panel shows models with T_{int}=240 K, f_{sed}=0.3. Metallicities from 100 to 300 × solar are shown.

Chapter 8

Conclusions and Future Work

In this thesis, I have presented work that shows our emerging understanding that clouds or hazes are ubiquitous in substellar atmospheres, existing in objects with a variety of masses and temperatures. The objects studied here include brown dwarfs with exotic clouds like sulfides and salts and colder brown dwarfs with water ice clouds that likely look like those in our own solar system. In super Earths studied to date like GJ 1214b, clouds and/or hazes appear to be thicker and more lofted than ever predicted in small planets. Clouds can thwart attempts to characterize properties like gas abundances by decreasing the size of features in transmission and emission spectra. They also give us information about the physics and chemistry of the planets themselves. Understanding the formation of clouds and hazes will be critical for understanding planets with *JWST* as well as future missions like the Wide-Field InfraRed Survey Telescope (*WFIRST*).

There are a number of avenues for future work that will provide insights into substellar atmospheres; cloud and haze modeling will play a crucial role in all of these paths forward. The

following sections describe frontiers in the study of exoplanets, from determining the nature of small planets to anchoring cloud and haze models in reality.

8.1 Compositions of Super Earths and Sub Neptunes

A legacy of the *Kepler* mission is that there are a plethora of planets in the galaxy with radii between that of Earth and Neptune. No such planets exist in our own solar system; it is not currently well-understood which of these planets are scaled-up Earths with mostly-rocky compositions and which are scaled-down Neptunes with more volatile-rich compositions. As we move toward characterization of small rocky planets, it is important to understand the continuum of worlds between gas and ice giants and rocky small planets. Atmospheric studies have been billed as the key to determine the difference between these types of objects, but for the most in-depth case study to date to measure the transmission spectrum of GJ 1214b, clouds or hazes have prevented us from determining the composition of its envelope.

At the same time, the Neptune-sized planet that has been studied in most detail to date, GJ 436b, appears to show evidence for very high ($\sim 1000 \times$ solar) metallicity atmosphere, very different from the compositions of ice giants in our own solar system. It remains to be determined whether these inferences are true. It is possible that there are unexpected systematic effects that change our observations of this planet, or that a crucial aspect of physics is missing from the models, skewing our interpretation of the data.

While *Kepler*'s results demonstrate unequivocally that small planets or short orbits exist in large numbers in the galaxy, the Transiting Exoplanet Survey Satellite (*TESS*) will find

the best targets for future characterization. TESS will launch in 2017 and discover transiting planets around bright, nearby stars; these are the targets that will form the majority of the target list for studying small planets with *JWST* (Sullivan *et al.*, 2015). *JWST* will provide high fidelity spectral observations for planets in this mass range. For many of these planets, we will be capable of measuring transmission spectra across the near- and mid-infrared. For some planets, we will also be able to measure thermal emission spectra, supplanting the broadband photometry of the *Spitzer* era. These observations, as we showed in Morley *et al.* (2015), should be able to distinguish cloudy and hazy models and shed new light on the nature of these small planets.

8.2 The Coldest Brown Dwarfs

The coldest brown dwarfs are the objects most similar to the solar system giant planets that we have been able to observe to date. Studying these objects will anchor our understanding of the physics and chemistry of substellar objects with volatile clouds, moving from a sample size of just two giant planets (Jupiter and Saturn) with effective temperatures around 100–130 K to a suite of objects that span the water and ammonia condensation temperatures. These coldest, nearest brown dwarfs are just within the detection limits of ground-based 8-m class telescopes, and, as we showed in Morley *et al.* (2014), will be detectable over a wide wavelength range in the mid-infrared with *JWST*.

Studies of these cold brown dwarfs will provide the benchmark objects to understand distant giant planets in planetary systems that resemble our own. These giant planets have been

discovered by radial velocity surveys but remain outside the realm of atmospheric characterization until the launch of *WFIRST* in the 2020s, when they will be targeted for reflected light spectroscopy.

8.3   The Youngest L Dwarfs

Objects that bridge the gap between brown dwarfs and planets have recently been discovered. These new objects include distant planetary mass companions to stars (e.g. Naud *et al.*, 2014), free-floating planetary mass objects in young moving groups (Liu *et al.*, 2013; Faherty *et al.*, 2013), and systems with multiple low-mass objects straddling hydrogen- and deuterium-burning limits (Bowler and Hillenbrand, 2015). They join a growing list of substellar objects in young moving groups that are spectroscopically distinct from older field objects (Cruz *et al.*, 2009; Faherty *et al.*, 2012; Allers and Liu, 2013; Gagné *et al.*, 2015). They represent a cleaner sample than true planets, unadulterated by stellar irradiation and likely lacking significant metal-enhancement from formation in a protoplanetary disk. Brown dwarfs are easier to observe spectroscopically at higher resolution and higher S/N than planets and therefore provide tests of the physics and chemistry of substellar atmospheres that planets cannot.

While all brown dwarfs above $\sim$1200 K have thick clouds of iron and silicates, there are hints that suggest the thickness and properties of these clouds are gravity-dependent; redder colors of lower-mass objects possibly indicate thicker clouds. The details about and reasons for this dependence of clouds on gravity are not yet well understood, but this set of objects is an ideal sample to determine the effect of gravity on cloud properties. The physics learned from

this study will be broadly applicable to planetary atmospheres. In addition, recent studies have suggested that disequilibrium chemistry should be strongly dependent on gravity (Zahnle and Marley, 2014). Brown dwarfs spanning a range of gravities give us an testbed to test this theory and understand the effect of gravity on the dynamics of substellar atmospheres.

8.4 The Power of Combining Retrieval and Self-Consistent Modeling Approaches

In the past decade, modern analytical tools have been popularized to rigorously determine the compositions and properties of exoplanets from their observed spectra. These retrieval algorithms have long been used in the solar system (Rodgers, 1976, 2000; Conrath *et al.*, 1998; Irwin *et al.*, 2008; Fletcher *et al.*, 2007) and recently to study exoplanets (Madhusudhan and Seager, 2009; Madhusudhan *et al.*, 2011b; Lee *et al.*, 2012; Barstow *et al.*, 2013a,b; Line *et al.*, 2012; Line and Yung, 2013a; Line *et al.*, 2014; Benneke and Seager, 2012, 2013; Benneke, 2015).

The retrieval approach brings many advantages, including the ability to fit spectra of planets that are not well-described by model grids, allowing us to probe a wider range of planetary compositions. However, limitations of these models quickly limit the science questions these methods can address. Exoplanet spectra are much lower signal-to-noise and lower spectral resolution than brown dwarf or solar system spectra, causing retrieved abundances to frequently include non-physical solutions (Line *et al.*, 2014). A major shortcoming with all of these previous methods is that there has been no way to judge the physical plausibility of the

stated outcomes. In addition, even for high fidelity data, most planets and brown dwarfs are in reality cloudy, and thus cloud-free retrievals derive incorrect compositions and underestimate systematic uncertainties (Madhusudhan *et al.*, 2014). Moreover, as new parameters are added, degeneracies in derived parameters increase. This means that additional—and, as shown in this thesis, critically important—physics such as clouds is prohibitively difficult for most retrieval approaches, requiring a number of additional parameters.

It is becoming clear that there is power in combining retrieval approaches with sophisticated forward models that are based on atmospheric physics and chemistry. Many retrieval approaches are now incorporating this approach (e.g. Benneke, 2015; Kreidberg *et al.*, 2015), and we demonstrate the capabilities of using both retrievals and self-consistent models in Chapter 7. This dual-pronged approach to modeling efforts is the way forward for understanding planetary atmospheres; only with both data-driven approaches and physics-driven models can we make progress to quantitatively assess the compositions and properties of planets and brown dwarfs.

8.5   Incorporating Microphysics Into Cloud Models

Another avenue for future work involves improving cloud models themselves. Each group that models clouds has assumptions inherent to their particular model, but often these models have not been tested over a wide range of atmospheric conditions. Incorporating additional microphysics into parameterized models will allow cloud models to better match reality.

For example, the Ackerman and Marley (2001) cloud model assumes homogeneous, spherical particles with fixed log-normal particle size distributions. This is numerically straight-

forward to calculate but does not recreate all properties of brown dwarf spectra or capture all of the expected physics. For example, Hiranaka et al. (in prep.) have shown that a log-normal particle size distribution, regardless of the chosen width, cannot match the slope of the opacity needed to match the spectra of particularly red brown dwarfs. A set of particles with a different distribution is required. In addition, models from e.g. Helling and Woitke (2006) show that particles are not expected to be homogeneous but instead of composed of multiple materials.

A major step forward will involve incorporating results from microphysical cloud models, which are more computationally intensive but allow us to account in a more physical way for each step of cloud formation, into parameterized cloud models like the BT-Settl models (Allard *et al.*, 2012) as well as our own models. In addition, incorporating results from laboratory experiments will provide additional validity to the chosen parameters. The resulting improved parameterized models can be used to run grids of models, or incorporated into retrieval algorithms.

8.6   Laboratory Experiments to Anchor Haze Models

Photochemical hazes remain a neglected but critical topic to understand for the study of cool planets. All the giant planets in our own solar system have photochemical hazes with varying properties, but it is not clear for which exoplanets hazes will be most substantial. Much of the uncertainty is due to the complexity of models necessary to numerically simulate the production of large hydrocarbons that would condense in these atmospheres.

In order to move forward, we will need to take a lead from solar system science;

studies of Titan's haze have long been plagued by similar issues. The 'tholin'-like hazes in Titan's upper atmosphere are impossible to simulate in a chemical kinetics model. Studies of haze formation in Titan are instead largely grounded in Earth laboratories. These types of experiments, to measure the formation of hazes for a variety of different compositions and temperatures, will inform atmospheric models. Studying their optical properties will also be extremely important; as we have shown in Chapter 6, whether the hazes are made of soot-like dark particles or tholin-like brighter particles has a major effect on all observations of a planet.

These laboratory studies are currently in their infancy for the exoplanetary temperature and composition regimes but will play a crucial role as telescopes like *JWST* allow us to observe cooler, smaller planets.

8.7   Future of Exoplanet Atmosphere Studies

Studies of exoplanet atmospheres have matured considerably over the duration of my PhD as observations have improved and new models have been developed. Meanwhile, brown dwarf studies are probing objects that increasingly overlap in mass and temperature with exoplanets and even solar system planets, drawing the fields of brown dwarf science, exoplanet science, and planetary science closer together. Clouds and hazes have emerged as a critical part of the puzzle to understand all substellar objects. New telescopes and instruments will continue the growth of atmospheric studies for the next decade and beyond, with the launch of missions like *TESS*, *JWST* and *WFIRST*, as we strive to understand our solar system's place in our galaxy full of strange and diverse worlds.

Bibliography

Ackerman, A. S. and Marley, M. S. Precipitating Condensation Clouds in Substellar Atmo-
spheres. ApJ **556**, 872 (2001).

Agúndez, M.; Venot, O.; Selsis, F. and Iro, N. The Puzzling Chemical Composition of GJ
436b's Atmosphere: Influence of Tidal Heating on the Chemistry. ApJ **781**, 68 (2014).

Allard, F.; Allard, N. F.; Homeier, D.; Kielkopf, J.; McCaughrean, M. J. and Spiegelman, F.
K-H$_2$ quasi-molecular absorption detected in the T-dwarf \varepsilon Indi Ba. A&A **474**,
L21 (2007).

Allard, F.; Hauschildt, P. H.; Alexander, D. R.; Tamanai, A. and Schweitzer, A. The Limiting
Effects of Dust in Brown Dwarf Model Atmospheres. ApJ **556**, 357 (2001).

Allard, F.; Hauschildt, P. H.; Baraffe, I. and Chabrier, G. Synthetic Spectra and Mass Determi-
nation of the Brown Dwarf GI 229B. ApJ **465**, L123 (1996).

Allard, F.; Homeier, D. and Freytag, B. Models of very-low-mass stars, brown dwarfs and
exoplanets. *Royal Society of London Philosophical Transactions Series A* **370**, 2765 (2012).

319

Allard, N. F.; Allard, F.; Hauschildt, P. H.; Kielkopf, J. F. and Machin, L. A new model for brown dwarf spectra including accurate unified line shape theory for the Na I and K I resonance line profiles. A&A **411**, L473 (2003).

Allard, N. F.; Allard, F. and Kielkopf, J. F. Theoretical profiles of light alkali resonance lines for brown dwarf atmosphere conditions. A&A **440**, 1195 (2005).

Allen, M.; Yung, Y. L. and Waters, J. W. Vertical transport and photochemistry in the terrestrial mesosphere and lower thermosphere /50-120 km/. J. Geophys. Res. **86**, 3617 (1981).

Allers, K. N. and Liu, M. C. A Near-infrared Spectroscopic Study of Young Field Ultracool Dwarfs. ApJ **772**, 79 (2013).

Anglada-Escudé, G.; Rojas-Ayala, B.; Boss, A. P.; Weinberger, A. J. and Lloyd, J. P. GJ 1214 reviewed. Trigonometric parallax, stellar parameters, new orbital solution, and bulk properties for the super-Earth GJ 1214b. A&A **551**, A48 (2013).

Apai, D.; Radigan, J.; Buenzli, E.; Burrows, A.; Reid, I. N. and Jayawardhana, R. HST Spectral Mapping of L/T Transition Brown Dwarfs Reveals Cloud Thickness Variations. ApJ **768**, 121 (2013).

Artigau, É.; Bouchard, S.; Doyon, R. and Lafrenière, D. Photometric Variability of the T2.5 Brown Dwarf SIMP J013656.5+093347: Evidence for Evolving Weather Patterns. ApJ **701**, 1534 (2009).

Asplund, M.; Grevesse, N.; Sauval, A. J. and Scott, P. The Chemical Composition of the Sun. ARA&A **47**, 481 (2009).

Bailer-Jones, C. A. L. and Mundt, R. Variability in ultra cool dwarfs: Evidence for the evolution of surface features. A&A **367**, 218 (2001).

Baines, K. H.; Carlson, R. W. and Kamp, L. W. Fresh Ammonia Ice Clouds in JupiterI. Spectroscopic Identification, Spatial Distribution, and Dynamical Implications. Icarus **159**, 74 (2002).

Baines, K. H.; Delitsky, M. L.; Momary, T. W.; Brown, R. H.; Buratti, B. J.; Clark, R. N. and Nicholson, P. D. Storm clouds on Saturn: Lightning-induced chemistry and associated materials consistent with Cassini/VIMS spectra. Planet. Space Sci. **57**, 1650 (2009).

Baines, K. H.; Drossart, P.; Momary, T. W.; Formisano, V.; Griffith, C.; Bellucci, G.; Bibring, J. P.; Brown, R. H.; Buratti, B. J.; Capaccioni, F.; Cerroni, P.; Clark, R. N.; Coradini, A.; Combes, M.; Cruikshank, D. P.; Jaumann, R.; Langevin, Y.; Matson, D. L.; McCord, T. B.; Mennella, V.; Nelson, R. M.; Nicholson, P. D.; Sicardy, B. and Sotin, C. The Atmospheres of Saturn and Titan in the Near-Infrared First Results of Cassini/vims. *Earth Moon and Planets* **96**, 119 (2005).

Barman, T. S.; Macintosh, B.; Konopacky, Q. M. and Marois, C. Clouds and Chemistry in the Atmosphere of Extrasolar Planet HR8799b. ApJ **733**, 65 (2011a).

Barman, T. S.; Macintosh, B.; Konopacky, Q. M. and Marois, C. The Young Planet-mass Object 2M1207b: A Cool, Cloudy, and Methane-poor Atmosphere. ApJ **735**, L39 (2011b).

Barshay, S. S. and Lewis, J. S. Chemical structure of the deep atmosphere of Jupiter. Icarus **33**, 593 (1978).

Barstow, J. K.; Aigrain, S.; Irwin, P. G. J.; Bowles, N.; Fletcher, L. N. and Lee, J.-M. On the potential of the EChO mission to characterize gas giant atmospheres. MNRAS **430**, 1188 (2013a).

Barstow, J. K.; Aigrain, S.; Irwin, P. G. J.; Fletcher, L. N. and Lee, J.-M. Constraining the atmosphere of GJ 1214b using an optimal estimation technique. MNRAS **434**, 2616 (2013b).

Batygin, K.; Laughlin, G.; Meschiari, S.; Rivera, E.; Vogt, S. and Butler, P. A Quasi-stationary Solution to Gliese 436b's Eccentricity. ApJ **699**, 23 (2009).

Baulch, D. L.; Cobos, C. J.; Cox, R. A.; Esser, C.; Frank, P.; Just, T.; Kerr, J. A.; Pilling, M. J.; Troe, J.; Walker, R. W. and Warnatz, J. Evaluated Kinetic Data for Combustion Modelling. *Journal of Physical and Chemical Reference Data* **21**, 411 (1992).

Bean, J. L.; Miller-Ricci Kempton, E. and Homeier, D. A ground-based transmission spectrum of the super-Earth exoplanet GJ 1214b. Nature **468**, 669 (2010).

Beaulieu, J.-P.; Tinetti, G.; Kipping, D. M.; Ribas, I.; Barber, R. J.; Cho, J. Y.-K.; Polichtchouk, I.; Tennyson, J.; Yurchenko, S. N.; Griffith, C. A.; Batista, V.; Waldmann, I.; Miller, S.; Carey, S.; Mousis, O.; Fossey, S. J. and Aylward, A. Methane in the Atmosphere of the Transiting Hot Neptune GJ436B? ApJ **731**, 16 (2011).

Becklin, E. E. and Zuckerman, B. A low-temperature companion to a white dwarf star. Nature **336**, 656 (1988).

Beichman, C.; Gelino, C. R.; Kirkpatrick, J. D.; Cushing, M. C.; Dodson-Robinson, S.; Marley, M. S.; Morley, C. V. and Wright, E. L. WISE Y Dwarfs as Probes of the Brown Dwarf-Exoplanet Connection. ApJ **783**, 68 (2014).

Benneke, B. Strict Upper Limits on the Carbon-to-Oxygen Ratios of Eight Hot Jupiters from Self-Consistent Atmospheric Retrieval. *ArXiv e-prints* (2015).

Benneke, B. and Seager, S. Atmospheric Retrieval for Super-Earths: Uniquely Constraining the Atmospheric Composition with Transmission Spectroscopy. ApJ **753**, 100 (2012).

Benneke, B. and Seager, S. How to Distinguish between Cloudy Mini-Neptunes and Water/Volatile-dominated Super-Earths. ApJ **778**, 153 (2013).

Berta, Z. K.; Charbonneau, D.; Désert, J.-M.; Miller-Ricci Kempton, E.; McCullough, P. R.; Burke, C. J.; Fortney, J. J.; Irwin, J.; Nutzman, P. and Homeier, D. The Flat Transmission Spectrum of the Super-Earth GJ1214b from Wide Field Camera 3 on the Hubble Space Telescope. ApJ **747**, 35 (2012).

Beuzit, J.-L.; Feldt, M.; Dohlen, K.; Mouillet, D.; Puget, P.; Antichi, J.; Baruffolo, A.; Baudoz, P.; Berton, A.; Boccaletti, A.; Carbillet, M.; Charton, J.; Claudi, R.; Downing, M.; Feautrier, P.; Fedrigo, E.; Fusco, T.; Gratton, R.; Hubin, N.; Kasper, M.; Langlois, M.; Moutou, C.; Mugnier, L.; Pragt, J.; Rabou, P.; Saisse, M.; Schmid, H. M.; Stadler, E.; Turrato, M.; Udry, S.; Waters, R. and Wildi, F. SPHERE: A 'Planet Finder' Instrument for the VLT. *The Messenger* **125**, 29 (2006).

Bevington, P. R. and Robinson, D. K. *Data reduction and error analysis for the physical sciences*. McGraw Hill (2003).

Biller, B. A.; Crossfield, I. J. M.; Mancini, L.; Ciceri, S.; Southworth, J.; Kopytova, T. G.; Bonnefoy, M.; Deacon, N. R.; Schlieder, J. E.; Buenzli, E.; Brandner, W.; Allard, F.; Homeier, D.; Freytag, B.; Bailer-Jones, C. A. L.; Greiner, J.; Henning, T. and Goldman, B. Weather on the Nearest Brown Dwarfs: Resolved Simultaneous Multi-wavelength Variability Monitoring of WISE J104915.57–531906.1AB. ApJ **778**, L10 (2013).

Blake, C. H.; Charbonneau, D.; White, R. J.; Marley, M. S. and Saumon, D. Multiepoch Radial Velocity Observations of L Dwarfs. ApJ **666**, 1198 (2007).

Bonnefoy, M.; Boccaletti, A.; Lagrange, A.-M.; Allard, F.; Mordasini, C.; Beust, H.; Chauvin, G.; Girard, J. H. V.; Homeier, D.; Apai, D.; Lacour, S. and Rouan, D. The near-infrared spectral energy distribution of β Pictoris b. A&A **555**, A107 (2013).

Borucki, W. J.; Koch, D. G.; Basri, G.; Batalha, N.; Boss, A.; Brown, T. M.; Caldwell, D.; Christensen-Dalsgaard, J.; Cochran, W. D.; DeVore, E.; Dunham, E. W.; Dupree, A. K.; Gautier, III, T. N.; Geary, J. C.; Gilliland, R.; Gould, A.; Howell, S. B.; Jenkins, J. M.; Kjeldsen, H.; Latham, D. W.; Lissauer, J. J.; Marcy, G. W.; Monet, D. G.; Sasselov, D.; Tarter, J.; Charbonneau, D.; Doyle, L.; Ford, E. B.; Fortney, J.; Holman, M. J.; Seager, S.; Steffen, J. H.; Welsh, W. F.; Allen, C.; Bryson, S. T.; Buchhave, L.; Chandrasekaran, H.; Christiansen, J. L.; Ciardi, D.; Clarke, B. D.; Dotson, J. L.; Endl, M.; Fischer, D.; Fressin, F.; Haas, M.; Horch, E.; Howard, A.; Isaacson, H.; Kolodziejczak, J.; Li, J.; MacQueen, P.; Meibom, S.; Prsa, A.; Quintana, E. V.; Rowe, J.; Sherry, W.; Tenenbaum, P.; Torres, G.;

Twicken, J. D.; Van Cleve, J.; Walkowicz, L. and Wu, H. Characteristics of Kepler Planetary Candidates Based on the First Data Set. ApJ **728**, 117 (2011).

Bowler, B. P. and Hillenbrand, L. A. Near-infrared Spectroscopy of 2M0441+2301 AabBab: A Quadruple System Spanning the Stellar to Planetary Mass Regimes. ApJ **811**, L30 (2015).

Bowler, B. P.; Liu, M. C.; Dupuy, T. J. and Cushing, M. C. Near-infrared Spectroscopy of the Extrasolar Planet HR 8799 b. ApJ **723**, 850 (2010).

Brown, M. E.; Roberts, J. E. and Schaller, E. L. Clouds on Titan during the Cassini prime mission: A complete analysis of the VIMS data. Icarus **205**, 571 (2010).

Brown, T. M. Transmission Spectra as Diagnostics of Extrasolar Giant Planet Atmospheres. ApJ **553**, 1006 (2001).

Buchner, J.; Georgakakis, A.; Nandra, K.; Hsu, L.; Rangel, C.; Brightman, M.; Merloni, A.; Salvato, M.; Donley, J. and Kocevski, D. X-ray spectral modelling of the AGN obscuring region in the CDFS: Bayesian model selection and catalogue. A&A **564**, A125 (2014).

Buck, A. L. New Equations for Computing Vapor Pressure and Enhancement Factor. *Journal of Applied Meteorology* **20**, 1527 (1981).

Buenzli, E.; Apai, D.; Morley, C. V.; Flateau, D.; Showman, A. P.; Burrows, A.; Marley, M. S.; Lewis, N. K. and Reid, I. N. Vertical Atmospheric Structure in a Variable Brown Dwarf: Pressure-dependent Phase Shifts in Simultaneous Hubble Space Telescope-Spitzer Light Curves. ApJ **760**, L31 (2012).

Buenzli, E.; Apai, D.; Radigan, J.; Reid, I. N. and Flateau, D. Brown Dwarf Photospheres are Patchy: A Hubble Space Telescope Near-infrared Spectroscopic Survey Finds Frequent Low-level Variability. ApJ **782**, 77 (2014).

Buras, R.; Dowling, T. and Emde, C. New secondary-scattering correction in DISORT with increased efficiency for forward scattering. J. Quant. Spec. Radiat. Transf. **112**, 2028 (2011).

Burgasser, A. J.; Geballe, T. R.; Leggett, S. K.; Kirkpatrick, J. D. and Golimowski, D. A. A Unified Near-Infrared Spectral Classification Scheme for T Dwarfs. ApJ **637**, 1067 (2006).

Burgasser, A. J.; Gillon, M.; Faherty, J. K.; Radigan, J.; Triaud, A. H. M. J.; Plavchan, P.; Street, R.; Jehin, E.; Delrez, L. and Opitom, C. A Monitoring Campaign for Luhman 16AB. I. Detection of Resolved Near-infrared Spectroscopic Variability. ApJ **785**, 48 (2014).

Burgasser, A. J.; Marley, M. S.; Ackerman, A. S.; Saumon, D.; Lodders, K.; Dahn, C. C.; Harris, H. C. and Kirkpatrick, J. D. Evidence of Cloud Disruption in the L/T Dwarf Transition. ApJ **571**, L151 (2002).

Burgasser, A. J.; Simcoe, R. A.; Bochanski, J. J.; Saumon, D.; Mamajek, E. E.; Cushing, M. C.; Marley, M. S.; McMurtry, C.; Pipher, J. L. and Forrest, W. J. Clouds in the Coldest Brown Dwarfs: Fire Spectroscopy of Ross 458C. ApJ **725**, 1405 (2010).

Burningham, B.; Leggett, S. K.; Homeier, D.; Saumon, D.; Lucas, P. W.; Pinfield, D. J.; Tinney, C. G.; Allard, F.; Marley, M. S.; Jones, H. R. A.; Murray, D. N.; Ishii, M.; Day-Jones, A.; Gomes, J. and Zhang, Z. H. The properties of the T8.5p dwarf Ross 458C. MNRAS **414**, 3590 (2011).

Burrows, A.; Burgasser, A. J.; Kirkpatrick, J. D.; Liebert, J.; Milsom, J. A.; Sudarsky, D. and Hubeny, I. Theoretical Spectral Models of T Dwarfs at Short Wavelengths and Their Comparison with Data. ApJ **573**, 394 (2002).

Burrows, A.; Hubbard, W. B.; Lunine, J. I. and Liebert, J. The theory of brown dwarfs and extrasolar giant planets. *Reviews of Modern Physics* **73**, 719 (2001).

Burrows, A.; Hubeny, I.; Hubbard, W. B.; Sudarsky, D. and Fortney, J. J. Theoretical Radii of Transiting Giant Planets: The Case of OGLE-TR-56b. ApJ **610**, L53 (2004).

Burrows, A.; Marley, M.; Hubbard, W. B.; Lunine, J. I.; Guillot, T.; Saumon, D.; Freedman, R.; Sudarsky, D. and Sharp, C. A Nongray Theory of Extrasolar Giant Planets and Brown Dwarfs. ApJ **491**, 856 (1997).

Burrows, A.; Marley, M. S. and Sharp, C. M. The Near-Infrared and Optical Spectra of Methane Dwarfs and Brown Dwarfs. ApJ **531**, 438 (2000).

Burrows, A. and Sharp, C. M. Chemical Equilibrium Abundances in Brown Dwarf and Extrasolar Giant Planet Atmospheres. ApJ **512**, 843 (1999).

Burrows, A.; Sudarsky, D. and Hubbard, W. B. A Theory for the Radius of the Transiting Giant Planet HD 209458b. ApJ **594**, 545 (2003a).

Burrows, A.; Sudarsky, D. and Hubeny, I. Theory for the Secondary Eclipse Fluxes, Spectra, Atmospheres, and Light Curves of Transiting Extrasolar Giant Planets. ApJ **650**, 1140 (2006).

Burrows, A.; Sudarsky, D. and Lunine, J. I. Beyond the T Dwarfs: Theoretical Spectra, Colors, and Detectability of the Coolest Brown Dwarfs. ApJ **596**, 587 (2003b).

Butler, R. P.; Vogt, S. S.; Marcy, G. W.; Fischer, D. A.; Wright, J. T.; Henry, G. W.; Laughlin, G. and Lissauer, J. J. A Neptune-Mass Planet Orbiting the Nearby M Dwarf GJ 436. ApJ **617**, 580 (2004).

Cahoy, K. L.; Marley, M. S. and Fortney, J. J. Exoplanet Albedo Spectra and Colors as a Function of Planet Phase, Separation, and Metallicity. ApJ **724**, 189 (2010).

Carlson, B. E.; Lacis, A. A. and Rossow, W. B. The abundance and distribution of water vapor in the Jovian troposphere as inferred from Voyager IRIS observations. ApJ **388**, 648 (1992).

Carlson, B. E.; Lacis, A. A. and Rossow, W. B. Belt-zone variations in the Jovian cloud structure. J. Geophys. Res. **99**, 14623 (1994).

Carlson, B. E.; Rossow, W. B. and Orton, G. S. Cloud microphysics of the giant planets. *Journal of Atmospheric Sciences* **45**, 2066 (1988).

Chamberlain, J. W. and Hunten, D. M. Theory of planetary atmospheres: an introduction to their physics and chemistry /2nd revised and enlarged edition/. *Orlando FL Academic Press Inc International Geophysics Series* **36** (1987).

Charbonneau, D.; Berta, Z. K.; Irwin, J.; Burke, C. J.; Nutzman, P.; Buchhave, L. A.; Lovis, C.; Bonfils, X.; Latham, D. W.; Udry, S.; Murray-Clay, R. A.; Holman, M. J.; Falco, E. E.; Winn, J. N.; Queloz, D.; Pepe, F.; Mayor, M.; Delfosse, X. and Forveille, T. A super-Earth transiting a nearby low-mass star. Nature **462**, 891 (2009).

Charbonneau, D.; Brown, T. M.; Noyes, R. W. and Gilliland, R. L. Detection of an Extrasolar Planet Atmosphere. ApJ **568**, 377 (2002).

Charnay, B.; Meadows, V. and Leconte, J. 3D Modeling of GJ1214b's Atmosphere: Vertical Mixing Driven by an Anti-Hadley Circulation. ApJ **813**, 15 (2015).

Clarke, F. J.; Hodgkin, S. T.; Oppenheimer, B. R.; Robertson, J. and Haubois, X. A search for J-band variability from late-L and T brown dwarfs. MNRAS **386**, 2009 (2008).

Conrath, B. J.; Gierasch, P. J. and Ustinov, E. A. Thermal Structure and Para Hydrogen Fraction on the Outer Planets from Voyager IRIS Measurements. Icarus **135**, 501 (1998).

Cooper, C. S.; Sudarsky, D.; Milsom, J. A.; Lunine, J. I. and Burrows, A. Modeling the Formation of Clouds in Brown Dwarf Atmospheres. ApJ **586**, 1320 (2003).

Croll, B.; Albert, L.; Jayawardhana, R.; Miller-Ricci Kempton, E.; Fortney, J. J.; Murray, N. and Neilson, H. Broadband Transmission Spectroscopy of the Super-Earth GJ 1214b Suggests a Low Mean Molecular Weight Atmosphere. ApJ **736**, 78 (2011).

Crossfield, I. J. M.; Barman, T. and Hansen, B. M. S. High-resolution, Differential, Near-infrared Transmission Spectroscopy of GJ 1214b. ApJ **736**, 132 (2011).

Crossfield, I. J. M.; Biller, B.; Schlieder, J. E.; Deacon, N. R.; Bonnefoy, M.; Homeier, D.; Allard, F.; Buenzli, E.; Henning, T.; Brandner, W.; Goldman, B. and Kopytova, T. A global cloud map of the nearest known brown dwarf. Nature **505**, 654 (2014).

Cruz, K. L.; Kirkpatrick, J. D. and Burgasser, A. J. Young L Dwarfs Identified in the Field: A Preliminary Low-Gravity, Optical Spectral Sequence from L0 to L5. AJ **137**, 3345 (2009).

Currie, T.; Burrows, A.; Itoh, Y.; Matsumura, S.; Fukagawa, M.; Apai, D.; Madhusudhan, N.; Hinz, P. M.; Rodigas, T. J.; Kasper, M.; Pyo, T.-S. and Ogino, S. A Combined Subaru/VLT/MMT 1-5 μm Study of Planets Orbiting HR 8799: Implications for Atmospheric Properties, Masses, and Formation. ApJ **729**, 128 (2011).

Cushing, M. C.; Kirkpatrick, J. D.; Gelino, C. R.; Griffith, R. L.; Skrutskie, M. F.; Mainzer, A.; Marsh, K. A.; Beichman, C. A.; Burgasser, A. J.; Prato, L. A.; Simcoe, R. A.; Marley, M. S.; Saumon, D.; Freedman, R. S.; Eisenhardt, P. R. and Wright, E. L. The Discovery of Y Dwarfs using Data from the Wide-field Infrared Survey Explorer (WISE). ApJ **743**, 50 (2011).

Cushing, M. C.; Marley, M. S.; Saumon, D.; Kelly, B. C.; Vacca, W. D.; Rayner, J. T.; Freedman, R. S.; Lodders, K. and Roellig, T. L. Atmospheric Parameters of Field L and T Dwarfs. ApJ **678**, 1372 (2008).

Cushing, M. C.; Roellig, T. L.; Marley, M. S.; Saumon, D.; Leggett, S. K.; Kirkpatrick, J. D.; Wilson, J. C.; Sloan, G. C.; Mainzer, A. K.; Van Cleve, J. E. and Houck, J. R. A Spitzer Infrared Spectrograph Spectral Sequence of M, L, and T Dwarfs. ApJ **648**, 614 (2006).

de Kok, R.; Irwin, P. G. J.; Teanby, N. A.; Nixon, C. A.; Jennings, D. E.; Fletcher, L.; Howett, C.; Calcutt, S. B.; Bowles, N. E.; Flasar, F. M. and Taylor, F. W. Characteristics of Titan's stratospheric aerosols and condensate clouds from Cassini CIRS far-infrared spectra. Icarus **191**, 223 (2007).

de Kok, R. J.; Helling, C.; Stam, D. M.; Woitke, P. and Witte, S. The influence of non-isotropic scattering of thermal radiation on spectra of brown dwarfs and hot exoplanets. A&A **531**, A67 (2011).

de Mooij, E. J. W.; Brogi, M.; de Kok, R. J.; Koppenhoefer, J.; Nefs, S. V.; Snellen, I. A. G.; Greiner, J.; Hanse, J.; Heinsbroek, R. C.; Lee, C. H. and van der Werf, P. P. Optical to near-infrared transit observations of super-Earth GJ 1214b: water-world or mini-Neptune? A&A **538**, A46 (2012).

Delorme, P.; Delfosse, X.; Albert, L.; Artigau, E.; Forveille, T.; Reylé, C.; Allard, F.; Homeier, D.; Robin, A. C.; Willott, C. J.; Liu, M. C. and Dupuy, T. J. CFBDS J005910.90-011401.3: reaching the T-Y brown dwarf transition? A&A **482**, 961 (2008).

Deming, D.; Harrington, J.; Laughlin, G.; Seager, S.; Navarro, S. B.; Bowman, W. C. and Horning, K. Spitzer Transit and Secondary Eclipse Photometry of GJ 436b. ApJ **667**, L199 (2007).

Deming, D.; Knutson, H.; Kammer, J.; Fulton, B. J.; Ingalls, J.; Carey, S.; Burrows, A.; Fortney, J. J.; Todorov, K.; Agol, E.; Cowan, N.; Desert, J.-M.; Fraine, J.; Langton, J.; Morley, C. and Showman, A. P. Spitzer Secondary Eclipses of the Dense, Modestly-irradiated, Giant Exoplanet HAT-P-20b Using Pixel-level Decorrelation. ApJ **805**, 132 (2015).

Deming, D.; Wilkins, A.; McCullough, P.; Burrows, A.; Fortney, J. J.; Agol, E.; Dobbs-Dixon, I.; Madhusudhan, N.; Crouzet, N.; Desert, J.-M.; Gilliland, R. L.; Haynes, K.; Knutson, H. A.; Line, M.; Magic, Z.; Mandell, A. M.; Ranjan, S.; Charbonneau, D.; Clampin, M.;

Seager, S. and Showman, A. P. Infrared Transmission Spectroscopy of the Exoplanets HD 209458b and XO-1b Using the Wide Field Camera-3 on the Hubble Space Telescope. ApJ **774**, 95 (2013).

Demory, B.-O.; Gillon, M.; Barman, T.; Bonfils, X.; Mayor, M.; Mazeh, T.; Queloz, D.; Udry, S.; Bouchy, F.; Delfosse, X.; Forveille, T.; Mallmann, F.; Pepe, F. and Perrier, C. Characterization of the hot Neptune GJ 436 b with Spitzer and ground-based observations. A&A **475**, 1125 (2007).

Désert, J.-M.; Bean, J.; Miller-Ricci Kempton, E.; Berta, Z. K.; Charbonneau, D.; Irwin, J.; Fortney, J.; Burke, C. J. and Nutzman, P. Observational Evidence for a Metal-rich Atmosphere on the Super-Earth GJ1214b. ApJ **731**, L40 (2011).

Diamond-Lowe, H.; Stevenson, K. B.; Bean, J. L.; Line, M. R. and Fortney, J. J. New Analysis Indicates No Thermal Inversion in the Atmosphere of HD 209458b. ApJ **796**, 66 (2014).

Dupuy, T. J. and Kraus, A. L. Distances, Luminosities, and Temperatures of the Coldest Known Substellar Objects. *Science* **341**, 1492 (2013).

Dupuy, T. J. and Liu, M. C. The Hawaii Infrared Parallax Program. I. Ultracool Binaries and the L/T Transition. ApJS **201**, 19 (2012).

Ehrenreich, D.; Bonfils, X.; Lovis, C.; Delfosse, X.; Forveille, T.; Mayor, M.; Neves, V.; Santos, N. C.; Udry, S. and Ségransan, D. Near-infrared transmission spectrum of the warm-Uranus GJ 3470b with the Wide Field Camera-3 on the Hubble Space Telescope. A&A **570**, A89 (2014).

Faherty, J. K.; Burgasser, A. J.; Walter, F. M.; Van der Bliek, N.; Shara, M. M.; Cruz, K. L.; West, A. A.; Vrba, F. J. and Anglada-Escudé, G. The Brown Dwarf Kinematics Project (BDKP). III. Parallaxes for 70 Ultracool Dwarfs. ApJ **752**, 56 (2012).

Faherty, J. K.; Rice, E. L.; Cruz, K. L.; Mamajek, E. E. and Núñez, A. 2MASS J035523.37+113343.7: A Young, Dusty, Nearby, Isolated Brown Dwarf Resembling a Giant Exoplanet. AJ **145**, 2 (2013).

Fegley, B. J. and Lodders, K. Chemical models of the deep atmospheres of Jupiter and Saturn. *Icarus* **110**, 117 (1994).

Fegley, B. J. and Lodders, K. Atmospheric Chemistry of the Brown Dwarf Gliese 229B: Thermochemical Equilibrium Predictions. ApJ **472**, L37 (1996).

Feroz, F.; Hobson, M. P. and Bridges, M. MULTINEST: an efficient and robust Bayesian inference tool for cosmology and particle physics. MNRAS **398**, 1601 (2009).

Fletcher, L. N.; Drossart, P.; Burgdorf, M.; Orton, G. S. and Encrenaz, T. Neptune's atmospheric composition from AKARI infrared spectroscopy. A&A **514**, A17 (2010).

Fletcher, L. N.; Irwin, P. G. J.; Teanby, N. A.; Orton, G. S.; Parrish, P. D.; de Kok, R.; Howett, C.; Calcutt, S. B.; Bowles, N. and Taylor, F. W. Characterising Saturn's vertical temperature structure from Cassini/CIRS. Icarus **189**, 457 (2007).

Fletcher, L. N.; Orton, G. S.; Teanby, N. A.; Irwin, P. G. J. and Bjoraker, G. L. Methane and its isotopologues on Saturn from Cassini/CIRS observations. Icarus **199**, 351 (2009).

Fortney, J. J. The effect of condensates on the characterization of transiting planet atmospheres with transmission spectroscopy. MNRAS **364**, 649 (2005).

Fortney, J. J.; Lodders, K.; Marley, M. S. and Freedman, R. S. A Unified Theory for the Atmospheres of the Hot and Very Hot Jupiters: Two Classes of Irradiated Atmospheres. ApJ **678**, 1419 (2008a).

Fortney, J. J.; Marley, M. S. and Barnes, J. W. Planetary Radii across Five Orders of Magnitude in Mass and Stellar Insolation: Application to Transits. ApJ **659**, 1661 (2007).

Fortney, J. J.; Marley, M. S.; Lodders, K.; Saumon, D. and Freedman, R. Comparative Planetary Atmospheres: Models of TrES-1 and HD 209458b. ApJ **627**, L69 (2005).

Fortney, J. J.; Marley, M. S.; Saumon, D. and Lodders, K. Synthetic Spectra and Colors of Young Giant Planet Atmospheres: Effects of Initial Conditions and Atmospheric Metallicity. ApJ **683**, 1104 (2008b).

Fortney, J. J.; Mordasini, C.; Nettelmann, N.; Kempton, E. M.-R.; Greene, T. P. and Zahnle, K. A Framework for Characterizing the Atmospheres of Low-mass Low-density Transiting Planets. ApJ **775**, 80 (2013).

Fortney, J. J.; Sudarsky, D.; Hubeny, I.; Cooper, C. S.; Hubbard, W. B.; Burrows, A. and Lunine, J. I. On the Indirect Detection of Sodium in the Atmosphere of the Planetary Companion to HD 209458. ApJ **589**, 615 (2003).

Fraine, J.; Deming, D.; Benneke, B.; Knutson, H.; Jordán, A.; Espinoza, N.; Madhusudhan, N.; Wilkins, A. and Todorov, K. Water vapour absorption in the clear atmosphere of a Neptune-sized exoplanet. Nature **513**, 526 (2014).

Fraine, J. D.; Deming, D.; Gillon, M.; Jehin, E.; Demory, B.-O.; Benneke, B.; Seager, S.; Lewis, N. K.; Knutson, H. and Désert, J.-M. Spitzer Transits of the Super-Earth GJ1214b and Implications for its Atmosphere. ApJ **765**, 127 (2013).

France, K.; Froning, C. S.; Linsky, J. L.; Roberge, A.; Stocke, J. T.; Tian, F.; Bushinsky, R.; Désert, J.-M.; Mauas, P.; Vieytes, M. and Walkowicz, L. M. The Ultraviolet Radiation Environment around M dwarf Exoplanet Host Stars. ApJ **763**, 149 (2013).

Freedman, R. S.; Lustig-Yaeger, J.; Fortney, J. J.; Lupu, R. E.; Marley, M. S. and Lodders, K. Gaseous Mean Opacities for Giant Planet and Ultracool Dwarf Atmospheres over a Range of Metallicities and Temperatures. ApJS **214**, 25 (2014).

Freedman, R. S.; Marley, M. S. and Lodders, K. Line and Mean Opacities for Ultracool Dwarfs and Extrasolar Planets. ApJS **174**, 504 (2008).

Freytag, B.; Allard, F.; Ludwig, H.-G.; Homeier, D. and Steffen, M. The role of convection, overshoot, and gravity waves for the transport of dust in M dwarf and brown dwarf atmospheres. A&A **513**, A19 (2010).

Friedson, A. J.; Wong, A.-S. and Yung, Y. L. Models for Polar Haze Formation in Jupiter's Stratosphere. Icarus **158**, 389 (2002).

Gagné, J.; Faherty, J. K.; Cruz, K. L.; Lafreniére, D.; Doyon, R.; Malo, L.; Burgasser, A. J.; Naud, M.-E.; Artigau, É.; Bouchard, S.; Gizis, J. E. and Albert, L. BANYAN. VII. A New Population of Young Substellar Candidate Members of Nearby Moving Groups from the BASS Survey. ApJS **219**, 33 (2015).

Galicher, R.; Marois, C.; Macintosh, B.; Barman, T. and Konopacky, Q. M-band Imaging of the HR 8799 Planetary System Using an Innovative LOCI-based Background Subtraction Technique. ApJ **739**, L41 (2011).

Gardner, J. P.; Mather, J. C.; Clampin, M.; Doyon, R.; Greenhouse, M. A.; Hammel, H. B.; Hutchings, J. B.; Jakobsen, P.; Lilly, S. J.; Long, K. S.; Lunine, J. I.; McCaughrean, M. J.; Mountain, M.; Nella, J.; Rieke, G. H.; Rieke, M. J.; Rix, H.-W.; Smith, E. P.; Sonneborn, G.; Stiavelli, M.; Stockman, H. S.; Windhorst, R. A. and Wright, G. S. The James Webb Space Telescope. Space Sci. Rev. **123**, 485 (2006).

Gautier, D. and Owen, T. *in Origin and Evolution of Planetary and Satellite Atmospheres, ed. S. K. Ateya, J. B. Pollack, & M. S. Matthews*, Tucson: Univ. of Arizona Press, pp. 487–512 (1989).

Geballe, T. R.; Saumon, D.; Golimowski, D. A.; Leggett, S. K.; Marley, M. S. and Noll, K. S. Spectroscopic Detection of Carbon Monoxide in Two Late-Type T Dwarfs. ApJ **695**, 844 (2009).

Gelino, C. R.; Marley, M. S.; Holtzman, J. A.; Ackerman, A. S. and Lodders, K. L Dwarf Variability: I-Band Observations. ApJ **577**, 433 (2002).

Gibbard, S. G.; de Pater, I.; Roe, H. G.; Martin, S.; Macintosh, B. A. and Max, C. E. The altitude of Neptune cloud features from high-spatial-resolution near-infrared spectra. Icarus **166**, 359 (2003).

Gibson, N. P.; Aigrain, S.; Pont, F.; Sing, D. K.; Désert, J.-M.; Evans, T. M.; Henry, G.; Husnoo, N. and Knutson, H. Probing the haze in the atmosphere of HD 189733b with Hubble Space Telescope/WFC3 transmission spectroscopy. MNRAS **422**, 753 (2012).

Gibson, N. P.; Pont, F. and Aigrain, S. A new look at NICMOS transmission spectroscopy of HD 189733, GJ-436 and XO-1: no conclusive evidence for molecular features. MNRAS **411**, 2199 (2011).

Gierasch, P. J. and Conrath, B. J. *Energy conversion processes in the outer planets*, pp. 121–146 (1985).

Gillon, M.; Demory, B.-O.; Barman, T.; Bonfils, X.; Mazeh, T.; Pont, F.; Udry, S.; Mayor, M. and Queloz, D. Accurate Spitzer infrared radius measurement for the hot Neptune GJ 436b. A&A **471**, L51 (2007a).

Gillon, M.; Pont, F.; Demory, B.-O.; Mallmann, F.; Mayor, M.; Mazeh, T.; Queloz, D.; Shporer, A.; Udry, S. and Vuissoz, C. Detection of transits of the nearby hot Neptune GJ 436 b. A&A **472**, L13 (2007b).

Gillon, M.; Triaud, A. H. M. J.; Jehin, E.; Delrez, L.; Opitom, C.; Magain, P.; Lendl, M. and Queloz, D. Fast-evolving weather for the coolest of our two new substellar neighbours. A&A **555**, L5 (2013).

Gizis, J. E.; Burgasser, A. J.; Berger, E.; Williams, P. K. G.; Vrba, F. J.; Cruz, K. L. and Metchev, S. Kepler Monitoring of an L Dwarf I. The Photometric Period and White Light Flares. ApJ **779**, 172 (2013).

Goldreich, P. and Soter, S. Q in the Solar System. Icarus **5**, 375 (1966).

Goody, R. M. and Yung, Y. L. *Atmospheric radiation : theoretical basis*. 2nd ed., New York, NY: Oxford University Press, 1989 (1989).

Greene, T. P.; Line, M. R.; Montero, C.; Fortney, J. J.; Lustig-Yaeger, J. and Luther, K. Characterizing Transiting Exoplanet Atmospheres with JWST. ApJ **817**, 17 (2016).

Hammel, H. B.; Beebe, R. F.; de Jong, E. M.; Hansen, C. J.; Howell, C. D.; Ingersoll, A. P.; Johnson, T. V.; Limaye, S. S.; Magalhaes, J. A.; Pollack, J. B.; Sromovsky, L. A.; Suomi, V. E. and Swift, C. E. Neptune's wind speeds obtained by tracking clouds in Voyager images. *Science* **245**, 1367 (1989).

Hansen, C. J.; Schwartz, J. C. and Cowan, N. B. Features in the broad-band eclipse spectra of exoplanets: signal or noise? MNRAS **444**, 3632 (2014).

Hauschildt, P. H.; Allard, F.; Ferguson, J.; Baron, E. and Alexander, D. R. The NEXTGEN Model Atmosphere Grid. II. Spherically Symmetric Model Atmospheres for Giant Stars with Effective Temperatures between 3000 and 6800 K. ApJ **525**, 871 (1999).

Helling, C.; Ackerman, A.; Allard, F.; Dehn, M.; Hauschildt, P.; Homeier, D.; Lodders, K.; Marley, M.; Rietmeijer, F.; Tsuji, T. and Woitke, P. A comparison of chemistry and dust cloud formation in ultracool dwarf model atmospheres. MNRAS **391**, 1854 (2008a).

Helling, C. and Woitke, P. Dust in brown dwarfs. V. Growth and evaporation of dirty dust grains. A&A **455**, 325 (2006).

Helling, C.; Woitke, P. and Thi, W.-F. Dust in brown dwarfs and extra-solar planets. I. Chemical composition and spectral appearance of quasi-static cloud layers. A&A **485**, 547 (2008b).

Hess, M.; Koepke, P. and Schult, I. Optical Properties of Aerosols and Clouds: The Software Package OPAC. *Bulletin of the American Meteorological Society* **79**, 831 (1998).

Hodapp, K. W.; Jensen, J. B.; Irwin, E. M.; Yamada, H.; Chung, R.; Fletcher, K.; Robertson, L.; Hora, J. L.; Simons, D. A.; Mays, W.; Nolan, R.; Bec, M.; Merrill, M. and Fowler, A. M. The Gemini Near-Infrared Imager (NIRI). PASP **115**, 1388 (2003).

Howard, A. W.; Marcy, G. W.; Bryson, S. T.; Jenkins, J. M.; Rowe, J. F.; Batalha, N. M.; Borucki, W. J.; Koch, D. G.; Dunham, E. W.; Gautier, III, T. N.; Van Cleve, J.; Cochran, W. D.; Latham, D. W.; Lissauer, J. J.; Torres, G.; Brown, T. M.; Gilliland, R. L.; Buchhave, L. A.; Caldwell, D. A.; Christensen-Dalsgaard, J.; Ciardi, D.; Fressin, F.; Haas, M. R.; Howell, S. B.; Kjeldsen, H.; Seager, S.; Rogers, L.; Sasselov, D. D.; Steffen, J. H.; Basri, G. S.; Charbonneau, D.; Christiansen, J.; Clarke, B.; Dupree, A.; Fabrycky, D. C.; Fischer, D. A.; Ford, E. B.; Fortney, J. J.; Tarter, J.; Girouard, F. R.; Holman, M. J.; Johnson, J. A.; Klaus, T. C.; Machalek, P.; Moorhead, A. V.; Morehead, R. C.; Ragozzine, D.; Tenenbaum, P.; Twicken, J. D.; Quinn, S. N.; Isaacson, H.; Shporer, A.; Lucas, P. W.; Walkowicz, L. M.; Welsh, W. F.; Boss, A.; Devore, E.; Gould, A.; Smith, J. C.; Morris, R. L.; Prsa, A.; Morton, T. D.; Still, M.; Thompson, S. E.; Mullally, F.; Endl, M. and MacQueen, P. J. Planet Occurrence within 0.25 AU of Solar-type Stars from Kepler. ApJS **201**, 15 (2012).

Howe, A. R. and Burrows, A. S. Theoretical Transit Spectra for GJ 1214b and Other "Super-Earths". ApJ **756**, 176 (2012).

Howell, S. B.; Sobeck, C.; Haas, M.; Still, M.; Barclay, T.; Mullally, F.; Troeltzsch, J.; Aigrain, S.; Bryson, S. T.; Caldwell, D.; Chaplin, W. J.; Cochran, W. D.; Huber, D.; Marcy, G. W.; Miglio, A.; Najita, J. R.; Smith, M.; Twicken, J. D. and Fortney, J. J. The K2 Mission: Characterization and Early Results. PASP **126**, 398 (2014).

Huang, X.; Freedman, R. S.; Tashkun, S. A.; Schwenke, D. W. and Lee, T. J. Semi-empirical $^{12}C^{16}O_2$ IR line lists for simulations up to 1500 K and 20,000 cm^{-1}. J. Quant. Spec. Radiat. Transf. **130**, 134 (2013).

Huang, X.; Gamache, R. R.; Freedman, R. S.; Schwenke, D. W. and Lee, T. J. Reliable infrared line lists for 13 CO_2 isotopologues up to E$\prime$=18,000 cm^{-1} and 1500 K, with line shape parameters. J. Quant. Spec. Radiat. Transf. **147**, 134 (2014).

Hubbard, W. B.; Fortney, J. J.; Lunine, J. I.; Burrows, A.; Sudarsky, D. and Pinto, P. Theory of Extrasolar Giant Planet Transits. ApJ **560**, 413 (2001).

Hubeny, I. and Burrows, A. A Systematic Study of Departures from Chemical Equilibrium in the Atmospheres of Substellar Mass Objects. ApJ **669**, 1248 (2007).

Huffman, D. R. and Wild, R. L. Optical Properties of α-MnS. *Physical Review* **156**, 989 (1967).

Irwin, P. G. J.; Teanby, N. A. and Davis, G. R. Latitudinal Variations in Uranus' Vertical Cloud Structure from UKIRT UIST Observations. ApJ **665**, L71 (2007).

Irwin, P. G. J.; Teanby, N. A.; de Kok, R.; Fletcher, L. N.; Howett, C. J. A.; Tsang, C. C. C.; Wilson, C. F.; Calcutt, S. B.; Nixon, C. A. and Parrish, P. D. The NEMESIS planetary atmosphere radiative transfer and retrieval tool. J. Quant. Spec. Radiat. Transf. **109**, 1136 (2008).

Janson, M.; Brandt, T. D.; Kuzuhara, M.; Spiegel, D. S.; Thalmann, C.; Currie, T.; Bonnefoy, M.; Zimmerman, N.; Sorahana, S.; Kotani, T.; Schlieder, J.; Hashimoto, J.; Kudo, T.; Kusakabe, N.; Abe, L.; Brandner, W.; Carson, J. C.; Egner, S.; Feldt, M.; Goto, M.; Grady, C. A.; Guyon, O.; Hayano, Y.; Hayashi, M.; Hayashi, S.; Henning, T.; Hodapp, K. W.; Ishii, M.; Iye, M.; Kandori, R.; Knapp, G. R.; Kwon, J.; Matsuo, T.; McElwain, M. W.; Mede, K.; Miyama, S.; Morino, J.-I.; Moro-Martín, A.; Nakagawa, T.; Nishimura, T.; Pyo, T.-S.; Serabyn, E.; Suenaga, T.; Suto, H.; Suzuki, R.; Takahashi, Y.; Takami, M.; Takato, N.; Terada, H.; Tomono, D.; Turner, E. L.; Watanabe, M.; Wisniewski, J.; Yamada, T.; Takami, H.; Usuda, T. and Tamura, M. Direct Imaging Detection of Methane in the Atmosphere of GJ 504 b. ApJ **778**, L4 (2013).

Kammer, J. A.; Knutson, H. A.; Line, M. R.; Fortney, J. J.; Deming, D.; Burrows, A.; Cowan, N. B.; Triaud, A. H. M. J.; Agol, E.; Desert, J.-M.; Fulton, B. J.; Howard, A. W.; Laughlin, G. P.; Lewis, N. K.; Morley, C. V.; Moses, J. I.; Showman, A. P. and Todorov, K. O. Spitzer Secondary Eclipse Observations of Five Cool Gas Giant Planets and Empirical Trends in Cool Planet Emission Spectra. ApJ **810**, 118 (2015).

Karkoschka, E. and Tomasko, M. The haze and methane distributions on Uranus from HST-STIS spectroscopy. Icarus **202**, 287 (2009).

Karkoschka, E. and Tomasko, M. G. The haze and methane distributions on Neptune from HST-STIS spectroscopy. Icarus **211**, 780 (2011).

Kataria, T.; Showman, A. P.; Fortney, J. J.; Marley, M. S. and Freedman, R. S. The Atmospheric Circulation of the Super Earth GJ 1214b: Dependence on Composition and Metallicity. ApJ **785**, 92 (2014).

Kempton, E. M.-R.; Perna, R. and Heng, K. High Resolution Transmission Spectroscopy as a Diagnostic for Jovian Exoplanet Atmospheres: Constraints from Theoretical Models. ApJ **795**, 24 (2014).

Khachai, H.; Khenata, R.; Bouhemadou, A.; Haddou, A.; Reshak, A. H.; Amrani, B.; Rached, D. and Soudini, B. FP-APW+lo calculations of the electronic and optical properties of alkali metal sulfides under pressure. *Journal of Physics Condensed Matter* **21**, 095404 (2009).

Khare, B. N.; Sagan, C.; Arakawa, E. T.; Suits, F.; Callcott, T. A. and Williams, M. W. Optical constants of organic tholins produced in a simulated Titanian atmosphere - From soft X-ray to microwave frequencies. Icarus **60**, 127 (1984).

Kim, W.; Park, Y. H.; Shin, J. Y.; Lee, A. C. and Lee, D. W. Size Determination of Diesel Soot Particles Using Flow and Sedimentation Field-Flow Fractionation. *Analytical Chemistry* **71**, 3265 (1999).

Kirkpatrick, J. D. New Spectral Types L and T. ARA&A **43**, 195 (2005).

Kirkpatrick, J. D.; Cushing, M. C.; Gelino, C. R.; Beichman, C. A.; Tinney, C. G.; Faherty, J. K.; Schneider, A. and Mace, G. N. Discovery of the Y1 Dwarf WISE J064723.23–623235.5. ApJ **776**, 128 (2013).

Kirkpatrick, J. D.; Cushing, M. C.; Gelino, C. R.; Griffith, R. L.; Skrutskie, M. F.; Marsh, K. A.; Wright, E. L.; Mainzer, A.; Eisenhardt, P. R.; McLean, I. S.; Thompson, M. A.; Bauer, J. M.; Benford, D. J.; Bridge, C. R.; Lake, S. E.; Petty, S. M.; Stanford, S. A.; Tsai, C.-W.; Bailey, V.; Beichman, C. A.; Bloom, J. S.; Bochanski, J. J.; Burgasser, A. J.; Capak, P. L.; Cruz, K. L.; Hinz, P. M.; Kartaltepe, J. S.; Knox, R. P.; Manohar, S.; Masters, D.; Morales-Calderón, M.; Prato, L. A.; Rodigas, T. J.; Salvato, M.; Schurr, S. D.; Scoville, N. Z.; Simcoe, R. A.; Stapelfeldt, K. R.; Stern, D.; Stock, N. D. and Vacca, W. D. The First Hundred Brown Dwarfs Discovered by the Wide-field Infrared Survey Explorer (WISE). ApJS **197**, 19 (2011).

Kirkpatrick, J. D.; Gelino, C. R.; Cushing, M. C.; Mace, G. N.; Griffith, R. L.; Skrutskie, M. F.; Marsh, K. A.; Wright, E. L.; Eisenhardt, P. R.; McLean, I. S.; Mainzer, A. K.; Burgasser, A. J.; Tinney, C. G.; Parker, S. and Salter, G. Further Defining Spectral Type "Y" and Exploring the Low-mass End of the Field Brown Dwarf Mass Function. ApJ **753**, 156 (2012).

Knapp, G. R.; Leggett, S. K.; Fan, X.; Marley, M. S.; Geballe, T. R.; Golimowski, D. A.; Finkbeiner, D.; Gunn, J. E.; Hennawi, J.; Ivezić, Z.; Lupton, R. H.; Schlegel, D. J.; Strauss, M. A.; Tsvetanov, Z. I.; Chiu, K.; Hoversten, E. A.; Glazebrook, K.; Zheng, W.; Hendrickson, M.; Williams, C. C.; Uomoto, A.; Vrba, F. J.; Henden, A. A.; Luginbuhl, C. B.; Guetter, H. H.; Munn, J. A.; Canzian, B.; Schneider, D. P. and Brinkmann, J. Near-Infrared Photom-

etry and Spectroscopy of L and T Dwarfs: The Effects of Temperature, Clouds, and Gravity. AJ **127**, 3553 (2004).

Knutson, H. A.; Benneke, B.; Deming, D. and Homeier, D. A featureless transmission spectrum for the Neptune-mass exoplanet GJ436b. Nature **505**, 66 (2014a).

Knutson, H. A.; Charbonneau, D.; Allen, L. E.; Burrows, A. and Megeath, S. T. The 3.6-8.0 μm Broadband Emission Spectrum of HD 209458b: Evidence for an Atmospheric Temperature Inversion. ApJ **673**, 526 (2008).

Knutson, H. A.; Dragomir, D.; Kreidberg, L.; Kempton, E. M.-R.; McCullough, P. R.; Fortney, J. J.; Bean, J. L.; Gillon, M.; Homeier, D. and Howard, A. W. Hubble Space Telescope Near-IR Transmission Spectroscopy of the Super-Earth HD 97658b. ApJ **794**, 155 (2014b).

Knutson, H. A.; Fulton, B. J.; Montet, B. T.; Kao, M.; Ngo, H.; Howard, A. W.; Crepp, J. R.; Hinkley, S.; Bakos, G. Á.; Batygin, K.; Johnson, J. A.; Morton, T. D. and Muirhead, P. S. Friends of Hot Jupiters. I. A Radial Velocity Search for Massive, Long-period Companions to Close-in Gas Giant Planets. ApJ **785**, 126 (2014c).

Knutson, H. A.; Madhusudhan, N.; Cowan, N. B.; Christiansen, J. L.; Agol, E.; Deming, D.; Désert, J.-M.; Charbonneau, D.; Henry, G. W.; Homeier, D.; Langton, J.; Laughlin, G. and Seager, S. A Spitzer Transmission Spectrum for the Exoplanet GJ 436b, Evidence for Stellar Variability, and Constraints on Dayside Flux Variations. ApJ **735**, 27 (2011).

Konopacky, Q. M.; Barman, T. S.; Macintosh, B. A. and Marois, C. Detection of Carbon Monoxide and Water Absorption Lines in an Exoplanet Atmosphere. *Science* **339**, 1398

(2013).

Kostov, V. and Apai, D. Mapping Directly Imaged Giant Exoplanets. ApJ **762**, 47 (2013).

Kreidberg, L.; Bean, J. L.; Désert, J.-M.; Benneke, B.; Deming, D.; Stevenson, K. B.; Seager, S.; Berta-Thompson, Z.; Seifahrt, A. and Homeier, D. Clouds in the atmosphere of the super-Earth exoplanet GJ1214b. Nature **505**, 69 (2014a).

Kreidberg, L.; Bean, J. L.; Désert, J.-M.; Line, M. R.; Fortney, J. J.; Madhusudhan, N.; Stevenson, K. B.; Showman, A. P.; Charbonneau, D.; McCullough, P. R.; Seager, S.; Burrows, A.; Henry, G. W.; Williamson, M.; Kataria, T. and Homeier, D. A Precise Water Abundance Measurement for the Hot Jupiter WASP-43b. ApJ **793**, L27 (2014b).

Kreidberg, L.; Line, M. R.; Bean, J. L.; Stevenson, K. B.; Désert, J.-M.; Madhusudhan, N.; Fortney, J. J.; Barstow, J. K.; Henry, G. W.; Williamson, M. H. and Showman, A. P. A Detection of Water in the Transmission Spectrum of the Hot Jupiter WASP-12b and Implications for Its Atmospheric Composition. ApJ **814**, 66 (2015).

Kuzuhara, M.; Tamura, M.; Kudo, T.; Janson, M.; Kandori, R.; Brandt, T. D.; Thalmann, C.; Spiegel, D.; Biller, B.; Carson, J.; Hori, Y.; Suzuki, R.; Burrows, A.; Henning, T.; Turner, E. L.; McElwain, M. W.; Moro-Martín, A.; Suenaga, T.; Takahashi, Y. H.; Kwon, J.; Lucas, P.; Abe, L.; Brandner, W.; Egner, S.; Feldt, M.; Fujiwara, H.; Goto, M.; Grady, C. A.; Guyon, O.; Hashimoto, J.; Hayano, Y.; Hayashi, M.; Hayashi, S. S.; Hodapp, K. W.; Ishii, M.; Iye, M.; Knapp, G. R.; Matsuo, T.; Mayama, S.; Miyama, S.; Morino, J.-I.; Nishikawa, J.; Nishimura, T.; Kotani, T.; Kusakabe, N.; Pyo, T.-S.; Serabyn, E.; Suto, H.; Takami, M.;

Takato, N.; Terada, H.; Tomono, D.; Watanabe, M.; Wisniewski, J. P.; Yamada, T.; Takami, H. and Usuda, T. Direct Imaging of a Cold Jovian Exoplanet in Orbit around the Sun-like Star GJ 504. ApJ **774**, 11 (2013).

Lanotte, A. A.; Gillon, M.; Demory, B.-O.; Fortney, J. J.; Astudillo, N.; Bonfils, X.; Magain, P.; Delfosse, X.; Forveille, T.; Lovis, C.; Mayor, M.; Neves, V.; Pepe, F.; Queloz, D.; Santos, N. and Udry, S. A global analysis of Spitzer and new HARPS data confirms the loneliness and metal-richness of GJ 436 b. A&A **572**, A73 (2014).

Lavvas, P.; Sander, M.; Kraft, M. and Imanaka, H. Surface Chemistry and Particle Shape: Processes for the Evolution of Aerosols in Titan's Atmosphere. ApJ **728**, 80 (2011).

Lecavelier Des Etangs, A.; Vidal-Madjar, A.; Désert, J.-M. and Sing, D. Rayleigh scattering by H_2 in the extrasolar planet HD 209458b. A&A **485**, 865 (2008).

Lee, J.-M.; Fletcher, L. N. and Irwin, P. G. J. Optimal estimation retrievals of the atmospheric structure and composition of HD 189733b from secondary eclipse spectroscopy. MNRAS **420**, 170 (2012).

Leggett, S. K.; Currie, M. J.; Varricatt, W. P.; Hawarden, T. G.; Adamson, A. J.; Buckle, J.; Carroll, T.; Davies, J. K.; Davis, C. J.; Kerr, T. H.; Kuhn, O. P.; Seigar, M. S. and Wold, T. JHK observations of faint standard stars in the Mauna Kea Observatories near-infrared photometric system. MNRAS **373**, 781 (2006).

Leggett, S. K.; Marley, M. S.; Freedman, R.; Saumon, D.; Liu, M. C.; Geballe, T. R.; Golimowski, D. A. and Stephens, D. C. Physical and Spectral Characteristics of the T8

and Later Type Dwarfs. ApJ **667**, 537 (2007a).

Leggett, S. K.; Morley, C. V.; Marley, M. S.; Saumon, D.; Fortney, J. J. and Visscher, C. A Comparison of Near-infrared Photometry and Spectra for Y Dwarfs with a New Generation of Cool Cloudy Models. ApJ **763**, 130 (2013).

Leggett, S. K.; Saumon, D.; Marley, M. S.; Geballe, T. R.; Golimowski, D. A.; Stephens, D. and Fan, X. 3.6-7.9 μm Photometry of L and T Dwarfs and the Prevalence of Vertical Mixing in their Atmospheres. ApJ **655**, 1079 (2007b).

Leggett, S. K.; Saumon, D.; Marley, M. S.; Lodders, K.; Canty, J.; Lucas, P.; Smart, R. L.; Tinney, C. G.; Homeier, D.; Allard, F.; Burningham, B.; Day-Jones, A.; Fegley, B.; Ishii, M.; Jones, H. R. A.; Marocco, F.; Pinfield, D. J. and Tamura, M. The Properties of the 500 K Dwarf UGPS J072227.51-054031.2 and a Study of the Far-red Flux of Cold Brown Dwarfs. ApJ **748**, 74 (2012).

Lewis, N. K.; Knutson, H. A.; Showman, A. P.; Cowan, N. B.; Laughlin, G.; Burrows, A.; Deming, D.; Crepp, J. R.; Mighell, K. J.; Agol, E.; Bakos, G. Á.; Charbonneau, D.; Désert, J.-M.; Fischer, D. A.; Fortney, J. J.; Hartman, J. D.; Hinkley, S.; Howard, A. W.; Johnson, J. A.; Kao, M.; Langton, J. and Marcy, G. W. Orbital Phase Variations of the Eccentric Giant Planet HAT-P-2b. ApJ **766**, 95 (2013).

Liang, M.; Seager, S.; Parkinson, C. D.; Lee, A. Y.-T. and Yung, Y. L. On the Insignificance of Photochemical Hydrocarbon Aerosols in the Atmospheres of Close-in Extrasolar Giant Planets. ApJ **605**, L61 (2004).

Line, M. R.; Knutson, H.; Wolf, A. S. and Yung, Y. L. A Systematic Retrieval Analysis of Secondary Eclipse Spectra. II. A Uniform Analysis of Nine Planets and their C to O Ratios. ApJ **783**, 70 (2014).

Line, M. R.; Liang, M. C. and Yung, Y. L. High-temperature Photochemistry in the Atmosphere of HD 189733b. ApJ **717**, 496 (2010).

Line, M. R. and Parmentier, V. The Influence of Nonuniform Cloud Cover on Transit Transmission Spectra. ApJ **820**, 78 (2016).

Line, M. R.; Teske, J.; Burningham, B.; Fortney, J. J. and Marley, M. S. Uniform Atmospheric Retrieval Analysis of Ultracool Dwarfs. I. Characterizing Benchmarks, Gl 570D and HD 3651B. ApJ **807**, 183 (2015).

Line, M. R.; Vasisht, G.; Chen, P.; Angerhausen, D. and Yung, Y. L. Thermochemical and Photochemical Kinetics in Cooler Hydrogen-dominated Extrasolar Planets: A Methane-poor GJ436b? ApJ **738**, 32 (2011).

Line, M. R.; Wolf, A. S.; Zhang, X.; Knutson, H.; Kammer, J. A.; Ellison, E.; Deroo, P.; Crisp, D. and Yung, Y. L. A Systematic Retrieval Analysis of Secondary Eclipse Spectra. I. A Comparison of Atmospheric Retrieval Techniques. ApJ **775**, 137 (2013).

Line, M. R. and Yung, Y. L. A Systematic Retrieval Analysis of Secondary Eclipse Spectra. III. Diagnosing Chemical Disequilibrium in Planetary Atmospheres. ApJ **779**, 3 (2013a).

Line, M. R. and Yung, Y. L. A Systematic Retrieval Analysis of Secondary Eclipse Spectra. III. Diagnosing Chemical Disequilibrium in Planetary Atmospheres. ApJ **779**, 3 (2013b).

Line, M. R.; Zhang, X.; Vasisht, G.; Natraj, V.; Chen, P. and Yung, Y. L. Information Content of Exoplanetary Transit Spectra: An Initial Look. ApJ **749**, 93 (2012).

Liu, M. C.; Delorme, P.; Dupuy, T. J.; Bowler, B. P.; Albert, L.; Artigau, E.; Reylé, C.; Forveille, T. and Delfosse, X. CFBDSIR J1458+1013B: A Very Cold (>T10) Brown Dwarf in a Binary System. ApJ **740**, 108 (2011).

Liu, M. C.; Dupuy, T. J.; Bowler, B. P.; Leggett, S. K. and Best, W. M. J. Two Extraordinary Substellar Binaries at the T/Y Transition and the Y-band Fluxes of the Coolest Brown Dwarfs. ApJ **758**, 57 (2012).

Liu, M. C.; Magnier, E. A.; Deacon, N. R.; Allers, K. N.; Dupuy, T. J.; Kotson, M. C.; Aller, K. M.; Burgett, W. S.; Chambers, K. C.; Draper, P. W.; Hodapp, K. W.; Jedicke, R.; Kaiser, N.; Kudritzki, R.-P.; Metcalfe, N.; Morgan, J. S.; Price, P. A.; Tonry, J. L. and Wainscoat, R. J. The Extremely Red, Young L Dwarf PSO J318.5338-22.8603: A Free-floating Planetary-mass Analog to Directly Imaged Young Gas-giant Planets. ApJ **777**, L20 (2013).

Lodders, K. Alkali Element Chemistry in Cool Dwarf Atmospheres. ApJ **519**, 793 (1999).

Lodders, K. Titanium and Vanadium Chemistry in Low-Mass Dwarf Stars. ApJ **577**, 974 (2002).

Lodders, K. Solar System Abundances and Condensation Temperatures of the Elements. ApJ **591**, 1220 (2003).

Lodders, K. Exoplanet Chemistry. *ArXiv e-prints* (2009).

Lodders, K. and Fegley, B. Atmospheric Chemistry in Giant Planets, Brown Dwarfs, and Low-Mass Dwarf Stars. I. Carbon, Nitrogen, and Oxygen. *Icarus* **155**, 393 (2002).

Lodders, K. and Fegley, B. *Astrophysics Update 2*. Springer Praxis Books, Berlin: Springer, 2006 (2006).

Lodieu, N.; Béjar, V. J. S. and Rebolo, R. GTC OSIRIS z-band imaging of Y dwarfs. A&A **550**, L2 (2013).

Lopez, E. D. and Fortney, J. J. The Role of Core Mass in Controlling Evaporation: The Kepler Radius Distribution and the Kepler-36 Density Dichotomy. ApJ **776**, 2 (2013).

Lopez, E. D.; Fortney, J. J. and Miller, N. How Thermal Evolution and Mass-loss Sculpt Populations of Super-Earths and Sub-Neptunes: Application to the Kepler-11 System and Beyond. ApJ **761**, 59 (2012).

Lucas, P. W.; Tinney, C. G.; Burningham, B.; Leggett, S. K.; Pinfield, D. J.; Smart, R.; Jones, H. R. A.; Marocco, F.; Barber, R. J.; Yurchenko, S. N.; Tennyson, J.; Ishii, M.; Tamura, M.; Day-Jones, A. C.; Adamson, A.; Allard, F. and Homeier, D. The discovery of a very cool, very nearby brown dwarf in the Galactic plane. MNRAS **408**, L56 (2010).

Luhman, K. L. Discovery of a ~250 K Brown Dwarf at 2 pc from the Sun. ApJ **786**, L18 (2014).

Luhman, K. L.; Burgasser, A. J.; Labbé, I.; Saumon, D.; Marley, M. S.; Bochanski, J. J.; Monson, A. J. and Persson, S. E. Confirmation of One of the Coldest Known Brown Dwarfs. ApJ **744**, 135 (2012).

Lunine, J. I.; Hubbard, W. B.; Burrows, A.; Wang, Y.-P. and Garlow, K. The effect of gas and grain opacity on the cooling of brown dwarfs. ApJ **338**, 314 (1989).

Lunine, J. I.; Hubbard, W. B. and Marley, M. S. Evolution and infrared spectra of brown dwarfs. ApJ **310**, 238 (1986).

Luszcz-Cook, S. H. and de Pater, I. Constraining the origins of Neptune's carbon monoxide abundance with CARMA millimeter-wave observations. Icarus **222**, 379 (2013).

Mace, G. N.; Kirkpatrick, J. D.; Cushing, M. C.; Gelino, C. R.; Griffith, R. L.; Skrutskie, M. F.; Marsh, K. A.; Wright, E. L.; Eisenhardt, P. R.; McLean, I. S.; Thompson, M. A.; Mix, K.; Bailey, V.; Beichman, C. A.; Bloom, J. S.; Burgasser, A. J.; Fortney, J. J.; Hinz, P. M.; Knox, R. P.; Lowrance, P. J.; Marley, M. S.; Morley, C. V.; Rodigas, T. J.; Saumon, D.; Sheppard, S. S. and Stock, N. D. A Study of the Diverse T Dwarf Population Revealed by WISE. ApJS **205**, 6 (2013).

Macintosh, B.; Graham, J.; Palmer, D.; Doyon, R.; Gavel, D.; Larkin, J.; Oppenheimer, B.; Saddlemyer, L.; Wallace, J. K.; Bauman, B.; Evans, J.; Erikson, D.; Morzinski, K.; Phillion, D.; Poyneer, L.; Sivaramakrishnan, A.; Soummer, R.; Thibault, S. and Veran, J.-P. The Gemini Planet Imager. In *Advances in Adaptive Optics II. Edited by Ellerbroek, Brent L.; Bonaccini Calia, Domenico. Proceedings of the SPIE, Volume 6272, pp. 62720L (2006).* (2006), vol. 6272 of *Presented at the Society of Photo-Optical Instrumentation Engineers (SPIE) Conference*.

Madhusudhan, N. C/O Ratio as a Dimension for Characterizing Exoplanetary Atmospheres. ApJ **758**, 36 (2012).

Madhusudhan, N.; Burrows, A. and Currie, T. Model Atmospheres for Massive Gas Giants with Thick Clouds: Application to the HR 8799 Planets and Predictions for Future Detections. ApJ **737**, 34 (2011a).

Madhusudhan, N.; Crouzet, N.; McCullough, P. R.; Deming, D. and Hedges, C. H_2O Abundances in the Atmospheres of Three Hot Jupiters. ApJ **791**, L9 (2014).

Madhusudhan, N.; Harrington, J.; Stevenson, K. B.; Nymeyer, S.; Campo, C. J.; Wheatley, P. J.; Deming, D.; Blecic, J.; Hardy, R. A.; Lust, N. B.; Anderson, D. R.; Collier-Cameron, A.; Britt, C. B. T.; Bowman, W. C.; Hebb, L.; Hellier, C.; Maxted, P. F. L.; Pollacco, D. and West, R. G. A high C/O ratio and weak thermal inversion in the atmosphere of exoplanet WASP-12b. Nature **469**, 64 (2011b).

Madhusudhan, N.; Mousis, O.; Johnson, T. V. and Lunine, J. I. Carbon-rich Giant Planets: Atmospheric Chemistry, Thermal Inversions, Spectra, and Formation Conditions. ApJ **743**, 191 (2011c).

Madhusudhan, N. and Seager, S. A Temperature and Abundance Retrieval Method for Exoplanet Atmospheres. ApJ **707**, 24 (2009).

Madhusudhan, N. and Seager, S. High Metallicity and Non-equilibrium Chemistry in the Dayside Atmosphere of hot-Neptune GJ 436b. ApJ **729**, 41 (2011).

352

Mainzer, A. K.; Roellig, T. L.; Saumon, D.; Marley, M. S.; Cushing, M. C.; Sloan, G. C.; Kirkpatrick, J. D.; Leggett, S. K. and Wilson, J. C. Moderate-Resolution Spitzer Infrared Spectrograph Observations of M, L, and T Dwarfs. ApJ **662**, 1245 (2007).

Mandel, K. and Agol, E. Analytic Light Curves for Planetary Transit Searches. ApJ **580**, L171 (2002).

Marley, M. The Role of Condensates in L- and T-dwarf Atmospheres. In C. A. Griffith & M. S. Marley, ed., *From Giant Planets to Cool Stars* (2000), vol. 212 of *Astronomical Society of the Pacific Conference Series*, p. 152.

Marley, M. S.; Ackerman, A. S.; Burgasser, A. J.; Saumon, D.; Lodders, K. and Freedman, R. Clouds and Clearings in the Atmospheres of the L and T Dwarfs. In Martín, E., ed., *Brown Dwarfs* (2003), vol. 211 of *IAU Symposium*, p. 333.

Marley, M. S.; Ackerman, A. S.; Cuzzi, J. N. and Kitzmann, D. Clouds and Hazes in Exoplanet Atmospheres. *ArXiv e-prints* (2013).

Marley, M. S.; Gelino, C.; Stephens, D.; Lunine, J. I. and Freedman, R. Reflected Spectra and Albedos of Extrasolar Giant Planets. I. Clear and Cloudy Atmospheres. ApJ **513**, 879 (1999).

Marley, M. S. and McKay, C. P. Thermal Structure of Uranus' Atmosphere. Icarus **138**, 268 (1999a).

Marley, M. S. and McKay, C. P. Thermal Structure of Uranus' Atmosphere. *Icarus* **138**, 268 (1999b).

Marley, M. S.; Saumon, D.; Cushing, M.; Ackerman, A. S.; Fortney, J. J. and Freedman, R. Masses, Radii, and Cloud Properties of the HR 8799 Planets. ApJ **754**, 135 (2012).

Marley, M. S.; Saumon, D. and Goldblatt, C. A Patchy Cloud Model for the L to T Dwarf Transition. ApJ **723**, L117 (2010).

Marley, M. S.; Saumon, D.; Guillot, T.; Freedman, R. S.; Hubbard, W. B.; Burrows, A. and Lunine, J. I. Atmospheric, evolutionary, and spectral models of the brown dwarf Gliese 229B. *Science* **272**, 1919 (1996).

Marley, M. S.; Seager, S.; Saumon, D.; Lodders, K.; Ackerman, A. S.; Freedman, R. S. and Fan, X. Clouds and Chemistry: Ultracool Dwarf Atmospheric Properties from Optical and Infrared Colors. ApJ **568**, 335 (2002).

Marois, C.; Macintosh, B.; Barman, T.; Zuckerman, B.; Song, I.; Patience, J.; Lafrenière, D. and Doyon, R. Direct Imaging of Multiple Planets Orbiting the Star HR 8799. *Science* **322**, 1348 (2008).

Marsh, K. A.; Wright, E. L.; Kirkpatrick, J. D.; Gelino, C. R.; Cushing, M. C.; Griffith, R. L.; Skrutskie, M. F. and Eisenhardt, P. R. Parallaxes and Proper Motions of Ultracool Brown Dwarfs of Spectral Types Y and Late T. ApJ **762**, 119 (2013).

Max, C. E.; Macintosh, B. A.; Gibbard, S. G.; Gavel, D. T.; Roe, H. G.; de Pater, I.; Ghez, A. M.; Acton, D. S.; Lai, O.; Stomski, P. and Wizinowich, P. L. Cloud Structures on Neptune Observed with Keck Telescope Adaptive Optics. AJ **125**, 364 (2003).

McBride, J.; Graham, J. R.; Macintosh, B.; Beckwith, S. V. W.; Marois, C.; Poyneer, L. A. and Wiktorowicz, S. J. Experimental Design for the Gemini Planet Imager. PASP **123**, 692 (2011).

McKay, C. P.; Coustenis, A.; Samuelson, R. E.; Lemmon, M. T.; Lorenz, R. D.; Cabane, M.; Rannou, P. and Drossart, P. Physical properties of the organic aerosols and clouds on Titan. Planet. Space Sci. **49**, 79 (2001).

McKay, C. P.; Lorenz, R. D. and Lunine, J. I. Analytic Solutions for the Antigreenhouse Effect: Titan and the Early Earth. Icarus **137**, 56 (1999).

McKay, C. P.; Pollack, J. B. and Courtin, R. The thermal structure of Titan's atmosphere. *Icarus* **80**, 23 (1989).

McKay, C. P.; Pollack, J. B. and Courtin, R. The greenhouse and antigreenhouse effects on Titan. *Science* **253**, 1118 (1991).

Metchev, S. A. and Hillenbrand, L. A. HD 203030B: An Unusually Cool Young Substellar Companion near the L/T Transition. ApJ **651**, 1166 (2006).

Miller-Ricci, E. and Fortney, J. J. The Nature of the Atmosphere of the Transiting Super-Earth GJ 1214b. ApJ **716**, L74 (2010).

Miller-Ricci, E.; Seager, S. and Sasselov, D. The Atmospheric Signatures of Super-Earths: How to Distinguish Between Hydrogen-Rich and Hydrogen-Poor Atmospheres. ApJ **690**, 1056 (2009).

Miller-Ricci Kempton, E.; Zahnle, K. and Fortney, J. J. The Atmospheric Chemistry of GJ 1214b: Photochemistry and Clouds. ApJ **745**, 3 (2012).

Montaner, A.; Galtier, M.; Benoit, C. and Bill, H. Optical constants of sodium sulphide. *Physica Status Solidi Applied Research* **52**, 597 (1979).

Montmessin, F.; Bertaux, J.-L.; Quémerais, E.; Korablev, O.; Rannou, P.; Forget, F.; Perrier, S.; Fussen, D.; Lebonnois, S.; Rébérac, A. and Dimarellis, E. Subvisible CO_2 ice clouds detected in the mesosphere of Mars. Icarus **183**, 403 (2006).

Morley, C. V.; Fortney, J. J.; Kempton, E. M.-R.; Marley, M. S.; Visscher, C. and Zahnle, K. Quantitatively Assessing the Role of Clouds in the Transmission Spectrum of GJ 1214b. ApJ **775**, 33 (2013).

Morley, C. V.; Fortney, J. J.; Marley, M. S.; Visscher, C.; Saumon, D. and Leggett, S. K. Neglected Clouds in T and Y Dwarf Atmospheres. ApJ **756**, 172 (2012).

Morley, C. V.; Fortney, J. J.; Marley, M. S.; Zahnle, K.; Line, M.; Kempton, E.; Lewis, N. and Cahoy, K. Thermal Emission and Reflected Light Spectra of Super Earths with Flat Transmission Spectra. ApJ **815**, 110 (2015).

Morley, C. V.; Marley, M. S.; Fortney, J. J.; Lupu, R.; Saumon, D.; Greene, T. and Lodders, K. Water Clouds in Y Dwarfs and Exoplanets. ApJ **787**, 78 (2014).

Moses, J. I.; Fouchet, T.; Bézard, B.; Gladstone, G. R.; Lellouch, E. and Feuchtgruber, H. Photochemistry and diffusion in Jupiter's stratosphere: Constraints from ISO observations

and comparisons with other giant planets. *Journal of Geophysical Research (Planets)* **110**, 8001 (2005).

Moses, J. I.; Line, M. R.; Visscher, C.; Richardson, M. R.; Nettelmann, N.; Fortney, J. J.; Stevenson, K. B. and Madhusudhan, N. Compositional diversity in the atmospheres of hot Neptunes, with application to GJ 436b. *ArXiv e-prints* (2013).

Moses, J. I.; Richardson, M. R.; Madhusudhan, N.; Line, M. R.; Visscher, C. and Fortney, J. J. The Chemistry of Metal-Rich Hot Neptunes. In *AAS/Division for Planetary Sciences Meeting Abstracts* (2012), vol. 44 of *AAS/Division for Planetary Sciences Meeting Abstracts*, p. 103.02.

Moses, J. I.; Visscher, C.; Fortney, J. J.; Showman, A. P.; Lewis, N. K.; Griffith, C. A.; Klippenstein, S. J.; Shabram, M.; Friedson, A. J.; Marley, M. S. and Freedman, R. S. Disequilibrium Carbon, Oxygen, and Nitrogen Chemistry in the Atmospheres of HD 189733b and HD 209458b. ApJ **737**, 15 (2011).

Murgas, F.; Pallé, E.; Cabrera-Lavers, A.; Colón, K. D.; Martín, E. L. and Parviainen, H. Narrow band Hα photometry of the super-Earth GJ 1214b with GTC/OSIRIS tunable filters. A&A **544**, A41 (2012).

Nakajima, T.; Oppenheimer, B. R.; Kulkarni, S. R.; Golimowski, D. A.; Matthews, K. and Durrance, S. T. Discovery of a Cool Brown Dwarf. Nature **378**, 463 (1995).

Naud, M.-E.; Artigau, É.; Malo, L.; Albert, L.; Doyon, R.; Lafrenière, D.; Gagné, J.; Saumon, D.; Morley, C. V.; Allard, F.; Homeier, D.; Beichman, C. A.; Gelino, C. R. and Boucher, A.

Discovery of a Wide Planetary-mass Companion to the Young M3 Star GU Psc. ApJ **787**, 5 (2014).

Nettelmann, N.; Fortney, J. J.; Kramm, U. and Redmer, R. Thermal Evolution and Structure Models of the Transiting Super-Earth GJ 1214b. ApJ **733**, 2 (2011).

Nettelmann, N.; Kramm, U.; Redmer, R. and Neuhäuser, R. Interior structure models of GJ 436b. A&A **523**, A26 (2010).

Noll, K. S.; Geballe, T. R. and Marley, M. S. Detection of Abundant Carbon Monoxide in the Brown Dwarf Gliese 229B. ApJ **489**, L87 (1997).

Oppenheimer, B. R.; Kulkarni, S. R.; Matthews, K. and Nakajima, T. Infrared Spectrum of the Cool Brown Dwarf GL:229B. *Science* **270**, 1478 (1995).

Orton, G.; Ortiz, J. L.; Baines, K.; Bjoraker, G.; Carsenty, U.; Colas, F.; Dayal, A.; Deming, D.; Drossart, P.; Frappa, E.; Friedson, J.; Goguen, J.; Golisch, W.; Griep, D.; Hernandez, C.; Hoffmann, W.; Jennings, D.; Kaminski, C.; Kuhn, J.; Laques, P.; Limaye, S.; Lin, H.; Lecacheux, J.; Martin, T.; McCabe, G.; Momary, T.; Parker, D.; Puetter, R.; Ressler, M.; Reyes, G.; Sada, P.; Spencer, J.; Spitale, J.; Stewart, S.; Varsik, J.; Warell, J.; Wild, W.; Yanamandra-Fisher, P.; Fazio, G.; Hora, J. and Deutsch, L. Earth-Based Observations of the Galileo Probe Entry Site. *Science* **272**, 839 (1996).

Pál, A.; Bakos, G. Á.; Torres, G.; Noyes, R. W.; Fischer, D. A.; Johnson, J. A.; Henry, G. W.; Butler, R. P.; Marcy, G. W.; Howard, A. W.; Sipőcz, B.; Latham, D. W. and Esquerdo, G. A.

Refined stellar, orbital and planetary parameters of the eccentric HAT-P-2 planetary system. MNRAS **401**, 2665 (2010).

Parmentier, V. and Guillot, T. A non-grey analytical model for irradiated atmospheres. I. Derivation. A&A **562**, A133 (2014).

Pollack, J. B.; Rages, K.; Pope, S. K.; Tomasko, M. G. and Romani, P. N. Nature of the stratospheric haze on Uranus - Evidence for condensed hydrocarbons. J. Geophys. Res. **92**, 15037 (1987).

Pont, F.; Gilliland, R. L.; Knutson, H.; Holman, M. and Charbonneau, D. Transit infrared spectroscopy of the hot Neptune around GJ 436 with the Hubble Space Telescope. MNRAS **393**, L6 (2009).

Pont, F.; Knutson, H.; Gilliland, R. L.; Moutou, C. and Charbonneau, D. Detection of atmospheric haze on an extrasolar planet: the 0.55-1.05 μm transmission spectrum of HD 189733b with the Hubble Space Telescope. MNRAS **385**, 109 (2008).

Pont, F.; Sing, D. K.; Gibson, N. P.; Aigrain, S.; Henry, G. and Husnoo, N. The prevalence of dust on the exoplanet HD 189733b from Hubble and Spitzer observations. *ArXiv e-prints* (2012).

Prinn, R. G. Venus: Composition and Structure of the Visible Clouds. *Science* **182**, 1132 (1973).

Prinn, R. G. and Lewis, J. S. Phosphine on Jupiter and implications for the Great Red SPOT. *Science* **190**, 274 (1975).

Querry, M. R. *Optical Constants of Minerals and Other Materials From the Millimeter to the Ultraviolet*. U.S. Army Armament Munitions Chemical Command (1987).

Radigan, J.; Jayawardhana, R.; Lafrenière, D.; Artigau, É.; Marley, M. and Saumon, D. Large-amplitude Variations of an L/T Transition Brown Dwarf: Multi-wavelength Observations of Patchy, High-contrast Cloud Features. ApJ **750**, 105 (2012).

Radigan, J.; Lafrenière, D.; Jayawardhana, R. and Artigau, E. Strong Brightness Variations Signal Cloudy-to-Clear Transition of Brown Dwarfs. *ArXiv e-prints* (2014).

Rages, K.; Beebe, R. and Senske, D. Jovian Stratospheric Hazes: The High Phase Angle View from Galileo. *Icarus* **139**, 211 (1999).

Rages, K.; Pollack, J. B.; Tomasko, M. G. and Doose, L. R. Properties of scatterers in the troposphere and lower stratosphere of Uranus based on Voyager imaging data. Icarus **89**, 359 (1991).

Ranjan, S.; Charbonneau, D.; Désert, J.-M.; Madhusudhan, N.; Deming, D.; Wilkins, A. and Mandell, A. M. Atmospheric Characterization of Five Hot Jupiters with the Wide Field Camera 3 on the Hubble Space Telescope. ApJ **785**, 148 (2014).

Rhines, P. Edge-, bottom-, and Rossby waves in a rotating stratified fluid. *Geophysical and Astrophysical Fluid Dynamics* **1**, 273 (1970).

Ribas, I.; Font-Ribera, A. and Beaulieu, J.-P. A ~5 M$_?$ Super-Earth Orbiting GJ 436? The Power of Near-Grazing Transits. ApJ **677**, L59 (2008).

Richard, C.; Gordon, I. E.; Rothman, L. S.; Abel, M.; Frommhold, L.; Gustafsson, M.; Hart-
mann, J.-M.; Hermans, C.; Lafferty, W. J.; Orton, G. S.; Smith, K. M. and Tran, H. New
section of the HITRAN database: Collision-induced absorption (CIA). J. Quant. Spec. Ra-
diat. Transf. **113**, 1276 (2012).

Ricker, G. R.; Winn, J. N.; Vanderspek, R.; Latham, D. W.; Bakos, G. Á.; Bean, J. L.; Berta-
Thompson, Z. K.; Brown, T. M.; Buchhave, L.; Butler, N. R.; Butler, R. P.; Chaplin, W. J.;
Charbonneau, D.; Christensen-Dalsgaard, J.; Clampin, M.; Deming, D.; Doty, J.; De Lee,
N.; Dressing, C.; Dunham, E. W.; Endl, M.; Fressin, F.; Ge, J.; Henning, T.; Holman, M. J.;
Howard, A. W.; Ida, S.; Jenkins, J.; Jernigan, G.; Johnson, J. A.; Kaltenegger, L.; Kawai, N.;
Kjeldsen, H.; Laughlin, G.; Levine, A. M.; Lin, D.; Lissauer, J. J.; MacQueen, P.; Marcy,
G.; McCullough, P. R.; Morton, T. D.; Narita, N.; Paegert, M.; Palle, E.; Pepe, F.; Pepper,
J.; Quirrenbach, A.; Rinehart, S. A.; Sasselov, D.; Sato, B.; Seager, S.; Sozzetti, A.; Stas-
sun, K. G.; Sullivan, P.; Szentgyorgyi, A.; Torres, G.; Udry, S. and Villasenor, J. Transiting
Exoplanet Survey Satellite (TESS). In *Society of Photo-Optical Instrumentation Engineers
(SPIE) Conference Series* (2014), vol. 9143 of *Society of Photo-Optical Instrumentation En-
gineers (SPIE) Conference Series*, p. 20.

Robinson, T. D.; Maltagliati, L.; Marley, M. S. and Fortney, J. J. Titan solar occultation ob-
servations reveal transit spectra of a hazy world. *Proceedings of the National Academy of
Science* **111**, 9042 (2014).

Robinson, T. D. and Marley, M. S. Temperature Fluctuations as a Source of Brown Dwarf
Variability. ApJ **785**, 158 (2014).

Rodgers, C. D. Approximate methods of calculating transmission by bands of spectral lines. Tech. rep. (1976).

Rodgers, C. D. Inverse Methods for Atmospheric Sounding - Theory and Practice. *Inverse Methods for Atmospheric Sounding - Theory and Practice. Series: Series on Atmospheric Oceanic and Planetary Physics, ISBN: <ISBN>9789812813718</ISBN>. World Scientific Publishing Co. Pte. Ltd., Edited by Clive D. Rodgers, vol. 2* **2** (2000).

Rogers, L. A. Most 1.6 Earth-radius Planets are Not Rocky. ApJ **801**, 41 (2015).

Rogers, L. A. and Seager, S. Three Possible Origins for the Gas Layer on GJ 1214b. ApJ **716**, 1208 (2010).

Rossow, W. B. Cloud microphysics - Analysis of the clouds of Earth, Venus, Mars, and Jupiter. Icarus **36**, 1 (1978).

Sánchez-Lavega, A.; del Río-Gaztelurrutia, T.; Hueso, R.; Gómez-Forrellad, J. M.; Sanz-Requena, J. F.; Legarreta, J.; García-Melendo, E.; Colas, F.; Lecacheux, J.; Fletcher, L. N.; Barrado y Navascués, D.; Parker, D.; International Outer Planet Watch Team; Akutsu, T.; Barry, T.; Beltran, J.; Buda, S.; Combs, B.; Carvalho, F.; Casquinha, P.; Delcroix, M.; Ghomizadeh, S.; Go, C.; Hotershall, J.; Ikemura, T.; Jolly, G.; Kazemoto, A.; Kumamori, T.; Lecompte, M.; Maxson, P.; Melillo, F. J.; Milika, D. P.; Morales, E.; Peach, D.; Phillips, J.; Poupeau, J. J.; Sussenbach, J.; Walker, G.; Walker, S.; Tranter, T.; Wesley, A.; Wilson, T. and Yunoki, K. Deep winds beneath Saturn's upper clouds from a seasonal long-lived planetary-scale storm. Nature **475**, 71 (2011).

Saumon, D.; Geballe, T. R.; Leggett, S. K.; Marley, M. S.; Freedman, R. S.; Lodders, K.; Fegley, B. and Sengupta, S. K. Molecular Abundances in the Atmosphere of the T Dwarf GL 229B. ApJ **541**, 374 (2000).

Saumon, D. and Marley, M. S. The Evolution of L and T Dwarfs in Color-Magnitude Diagrams. ApJ **689**, 1327 (2008).

Saumon, D.; Marley, M. S.; Abel, M.; Frommhold, L. and Freedman, R. S. New H_2 Collision-induced Absorption and NH_3 Opacity and the Spectra of the Coolest Brown Dwarfs. ApJ **750**, 74 (2012).

Saumon, D.; Marley, M. S.; Cushing, M. C.; Leggett, S. K.; Roellig, T. L.; Lodders, K. and Freedman, R. S. Ammonia as a Tracer of Chemical Equilibrium in the T7.5 Dwarf Gliese 570D. ApJ **647**, 552 (2006).

Saumon, D.; Marley, M. S.; Leggett, S. K.; Geballe, T. R.; Stephens, D.; Golimowski, D. A.; Cushing, M. C.; Fan, X.; Rayner, J. T.; Lodders, K. and Freedman, R. S. Physical Parameters of Two Very Cool T Dwarfs. ApJ **656**, 1136 (2007).

Seager, S.; Kuchner, M.; Hier-Majumder, C. A. and Militzer, B. Mass-Radius Relationships for Solid Exoplanets. ApJ **669**, 1279 (2007).

Seager, S. and Sasselov, D. D. Theoretical Transmission Spectra during Extrasolar Giant Planet Transits. ApJ **537**, 916 (2000).

Shabram, M.; Fortney, J. J.; Greene, T. P. and Freedman, R. S. Transmission Spectra of Transiting Planet Atmospheres: Model Validation and Simulations of the Hot Neptune GJ 436b for the James Webb Space Telescope. ApJ **727**, 65 (2011).

Showman, A. P.; Fortney, J. J.; Lian, Y.; Marley, M. S.; Freedman, R. S.; Knutson, H. A. and Charbonneau, D. Atmospheric Circulation of Hot Jupiters: Coupled Radiative-Dynamical General Circulation Model Simulations of HD 189733b and HD 209458b. ApJ **699**, 564 (2009).

Showman, A. P. and Kaspi, Y. Atmospheric Dynamics of Brown Dwarfs and Directly Imaged Giant Planets. ApJ **776**, 85 (2013).

Showman, A. P.; Menou, K. and Cho, J. Y.-K. Atmospheric Circulation of Hot Jupiters: A Review of Current Understanding. In Fischer, D.; Rasio, F. A.; Thorsett, S. E. and Wolszczan, A., eds., *Astronomical Society of the Pacific Conference Series* (2008), vol. 398 of *Astronomical Society of the Pacific Conference Series*, pp. 419–+.

Simcoe, R. A.; Burgasser, A. J.; Bernstein, R. A.; Bigelow, B. C.; Fishner, J.; Forrest, W. J.; McMurtry, C.; Pipher, J. L.; Schechter, P. L. and Smith, M. FIRE: a near-infrared cross-dispersed echellette spectrometer for the Magellan telescopes. In *Society of Photo-Optical Instrumentation Engineers (SPIE) Conference Series* (2008), vol. 7014 of *Society of Photo-Optical Instrumentation Engineers (SPIE) Conference Series*.

Simcoe, R. A.; Burgasser, A. J.; Bochanski, J. J.; Schechter, P. L.; Bernstein, R. A.; Bigelow, B. C.; Pipher, J. L.; Forrest, W.; McMurtry, C.; Smith, M. J. and Fishner, J. The FIRE

infrared spectrometer at Magellan: construction and commissioning. In *Society of Photo-Optical Instrumentation Engineers (SPIE) Conference Series* (2010), vol. 7735 of *Society of Photo-Optical Instrumentation Engineers (SPIE) Conference Series*.

Sing, D. K.; Fortney, J. J.; Nikolov, N.; Wakeford, H. R.; Kataria, T.; Evans, T. M.; Aigrain, S.; Ballester, G. E.; Burrows, A. S.; Deming, D.; Désert, J.-M.; Gibson, N. P.; Henry, G. W.; Huitson, C. M.; Knutson, H. A.; Etangs, A. L. D.; Pont, F.; Showman, A. P.; Vidal-Madjar, A.; Williamson, M. H. and Wilson, P. A. A continuum from clear to cloudy hot-Jupiter exoplanets without primordial water depletion. Nature **529**, 59 (2016).

Sing, D. K.; Pont, F.; Aigrain, S.; Charbonneau, D.; Désert, J.-M.; Gibson, N.; Gilliland, R.; Hayek, W.; Henry, G.; Knutson, H.; Lecavelier Des Etangs, A.; Mazeh, T. and Shporer, A. Hubble Space Telescope transmission spectroscopy of the exoplanet HD 189733b: high-altitude atmospheric haze in the optical and near-ultraviolet with STIS. MNRAS **416**, 1443 (2011).

Sing, D. K.; Vidal-Madjar, A.; Désert, J.-M.; Lecavelier des Etangs, A. and Ballester, G. Hubble Space Telescope STIS Optical Transit Transmission Spectra of the Hot Jupiter HD 209458b. ApJ **686**, 658 (2008).

Skemer, A.; Apai, D.; Bailey, V.; Biller, B.; Bonnefoy, M.; Brandner, W.; Buenzli, E.; Close, L.; Crepp, J.; Defrere, D.; Desidera, S.; Eisner, J.; Esposito, S.; Fortney, J.; Henning, T.; Hinz, P.; Hofmann, K.-H.; Leisenring, J.; Males, J.; Millan-Gabet, R.; Morzinski, K.; Oza, A.; Pascucci, I.; Patience, J.; Rieke, G.; Schertl, D.; Schlieder, J.; Skrutskie, M.; Su, K.; Weigelt, G.; Woodward, C. E. and Zimmerman, N. LEECH: A 100 Night Exoplanet Imaging

Survey at the LBT. In Booth, M.; Matthews, B. C. and Graham, J. R., eds., *IAU Symposium* (2014), vol. 299 of *IAU Symposium*, pp. 70–71.

Skemer, A. J.; Marley, M. S.; Hinz, P. M.; Morzinski, K. M.; Skrutskie, M. F.; Leisenring, J. M.; Close, L. M.; Saumon, D.; Bailey, V. P.; Briguglio, R.; Defrere, D.; Esposito, S.; Follette, K. B.; Hill, J. M.; Males, J. R.; Puglisi, A.; Rodigas, T. J. and Xompero, M. Directly Imaged L-T Transition Exoplanets in the Mid-Infrared. *ArXiv e-prints* (2013).

Slowik, J. G.; Stainken, K.; Davidovits, P.; Williams, L.; Tayne, J.; Kolb, C.; Worsnop, D.; Rudich, Y.; P.F., C. and Jimenez, J. Particle Morphology and Density Characterization by Combined Mobility and Aerodynamic Diameter Measurements. Part 2: Application to Combustion-Generated Soot Aerosols as a Function of Fuel Equivalence Ratio. *Aerosol Science and Technology* **38**, 1206 (2004).

Smith, M. D. Estimation of a Length Scale to Use with the Quench Level Approximation for Obtaining Chemical Abundances. Icarus **132**, 176 (1998).

Snellen, I. A. G.; Brandl, B. R.; de Kok, R. J.; Brogi, M.; Birkby, J. and Schwarz, H. Fast spin of the young extrasolar planet β Pictoris b. Nature **509**, 63 (2014).

Sorahana, S.; Suzuki, T. K. and Yamamura, I. A signature of chromospheric activity in brown dwarfs revealed by 2.5-5.0 μm AKARI spectra. MNRAS **440**, 3675 (2014).

Sousa-Silva, C.; Al-Refaie, A. F.; Tennyson, J. and Yurchenko, S. N. ExoMol line lists - VII. The rotation-vibration spectrum of phosphine up to 1500 K. MNRAS **446**, 2337 (2015).

Spergel, D.; Gehrels, N.; Baltay, C.; Bennett, D.; Breckinridge, J.; Donahue, M.; Dressler, A.; Gaudi, B. S.; Greene, T.; Guyon, O.; Hirata, C.; Kalirai, J.; Kasdin, N. J.; Macintosh, B.; Moos, W.; Perlmutter, S.; Postman, M.; Rauscher, B.; Rhodes, J.; Wang, Y.; Weinberg, D.; Benford, D.; Hudson, M.; Jeong, W.-S.; Mellier, Y.; Traub, W.; Yamada, T.; Capak, P.; Colbert, J.; Masters, D.; Penny, M.; Savransky, D.; Stern, D.; Zimmerman, N.; Barry, R.; Bartusek, L.; Carpenter, K.; Cheng, E.; Content, D.; Dekens, F.; Demers, R.; Grady, K.; Jackson, C.; Kuan, G.; Kruk, J.; Melton, M.; Nemati, B.; Parvin, B.; Poberezhskiy, I.; Peddie, C.; Ruffa, J.; Wallace, J. K.; Whipple, A.; Wollack, E. and Zhao, F. Wide-Field InfrarRed Survey Telescope-Astrophysics Focused Telescope Assets WFIRST-AFTA 2015 Report. *ArXiv e-prints* (2015).

Sromovsky, L. A.; Fry, P. M. and Kim, J. H. Methane on Uranus: The case for a compact CH_4 cloud layer at low latitudes and a severe CH_4 depletion at high-latitudes based on re-analysis of Voyager occultation measurements and STIS spectroscopy. Icarus **215**, 292 (2011).

Sromovsky, L. A.; Revercomb, H. E.; Krauss, R. J. and Suomi, V. E. Voyager 2 observations of Saturn's northern mid-latitude cloud features - Morphology, motions, and evolution. J. Geophys. Res. **88**, 8650 (1983).

Stamnes, K.; Tsay, S.-C.; Jayaweera, K. and Wiscombe, W. Numerically stable algorithm for discrete-ordinate-method radiative transfer in multiple scattering and emitting layered media. Appl. Opt. **27**, 2502 (1988).

Stashchuk, V. S.; Dobrovolskaya, M. T. and Tkachenko, S. N. Optical properties and electronic characteristics of chromium. *Optics and Spectroscopy* **56**, 594 (1984).

Stephens, D. C.; Leggett, S. K.; Cushing, M. C.; Marley, M. S.; Saumon, D.; Geballe, T. R.; Golimowski, D. A.; Fan, X. and Noll, K. S. The 0.8-14.5 μm Spectra of Mid-L to Mid-T Dwarfs: Diagnostics of Effective Temperature, Grain Sedimentation, Gas Transport, and Surface Gravity. ApJ **702**, 154 (2009).

Stevenson, K. B.; Harrington, J.; Lust, N. B.; Lewis, N. K.; Montagnier, G.; Moses, J. I.; Visscher, C.; Blecic, J.; Hardy, R. A.; Cubillos, P. and Campo, C. J. Two nearby Sub-Earth-sized Exoplanet Candidates in the GJ 436 System. ApJ **755**, 9 (2012).

Stevenson, K. B.; Harrington, J.; Nymeyer, S.; Madhusudhan, N.; Seager, S.; Bowman, W. C.; Hardy, R. A.; Deming, D.; Rauscher, E. and Lust, N. B. Possible thermochemical disequilibrium in the atmosphere of the exoplanet GJ 436b. Nature **464**, 1161 (2010).

Sudarsky, D.; Burrows, A. and Hubeny, I. Theoretical Spectra and Atmospheres of Extrasolar Giant Planets. ApJ **588**, 1121 (2003).

Sudarsky, D.; Burrows, A.; Hubeny, I. and Li, A. Phase Functions and Light Curves of Wide-Separation Extrasolar Giant Planets. ApJ **627**, 520 (2005).

Sudarsky, D.; Burrows, A. and Pinto, P. Albedo and Reflection Spectra of Extrasolar Giant Planets. ApJ **538**, 885 (2000).

Sullivan, P. W.; Winn, J. N.; Berta-Thompson, Z. K.; Charbonneau, D.; Deming, D.; Dressing, C. D.; Latham, D. W.; Levine, A. M.; McCullough, P. R.; Morton, T.; Ricker, G. R.; Vanderspek, R. and Woods, D. The Transiting Exoplanet Survey Satellite: Simulations of Planet Detections and Astrophysical False Positives. ApJ **809**, 77 (2015).

Swain, M. R.; Vasisht, G. and Tinetti, G. The presence of methane in the atmosphere of an extrasolar planet. Nature **452**, 329 (2008).

Teske, J. K.; Turner, J. D.; Mueller, M. and Griffith, C. A. Optical observations of the transiting exoplanet GJ 1214b. MNRAS **431**, 1669 (2013).

Tinney, C. G.; Faherty, J. K.; Kirkpatrick, J. D.; Wright, E. L.; Gelino, C. R.; Cushing, M. C.; Griffith, R. L. and Salter, G. WISE J163940.83-684738.6: A Y Dwarf Identified by Methane Imaging. ApJ **759**, 60 (2012).

Tokunaga, A. T. and Vacca, W. D. The Mauna Kea Observatories Near-Infrared Filter Set. III. Isophotal Wavelengths and Absolute Calibration. PASP **117**, 421 (2005).

Toon, O. B.; McKay, C. P.; Ackerman, T. P. and Santhanam, K. Rapid calculation of radiative heating rates and photodissociation rates in inhomogeneous multiple scattering atmospheres. *Journal of Geophysical Research* **94**, 16287 (1989).

Toon, O. B.; Pollack, J. B. and Sagan, C. Physical properties of the particles composing the Martian dust storm of 1971-1972. Icarus **30**, 663 (1977).

Tsuji, T.; Ohnaka, K. and Aoki, W. Warm Dust in the Cool Brown Dwarf Gliese 229B and Spectroscopic Diagnosis of Dusty Photospheres. ApJ **520**, L119 (1999).

Tsuji, T.; Ohnaka, K.; Aoki, W. and Nakajima, T. Evolution of dusty photospheres through red to brown dwarfs: how dust forms in very low mass objects. A&A **308**, L29 (1996).

Tsuji, T.; Yamamura, I. and Sorahana, S. AKARI Observations of Brown Dwarfs. II. CO_2 as Probe of Carbon and Oxygen Abundances in Brown Dwarfs. ApJ **734**, 73 (2011).

Visscher, C.; Lodders, K. and Fegley, Jr., B. Atmospheric Chemistry in Giant Planets, Brown Dwarfs, and Low-mass Dwarf Stars. III. Iron, Magnesium, and Silicon. ApJ **716**, 1060 (2010).

Visscher, C.; Lodders, K. and Fegley, B. J. Atmospheric Chemistry in Giant Planets, Brown Dwarfs, and Low-Mass Dwarf Stars. II. Sulfur and Phosphorus. ApJ **648**, 1181 (2006).

Visscher, C. and Moses, J. I. Quenching of Carbon Monoxide and Methane in the Atmospheres of Cool Brown Dwarfs and Hot Jupiters. ApJ **738**, 72 (2011).

von Braun, K.; Boyajian, T. S.; Kane, S. R.; Hebb, L.; van Belle, G. T.; Farrington, C.; Ciardi, D. R.; Knutson, H. A.; ten Brummelaar, T. A.; López-Morales, M.; McAlister, H. A.; Schaefer, G.; Ridgway, S.; Collier Cameron, A.; Goldfinger, P. J.; Turner, N. H.; Sturmann, L. and Sturmann, J. The GJ 436 System: Directly Determined Astrophysical Parameters of an M Dwarf and Implications for the Transiting Hot Neptune. ApJ **753**, 171 (2012).

Wakeford, H. R.; Sing, D. K.; Deming, D.; Gibson, N. P.; Fortney, J. J.; Burrows, A. S.; Ballester, G.; Nikolov, N.; Aigrain, S.; Henry, G.; Knutson, H.; Lecavelier des Etangs, A.; Pont, F.; Showman, A. P.; Vidal-Madjar, A. and Zahnle, K. HST hot Jupiter transmission spectral survey: detection of water in HAT-P-1b from WFC3 near-IR spatial scan observations. MNRAS **435**, 3481 (2013).

Warren, S. G. Optical constants of ice from the ultraviolet to the microwave. Appl. Opt. **23**, 1206 (1984).

West, R. A.; Baines, K. H.; Friedson, A. J.; Banfield, D.; Ragent, B. and Taylor, F. W. *Jovian clouds and haze*, pp. 79–104 (2004).

Westphal, J. A. Observations of localised 5-micron radiation from Jupiter. ApJ **157**, L63 (1969).

Westphal, J. A.; Matthews, K. and Terrile, R. J. Five-micron pictures of Jupiter. ApJ **188**, L111 (1974).

Whiteway, J. A.; Komguem, L.; Dickinson, C.; Cook, C.; Illnicki, M.; Seabrook, J.; Popovici, V.; Duck, T. J.; Davy, R.; Taylor, P. A.; Pathak, J.; Fisher, D.; Carswell, A. I.; Daly, M.; Hipkin, V.; Zent, A. P.; Hecht, M. H.; Wood, S. E.; Tamppari, L. K.; Renno, N.; Moores, J. E.; Lemmon, M. T.; Daerden, F. and Smith, P. H. Mars Water-Ice Clouds and Precipitation. *Science* **325**, 68 (2009).

Witte, S.; Helling, C.; Barman, T.; Heidrich, N. and Hauschildt, P. H. Dust in brown dwarfs and extra-solar planets. III. Testing synthetic spectra on observations. A&A **529**, A44 (2011).

Witte, S.; Helling, C. and Hauschildt, P. H. Dust in brown dwarfs and extra-solar planets. II. Cloud formation for cosmologically evolving abundances. A&A **506**, 1367 (2009).

Wolfgang, A. and Lopez, E. How Rocky Are They? The Composition Distribution of Kepler's Sub-Neptune Planet Candidates within 0.15 AU. ApJ **806**, 183 (2015).

Wong, A.-S.; Yung, Y. L. and Friedson, A. J. Benzene and Haze Formation in the Polar Atmosphere of Jupiter. Geophys. Res. Lett. **30**, 1447 (2003).

Wong, I.; Knutson, H. A.; Lewis, N. K.; Kataria, T.; Burrows, A.; Fortney, J. J.; Schwartz, J.; Agol, E.; Cowan, N. B.; Deming, D.; Désert, J.-M.; Fulton, B. J.; Howard, A. W.; Langton,

J.; Laughlin, G.; Showman, A. P. and Todorov, K. 3.6 and 4.5 μm Phase Curves of the Highly Irradiated Eccentric Hot Jupiter WASP-14b. ApJ **811**, 122 (2015).

Wong, M. H.; Mahaffy, P. R.; Atreya, S. K.; Niemann, H. B. and Owen, T. C. Updated Galileo probe mass spectrometer measurements of carbon, oxygen, nitrogen, and sulfur on Jupiter. *Icarus* **171**, 153 (2004).

Yamamura, I.; Tsuji, T. and Tanabé, T. AKARI Observations of Brown Dwarfs. I. CO and CO_2 Bands in the Near-infrared Spectra. ApJ **722**, 682 (2010).

Young, L. A.; Yelle, R. V.; Young, R.; Seiff, A. and Kirk, D. B. Gravity waves in Jupiter's thermosphere. *Science* **276**, 108 (1997).

Yung, Y. L.; Allen, M. and Pinto, J. P. Photochemistry of the atmosphere of Titan - Comparison between model and observations. ApJS **55**, 465 (1984).

Yurchenko, S. N.; Barber, R. J. and Tennyson, J. A variationally computed line list for hot NH_3. MNRAS **413**, 1828 (2011).

Yurchenko, S. N. and Tennyson, J. ExoMol line lists - IV. The rotation-vibration spectrum of methane up to 1500 K. MNRAS **440**, 1649 (2014).

Yurchenko, S. N.; Tennyson, J.; Barber, R. J. and Thiel, W. Vibrational transition moments of CH_4 from first principles. *Journal of Molecular Spectroscopy* **291**, 69 (2013).

Zahnle, K.; Marley, M. S. and Fortney, J. J. Thermometric Soots on Warm Jupiters? *ArXiv e-prints* (2009a).

Zahnle, K.; Marley, M. S.; Freedman, R. S.; Lodders, K. and Fortney, J. J. Atmospheric Sulfur Photochemistry on Hot Jupiters. ApJ **701**, L20 (2009b).

Zahnle, K. J. and Marley, M. S. Methane, Carbon Monoxide, and Ammonia in Brown Dwarfs and Self-Luminous Giant Planets. ApJ **797**, 41 (2014).

Zellem, R. T.; Lewis, N. K.; Knutson, H. A.; Griffith, C. A.; Showman, A. P.; Fortney, J. J.; Cowan, N. B.; Agol, E.; Burrows, A.; Charbonneau, D.; Deming, D.; Laughlin, G. and Langton, J. The 4.5 μm Full-orbit Phase Curve of the Hot Jupiter HD 209458b. ApJ **790**, 53 (2014).

Zhang, K. and Hamilton, D. P. Orbital resonances in the inner neptunian system. II. Resonant history of Proteus, Larissa, Galatea, and Despina. Icarus **193**, 267 (2008).

Zhang, X. and Showman, A. P. Atmospheric Circulation of Brown Dwarfs: Jets, Vortices, and Time Variability. *ArXiv e-prints* (2014).